FACULDADE DE ENGENHARIA DA UNIVERSIDADE DO PORTO

Creep Behaviour of Composite Bonded Joints

Rui Filipe Magalhães Couto

Master's degree in Mechanical Engineering

Supervisor: Prof. Dr. Marcelo Francisco de Sousa Ferreira de Moura

Co-Supervisor: Prof. Dr. António Gonçalves de Magalhães

July 15, 2023

Creep Behaviour of Composite Bonded Joints

Rui Filipe Magalhães Couto

Master's degree in Mechanical Engineering

July 15, 2023

Abstract

Nowadays, adhesively bonded joints and repairs have been implemented in composite structures in various industries, such as automotive, aeronautical, aerospace and naval. Other industries such as the manufacturing of electronic components, civil construction, medicine, and even textile industry have been also contributing for developments in the field. Nevertheless, major scientific investigations have been presented by the aeronautical and aerospace industries, whose same technology can be implemented in composite bonded repairs, playing an important role in environmental protection and circular economy.

Composite bonded joints and repairs have been widely investigated in quasi-static and dynamic loading scenarios, where various properties are predicted, such as strength, stiffness, as well as fatigue life. In the aeronautical industry, ductile adhesives are frequently applied, presenting a viscoelastic nature. Consequently, long term static loads induce viscoelastic phenomena in the adhesive layer, possibly resulting in structural failure. A given composite structure, adhesively joined or repaired, may fail under those loading scenarios within a given lifetime.

Numerical models, implementing damage laws, related to cohesive zone modelling, using the finite element method, have been widely studied in quasi-static and fatigue loading scenarios. However, the numerical prediction of creep behaviour has not been as investigated as other conditions, specially in adhesively bonded joints and repairs. Several creep damage laws are well established in the literature, but for metallic materials. Indeed, it is necessary to postulate new numerical developments on creep analysis of bonded joints and repairs. Those laws can be adapted, combining other formulations where viscoelastic and degradation phenomena are taken into account. In this way, twelve creep damage laws are derived in this dissertation, being specially adapted for the creep damage analysis of bonded joints and repairs. Base laws already established for metallic materials, are combined with classical viscoelastic laws and also other formulations predicting degradation effects. These laws can be applied in a cohesive zone modelling environment, integrated in user-subroutines in a finite element software.

Both pure modes I and II were investigated in this dissertation, under creep loading, presenting numerical developments with corresponding experimental validation. Cohesive zone modelling, taking into account creep damage, was implemented, being able to predict the three creep stages: primary, secondary, and tertiary. Parametric studies were performed *"a priori"*, where a sensitivity of the laws to the involved parameters was analysed. Different loading levels were tested experimentally. Pure mode I loading scenarios demonstrated to be not only sensible to the applied load, but also to dimensional and geometrical defects. Due to the ductile nature of the adhesive, a creep threshold was found while testing under pure mode II loading. Established numerical laws allowed the prediction of all conditions, revealing good correlation between numerical and experimental results. In this way, this dissertation was able to present a new cohesive zone model related with creep analysis in composite bonded joints and repairs. Future studies can be performed for mixed-mode I+II loading, using the presented creep damage laws, for the analysis of composite bonded repairs under creep conditions.

Resumo

Atualmente, as juntas adesivas em materiais compósitos têm sido implementadas em várias indústrias, tais como a automóvel, aeronáutica, aeroespacial, naval, mas também noutras indústrias tais como o fabrico de componentes elétricos, construção civil, medicina, tecnologia têxtil, entre outras. No entanto, os desenvolvimentos que têm protagonizado avanços científicos estão relacionados com as indústrias aeronáutica e aeroespacial, em que a mesma tecnologia também é implementada em reparações estruturais, cuja utilização apresenta um papel crucial na proteção ambiental e economia circular.

As juntas e reparações adesivas com aplicação em estruturas compósitas têm sido investigadas em esforços quase-estáticos e dinâmicos, determinando diversas propriedades, tais como resistência e rigidez, bem como a sua longevidade à fadiga. Na indústria aeronáutica, os adesivos dúcteis são frequentemente utilizados, cujas propriedades favorecem um comportamento viscoelástico. Esforços estáticos de longa duração podem trazer fenómenos viscoelásticos na camada adesiva, podendo resultar numa falha estrutural ao fim de um dado período tempo.

Diversos modelos numéricos com leis de dano bem definidas, associadas a modelos coesivos, com uso do método dos elementos finitos, têm sido desenvolvidos para situações estáticas e de fadiga. No entanto, pouco desenvolvimento tem sido apresentado na previsão de falha por fluência em juntas e reparações adesivas. Adicionalmente, diversas leis de dano à fluência já se encontram estabelecidas, mas para materiais metálicos. São necessários desenvolvimentos numéricos, no que toca ao estudo do comportamento à fluência em adesivos. As leis já estabelecidas podem ser adaptadas, contabilizando fenómenos viscoelásticos e de degradação. Para o efeito, doze leis numéricas, apropriadas para o estudo do comportamento à fluência de adesivos, são postuladas nesta dissertação, juntando leis de base já estabelecidas para materiais metálicos com leis da viscoelasticade clássica e de degradação que contabilizam parâmetros físicos. Tais leis podem ser aplicadas num modelo de dano coesivo, integrando subrotinas em *software* de elementos finitos.

Nesta dissertação foram investigadas solictações de puro modo I e puro modo II à fluência, com desenvolvimentos numéricos, e respetiva validação experimental. Novos modelos coesivos, contabilizando as leis de dano à fluência, foram implementados, tendo sido capazes de prever os três estágios de fluência: primária, secundária e terciária. Um estudo paramétrico prévio foi executado, de forma a conhecer a sensibilidade dos resultados aos diferentes parâmetros. Diferentes níveis de carga foram testados experimentalmente, em que condições de modo I puro se reveleram extremamente sensíveis, não só a cenários de carregamento, mas também a defeitos dimensionais e geométricos. Devido à natureza dúctil do adesivo, foi detetado um limiar de fluência em condições de modo II puro. As leis numéricas estabelecidas tornaram possível a previsão de todas estas condições, revelando elevada similaridade entre resultados experimentais e numéricos. Este aspeto é crucial tendo em consideração que o objetivo último se centra no desenvolvimento de um modelo coesivo de modo misto I+II, capaz de prever o comportamento de juntas reparadas de materiais compósitos sob solicitações de fluência.

Agradecimentos

Neste longo percurso, que é o Mestrado em Engenharia Mecânica, tenho, em primeiro lugar, a agradecer a todos os professores da FEUP associados ao ramo de especialização de Estruturas Aeronáuticas e de Veículos. Todos eles contribuíram para os grandes ensinamentos passados, desde o primeiro dia.

Devo um especial agradecimento ao meu orientador, Prof. Dr. Marcelo Francisco Sousa Ferreira de Moura, Professor Associado da FEUP, cujo papel foi crucial para o sucesso desta dissertação. Mesmo tendo iniciado a pesquisa antes do início do segundo semestre, desde o primeiro dia, sempre se mostrou disponível a oferecer ajuda, conseguindo sempre uma janela de tempo, apesar da sua vasta atividade de investigação e ensino, tanto a nível de licenciatura, mestrado e doutoramento. Agradeço também a confiança que depositou em mim, mesmo sendo eu ainda um aluno de mestrado. Sei perfeitamente que foi uma exceção. Nunca esquecerei a grande ajuda prestada no período em que iniciei funções na indústria em regime laboral. Ficarei eternamente agradecido por ter a disponibilidade de ficar na faculdade até mais tarde para podermos reunir. Para mim foi um prazer enorme, e orgulho, tê-lo como orientador. Desde o início do meu percurso académico que tenho acompanhado o excelente trabalho desenvolvido, mesmo antes de o conhecer, e sequer de pertencer a esta belíssima casa. Para mim, foi um objetivo concretizado ter tido esta oportunidade de contribuir para a continuação dos exímios desenvolvimentos que tem apresentado. De facto, esta minha contribuição ainda não terminou, pois continuaremos o trabalho que será demonstrado em publicações científicas. Por último, ficarei eternamente grato pelos valores ensinados e pelo desenvolvimento pessoal que proporcionou. Em tudo o que faz, sempre valorizou o mérito, a qualidade e o esforço. É com certeza alguém que tenho o prazer de partilhar a paixão pela engenharia. Será para sempre uma referência para mim, e um exemplo a seguir.

Um grande obrigado ao meu co-orientador, Prof. Dr. António Gonçalves de Magalhães, Professor Coordenador do ISEP. Foi alguém que me acompanhou desde o momento em que nasci para a engenharia, e sempre me ajudou em todo o percurso realizado. Por isso, este agradecimento não fica apenas limitado a esta dissertação, mas fica destinado a longos, mas ao mesmo tempo breves, cinco anos de trabalho. Um especial agradecimento por me ter acompanhado em mais uma grande etapa. Sem dúvida, teve um crucial papel no desenvolvimento da componente experimental desta dissertação. Agradeço também todos os ensinamentos prestados na área da fluência de juntas adesivas, e por ter partilhado conhecimentos da sua vasta experiência de investigação. Muito obrigado por ter acompanhado todo o processo de ensaios, mesmo em regime pós-laboral, estendendo, muitas das vezes, o seu horário de trabalho. O Prof. Dr. António Gonçalves de Magalhães mostrou-se sempre um profissional exemplar, desde o primeiro dia que o conheço. Para mim, foi sempre um exemplo a seguir e também uma referência, e é dos melhores amigos que o meu percurso académico me deixou. Um eterno obrigado por tudo.

Um enorme obrigado ao Prof. Dr. Raúl Moreira, por toda a ajuda prestada. Na verdade, foi mais um orientador, sempre participando ativamente no suporte dos trabalhos. Agradeço por me ter acompanhado no fabrico de todos os provetes, e obrigado por me ter concedido longas horas do seu tempo. Tenho também a agradecer todas as dicas e conselhos que me foram passados, tendo por base toda a experiência do seu exímio trabalho de doutoramento. Toda a ajuda foi essencial no desenvolvimento desta dissertação, desde a componente experimental à componente numérica, revelando uma contribuição multidisciplinar e transversal a todos os temas abordados. Muito obrigado por todos os valores transmitidos, essencialmente no que toca ao mérito e à qualidade em tudo o que é feito. Deixou sempre claro que a engenharia é uma arte, e não um simples trabalho. Será sempre um amigo e uma referência a seguir.

Institucionalmente, tenho a agradecer à FEUP, no âmbito da realização desta dissertação de mestrado, ao INEGI, por me conceder o Laboratório de Materiais Compósitos, e ao LAETA, no âmbito do projeto de investigação em que este tema se encontra inserido. Um especial obrigado ao ISEP por me conceder o Laboratório de Ensaios Tecnológicos, ficando agradecido ao Prof. Dr. Arnaldo Guedes Pinto, bem como à Eng.ª Fátima Andrade, responsáveis pelas instalações.

Obrigado a todos os docentes que contribuíram com pequenas dicas e contribuições. Agradeço ao Prof. Dr. Volnei Tita, Docente Afiliado da FEUP, e Professor da Universidade de São Paulo, pela bibliografia aconselhada para o desenvolvimento do estado-de-arte no que toca à certificação aeronáutica de reparações adesivas. Agradeço ao Prof. Dr. João Francisco Silva, bem como ao Prof. Dr. Púria Esfandiari, do ISEP, por todos os conselhos dados durante o desenvolvimento da fase experimental.

Devo um agradecimento aos meus colegas de curso e de ramo de mestrado da FEUP, que são amigos que esta casa me trouxe. Todos nós trabalhamos em equipa, desde o início do mestrado, com um grande espírito de ajuda e cooperação. Por isso, um espacial obrigado à Ana Mafalda Couto, ao José Nascimento, ao Vasco Couto Rodrigues, à Ana Rita Ribeiro, à Ana Leonor Ribeiro, ao Nuno Costa, ao Vasco Pires, ao Guilherme Coelho, ao Ricardo Faria, à Dilki Dias Arachchige e ao Douglas Rodriguez Nascimento.

Por último, e não menos importante, agradeço à empresa à qual pertenço, e à minha nova casa, Vestas, apesar não ter tido qualquer relação com a realização desta dissertação. Pertencer à Vestas ajudou-me a reencontrar o rumo certo, e a aumentar ainda mais a minha paixão pela engenharia. Ver a concretização da minha vontade de ir à descoberta da engenharia real foi muito gratificante, e ficarei eternamente grato pela motivação que trabalhar na Vestas me deu para o desenvolvimento desta dissertação na parte final do semestre. Agradeço os conselhos dos meus colegas do departamento de Loads & Control (LaC), que estiveram na mesma situação, no que toca à combinação de trabalho laboral com dissertação, em regimes diferentes.

Rui Couto

“As armas e os barões assinalados
Que da Ocidental praia Lusitana,
Por mares nunca dantes navegados
Passaram ainda além da Taprobana,
Em perigos e guerras esforçados
Mais do que prometia a força humana,
E entre gente remota edificaram
Novo Reino, que tanto sublimaram.”

Luís Vaz de Camões, em *“Os Lusíadas”* (Canto I)

Contents

1 Introduction **1**
1.1 Context and Motivation . . . 1
1.2 Objectives and Methodology . . . 2
1.3 Document Structure and Outline . . . 3

2 Literature Review **4**
2.1 Fundaments on Adhesive Bonding . . . 4
2.1.1 Composite Materials and Importance of Repairing . . . 5
2.1.2 Historical Perspective and Applications . . . 7
2.1.3 Advantages and Disadvantages . . . 10
2.2 Bonded Joints and Repairs: Design and Manufacturing . . . 13
2.2.1 Theory of Adhesion . . . 13
2.2.2 Design Principles . . . 16
2.2.3 Background on Bonded Repairs: Design and Research Developments . . . 21
2.2.4 Manufacturing and Inspection Techniques of Bonded Repairs . . . 27
2.2.5 Durability and Environmental Effects of Bonded Repairs . . . 32
2.2.6 Aeronautical Certification of Composite Bonded Repairs . . . 42

3 Experimental Procedures **55**
3.1 Materials . . . 56
3.1.1 Carbon-Epoxy HS160REM . . . 56
3.1.2 Adhesive ARALDITE® 2015-1 . . . 56
3.2 Geometries and Nominal Dimensions . . . 56
3.2.1 Double-Cantilever-Beam (DCB) . . . 58
3.2.2 End-Notched-Flexure (ENF) . . . 59
3.3 Specimen Preparation . . . 60
3.4 Experimental Testing for Fracture Characterisation . . . 65
3.4.1 Experimental Testing considering Pure Mode I Loading . . . 66
3.4.2 Experimental Testing considering Pure Mode II Loading . . . 71

4 Numerical Developments **76**
4.1 Viscoelastic Models for Creep and Stress Relaxation . . . 77
4.1.1 Linear Viscoelastic Constitutive Models . . . 77
4.1.2 Nonlinear Creep and Stress Relaxation . . . 88
4.1.3 Applied Models on the Material Characterisation under Creep and Stress Relaxation . . . 91
4.2 Creep Crack Growth Prediction . . . 100
4.2.1 Cohesive Zone Modelling (CZM) . . . 100

4.2.2 Theoretical Background on Creep Crack Growth 105
4.2.3 Principles of CZM applied to Creep of Bonded Joints 115
4.3 Crack Damage Laws considering Rheological Parameters 119
4.3.1 Pure Mode I Loading 123
4.3.2 Pure Mode II Loading 144

5 Conclusions **163**

List of Figures

2.1 Aerospace materials evolution: (a) aluminium, (b) composite materials, (Mouritz, 2012). 5
2.2 Material constitution of the Boeing 787 (Bona, 2019). 6
2.3 Environmental effects related to pyrolysis: calculations per 1 kg of CFRP waste (Khalil, 2018). 7
2.4 Fokker Dr.I used in the WWI (USAF, 2022a). 8
2.5 De Havilland Mosquito used in the WWII (USAF, 2022b). 9
2.6 Airbus A350 XWB (Airbus, 2016). 10
2.7 Comparison between bolted and bonded joints in terms of stress distribution (Daylan, 2021). 11
2.8 Crack propagation of repairs: (a) bolted, (b) bonded, (Baker et al., 2002). 11
2.9 Effects of peel stresses on composite adherends (da Silva and Adams, 2006). 12
2.10 Localised peel stresses in the adhesive ends. 13
2.11 Multidisciplinary nature of adhesion science (Petrie, 2007). 14
2.12 Physical and chemical adsorption representation (da Silva et al., 2007; ManoxBlog, 2020). 15
2.13 Representation scheme of a hybrid bonded joint containing *"chicken-rivets"* (Sadowski et al., 2010). 17
2.14 Real representation of a hybrid bonded joint containing *"chicken-rivets"* (Sadowski et al., 2010). 17
2.15 Loading scenarios in adhesively bonded joints (da Silva et al., 2007). 18
2.16 Failure modes in adhesively bonded joints (da Silva et al., 2007, 2011). 19
2.17 Structure of an adhesive joint/repair (Petrie, 2007; da Silva et al., 2007, 2011). 19
2.18 Configurations of adhesively bonded joints (Petrie, 2007; da Silva et al., 2007): (a) butt joints, (b) overlap joints. 20
2.19 Bonded repair configurations (Moreira et al., 2020a): (a) single-strap, (b) double-strap, (c) scarf, (d) one-stepped, (e) two-stepped. 23
2.20 Doubler ply overlap in a scarf repair (Baker et al., 1999). 24
2.21 Adhesive application on a wing structure for a composite bonded repair (TCA, 2022). 28
2.22 Curing process by vacuum bagging applied to a composite bonded repair (DCMC, 2021). 29
2.23 Inspection composite bonded joints or repairs: (a) UT, (b) IRT (Evident, 2022; Galietti et al., 2012) 30
2.24 Manufacturing timeline of a composite bonded repair (Budhe et al., 2018). 30
2.25 Thermal ageing on a typical epoxy adhesive (Petrie, 2007). 33
2.26 Load-displacement curves of DCB tests showing the recovery of drying processes (Budhe et al., 2014). 36

2.27 Model considered by Wang et al. (2021): (a) steel stringer, (b) cast iron stringer. . . 39
2.28 Image processing methodology by the concept of *"damaged pixels"* (Schrader et al., 2022). 39
2.29 Comparison between optical and compliance-based methodologies in the determination of crack propagation rate (Schrader et al., 2022). 40
2.30 Ultrasonic testing explained by FAA (2012). 45
2.31 Storage of prepregs (FAA, 2012). 47
2.32 Heat affected zones and corresponding inspection (FAA, 2012). 50
2.33 Testing pyramid for aircraft structures (FAA, 2009). 51
2.34 Flowchart related to certification process of repairs on PSEs (Baker et al., 2015). 53
2.35 Flowchart describing the design procedure of a repair (Poudel et al., 2015). . . . 54

3.1 WENDT® cutting machine. 57
3.2 Carbon-epoxy plate with 16 unidirectional layers. 57
3.3 200 mL bi-component cartridges corresponding to ARALDITE® 2015-1. 58
3.4 DCB geometry and boundary conditions. 59
3.5 ENF geometry and boundary conditions. 59
3.6 Substrates after surface preparation. 61
3.7 Mould cleaner: (a) product reference, (b) danger caution. 61
3.8 Semi-permanent mould release agent: (a) product reference, (b) danger caution. . 62
3.9 Accessories for pre-crack preparation. 62
3.10 Substrates after adhesive application. 63
3.11 Specimens after joining substrates. 64
3.12 PROXXON® disc sander. 64
3.13 Hinges for load application. 65
3.14 DCB specimen with bonded hinges. 65
3.15 SHIMADZU® AG-I universal testing machine. 66
3.16 Creep curves of DCB tests from the first campaign. 67
3.17 Load-displacement curves of DCB tests. 67
3.18 Creep curves of DCB tests. 68
3.19 Creep curves of DCB tests: (a) 80% of P_{max}, (b) 85% of P_{max}. 69
3.20 Creep curves of DCB tests presenting adhesive failure. 70
3.21 Load-displacement curves of ENF tests. 71
3.22 Creep curves of ENF tests. 73
3.23 Creep curves of ENF tests and corresponding failure aspects: (a) 70% of P_{max}, (b) 75% of P_{max}, (c) 80% of P_{max}, (d) 85% of P_{max}. 73

4.1 Individual behaviours of a spring and dashpot (Findley et al., 1976). 78
4.2 Representative creep and relaxation behaviour by Maxwell model (Findley et al., 1976; Tanaka and Eijden, 2003). 79
4.3 Representative creep and relaxation behaviour by Voigt-Kelvin model (Findley et al., 1976; Tanaka and Eijden, 2003). 80
4.4 Representative creep and relaxation behaviour by a Zener model, following Tanaka and Eijden (2003). 82
4.5 Representative creep and relaxation behaviour by Burgers model, following (Findley et al., 1976; Arrospide et al., 2017). 83
4.6 Generalised model to represent the elastic and viscous components, as well as the *"delayed elasticity"* (Findley et al., 1976; Arrospide et al., 2017). 87
4.7 Demonstration of the Boltzmann's superposition principle in creep (Geiss, 2011). 88

4.8 Creep compliance calculation using a Prony series (Simsiriwong et al., 2015). . . 94
4.9 Shape of the cohesive damage laws available in the literature (Fernandes and Campilho, 2016): (a) triangular and linear-exponential, (b) trapezoidal. 101
4.10 Strain and time to failure determination method considered in Nikbin et al. (1984). 106
4.11 Stress degradation during creep, considered in Nikbin et al. (1984). 107
4.12 Errors in the determination of shear fracture energy: comparison between numerical and experimental results (data provided in Neto et al. (2022c)). 117
4.13 Degradation during phenomena of the CZM law (Neto et al., 2022b). 118
4.14 Parametric effects on the creep damage rate considering pure mode I loading: (a) A, (b) B. 125
4.15 Parametric effects on the creep damage rate considering pure mode I loading: Q. 126
4.16 Parametric effects on the creep damage rate considering pure mode I loading: η. 126
4.17 Parametric effects on the creep damage rate considering pure mode I loading: R. . 127
4.18 Parametric effects on the creep damage rate considering pure mode I loading: τ. . 127
4.19 Parametric effects on the creep damage rate considering pure mode I loading: (a) θ, (b) ϕ. 128
4.20 Parametric effects on the creep damage rate considering pure mode I loading: (a) n, (b) χ. 129
4.21 Parametric effects on the creep damage rate considering pure mode I loading: (a) T_c, (b) σ_t. 129
4.22 Boundary conditions and mesh for a DCB: (a) undeformed, (b) deformed. 131
4.23 Strength prediction: DCB. 131
4.24 Bilinear cohesive law for pure mode I loading. 132
4.25 Creep response, considering pure mode I loading, of damage laws proposed by Sun et al. (2012) and Haque and Maurice (2019). 134
4.26 Creep response, considering pure mode I loading, of damage laws based on the Maxwell viscoelastic model. 134
4.27 Creep response, considering pure mode I loading, of damage laws based on the Voigt-Kelvin viscoelastic model. 135
4.28 Creep response, considering pure mode I loading, of damage laws based on the Burgers viscoelastic model. 136
4.29 Creep response comparison, considering pure mode I loading, between the proposed laws and the literature (Sun et al., 2012; Haque and Maurice, 2019). 137
4.30 Effects of θ on the curve shape considering pure mode I loading. 137
4.31 Effects of θ on the curve shape considering pure mode I loading: amplified scale. 138
4.32 Effects of n on the curve shape considering pure mode I loading. 138
4.33 Effects of n on the curve shape considering pure mode I loading: amplified scale. 139
4.34 Effects of ϕ on the curve shape considering pure mode I loading. 139
4.35 Effects of ϕ on the curve shape considering pure mode I loading: amplified scale. 140
4.36 Effects of χ on the curve shape considering pure mode I loading. 141
4.37 Effects of χ on the curve shape considering pure mode I loading: amplified scale. 141
4.38 Numerical validation considering pure mode I loading: (a) KRVK (80% P_{max}), (b) KRVK (85% P_{max}), (c) LMVK (80% P_{max}), (d) LMVK (85% P_{max}), (e) KRVKS (80% P_{max}), (f) KRVKS (85% P_{max}), (g) LMVKH (80% P_{max}), (h) LMVKH (85% P_{max}). 143
4.39 Parametric effects on the creep damage rate considering pure mode II loading: (a) A, (b) B. 145
4.40 Parametric effects on the creep damage rate considering pure mode II loading: Q 146

4.41 Parametric effects on the creep damage rate considering pure mode II loading: η 147
4.42 Parametric effects on the creep damage rate considering pure mode II loading: R 147
4.43 Parametric effects on the creep damage rate considering pure mode II loading: τ . 148
4.44 Parametric effects on the creep damage rate considering pure mode II loading: (a) θ, (b) ϕ. 149
4.45 Parametric effects on the creep damage rate considering pure mode II loading: (a) n, (b) χ. 149
4.46 Parametric effects on the creep damage rate considering pure mode II loading: (a) T_c, (b) σ_t. 150
4.47 Strength prediction: ENF. 151
4.48 ENF mesh configuration: (a) undeformed, (b) deformed. 151
4.49 Bilinear cohesive law for pure mode II loading. 152
4.50 Creep response, considering pure mode II loading, of damage laws proposed by Sun et al. (2012) and Haque and Maurice (2019). 153
4.51 Creep response, considering pure mode II loading, of damage laws based on the Maxwell viscoelastic model. 154
4.52 Creep response, considering pure mode II loading, of damage laws based on the Voigt-Kelvin viscoelastic model. 155
4.53 Creep response, considering pure mode II loading, of damage laws based on the Burgers viscoelastic model. 155
4.54 Creep response comparison, considering pure mode II loading, between the proposed laws and the literature (Sun et al., 2012; Haque and Maurice, 2019). 156
4.55 Effects of θ on the curve shape considering pure mode II loading. 157
4.56 Effects of n on the curve shape considering pure mode II loading. 157
4.57 Effects of ϕ on the curve shape considering pure mode II loading. 158
4.58 Effects of χ on the curve shape considering pure mode II loading. 159
4.59 Numerical validation considering pure mode II loading: (a) KRVK (80% P_{max}), (b) LMVK (80% P_{max}), (c) KRVKS (80% P_{max}), (d) LMVKH (80% P_{max}). 161
4.60 Numerical validation considering pure mode II loading: (a) KRVK (70% P_{max}), (b) KRVK (75% P_{max}), (c) LMVK (70% P_{max}), (d) LMVK (75% P_{max}), (e) KRVKS (70% P_{max}), (f) KRVKS (75% P_{max}), (g) LMVKH (70% P_{max}), (h) LMVKH (75% P_{max}). 162

List of Tables

2.1 Historical development on synthetic adhesives (Fay, 2021). 9
2.2 Certification approach for a bonded repair proposed by Chalkley and Baker (1999). 52

3.1 Material properties of carbon-epoxy HS160REM (Moreira, 2021; Moreira et al., 2018a,b; Silva et al., 2020). 56
3.2 Material properties of ARALDITE® 2015-1 (Samaro, 2023; Moreira, 2021; Alves et al., 2018; Barbosa et al., 2018). 58
3.3 Geometric dimensions: DCB. 59
3.4 Geometric dimensions: ENF. 60
3.5 Dimensions and maximum values for strength and displacement considering DCB specimens. 68
3.6 Slope of the secondary phase on experimental DCB creep curves. 69
3.7 Dimensions and maximum values for strength and displacement considering ENF specimens. 71

4.1 Classical empirical laws for time-dependent creep strain. 92
4.2 Creep damage laws applicable on bonded joints. 123
4.3 Reference parametric values for analysis considering pure mode I loading. 124
4.4 Material properties of carbon-epoxy. 130
4.5 Material properties of ARALDITE® 2015. 130
4.6 Geometric dimensions: DCB. 130
4.7 Calibrated parameters of KRVK and LMVK for numerical validation considering pure mode I loading. 142
4.8 Calibrated parameters of KRVKS and LMVKH for numerical validation considering pure mode I loading. 142
4.9 Reference parametric values for analysis. 145
4.10 Geometric dimensions: ENF. 150
4.11 Calibrated parameters of KRVK and LMVK for numerical validation considering pure mode II loading. 159
4.12 Calibrated parameters of KRVKS and LMVKH for numerical validation considering pure mode II loading. 160

Abbreviations and Symbols

AC	Advisory Circular
AE	Acoustic Emission
CBBM	Compliance-Based-Beam-Method
CFRP	Carbon Fibre Reinforced Plastic
CLT	Classical Laminate Theory
CDM	Continuum Damage Mechanics
CFR	Code of Federal Regulations
CZM	Cohesive Zone Modelling
DAH	Design Approval Holder
DCB	Double-Cantilever-Beam
DIC	Digital Image Correlation
DLL	Design Limit Load
DMA	Dynamic Mechanical Analysis
DOA	Design Organisation Approval
DUL	Design Ultimate Load
EASA	European Aviation Safety Administration
ENF	End-Notched-Flexural
ERR	Energy Release Rate
FAA	Federal Aviation Administration
FE	Finite Element
FPZ	Fracture Process Zone
ICA	Instructions for Continued Airworthiness
ICAO	International Civil Aviation Organisation
IRT	Infrared Thermography
KRB	Kachanov-Rabotnov-Burgers
KRM	Kachanov-Rabotnov-Maxwell
KRVK	Kachanov-Rabotnov-Voigt-Kelvin
KRBS	Kachanov-Rabotnov-Burgers-Sun
KRMS	Kachanov-Rabotnov-Maxwell-Sun
KRVKS	Kachanov-Rabotnov-Voigt-Kelvin-Sun
LMB	Liu-Murakami-Burgers
LMM	Liu-Murakami-Maxwell
LMVK	Liu-Murakami-Voigt-Kelvin
LMBH	Liu-Murakami-Burgers-Hyperbolic
LMMH	Liu-Murakami-Maxwell-Hyperbolic
LMVKH	Liu-Murakami-Voigt-Kelvin-Hyperbolic
LT	Lock-In Thermography
micro-CT	X-ray Micro-Computed Tomography
MO	Maintenance Organisations
NDI	Non Destructive Inspection

NDT	Non Destructive Testing
OEM	Original Equipment Manufacturer
PP	Polypropylene
PPT	Pulsed Phase Thermography
PSA	Pressure-Sensitive-Adhesive
PSE	Primary Structural Element
QC	Quality Control
RH	Relative Humidity
SEM	Scanning Electron Microscopy
SHM	Structural Health Monitoring
SLB	Single-Leg-Bending
SRM	Structural Repair Manual
TT	Transient Thermography
UMAT	User-Defined Material Subroutine
USAF	United States Air Force
USDFLD	User-Defined Field Variable Subroutine
UT	Ultrasonic Testing
UV	Ultra-Violet
WWI	World War I
WWII	World War II
XFEM	Extended Finite Element Method

Chapter 1

Introduction

Nowadays, adhesive bonding constitutes an emergent technology, being widely applied on several industries, whose major developments have been presented in the aviation sector. This dissertation presents studies where the creep behaviour of adhesive joints is analysed. This introduction exposes the context (Section 1.1), the objectives of the conductive studies (Section 1.2), and finally the structure adopted through this document through different chapters (Section 1.3).

1.1 Context and Motivation

Adhesively bonded joints are structural elements, whose potential applications, specially in composite aeronautical structures, are associated to several advantages, such as the mitigation of stress concentration phenomena. Bonded repairs are also more advantageous to be applied in composite aeronautical structures, whose superiority is notable, in terms of mechanical performance, in comparison with bolted repairs.

In the aviation sector, adhesive bonding is still faced as a novel technology by certification authorities. Matured scientific developments are needed, demonstrating a high technological readiness level and a strong application capability in bonding and repairing composite structural elements. Mechanical and fracture behaviours, under different loading scenarios (pure modes I and II, and also mixed-mode I+II), have to be accessed. Great scientific efforts are revealed for bonded joints under quasi-static loading. The influence in terms of adhesive types, geometry and dimensions is widely studied in the literature, both using experimental and numerical procedures. More recently, fatigue loading has been investigated, playing an important role in terms of the certification of composite aeronautical structures containing adhesive bonded joints or repairs, where original equipment manufacturers are able to prove the structural lifetime capabilities.

In order to create procedures for the assessment of static and fatigue behaviours of adhesive joints/repairs, numerical models have been established for those conditions. Various studies have presented cohesive zone models, with an interface with finite element modelling, but only considering quasi-static and fatigue loading scenarios. In fact, not only dynamic conditions contribute for the structural lifetime, but also situations where a constant load is applied for long time periods. These conditions constitute creep, where the adhesive layer shows a viscoelastic behaviour. Molecular phenomena are possible to occur, whose mechanical properties are modified along time, such as stiffness, allowing the increase in displacement, even under a constant applied load. A depth investigation is needed in order to analyse composite bonded joints and repairs under creep loading. Current literature has only showed developments, in terms of creep analysis, for metallic materials or polymers. A cohesive zone model was never established successfully to describe the creep crack growth of adhesively bonded joints. Several creep damage laws were derived, both for ductile polymers and adhesives, but solely with an empirical nature, where huge experimental efforts are continuously required. A new cohesive zone model needs to be established in order to describe the creep fracture behaviour of adhesively bonded joints and repairs. Novel creep damage laws with a phenomenological nature, taking into account viscoelastic properties which are material dependent, have to be postulated, being embedded in the cohesive zone model formulation. In this way, the established numerical models bring value to engineering design of adhesive bonded joints/repairs under creep loading, being possible to use by original equipment manufacturers, without the need to perform extensive experimental campaigns, continuously, to determine empirical constants.

1.2 Objectives and Methodology

Considering the context and motivation for the conducted studies in this dissertation, exposed in the last section, the main objective consists in the establishment of a new cohesive zone model, capable to predict creep lifetime in adhesive bonded joints, as well as describing the whole fracture process, detailing the three creep stages: primary, secondary and tertiary. Pure modes I and II loading scenarios were considered in this dissertation, constituting a solid basis for further developments considering mixed-mode I+II loading, having the ultimate objective to establish a computational tool for the design of composite bonded repairs under creep conditions.

Creep damage laws are embedded in the new cohesive zone model. For this purpose, the following developments were conducted, from an experimental campaign to the derivation of novel laws:

1. An experimental campaign of creep tests was performed. All the experiments were conducted until failure, describing the three creep stages experimentally. Double-cantilever-beam tests were performed for the evaluation of the creep behaviour under pure mode I loading. End-notched-flexure specimens were used for the part of the experimental campaign, where the creep behaviour under pure mode II loading was accessed. Experimental data was generated, being used in order to validate the new cohesive zone model proposed in this dissertation.

2. Twelve creep damage laws were postulated, combining formulations for creep analysis of metallic materials with classical viscoelastic models, performing appropriate adaptations

for the evaluation of creep phenomena in bonded joints. The determination of creep damage laws with a predominant phenomenological nature was possible by taking into account rheological and stress degradation effects, which are characteristic behaviours of structures under long loading exposures. The considered laws were inspired in the Paris law. In this way, proportional and power law constants are included in the formulations, constituting a residual empirical nature.

3. Parametric analyses were conducted for the developed creep damage laws, accessing the corresponding sensitivity to the variation of parameters. Range values of proportional and power law constants were established for possible creep lifetimes, according to data available in the literature, in order to facilitate a further numerical validation.

4. Results from the new cohesive zone model were directly confronted with experimental data, where the proportional and power law constants were determined. The most appropriate creep damage laws were selected for each loading scenario. Finally, the whole computational tool was validated, constituting a basis for future developments of design tools appropriate to evaluate creep conditions of composite bonded repairs.

1.3 Document Structure and Outline

A literature review is presented in Chapter 2. Fundaments on adhesive bonding, essential topics on theory of adhesion, main design principles of bonded joints and also current manufacturing and inspection mechanisms were reviewed. Durability and environmental effects were introduced as well, being associated to creep loading. Topics on aeronautical certification, regarding composite bonded repairs were also mentioned.

Experimental procedures are exposed in Chapter 3, presenting materials, specimen configurations, as well as the used testing methods. The implemented specimen preparation was detailed. Results for creep tests, under pure modes I and II loading scenarios, were presented for different applied loads.

Chapter 4 presents developments in terms of numerical models for the analysis of creep conditions in adhesively bonded joints. First of all, viscoelastic models are reviewed, from linear to non-linear, and from classic to current developed laws in research. Studies in terms of creep crack growth are introduced, serving as complement for the development of new mathematical laws. Twelve creep laws were derived for the evaluation of creep conditions in bonded joints. Corresponding implementation in cohesive zone modelling, while using a commercial finite element software as an interface, was demonstrated. The sensitivity of the laws to different parametric values was accessed. A numerical validation was shown, according to experimental results presented in Chapter 3.

Conclusions related to studies conducted on this dissertation are mentioned in Chapter 5. The main problem is recapped, presenting corresponding solutions. At the end, results, either experimental and numerical ones, are resumed.

Chapter 2

Literature Review

A state-of-art review is presented in this chapter on composite bonded joints and repairs. A historical overview about composite materials is presented as well as the major applications in the last few years, showing the importance of structural repairs. Historical perspective on adhesive bonding and major applications are exposed. Advantages and disadvantages of this type of technology is analysed.

In a second phase, design and manufacturing methodologies on bonded joints and repairs are presented in Section 2.2. First of all, the theory of adhesion is introduced, and then, design principles are overviewed. A background on bonded repairs is presented, demonstrating different studies regarding different mechanical loading phenomena. Correct procedures for the manufacturing and inspection of adhesively bonded repairs are then described, including surface preparation methods. The implementation of bonded repairs in aeronautical structures, especially *in situ*, is emphasised. The investigation of creep loaded bonded joints and repairs is introduced in the Section 2.2.5, by exposing the state-of-art regarding durability and environmental effects. Applications in aeronautical structures are emphasized. Bonded repairs are strictly regulated and some requirements must be met under certification, specially regarding design and manufacturing. Present certification requirements are described in the same section (2.2), and future challenges are analysed and investigated for massive certification of adhesively bonded repairs on damage tolerant composite structures. Acceptable means of compliance provided by certification authorities can constitute guidelines for design and manufacturing procedures.

2.1 Fundaments on Adhesive Bonding

The present section is subdivided in three parts. The problem is stated in Section 2.1.1, presenting the implementation of composite structures and the importance of repairing, over replacement. Trends for aerospace materials are analysed, exposing the importance of composite bonded joints. Adhesively bonded joints are introduced in Section 2.1.2, presenting major historical developments since the beginning of the 20^{th} century. Advantages and disadvantages of adhesive bonding are explained in Section 2.1.3.

2.1.1 Composite Materials and Importance of Repairing

Composite materials have been widely used for several applications, gaining importance specially in the automotive, naval, aeronautical, and aerospace industries. de Moura et al. (2011) also mention applications such as in the electronic components, sportif goods and civil construction.

Mouritz (2012) describes the evolution of aerospace materials from the era of using wood, exposing also the era of aluminium and other lightweight alloys, to the new era of implementing composite materials. In the 21st century, the use of aluminium in the aeronautical industry was strongly decreased. On the other hand, this same literature exposed the increasing use of composite materials, even since 1960. The implementation started on military aircraft, but the transition to civil aviation was quite efficient as the technology evolved, since the 1980. Comparison between the two evolutions is captured in Figure 2.1.

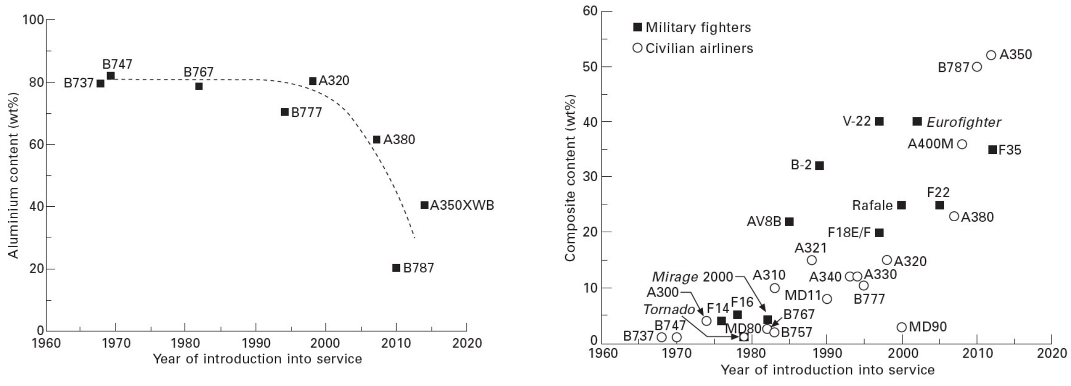

(a) (b)

Figure 2.1: Aerospace materials evolution: (a) aluminium, (b) composite materials, (Mouritz, 2012).

CFRP (carbon fibre reinforced plastic) is commonly used in the aerospace industry as a composite material for several components. Figure 2.2 presents the material constitution of the Boeing 787. It is noticed that the majority of the structures correspond to CFRP laminates, even including primary structural elements such as fuselage and wing panels. In addition, it is also verified the application of sandwich structures to control devices. In this way those are lighter but also stiffer under bending loads, being less prone to flutter problems. In this way, mechanical efforts exerted on hydraulic actuation systems are reduced, allowing the integration of lighter mechanical components, but also allowing the reduction of maintenance needs and, consequently, costs (Moir and Seabridge, 2008). The *"pie"* chart presented in Figure 2.2 demonstrated that 50% of the weight of the aircraft corresponds to composite materials. In fact, almost 90% of the Boeing 787 is made of composite structures, which demonstrates the low weight of the corresponding materials.

Numerous advantages could be referred about using composite materials, but the main ones for structural applications consist on higher specific strength and stiffness (de Moura et al., 2011). Nevertheless, the use of these materials still include *"special conditions"* to be considered under

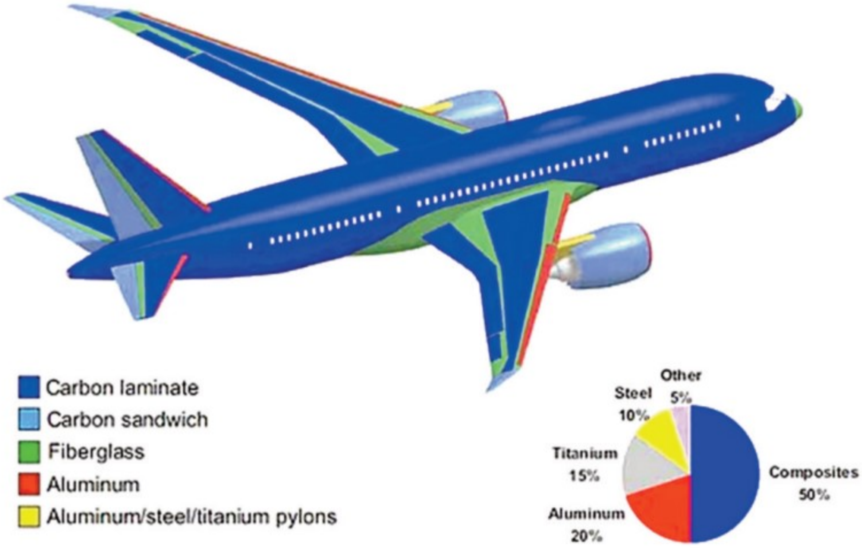

Figure 2.2: Material constitution of the Boeing 787 (Bona, 2019).

aeronautical certification. Those are mentioned in the AC (Advisory Circular) 20-107B, presented by Federal Aviation Administration FAA (2009):

- sensitivity to environmental conditions;
- low ductility, but vulnerable to impact damage;
- exponential crack growth, despite of the higher fatigue resistance;
- variability of mechanical properties to manufacturing processes;
- non-standardised methods for material characterisation;
- low electrical conductivity.

Consequently, there are several challenges to overcome while designing a composite structure. Since 1980, the main failure causes related to composite structures were reported due to the use of sandwich structures and, essentially, bonded joints and repairs. They can be very advantageous to composite materials, but their use constitutes the main challenges to overcome in the future.

Nowadays, the world is facing environmental concerns, and it is also related with accumulation of scrap materials in landfills. It is significantly contributed by the wast of most of the composite structures using thermoset resins that are impossible to recycle. Several studies have been presenting methodologies of recycling, as presented by Pimenta and Pinho (2010). Despite of all the efforts done by introducing novel technology, both in terms of mechanical and chemical recycling, it seemed to be very difficult to maintain the same mechanical properties of the recycled fibres, in comparison to the virgin ones. Mechanical recycling is usually implemented on thermoset based composite structures, being impossible to manufacture recycled components with continuous fibres. Due to this, strength can be reduced in almost 50%. Chemical processes as pyrolysis seemed to retain efficiently mechanical properties, being capable to retain higher than 90% of fibre longitudinal strength, as reported by Meyer et al. (2009). However, the environmental impact of chemical processes can become hazardous even for human health (Khalil, 2018), as demonstrated in Figure 2.3, and the associated costs and energy consumption can be inefficient (Rosa et al., 2021).

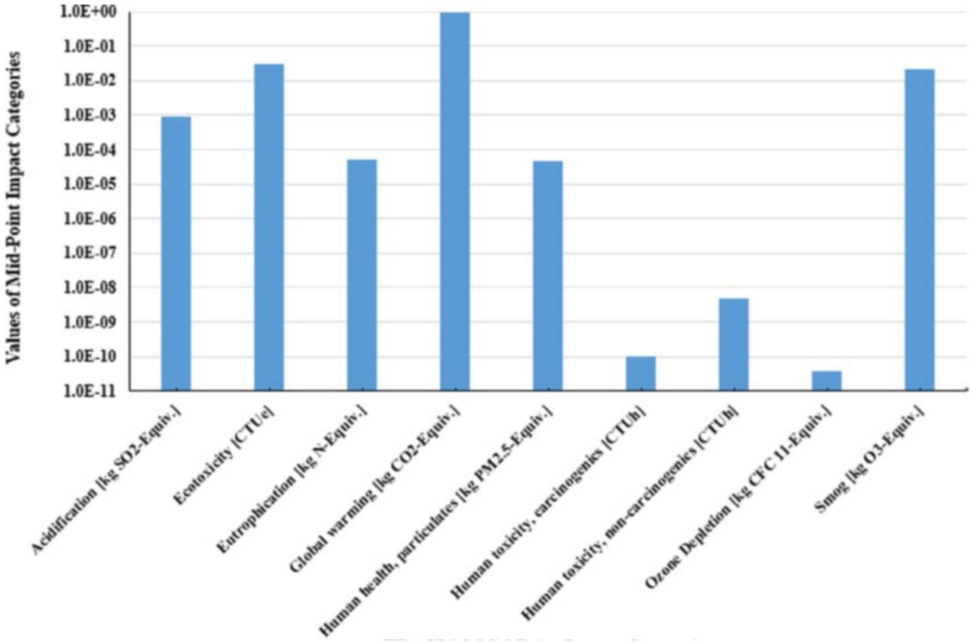

Figure 2.3: Environmental effects related to pyrolysis: calculations per 1 kg of CFRP waste (Khalil, 2018).

These difficulties related to recycling of thermoset based composites are a great obstacle seen by certification agencies to approve their use in aircraft structures. A more viable solution, in relation to replacement, is to extend the structural life of the component, and it can be made by a more robust design. Nevertheless, it increases weight and, consequently, fuel consumption, which is not appropriate to reach established goals for the decrease of CO_2 emissions accorded globally. Using a damage tolerant design philosophy, which is still being matured in the aeronautical industry, structural repairs can be implemented. The application of bonded repairs to composite structures have been widely studied, but mechanical behaviour need to be fully understood. This work presents the analysis of bonded repairs under creep and stress relaxation, contributing for the acceptance of this type of technology to the aeronautical certification authorities.

2.1.2 Historical Perspective and Applications

Adhesive bonding has been used nowadays for several applications. This technology has been developed not only in technical industries. Fay (2021) reported applications such as the automotive, electrical and electronic, footwear, maritime and shipbuilding, civil construction, packaging, and even medicine. Nevertheless, the aeronautical industry is the main responsible for technical developments since the beginning of the last century.

Adhesive bonding has been applied since the pre-history. Fay (2021) described the evolution of adhesive bonding technology since the era of Stone Age Humans, analysing through classical, mediaeval, and renaissance civilisations, until the industrialisation of glue making, using synthetic adhesives on the 20^{th} century. Finally, applications on modern industries, specially aeronautical and aerospace, were described by this same literature.

Until 1920s, most of the compounds used industrially were natural adhesives. Judge (1921), which is an author cited by Fay (2021), reported several natural adhesives used in that decade, and some of them were implemented during the WWI (World War I) in military aircraft. Some of them were also used for conservation and repair in several applications. The main used compound was casein, which was used as a structural adhesive for joints between plywood components in an aircraft. The inspection technique consisted on feeling the smell released by the bonded joints. Due to environmental conditions, casein can deteriorate, releasing a smell identical to cheese or sour milk (Bishopp, 2005). Figure 2.4 shows an airplane named Fokker Dr.I, used in the WWI, employing casein based adhesive joints.

Figure 2.4: Fokker Dr.I used in the WWI (USAF, 2022a).

Even before the WWII (World War II), synthetic polymers were used to bond plywood structures. Environmental conditions were mentioned at that time, as being one of the most influential aspects for degradation, mentioning the need of resistance to moisture, insects and fungi (Fay, 2021). Consequently, synthetic compounds were implemented, using phenol-formaldehyde and urea-formaldehyde. A good resistance to weather was achieved in comparison to natural adhesives, specially casein. Efforts on these developments allowed great evolutions in terms of structural strength, where bonded joints were applied. Bonding metallic structures, urea-formaldehyde was used for structural joints in the De Havilland Mosquito DH 98, during the WWII (da Silva et al., 2007). Figure 2.5 presents the corresponding aircraft.

During the 20^{th} century, new compounds were created becoming available commercially for structural applications. Table 2.1 shows historical developments on synthetic adhesives.

Figure 2.5: De Havilland Mosquito used in the WWII (USAF, 2022b).

Table 2.1: Historical development on synthetic adhesives (Fay, 2021).

Commercial Availability	Type of Adhesive
1910	Phenol-formaldehyde
1930	Urea-formaldehyde
1940	Nitrile-phenolic, vinyl-phenolic, acrylic, polyurethane
1950	Epoxies, cyanoacrylates, anaerobics
1960	Polyimide, polybenzimidazole, polyquinoxaline
1970	2^{nd} generation acrylic

After WWII, great developments are verified, introducing epoxy and acrylic adhesives, which are widely used industrially nowadays, specially in the aviation sector (Hart-Smith, 2021). Those compounds allowed industries in commercial aviation to show compliance to regulations, demonstrating sufficient maturity on the implementation of adhesive bonding. Fay (2021) mentioned that the evolution on synthetic polymers was accompanied by developments on analytical tools, surface analysis methods, stress analysis, fracture mechanics and inspection techniques. All these factors allowed the transfer from the military aviation to the commercial aviation. In this way, Fay (2021) report Boeing 727 as one of the first commercial aircraft using epoxy based adhesives in 1963.

Already two eras of materials in aviation were referred in this section: wood and metals (Fay, 2021). Nevertheless, there is a third era widely using composite materials, mentioned in Section 2.1.1. Bolted joints and repairs, previously used in metallic components, should be replaced using adhesive bonding, because of several advantages to be analysed further in this work. One of the main advantages consists in reducing stress concentrations (da Silva et al., 2007), which is essential to avoid peel stresses in composite structures, causing failures by delamination (de Moura et al., 2011). Boeing 787 and Airbus A350 XWB are the most recent aircraft using adhesive bonding, either in joints and repairs, with the presence of composite materials. Figure 2.6 shows the Airbus A350 XWB. Comparing to Figures 2.4 and 2.5, huge developments, showing maturity of adhesive bonding technology, are proved.

Figure 2.6: Airbus A350 XWB (Airbus, 2016).

According to Hart-Smith (2021), aeronautical certification authorities mandate two conditions regarding adhesive bonding: the adhesive must stay stuck for the life of the structure, in all service and storage environments, and it must be ensured that the adhesive is not the weakest point in a structure, so that it can not fail even under fracture of the surrounding structure. Due to the difficulty of meeting these conditions, certification agencies are still rejecting the use of adhesive bonding both for structural joints and repairs, introduced by several OEMs (Original Equipment Manufacturer) in terms of special conditions, essentially when composite materials are used. Design and manufacturing technologies have to demonstrate higher level of confidence. Complex mechanical phenomena must also be assessed designing beyond the static consideration. Failure by creep and stress relaxation is still not clearly understood in the literature. This work contributes for that development, aiding to increase maturity and level of confidence on adhesive bonding.

2.1.3 Advantages and Disadvantages

Advantages and disadvantages of bonded over bolted joints have to be covered, in order to understand what are the main design principles to consider. da Silva et al. (2007) mention several aspects.

The main advantage mentioned was the higher stress distribution, demonstrated in Figure 2.7, increasing the load capability, allowing weight reductions. da Silva et al. (2007) report a higher fatigue resistance. Analogously, this same stress distribution seemed to be favourable under creep and stress relaxation.

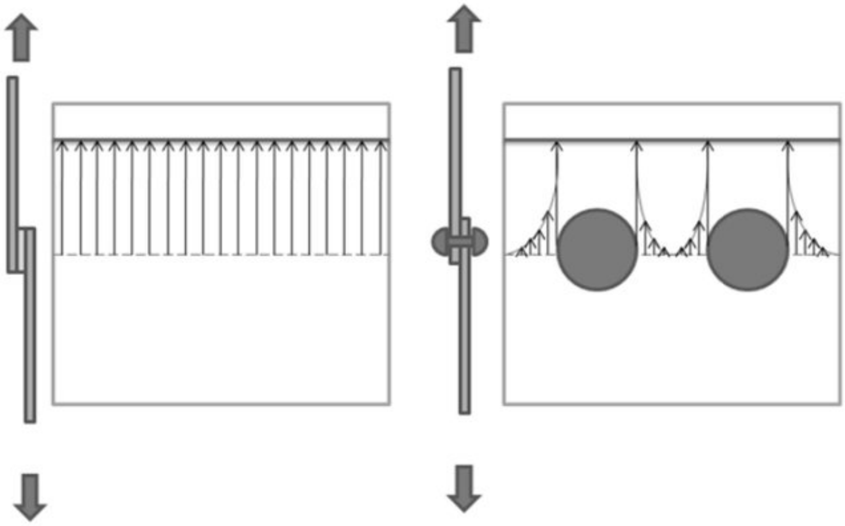

Figure 2.7: Comparison between bolted and bonded joints in terms of stress distribution (Daylan, 2021).

Another advantage that is favourable to enhance fatigue resistance is the vibration damping. Kroshmanesh et al. (2022) demonstrated the interaction between the vibration damping and fatigue damage evolution, and how it can retard failure. In addition, adhesive bonding is also capable of retarding crack propagation (Baker et al., 2002), as shown in Figure 2.8, and it is related also to a more constant stress distribution.

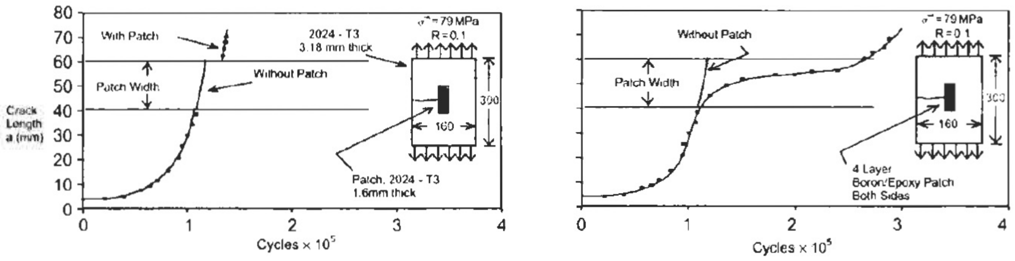

(a) (b)

Figure 2.8: Crack propagation of repairs: (a) bolted, (b) bonded, (Baker et al., 2002).

Specifically regarding composite materials, sometimes adherends are very thin being prone to several failure modes if bolted joints are used. In those cases, adhesive bonding seemed to be a more efficient solution. These advantages combined allow the reduction of structural weight, as well as reducing costs. In addition, using adhesive joints and repairs can provide easily smooth and regular surfaces with a continuum contact between adherends. These conditions seemed very suitable to composite structures.

Nevertheless, there are some disadvantages to take into account, specially while designing (da Silva et al., 2007). The need to avoid peel stresses is practically mandatory both in static and dynamic conditions, such as creep, stress relaxation, or even fatigue. da Silva and Adams (2006) present what peel stresses can cause, specially on composite adherends. Figure 2.9 demonstrates different phases of a delamination caused by peel stresses on composite structures. Techniques to overcome these failure modes are demonstrated when design principles are discussed in Section 2.2.2. Peel stresses not only cause delamination, but they are also the main cause for cohesive failures when ductile adhesives are used, which are commonly implemented in bonded repairs. These peel stresses can appear locally in the adhesive ends, being responsible for failure initiation. Figure 2.10 presents results for vertical stresses from a FE (finite element) model, under tensile loading. It shows how localised those peel stresses are in the adhesive ends, promoting cohesive failure. Another limitation referred by da Silva et al. (2007) was the sensitivity to environmental conditions, essentially temperature and moisture. Generally, those two factors seemed to decrease strength both in static and dynamic conditions.

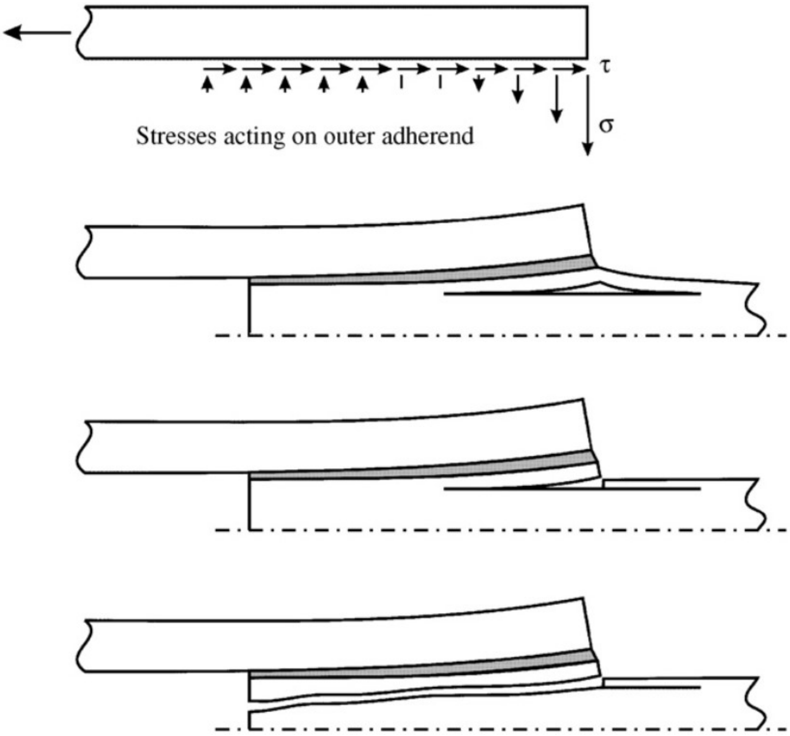

Figure 2.9: Effects of peel stresses on composite adherends (da Silva and Adams, 2006).

Additional disadvantages are related with manufacturing, requiring fixation tools, surface preparation, curing process and quality control. They can bring difficulties on the implementation of bonded repairs *"in situ"* in *"out-of-autoclave"* conditions, constituting several challenges to investigate. In terms of quality control, inspection can be difficult, specially when the presence of weak adhesion is verified. Details are given further in Section 2.2.4. The absence of standardisation in design can be a disadvantage, similarly to what happens in composite materials. This is one of the major obstacles for certification of bonded joints and repairs in the aviation sector.

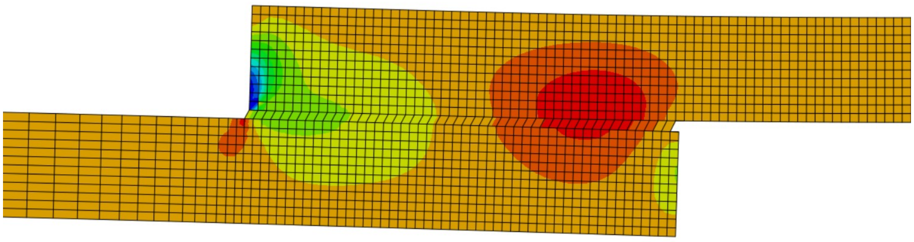

Figure 2.10: Localised peel stresses in the adhesive ends.

Verifying all the mentioned advantages, bonded joints and repairs seemed to be more suitable for composite structures, rather than bolted joints and repairs. However, the presented disadvantages bring several challenges to consider in design and manufacturing. Actual methodologies, as well as developments for future implementation, are presented in Section 2.2.

2.2 Bonded Joints and Repairs: Design and Manufacturing

Design and manufacturing methodologies are presented in this section. The theory of adhesion is exposed in Section 2.2.1. Design principles are then analysed in Section 2.2.2, as well as demonstrating different joint types, typical behaviour to several loading conditions, fracture modes and different geometries. A background on bonded repairs is presented, referring the classic literature in the field, as well as reviewing the current state-of-art, specially regarding the mechanical behaviour of composite bonded repairs. Steps for a correct manufacturing and inspections procedures are presented in Section 2.2.4, while describing conditions for *"in situ"* implementation and methodologies for surface preparation is carefully described. Environmental effects on adhesive joints and repairs are analysed in Section 2.2.5, but a special attention is given to the mechanical behaviour under creep loading, assessing the capability of adhesive joints and repairs in terms of durability. Finally, the main certification requirements are analysed and stated in Section 2.2.6, describing the acceptable means of compliance proposed by certification agencies.

2.2.1 Theory of Adhesion

da Silva et al. (2007) mention that adhesive bonding is assured by intermolecular and intramolecular forces, so constituting not only a physical, but also a chemical linkage. In fact, the knowledge required to understand the adhesion phenomenon is a multidisciplinary science (Petrie, 2007). A design of a bonded joint or repair involves an interaction between physics, chemistry and mechanics. The interaction between physics and chemistry is the basis for surface science. The association of mechanics with chemistry results in the knowledge about polymeric materials which can be the basis for the determination of the adhesive mechanical properties. Finally, mechanics and physics together result in the joint design. Figure 2.11 summarises the mentioned interactions.

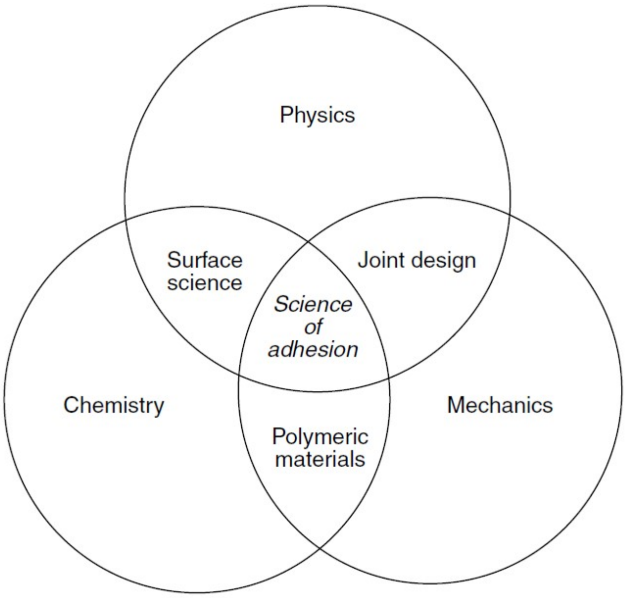

Figure 2.11: Multidisciplinary nature of adhesion science (Petrie, 2007).

Following da Silva et al. (2007, 2011) there are five theories of adhesion:

- mechanical theory;
- adsorption theory;
- diffusion theory;
- electrostatic theory;
- weak-boundary-layer theory.

Those theories have been explaining the phenomenon of adhesion in the last years, but it is still being investigated, so that there is no theory, yet, capable of explaining adhesion in a complete and generalised way.

The mechanical theory is the primary explanation of adhesion. It consists on the effect of mechanical anchorage, so that adhesion is guaranteed by the penetration of a liquid in the cavities of a solid surface. This theory was denied in the 1950s due to the fact that adhesion between similar surfaces but with different levels of roughness was possible (da Silva et al., 2011). Nevertheless, an inverse relationship between roughness and practical adhesion was generally shown. According to da Silva et al. (2007), adhesion is improved with surface treatments that allow the formation of micro-cavities. Those micro-cavities are responsible for the penetration of the adhesive into the substrate, improving strength and durability of the joint/repair, due to mechanical anchorage. However, in those same surface treatments, it is crucial to guarantee a correct cleanliness, providing a higher contact surface for bonding, an improved wetting, and reducing the probability of voids and defects that would harm the mechanical behaviour, specially using ductile adhesives (da Silva et al., 2007, 2011).

Having a sufficiently small surface distance between the adhesive and the substrate, it is possible to provide adhesion with intermolecular/intramolecular forces, as mentioned before (da Silva et al., 2007). This is the fundaments of the adsorption theory. London forces allow physical adsorption, which is the most important to provide strength in an adhesively bonded joint or repair. *"Chemisorption"* is also possible by having primary bonds, providing strong links, allowing a chemical reaction between the adhesive and the substrate. Figure 2.12 shows a representation of a physical adsorption, as well as of a *"Chemisorption"*.

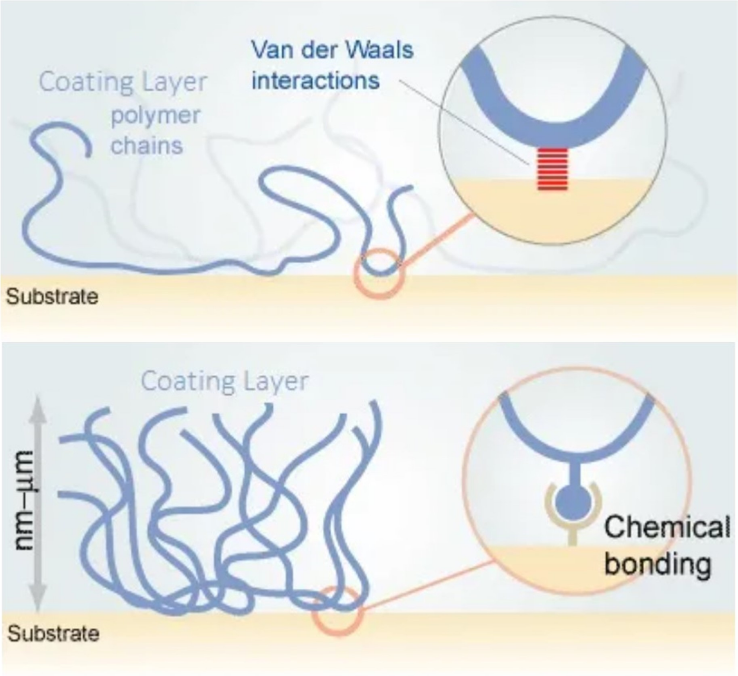

Figure 2.12: Physical and chemical adsorption representation (da Silva et al., 2007; ManoxBlog, 2020).

The diffusion theory is only valid in the bonding of polymeric materials, being applied essentially in the welding of thermoplastic polymers. The involved polymers have to be chemically compatible and miscible. A diffusion exists if a molecule of an adhesive is inserted into the structure of a substrate. A diffusion process occurs if the temperature of the adhesive is higher than the corresponding glass transition temperature (T_g) (da Silva et al., 2007).

Only the pressure sensitive adhesives are subjected to the electrostatic theory. Adhesion strength is guaranteed by transferring electrons (da Silva et al., 2007). Free charges, disposed between an adhesive and a substrate, with opposite signs, are attracted, providing adhesion. Following da Silva et al. (2011), in the 1950s, some researchers believed that the electrostatic theory was the main explanation for adhesion processes, in most of the adhesive joints. Even by the main researchers postulating that in the 1950s, they admitted the following in 1978 (Deryagin et al., 1978): *"an adhesive bond is always caused by either the forces of chemical bonding or by so-called van der Waals forces."*.

Regarding the weak-boundary-layer theory, da Silva et al. (2011) mentioned that the weak-boundary-layer consists on a cohesively weak layer in the interfacial region, also known as *"interphase"*. This can provide weakness to the adhesive joint, failing under lower stress levels and lower fracture energies. Beyond this theory, the importance of surface treatments are markedly emphasised, being classified by the authors as a *"prerequisite to success"*. Any surface in a given adherend may contain contaminants or other impurities that harm its cleanliness, leading to bad wetting properties, providing a poor adhesion, and consequently a boundary layer that is cohesively weak. da Silva et al. (2011) also mentioned the need to surface treatments in polymers, referring the presence of additives, that low-molecular-weight species, in the substrate-adhesive interface, which can provide a weak boundary layer. This theory is strongly considered in design, since a given bonded joint/repair fails, most of the times, through a weak-boundary-layer, in the *"interphase"*.

As a conclusion regarding theories of adhesion, adsorption theory is the fundamental one, explaining the adhesion process in most of adhesive joints and repairs applied to several structural applications.

2.2.2 Design Principles

As previously mentioned, composite structures have been widely used, recently, in the aviation sector. Nevertheless, certification processes, as analysed in Section 2.2.6, are very rigorous. Certification agencies, mainly FAA and EASA, takes redundancy as the main key in aeronautical construction including not only composite materials, but also bonded joints/repairs. Since the implementation of novel structural technology, in the 1980s, associated with composite materials, the main accidental issues are related with sandwich structures and adhesively bonded joints. Most of the times, the issues related with sandwich structures are associated with the existing bonding between the plies and the core.

As the industry is taken to employ very conservative designs in primary structures, Hart-Smith (1985) mentions that bolted and bonded joints can be combined, constituting a fail-safe design principle, avoiding peel stresses. Those rivets used are usually called *"chicken-rivets"* in the aviation sector. Nevertheless, it is mentioned that the adhesive bond load path is significantly stiffer in comparison to the load path associated with the bolted/riveted line. In fact, the combined strength is not higher than a solely adhesively bonded joint. The author still mentioned the importance of using *"chicken-rivets"*, specially in structural repairs if mode I loading is presented. Consequently, the use of *"chicken-rivets"* is very common in the aviation sector, constituting an important type of joint/repair to consider. Figure 2.13 shows a representation scheme of a hybrid bonded joint, which could be extended to a bonded repair.

A corresponding real picture is presented in Figure 2.14.

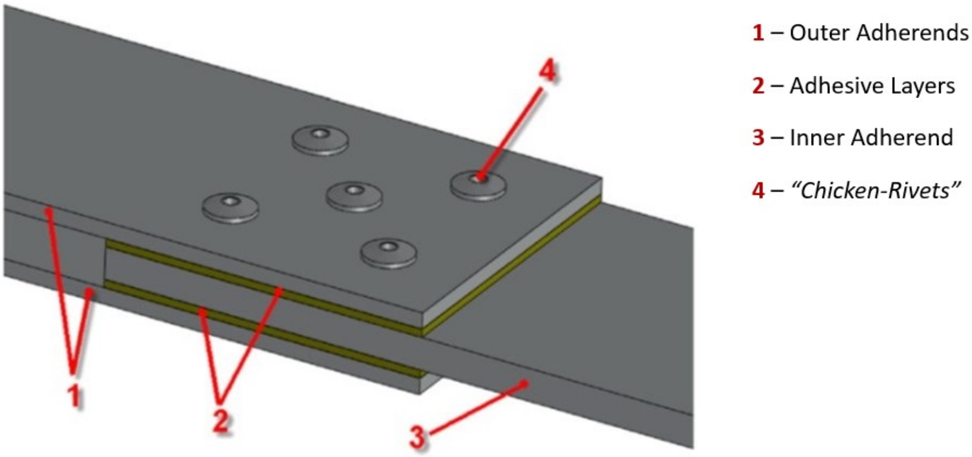

Figure 2.13: Representation scheme of a hybrid bonded joint containing *"chicken-rivets"* (Sadowski et al., 2010).

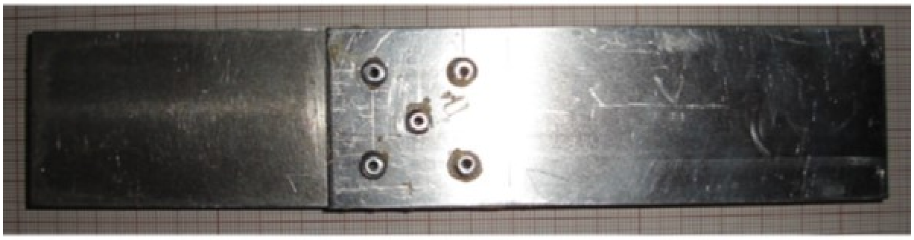

Figure 2.14: Real representation of a hybrid bonded joint containing *"chicken-rivets"* (Sadowski et al., 2010).

Before exposing the several existing configurations of bonded joints and repairs, it is essential to analyse their behaviour under different loading scenarios. Figure 2.15 presents the main loading scenarios: cleavage, peeling, shear, and tension/compression.

When the load is applied in parallel relative to the plane associated with the adhesive layer, shear stresses are induced. Mode II dominates in this type of loading, however, mode I loading can appear depending on the geometric configuration. Geometries where shear loads are dominant are widely used in practical terms, and are usually easy to manufacture (da Silva et al., 2007). Figure 2.18 represents a single-lap joint that is simple to analyse, in terms of design, being also simple to manufacture.

Mode I loading dominates in cleavage and peeling scenarios, and are the most critical for bonded joints/repairs, easily inducing failure (da Silva et al., 2007). Cleavage is defined by a loading condition that tends to separate rigid substrates, resulted by forces applied in adherend ends. The phenomenon of peeling is analogous to cleavage, but, at least, one substrate is ductile. From these loading conditions, peeling stresses are induced in the adhesive layer. Joints/repairs subjected to cleavage/peeling loading conditions have lower strength, when compared to the ones

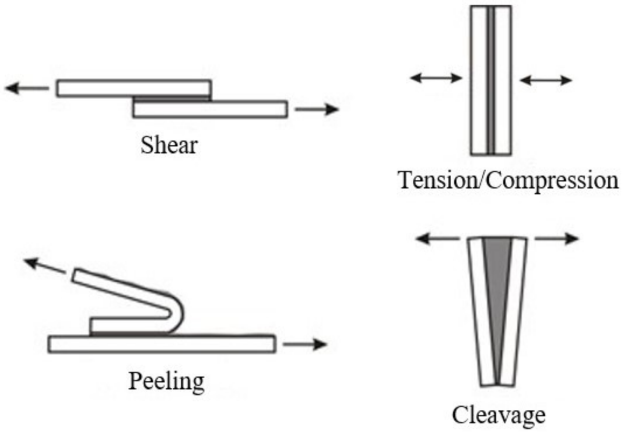

Figure 2.15: Loading scenarios in adhesively bonded joints (da Silva et al., 2007).

only subjected to shear. Under shear loading conditions, the stress is significantly more distributed along the adhesive. When the joint/repair is suffering from cleavage/peeling conditions, the stress is concentrated in the adhesive end, where the load is applied (da Silva et al., 2007). The authors also mentioned that ductile adhesives are more suitable for cleavage/peeling conditions, in comparison to stiff adhesives. This is justified by the fact that ductile adhesives favour stress distribution.

Traction is responsible to induce pure mode I loading, if the substrates are sufficiently stiff to provide a uniform stress distribution. Nevertheless, the thickness of the bonding line is difficult to control while manufacturing. Consequently, some localised stress concentrations, causing cleavage/peeling, are possible to occur, due to differences in thickness along the adhesive layer (da Silva et al., 2007). Inducing a constant stress distribution along the adhesive layer has the same importance under compression loading scenarios. A given joint/repair can only fail if a pure compression state is not assured, resulting in undesirable cleavage or peeling phenomena (da Silva et al., 2007).

The referred loading conditions can cause different cohesive and adhesive failures, or a combination of both (da Silva et al., 2011), as presented in Figure 2.16. A cohesive failure in the adhesive is more desirable to occur in a given adhesive joint/repair, specially in comparison to adhesive failure. The main reason is that adhesive failure is impossible to inspect in service, while cohesive failure can be predicted by several methods. While defining cohesive and adhesive failure mechanisms, it has to be noted that adhesion has a distinct meaning in comparison to cohesion. Following da Silva et al. (2007), adhesion is the attraction between two components resulting from corresponding intermolecular forces. On the other hand, cohesion is related to intermolecular forces but only in one component.

An adhesive joint/repair is composed by a given structure, represented in Figure 2.17, where there is an interphase, already mentioned in Section 2.2.1, having different chemical and physical properties when compared to the bulk adhesive and adherend. That interphase is an agent involved

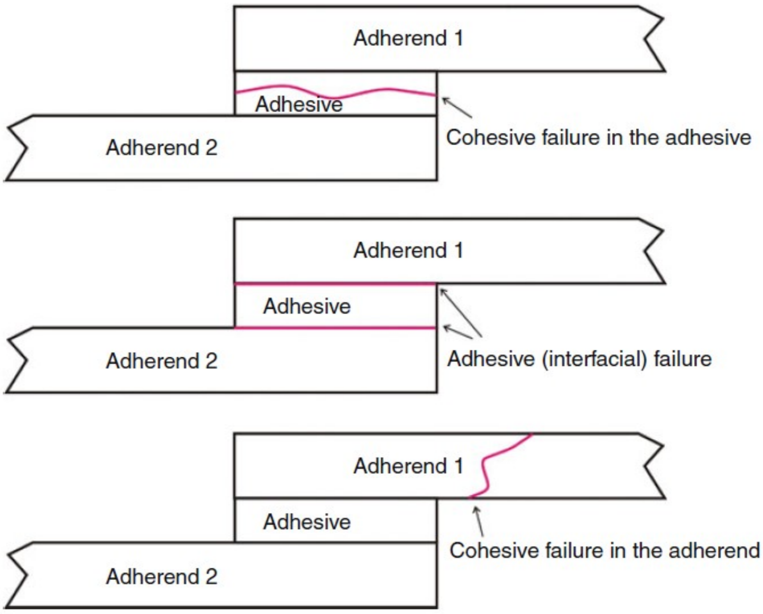

Figure 2.16: Failure modes in adhesively bonded joints (da Silva et al., 2007, 2011).

in adhesive failure mechanisms. Consequently, the interphase plays an important role in the determination of the mechanical properties of the adhesive bond, and of the bonded joint/repair in general (da Silva et al., 2011).

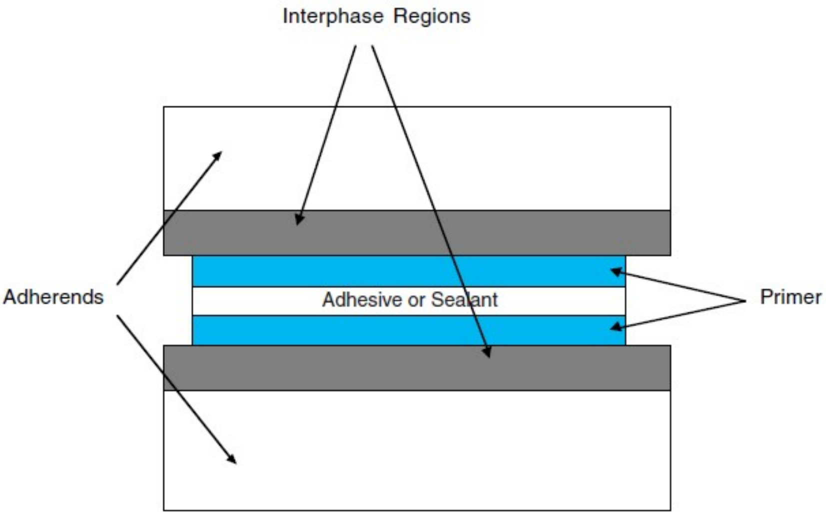

Figure 2.17: Structure of an adhesive joint/repair (Petrie, 2007; da Silva et al., 2007, 2011).

A given interphase is composed by one or more interfaces. An interface is defined as the plane of contact between surfaces of two materials (da Silva et al., 2007, 2011), being also designated as the boundary layer.

Figure 2.17 also includes a primer in the described structure associated to an adhesive joint/repair. This component is usually applied in order to improve adhesion or for surface protection (da Silva et al., 2007).

Several types of bonded joints are used in the aviation sector, but without rivets, and some of those are being investigated and optimised for further implementations. da Silva et al. (2007) enumerate several types of joints, such as butt, and lap joints. Figure 2.18 shows different configurations of adhesively bonded joints.

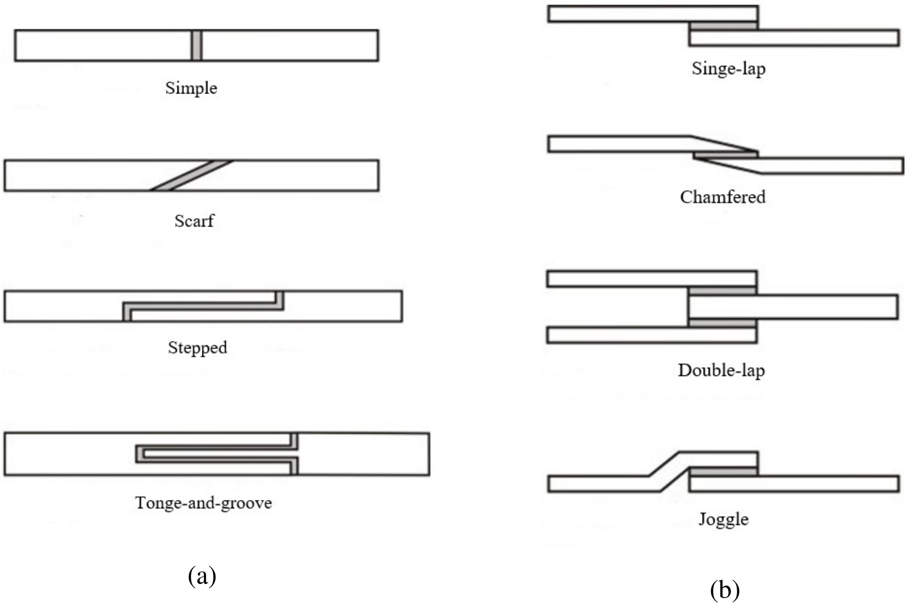

Figure 2.18: Configurations of adhesively bonded joints (Petrie, 2007; da Silva et al., 2007): (a) butt joints, (b) overlap joints.

Butt joints are not appropriate for bending conditions (da Silva et al., 2007). However, this type of geometry is associated to a simple manufacturing strategy. There are some typologies that have significant advantages, specially in terms of stress distribution, over the simple butt joint. Scarf joints are of great interest nowadays (Kimiaeifar et al., 2011; Alves et al., 2018), as their efficiency has been proved in several applications. Also stepped joints have comparable efficiency, being also investigated in the literature (Brito et al., 2021). Both scarf and stepped typologies have great potential for application in bonded repairs, as demonstrated in Section 2.2.3. Following da Silva et al. (2007), tongue-and-groove joints have particular advantages related to the protection of the adhesive layer in service, being isolated from contaminants by the own adherends.

Lap joints are the most common typology used in several structural applications, due to the related ease of implementation. Shear loading dominates in these type of bonded joints, which brings a higher joint strength. However, bending effects are caused by misalignments in the axis associated with the imposed loads, inducing cleavage/peeling in the overlap ends da Silva et al. (2007). This phenomenon is seen for the single-lap joint. By doing a chamfer in the adherends, the stress becomes more distributed along the adhesive layer, softening cleavage/peeling effects. Double-lap joints inhibit the occurrence of bending effects due to load misalignments, diminishing cleavage/peeling. Following da Silva et al. (2007), the joggle joint constitutes a simpler solution in order to obtain the load alignment desired to avoid cleavage/peeling in the overlap ends.

An additional joint typology is also described by da Silva et al. (2007). Those joint types introduce the concept of adhesive repairing. Single-strap, double-strap, recessed, or even scarf and stepped geometries are widely applied as bonded repairs, which are deeply analysed in Section 2.2.3.

2.2.3 Background on Bonded Repairs: Design and Research Developments

Bonded repairs have been widely investigated in the aviation field, due to its easy application, and potential to restore the full strength of a given structure, after an occurred damage. This topic started to be investigated in the early 1980s, with the introduction of composite materials applied to aircraft structures.

A basing literature in bonded repairs, applied in the aviation sector, is presented by Baker et al. (2002). As an introduction, the authors mentioned essentially that a repair scheme should be simple and non-intrusive to the structure, and at the same time, restoring its strength capability. It is also mentioned the importance of not compromising several structural functionalities such as the clearance on moving parts, aerodynamic smoothness, and balance which can be related to control surfaces.

The importance of using readily available and easily storable materials is markedly emphasised by Baker et al. (2002). Most of the times, repair operations are done *"in situ"*, bringing additional challenges in bonding operations. In fact, the surfaces have to be treated in order to have minimal conditions for a correct bond. Repairing in service leads to simpler manufacturing operations, when compared to the ones performed for adhesively bonded joints, in methods described by da Silva et al. (2007, 2011). However, if possible, a repair can be implemented in a factory level, whose facilities on surface preparation are available, and skilled personnel are in action.

While introducing adhesively bonded repairs, Baker et al. (2002) emphasise their high efficiency when compared to bolted repairs, which are prone to several problems related to stress concentrations. In addition, considering aircraft structures, drilling holes for bolted repairing purposes can damage hydraulic lines, electrical wires, optical fibres, or other aeronautical systems. On the other hand, it is mentioned that bonded repairs should be majorly shear loaded, having a large area of load transfer. Consequently, if these conditions are met, bonded repairs are much stiffer when compared to bolted repairs.

Through current developments being presented in the literature, Baker et al. (2002) refer that bonded repairs can be a versatile cost-effective solution, restoring strength. The authors exposed several situations where bonded repairs provide advantages in repair applications:

1. **Stress intensity reduction**:
    - in regions with fatigue cracks;
    - to increase damage tolerance capabilities.

2. **Strength and stiffness restoration**:
    - when allowable limits are not met after damage;
    - after re-shaping to minimise stress concentrations;
    - after heat damage;
    - after failure of a load-path in a multi-load-path structure.
3. **Stiffening under-designed regions**:
    - to reduce stress and strain concentrations;
    - to reduce secondary bending;
    - to reduce vibration and to prevent acoustic damage.

As already mentioned in Section 2.2.2, Hart-Smith (1985) referred the use of *"chicken-rivets"* in primary aeronautical structures, specially when critical damage is presented, making hybrid bolted-bonded repairs. This is deeply justified in Section 2.2.6, presenting mandatory rules dictated by certification agencies. In this way, Baker et al. (2002) mention the application of bonded repairs to primary aeronautical structures as the major goal in research. Consequently, the mechanical behaviour as well as the efficiency, in general, also related with aerodynamic smoothness, associated to bonded repairs have been investigated in the literature.

Several research developments are exposed in this section, along the last four decades. Before the introduction of any study, it is fundamental to describe the most common repair geometries. Moreira et al. (2020a) presented a numerical study of several types of composite bonded repairs under fatigue loading. Different repair configurations were described, being the most commonly used in the aviation sector: single-strap, double-strap, scarf, one-stepped, and two-stepped. Figure 2.19 shows corresponding representations.

As it was mentioned before, composite materials were introduced in aircraft structures in the early 1980s. At that time, in research, ways of repairing were immediately studied by several authors, such as Rogers et al. (1980) and Beck (1980). During this decade, several works were developed in the field, and the author of the main basing literature in bonded repairs (Baker et al., 2002), started to introduce bonded repairing with practical aspects in aircraft components (Baker, 1987). Still in the 20^{th} century, several other studies were presented investigating composite bonded repairs (Jones et al., 1988; Ong et al., 1990; Robson et al., 1994; Jones et al., 1994).

A complete investigation on composite bonded repairs, using experimental procedures, was performed by Charalambides et al. (1998a), where both static and fatigue strength were assessed in scarf repairs, considering hot/wet environmental conditions. Repair systems were immersed in distilled water at 50°C during 16 months. Results show that static strength showed to be slightly lower than the parent material. An efficiency of repair of 84% was registered. Nevertheless, the repair system under-performed significantly in terms of fatigue, in comparison to the parent material. Additionally, the authors proved the validity of the experimental techniques, where repair joints were tested, being representative of a repaired panel. In fact, results were compared between

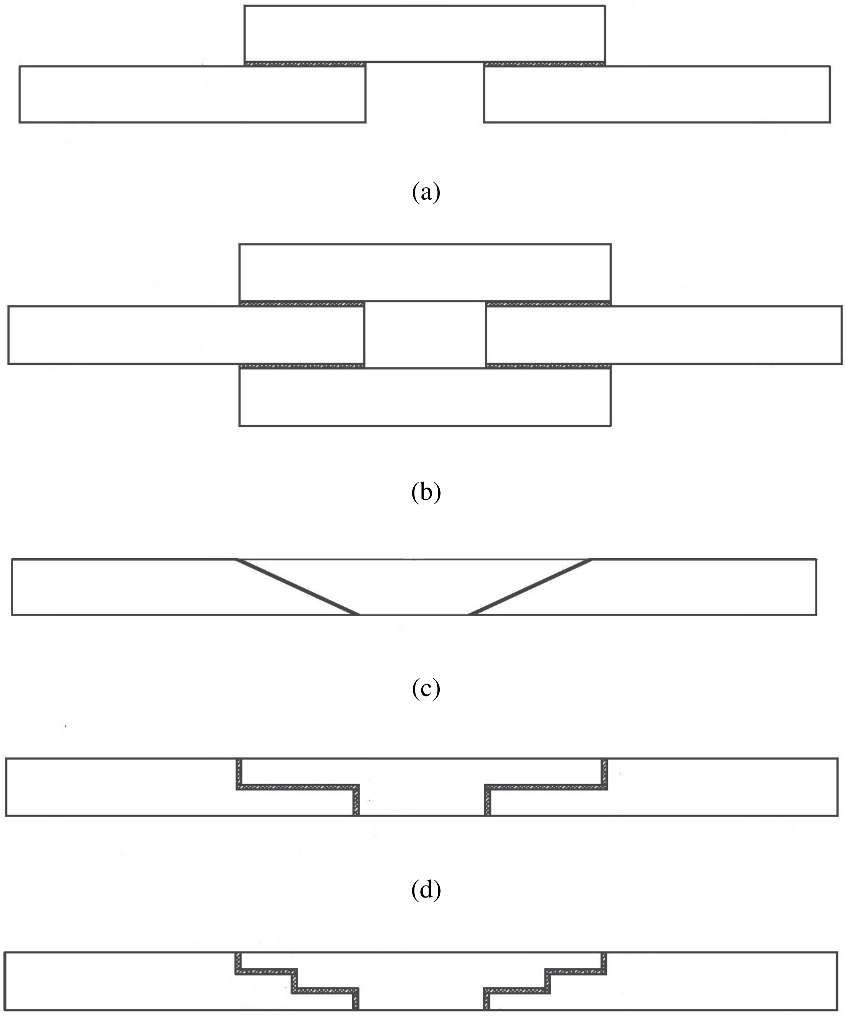

(a)

(b)

(c)

(d)

(e)

Figure 2.19: Bonded repair configurations (Moreira et al., 2020a): (a) single-strap, (b) double-strap, (c) scarf, (d) one-stepped, (e) two-stepped.

the two scales, and the static and fatigue behaviour of the repair joints were similar when compared to the behaviour demonstrated by repaired panels. This conclusion is very important, since most of the works developed consider a scale correspondent to a repair joint. Corresponding numerical developments were performed *"a posteriori"* (Charalambides et al., 1998b), using the FE method.

Studies developed by Ting et al. (1999) presented very important conclusions regarding the effect of a bonded repair in aircraft structures. A simple closed form solution was achieved, and 3D finite element models were developed for rib stiffened panels. The authors concluded that the stress intensity factor reaches an asymptotic value when a patch repair is applied, proving that a bonded repair can be seen also as a reinforcement to improve the mechanical performance.

Baker et al. (1999) studied graphite-epoxy scarf repairs implemented in a honeycomb structure of the horizontal stabiliser in the F/A-18. Both experimental and numerical results indicated significant strain concentrations in the doubler plies above the top end of the scarf patched area. This is justified by the incompatibility between the shear displacement verified in the doubler compared to the one verified in the scarf patch. Figure 2.20 shows the doubler ply overlap responsible for the described phenomenon.

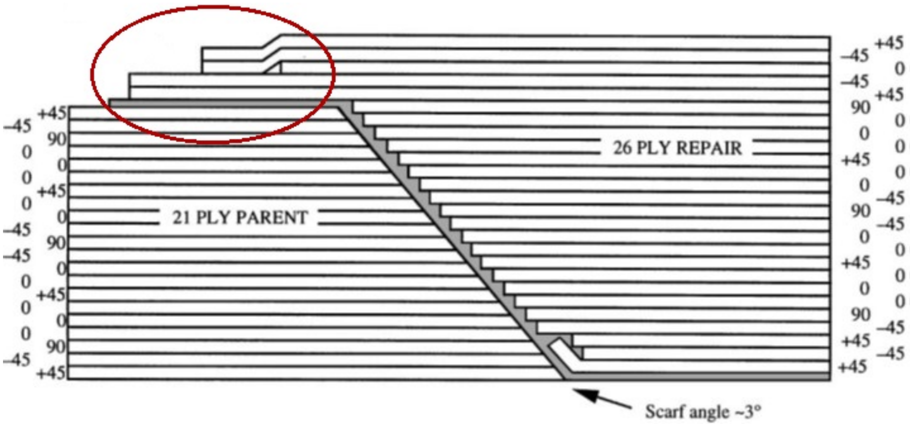

Figure 2.20: Doubler ply overlap in a scarf repair (Baker et al., 1999).

An experimental test was performed to the horizontal stabiliser of the F/A-18, incorporating the aforementioned scarf repair. The structure was able to sustain a load equal to the design limit load capability, showing that the repair operation was applied successfully. At that time, in 1999, that structure was mentioned as unrecoverable, due to the associated high strains. In fact, it would be impossible to recover the structural strength if bolted repair was used, due to stress concentration phenomena.

More recent studies have presenting work developments in order to predict crack onset and growth in bonded repairs, by considering the degradation of the adhesive layer. Campilho et al. (2007) proposed a cohesive zone model capable to predict stiffness degradation on the adhesive layer, in bonded repairs using ductile adhesives. Single-strap repairs were studied in terms of equivalent stiffness and strength, analysing parametrically the overlap length and patch thickness. The authors concluded that a slight increase in the equivalent stiffness is provided by an increase of the overlap length. Nevertheless, it is mentioned that this conclusion needs to be matured with more results. The increase in the patch thickness seemed to allow an increase in the equivalent stiffness. Generally, strength is increase under an increase in the overlap length. However, a gradual decrease in the failure load was registered when the patch thickness is increased, but only for lower patch thicknesses. Higher patch thicknesses inhibit the rotation of the repair, under tensile loading conditions, decreasing peeling effects, allowing an increase in the failure load with an increase in the patch thickness. With this work, the authors demonstrated several conclusions that are useful for the design of bonded repairs.

The same CZM law was also applied to scarf repairs, under tensile loading (Campilho et al., 2008). Different scarf angles were tested from 2° until 45°, in terms of failure load. It was concluded that increasing the scarf angle, the strength is exponentially decreased. Also experimental data were assessed, validating successfully results in terms of the repair initial stiffness, maximum load, limit displacement and corresponding failure modes. This study brings confidence for the use of CZM laws to predict the behaviour of adhesively bonded repairs.

The developed trapezoidal CZM law for mixed-mode conditions is also capable to predict damage in a 3D environment, where properties in mode III were considered to be equal to properties in mode II, since the experimental tests considered just pure modes I and II, using DCB (double-cantilever-beam) and ENF (end-notched-flexural) samples. Single-strap, as well as double-strap repairs were investigated under tensile loading conditions following both experimental and numerical procedures (Campilho et al., 2009). Different overlap lengths and patch thicknesses were analysed in terms of stiffness and strength. It was concluded that using a 5 mm overlap length led to a strength in both repair configurations, verifying a premature patch de-bonding. Regarding strength, the best result was achieved for a double-strap repair using 15 mm of overlap length. The authors concluded also that the strength was less influenced by variations in the patch thickness. Future studies should consider particular properties in mode III, investigating, deeply, the possibility of out-of-plane failure modes.

It was also possible to analyse scarf repairs in a 3D environment, using the same trapezoidal law, by Pinto et al. (2009). This study presented important guidelines in the design of scarf repairs. Different scarf angles, as well as the possibility of introducing over-laminating plies were analysed numerically. Same conclusions which were presented by Campilho et al. (2008) were achieved regarding the variation of the scarf angles: the strength increased exponentially when the scarf angle is decreased. It was referred that the implementation of over-laminating plies was an attempt to improve repair efficiency. Without over-laminating plies, the repair efficiency was 50% for small scarf angles. Applying over-laminating plies in both sides of the repair (outer and inner), that repair efficiency is increased to 70%. Nevertheless, in practical applications, the inner side is difficult, if impossible, to access *"in situ*. Consequently, it is recommended to use an over-laminating ply just in the outer side of the repaired structure, where the repair efficiency is about 60% for small scarf angles. It is markedly referred the importance to avoid aerodynamic disturbances, which explains the reason why scarf repairs are widely investigated in the literature. In fact, the application of over-laminating plies can decrease the aerodynamic smoothness. In the design of bonded repairs applied to aircraft structures, a decision has to be made by choosing between a higher repair efficiency, or a higher aerodynamic smoothness.

More advanced studies are being developed recently. Bendemra et al. (2015) optimised scarf and multi-stepped repairs. It is mentioned by the authors the potentiality associated to multi-stepped repairs, by corresponding manufacturing facilities in comparison to scarf repairs. Nevertheless, it is referred the risk of stress concentrations, and the presented study had the objective of mitigating those effects. Six parametric studies were performed analysing ply thickness, adhesive thickness, taper angle, stacking sequence, overlay lay-up, and over-ply lap length. A strong sensitivity to ply thickness, taper angle, and stacking sequence was noted for both repair configurations. The authors also referred the advantage of using over-plies, providing protection and additional stiffness at joint tips, reducing local stress concentrations from cleavage/peeling phenomena. However, a critical overlay lap length was identified, for an optimal stress distribution along the adhesive layer. In fact, Bendemra et al. (2015) concluded that high stress concentrations can be avoided in multi-stepped repairs by using over-plies. Additionally, it was mentioned that the parametric study helped to reduce stress concentrations in the corners, which are presented in multi-stepped repairs.

Fatigue loading is also an important mechanical phenomenon to be analysed in composite bonded repairs. Ideally, a bonded repair should be implemented just once during the life time of the corresponding structure. Nowadays, some developments on the analysis of the fatigue behaviour of adhesively bonded repairs have been performed. Moreira et al. (2015) characterised single-strap bonded repairs in bending under high-cycle fatigue loading, using both experimental and numerical techniques. After the CZM is established to analyse several cases in high-cycle fatigue conditions, considering mixed-mode loading, several numerical analyses were performed accessing the influence of the applied load, geometry, and material properties. The developed CZM law only includes a damage parameter accounting for quasi-static and fatigue damage accumulation. It was mentioned that good results were achieved, referring that the life-time of the structural repairs determined numerically were coherent in comparison to experimental results.

Developments considering high-cycle fatigue were also presented by Moreira et al. (2016), but under mixed-mode I+II loading was analysed numerically and experimentally, presenting applications in composite double-strap bonded repairs in bending. A linear softening cohesive zone model was used in order to account for static and fatigue degradation with solely one damage parameter. This model was validated using experimental data. The modified Paris law was used to impose fatigue degradation. It was stated a strong influence related to the corresponding exponent, specially in the mode I component. During the experimental work, the authors noted that the fatigue life is strongly influenced by small imperfections, geometric variations, and also material properties of the specimens. Special care in the preparation of the specimens was markedly noted.

Exactly the same analysis was performed by Moreira et al. (2020b), but for scarf repairs under bending, accessing the corresponding static strength and fatigue life. Good agreement between experimental and numerical results were found for a scarf angle of 10°, while considering CZM using linear softening and imposing a modified Paris law in order to model fatigue degradation, being capable of predicting all the mechanical behaviour under mixed-mode I+II loading. The developed numerical model was used in order to verify the influence of the scarf angle on the static strength and fatigue life. An exponential increase of the static strength was reported, while the scarf angle is decreased. The fatigue life was also considerably increased. The minimum tested angle was 3°. Lower angles can bring difficulties in terms of manufacturing, making the repair implementation almost inviable, specially *"in situ"*.

Using the same numerical model, Moreira et al. (2020a) compared several repair types, considering high-cycle fatigue under bending: single-strap, double-strap, scarf, one-stepped and two-stepped, being presented in Figure 2.19. For static conditions, the double-strap repair seemed to be present the highest strength. The one-stepped repair showed the lowest strength and stiffness, however presenting the highest displacement to failure. This same repair, under fatigue, showed a premature increase of compliance, due to early developments of damage. It was stated that the one-stepped repair is inappropriate for fatigue loading scenarios. The scarf repair was mentioned as the most efficient solution under fatigue loading. A reinforcement with a patch repair was also considered, and significant improvements in terms of strength and fatigue life were proved. The best solution both in terms of static and fatigue loading was the scarf repair using a reinforcement patch. However, a decision has to be made in terms of design, considering also the aerodynamic performance if it is applied in aero-structures.

Crucial developments have been presented both considering static and fatigue scenarios. However, few studies in the literature have been presenting developments considering creep phenomena in bonded repairs. Even pure modes I and II have to be analysed first, both experimentally, but specially in numerical terms, in order to access a complete fracture characterisation under creep conditions. This is the starting point for the analysis of bonded repairs, which includes mixed-mode I+II loading.

2.2.4 Manufacturing and Inspection Techniques of Bonded Repairs

Differently from adhesively bonded joints, bonded repairs have often to be implemented *"in situ"*, specially in aircraft structures. It is clearly mentioned by Baker et al. (2002) that *"on-aircraft"* repairs require several constraints on processes and procedures, essentially in terms of surface preparation. These constraints are divided into two components: accessibility and environment. Zones under repair must be accessible, eventually in an airport during maintenance operations. In addition, *"in situ"* repairs are implemented in environments out of control, being impossible to impose adequate pressure and temperature for an accelerated curing procedure. Safety, health and environmental concerns are even more difficult to avoid, so that repair operations *"in situ"* are restricted to use of chemical agents. It is also referred by Baker et al. (2002) that difficulty of repair in the proximity of fuel tanks and avionic bays. A manufacturing sequence of bonded repair is presented for applications in composite structures, being possible to implement *"in situ"*, where corresponding surface preparation techniques are deeply explained in 2.2.4.1.

A manufacturing procedure is summarised by Budhe et al. (2018), for applications on aircraft composite structures, presenting the following sequence:

1. **Check Damage Accessibility**
   Accessibility is so important that is referred as the first step of the manufacturing sequence. If the damaged area is not accessible, the component has to be disassembled, constituting an impossible operation, most of the times, when *"in situ"* repairs are implemented. That area may be assessed by NDI (non destructive inspection) (Katnam et al., 2013).

2. **Damage Removal and Cleaning Process**
   The damaged zone should be removed by cutting operations. In case of scarf, one-stepped, or two-stepped repairs, as shown in Figure 2.19, precision machining may be needed (Katnam et al., 2013). Particularly in scarf repairs, tolerances related with scarf angles and eccentricity can be required. After damage removal, all the area under repair must be properly cleaned.

3. **Surface Preparation**
   Surface preparation is the most crucial step of the sequence. Correct procedures avoid the appearance of voids and defects, which could harm significantly the structural performance (da Silva et al., 2007). As previously mentioned, *"in situ"* repair operations are most of the times restricted to some chemical agents. Surface preparation strategies are exposed in Section 2.2.4.1, considering the referred limitations. It has to be mentioned that the surface of the patch must be equally prepared.

4. **Moisture Removal**
   An additional step is emphasised by Budhe et al. (2018), where it is referred that a drying process is recommended after surface preparation, in order to eliminate all the moisture from the composite matrix. Localised heat can be applied, but without damaging fibres. In fact, this step could be performed before surface preparation, being included in the cleaning process.

5. **Adhesive Application**
   After surface preparation and proper cleaning and drying procedures, the adhesive can be applied. Film or paste adhesives can be used. Figure 2.21 shows the application of a paste adhesive during a composite bonded repair operation on a wing structure. This operation must be performed both on the patch and structure.

Figure 2.21: Adhesive application on a wing structure for a composite bonded repair (TCA, 2022).

6. **Patch Application**
   Patch application can be performed after the adhesive is applied and well scattered along the bonding surfaces. For embedded patch repairs, such as scarf, one-stepped, and two-steeped repair types, the position of the patch is assured by the geometric conditions. Nevertheless, a special care must considered in single-strap and double-strap repairs, regarding the correct patch positioning.

7. **Curing Process**

   As previously mentioned, the curing process is considerably more difficult *"in situ"* in comparison to an industrial environment, as it is often provided for the manufacturing of adhesively bonded joints. Under the unavailability of an autoclave, vacuum bagging is used with a special portable equipment. A heating blanket is used, providing some control in the thermal conditions possible to induce, allowing a better consolidation of the adhesive layer (Budhe et al., 2018). Figure 2.22 is detailing the vacuum bagging process applied to a composite bonded repair. For non-emergent conditions, the curing process can be performed in ambient conditions. However, a minimum curing time of 24 hours should be provided for some ductile paste adhesives, as ARALDITE® 2015 (Budhe et al., 2018). In addition, specialised equipment should be used to compress mechanically the repair system, avoiding the appearance of voids in the adhesive layer, while guaranteeing the corresponding desired thickness.

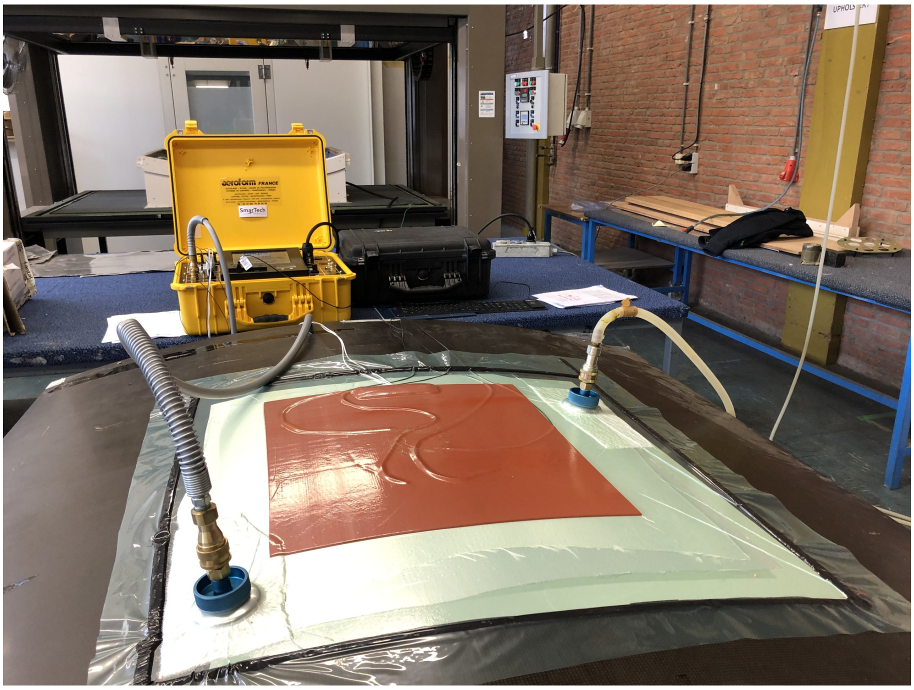

Figure 2.22: Curing process by vacuum bagging applied to a composite bonded repair (DCMC, 2021).

8. **Post-Repair Inspection**

   Voids and defects must be inspected after repair operations are completed. Zhou et al. (2021) mentioned five general NDI or NDT (non destructive testing) techniques, such as AE (acoustic emission), DIC (digital image correlation), IRT (infrared thermography), and micro-CT (X-ray micro-computed tomography). AE can be particularised to UT (ultrasonic testing), where it can be coupled to scanning techniques, such as C-scanning. In this way, it is possible to access defects visually. On the other hand, IRT can be specified in terms of LT (lock-in thermography), PPT (pulsed phase thermography), and TT (transient thermography). Figure 2.23 presents applications in terms of ultrasonic and thermographic inspection. An ultrasonic test is shown to a bonded repair. Thermographic inspection, using LT, is demonstrated for composite bonded joints, but the same procedure can be extended to composite bonded repairs.

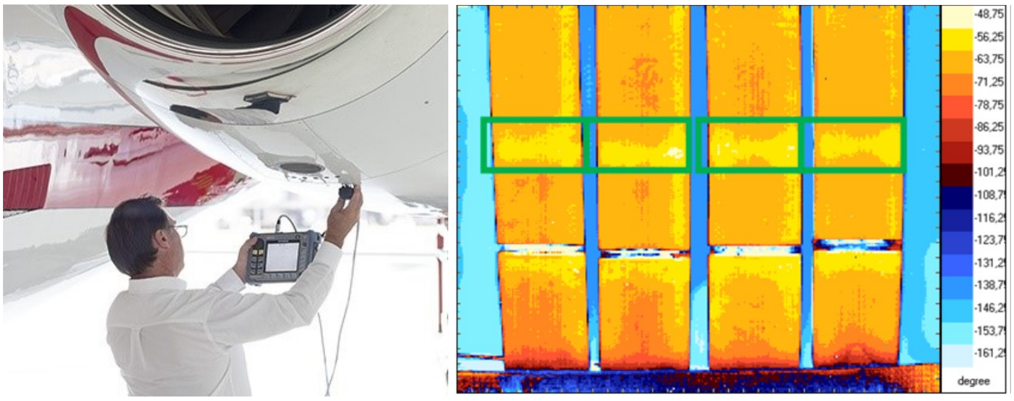

(a) (b)

Figure 2.23: Inspection composite bonded joints or repairs: (a) UT, (b) IRT (Evident, 2022; Galietti et al., 2012)

In this way, composite bonded repairs can be manufactured, following Budhe et al. (2018). These authors also demonstrated the proportional time for each step of the manufacturing sequence, being represented in Figure 2.24.

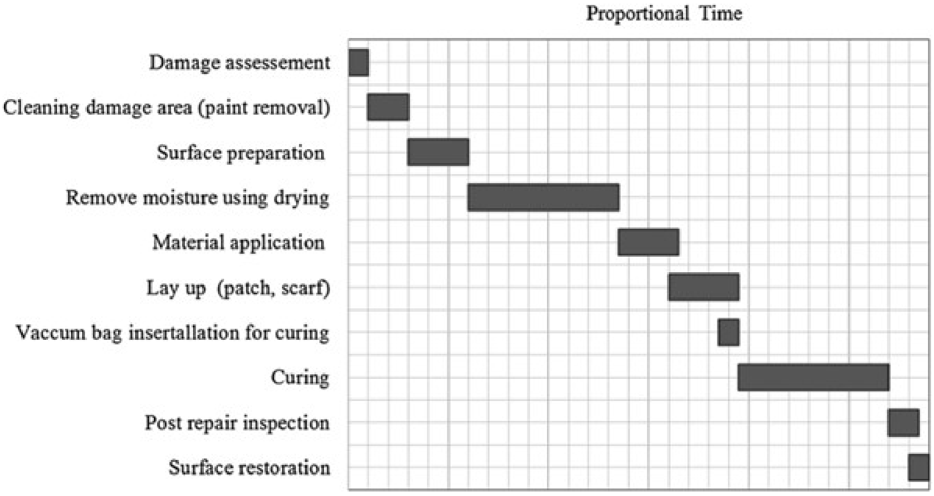

Figure 2.24: Manufacturing timeline of a composite bonded repair (Budhe et al., 2018).

2.2.4.1 Surface Preparation

Aircraft structures are often subjected to adverse environmental conditions, in terms of moisture and temperature. In this way, it is emphasised by Baker et al. (2002) that a surface treatment must ensure two conditions, as follow:

- adhesion forces between adhesive and substrates are stable even in the presence of hot/wet conditions;
- oxide layer hydration must be avoided, not weakening surface regions by the appearance of weak boundary layers.

Bond durability is strongly influenced by surface preparation. Baker et al. (2002) mentioned three basic factors:

- surface roughness;
- surface hydration;
- surface contamination.

Increasing surface roughness can increase bond durability, because mechanical anchorage is favoured, as it was stated before. Although, surface hydration and contamination decrease significantly bond durability, and consequently, the longevity of the repair system.

Prior to a detailed explanation of surface preparation in aluminium, titanium and also composite substrates, Baker et al. (2002) expose a generalised surface treatment procedure. The following preparation sequence is merged by topics mentioned by the authors while generalising but also while detailing for cases where composite substrates are used:

1. **Degreasing**
   Grease reduces significantly the surface energy, and sometimes is responsible to generate weak boundary layers. Degreasing operations are essential to decrease the level of organic contaminants on the surface of the substrate. In the case of composite bonded repairs, degreasing is usually performed using acetone.

2. **Abrasion**
   Abrasion operations have the main objective to provide active surfaces out of contaminants, while generating a rough topography. For composite substrates, sanding operations are usually sufficient, and, most of the times, are the most convenient under repair environments. It has to be mentioned that for substrates with unidirectional lay-up, the sanding direction should be parallel with the fibres. Care must be taken in order to avoid fibre damage or any fibre-matrix de-cohesion.

3. **Cleaning**
   After abrasion, the surface has to be cleaned using compressed air. Completing the cleaning procedure, the application of isopropyl alcohol is recommended. The surfaces must be maintained out of contamination until the adhesive is applied.

4. **Drying**
   In most of the environments where bonded repair operations are performed (*"in situ"*), drying operations are impossible, due to absence of specialised equipment. Although, if proper

conditions are met, composite substrates can be dried at 120°. Drying times are dependent on the laminate thickness, where Fick's law can be considered for a simple calculation. For a laminate with 6.3 mm, under a temperature of 135°, 24 h are needed for a complete drying process.

5. **Primer Application**
   The application of primers can be very difficult, if not impossible, considering *"in situ"* repair operations. Although, for maintenance operations where proper conditions are met, the application of a primer, prior to bonding, has the capability to improve wetting properties, not necessarily meaning that bonding performance is globally improved.

Considering this surface treatment sequence, it is possible to perform a correct surface preparation in composite substrates, under *"in situ"* conditions. By using acetone, sanding paper, compressed air, and isopropyl alcohol, is sufficient to prepare the surface of a composite substrate. However, it is emphasised by the authors that the nature of the surface to bonded determines the best surface preparation (Baker et al., 2002).

2.2.5 Durability and Environmental Effects of Bonded Repairs

Durability is intrinsically related to creep and fatigue, combined with environmental effects. Studying those factors is the way to predict the lifetime of a bonded repair in service. In this way, the introduction of creep analysis to bonded repairs should start in the review of corresponding durability.

The previous section was dedicated to manufacturing and also surface preparation techniques. In fact, all the described procedures have the special attention to avoid voids and defects, providing a high durability in a bonded repair. Inappropriate surface treatments can be responsible for short lifetimes.

There are several environmental factors affecting durability such as: high and low temperatures, moisture or relative humidity, chemical fluids, and even outdoor weathering (Petrie, 2007). The criticality of the combination of mechanical stress, in terms of creep or fatigue loading, with environmental effects is emphasised by Petrie (2007). It is referred that the combination of mechanical and chemical effects is more critical than the individual sum of both factors.

Petrie (2007) analysed particularly each environmental factor. It was mentioned by the authors that rheological properties are degraded by elevated temperatures, whose effect on creep behaviour is significant. In addition, the capability to sustain loads is reduced, due to thermal expansion of the adhesive layer. In this way, cohesive strength is reduced under high temperatures. Several adhesives can reasonably sustain their properties under elevated temperatures, but in a short period of time, where toughness is increased, but the shear strength is decreased. In fact, in most of the situations, thermal ageing is the main responsible for property degradation, where the bond line is weakened both cohesively and adhesively. High temperature adhesives were mentioned by Petrie (2007), being characterised by a rigid polymeric structure, a high softening temperature, and stable chemical groups. The authors proposed modified epoxy adhesives. Unmodified epoxy-based compounds are usually limited to 120°C. Figure 2.25 shows the degradation of the shear strength due to thermal ageing in typical epoxy adhesive. Nevertheless, epoxy-phenolic resins can sustain loads until 370°C in short term operations. In long term operations, a reasonable mechanical performance is retained until 180°C.

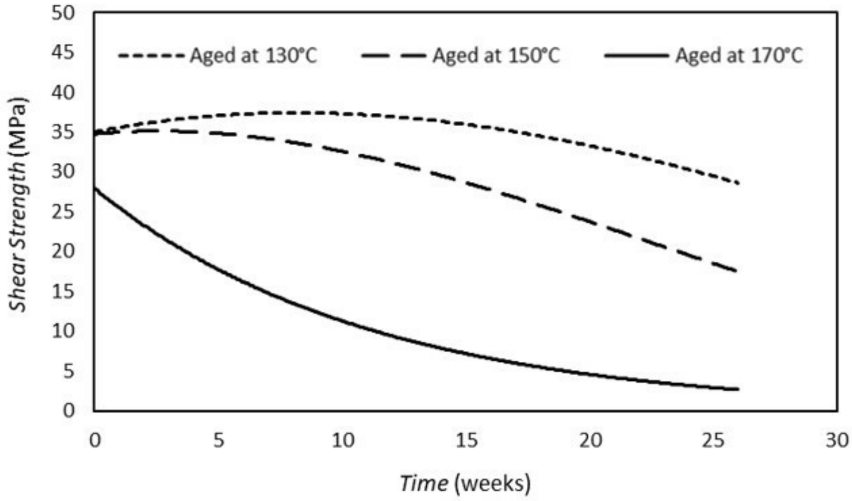

Figure 2.25: Thermal ageing on a typical epoxy adhesive (Petrie, 2007).

Not only high temperatures can affect significantly the mechanical performance, but also low temperatures. In this way, following Petrie (2007), the strength is mainly influenced by three factors, such as:

- differences in thermal expansion between adhesive and adherends;
- modifications in stiffness;
- thermal conductivity.

Stress concentrations can derived by differences in the thermal expansion, when the temperature is decreased. It is mentioned by the authors (Petrie, 2007) the importance of retaining properties in those conditions. Those stress concentrations may not be sufficiently released by an excessive increase in the modulus of elasticity at low temperatures. Avoiding stress gradients is also an important factor, and that is minimised by a lower thermal conductivity (Petrie, 2007).

Effects of moisture are even more notable on mechanical properties, rather than high/low temperatures. In fact, moisture can degrade (Petrie, 2007):

- properties of the bulk adhesive;
- adhesion properties at the interface;
- properties of adherends, as well as dimension changes.

Moisture penetrated into the interface adhesive-adherend, or in the interlaminar region fibre-matrix. Bulk properties are degraded by the reduction of the glass transition temperature, which is a result of force reduction between molecules, where cracks are nucleated and propagated, or by chemical reaction. This process is known as hydrolysis (Petrie, 2007). Degradation by moisture adsorption can be reversible if only physical phenomena takes place. Nevertheless, if chemical reaction occurs, such as hydrolysis, part of the degradation is not reversible. In terms of mechanical properties, both strength and stiffness are decreased. However, the elongation at break is increased.

In order to avoid degradation by moisture adsorption, promoting durability, Petrie (2007) proposed the use of additives. In this way, water is prevented from reaching the adhesive-adherend interface, through the following possibilities:

- selecting an adhesive with lower water permeability;
- incorporating inert fillers into the adhesive;
- coating edges using sealants with low permeability;
- chemical modification in the adhesive, reducing water permeation.

Low permeability favours the reduction of the moisture level in the bulk adhesive, and it is achieved by selecting an adhesive with lower permeability, by using coating edges with sealants, or even inducing chemical modifications. The incorporation of inert fillers reduces the adhesive volume which is affected by moisture (Petrie, 2007).

Durability and environmental effects have been widely investigated to adhesively bonded joints and repairs. All the developments established for joints are applicable for repairs.

Rider et al. (2010) investigated single-strap, one-stepped and scarf repairs (Figure 2.19) under cold/dry and hot/wet conditions. Also scarf repairs using a reinforcement patch were considered. Both using experimental and numerical techniques, the authors were able to prove that using a reinforcement patch in a scarf repair favoured significantly the retaining of strength under hot/wet conditions. It was stated that single-strap and scarf repairs present limitations in terms of the repair capability under hot/wet conditions, specially when temperatures approach the T_g value.

Moisture affects on single-strap repairs were demonstrated by Oudad et al. (2012). Both experimental and numerical techniques were imposed. The experimentally measured properties were used in a FE model, where moisture effects on composite bonded repairs are possible to analyse. The J integral was computed, as well as the shear stresses in the adhesive layer. The authors found experimentally that the water absorption by the adhesive layer increases the ductility, but decreasing the corresponding strength. Oudad et al. (2012) proved numerically that the repair efficiency is substantially decreased by moisture effects. Nevertheless, it was reported that water absorption can favour the durability of a composite bonded repair. This statement is strongly questionable, since it was proved numerically. However, it was seen experimentally that the ductility is increased by moisture effects, which favours the increase of strain energy release rate. In this way, the repair system has an improved energetic capability while sustaining loads. Nevertheless, Benyahia et al. (2014) performed a similar study, also using numerical techniques with applications to a single-strap repair system under tensile loading. The authors also stated that the ductility is increased by moisture effects, as well as the reduction of the repair efficiency, agreeing with what was mentioned by Oudad et al. (2012). Benyahia et al. (2014) proved that the stress intensity factor is increased with the humidity content in the adhesive layer, decreasing the fatigue life of the repair system. Consequently, Benyahia et al. (2014) stated that the durability of bonded repairs is reduced by moisture effects. This is the opposite to what was referred by Oudad et al. (2012). Additional experimental studies are needed, accessing the durability of bonded repairs after being exposed to wet conditions.

Moisture effects can be reversible, if only physical changes were induced. It is possible to extinguish those effects by drying processes. However, for repair applications, specially *"in situ"*, those processes have a limited time. Budhe et al. (2014) studied drying processes on DCB specimens, evaluating the recovery of mode I properties. After immersions of 336 h, the specimens were dried for 1 h and 24 h. It was reported a satisfactory recovery in strength after 24 h of drying. Nevertheless, this time was unable to induce a 100% recovery. Extended drying processes are needed for that purpose, which is very difficult in composite bonded repairs, even in normal maintenance operations. Figure 2.26 demonstrates the recovery induced by drying processes of 1 h and 24 h. Budhe et al. (2014) also evaluated the recovery in the mode I fracture toughness. A 50% recovery was obtained by drying processes corresponding to 24 h, in comparison to 1 h drying processes. The authors studied an adhesive film to apply as a pre-bond conditioning, avoiding interlaminar cracks in pre-cured adherends.

Effects of adverse conditions on properties corresponding to mode I, mode II, and mixed-mode I+II loadings were assessed by Silva et al. (2020). Additionally to DCB, ENF and SLB (single-leg-bending) tests, performing fracture characterisations under mode I, mode II, and mixed-mode I+II loadings, respectively, single-strap repairs were also analysed through 3-point-bending tests. Four temperatures (-20°C, 0°C, 50°C, and 65°C) and three humidity conditions were imposed to the specimens. Different fluids were used to impose adverse conditions through moisture effects: magnesium nitrate hexa-hydrate $[Mg(NO_3)_2, 6H_2O]$, with a RH (relative humidity) of 76%, sodium chloride $[NaCl]$, with a RH of 55%, and distilled water $[H_2O]$. Thermal effects were tested considering maximum exposures of 4 months, while moisture effects were tested considering a maximum of 8 months. With a total of 464 experimental fracture tests, three parameters were studied: initial stiffness, maximum load, and displacement at failure. Numerical techniques was used to evaluate the referred adverse conditions on single-strap repairs in flexural loading. A trapezoidal CZM law was applied, where mixed-mode I+II loading is considered. As general conclusions, Silva et al. (2020) stated that the fracture properties are degraded with time of exposure in all modes of loading. It was also stated that both thermal and moisture effects are notable only in early stages of exposure. This proves that long exposures do not provide additional information about the fracture behaviour under adverse conditions. Regarding single-strap repairs, it was reported that the strength remains uninfluenced by both thermal and moisture effects. However, the

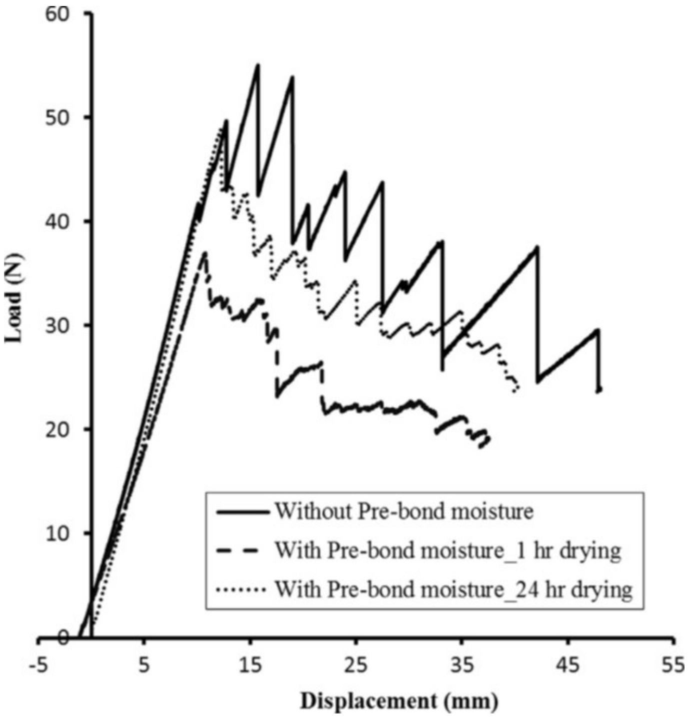

Figure 2.26: Load-displacement curves of DCB tests showing the recovery of drying processes (Budhe et al., 2014).

displacement at failure is decreased, indicating that a brittle behaviour is induced, while the stiffness is increased. Numerical results were validated, when compared to experimental data, where a linear energetic criterion was applied successfully.

Brito et al. (2020) also studied the fracture behaviour, only for mode I loading, under adverse conditions, but with applications to composite bonded joints. Two different bonding techniques (co-curing and co-bonding) were implemented under different thermal and hygrothermal conditions. As received specimens were subjected to temperatures of −54°C and 25°C. Additionally, specimens aged with moisture were subjected to temperatures of 25°C and 80°C. Failure mechanisms were assessed through the applications of DMA (dynamic mechanical analysis) and SEM (scanning electron microscopy). Regarding as received specimens, for co-curing, crack propagation started at the interlayer region between the two adherends. Crack seemed to migrate to one of the adherends, after a pre-determined propagation. For co-bonded specimens, still considering as received material, it was reported that the failure was generally cohesive. Regarding hygrothermally aged specimens, a fibre-tear failure in the adherends was observed for both bonding techniques. It was concluded that moisture effects present higher influences on the failure mechanism, comparing with thermal effects.

Most of the studies demonstrate the environmental effects on mechanical properties, but only individually. Fevery et al. (2021) demonstrated that an analysis must be performed in adhesively bonded joints so that the combination of environmental effects on mechanical properties is carefully studied. The residual strength of single-lap joints was analysed experimentally after ageing.

The following conditions are imposed, solely and also in combination: static and dynamic loading, UV radiation, temperature and humidity. The authors concluded that the residual strength is increased by a factor of 3, when the temperature increases. It was proved that the influence related to thermal conditions is notably dominant. UV radiation demonstrated to be less influent, revealing an increase of residual strength in 15.5%. Dynamic loading also demonstrated to increase residual strength, but in 25.4%. On the other hand, static loading revealed a decrease of residual strength in 27.6%. This study showed that mechanical properties can be slightly improved after ageing, specially due to thermal conditions, while promoting an increase in residual strength.

Not only adverse environmental conditions have huge effects on durability of bonded joints and repairs, but also mechanical loading conditions, such as fatigue and creep, where studies analysing fatigue loading conditions were already mentioned in Section 2.2.3. Creep loading conditions are often presented in aeronautical structures, where there are bonding applications both in joints and repairs. The current state-of-art in terms of analysis of creep loaded bonded joints and repairs is exposed in Section 2.2.5.1, where corresponding effects on durability is described.

2.2.5.1 Mechanical Behaviour and Durability under Creep Conditions

The time of exposure to a given load is an important factor on the durability of a structure. Mechanical properties can be substantially degraded during that exposure, specially in the adhesive layer.

Temperature effects on creep behaviour of adhesively bonded joints were assessed by Sadigh et al. (2019), while developing numerical techniques, justified with experimental data. Creep uniaxial tests were performed on ARALDITE® 2015 specimens, at three different stress levels (6.13 MPa, 7 MPa and 8.5 MPa), while being exposed at three different temperatures: 25°C, 40°C, and 55°C. Double-lap joints were also analysed experimentally, performing three creep uniaxial tests, considering the following thermal conditions: 45°C, 50°C and 55°C. A constant load of 765 N is applied, and the displacement is registered for 12 days. The creep life-time for the double-lap joint specimen under 55°C was lower than 12 days, where tertiary creep was captured. Although, that tertiary creep was only registered experimentally. The developed numerical technique was not capable to predict creep failure. Specimens under 45°C and 50°C demonstrated to have creep lifetimes higher than 12 days. The slope of the secondary phase was markedly increased for higher temperatures.

Creep loaded single-lap joints and double-strap repairs were analysed by Sadigh et al. (2020). Tensile and uniaxial creep tests were performed on adhesive and adherend materials, in order to access mechanical properties to develop numerical models. Those numerical models were validated with an experimental campaign, by performing creep tests in single-lap and double-strap specimens, considering uniaxial loading. Elongations observed experimentally in double-strap specimens were considerably lower when compared to elongations verified for single-lap specimens. Three different overlap lengths were tested: 19 mm, 29 mm and 39 mm. Differences in terms of creep compliance are diminished with the increase of the overlap length.

Long term normalised creep tensile tests were performed, on specimens made of cold-curing epoxy adhesives, by Cruz et al. (2021). Degreasing procedures were a variable under analysis. The influence of creep stress level and hygrothermal conditions on the viscoelastic response was also assessed. An experimental campaign was performed, where creep tests were considered with an exposure to load and environmental conditions within 2400 h. Three testing conditions were considered for the creep loaded specimens: application of 40% of the limit load at 55% of RH, application of 30% at 55% RH, and the application of 30%, but considering 98% of RH. All tests were performed at 20°C. Specimens were subjected to different treatment processes. For each load and environmental scenario, 2 reference specimens were considered, 2 other specimens were subjected to a given degreasing procedure, and the last specimens were subjected to a more aggressive degreasing process. Before performing creep tests, tensile properties were assessed on the epoxy specimens. It was found that strength and stiffness properties can be improved until 49%, while applying degreasing processes. Regarding creep testing, it was mentioned that hygrothermal conditions had great influence on the viscoelastic response. For specimens subjected to 55% of RH, only secondary creep was captured within 2400 h. On the other hand, tertiary creep was registered for specimens subjected to 98% of RH, within the creep testing time of 2400 h. Cruz et al. (2021) also used linear viscoelasticity in order to characterise the creep response of epoxy adhesives at different hygrothermal and degreasing conditions. A good agreement between experimental and analytical techniques was found, while applying the Burgers viscoelastic model. These type of models are introduced in this chapter in Section 4.1.1.

An adhesive joint between a metallic stringer and a carbon-epoxy skin was analysed by Wang et al. (2021). This consists in a highly scaled testing typology, where these types of joints are often used in aeronautical structures. Considering a certification parlance (Section 2.2.6), this scale level is referred to details in a structural level. The considered model by Wang et al. (2021) is presented in Figure 2.27. Ambient cured (20°C) epoxy adhesives were considered for the study. Thermomechanical properties of the adhesive for the generalised Maxwell model (Section 4.1.1.1) were assessed using DMA. In this procedure, the glass transition temperature (T_g) is determined, which is property of the adhesive. Every time that a different is used, DMA has to be applied in order to access the T_g, whose value is an input for the numerical models. FE modelling, using CZM for the adhesive layer, was applied to models presented in Figure 2.27, where the following temperature conditions were considered: 25°C, 40°C, and 55°C. It was referred that irreversible creep is possible, when the structural detail is subjected to high temperatures, only due to different thermal expansion coefficients between the stringer and the carbon-epoxy skin. The use of an adhesive with a T_g higher than the service temperature, in 15°C is strongly recommended. In general, creep damage is favoured for higher temperatures. Nevertheless, it was reported that even under 25°C, viscoelastic phenomena reduce the strengthening effectiveness between stringer and skin.

Creep behaviour of rubber-like adhesives under mode I loading was experimentally tested by Schrader et al. (2022), using DCB specimens. The main focus of this study was to access the dependency of crack resistance and its relation with crack propagation rate. Additionally, the authors

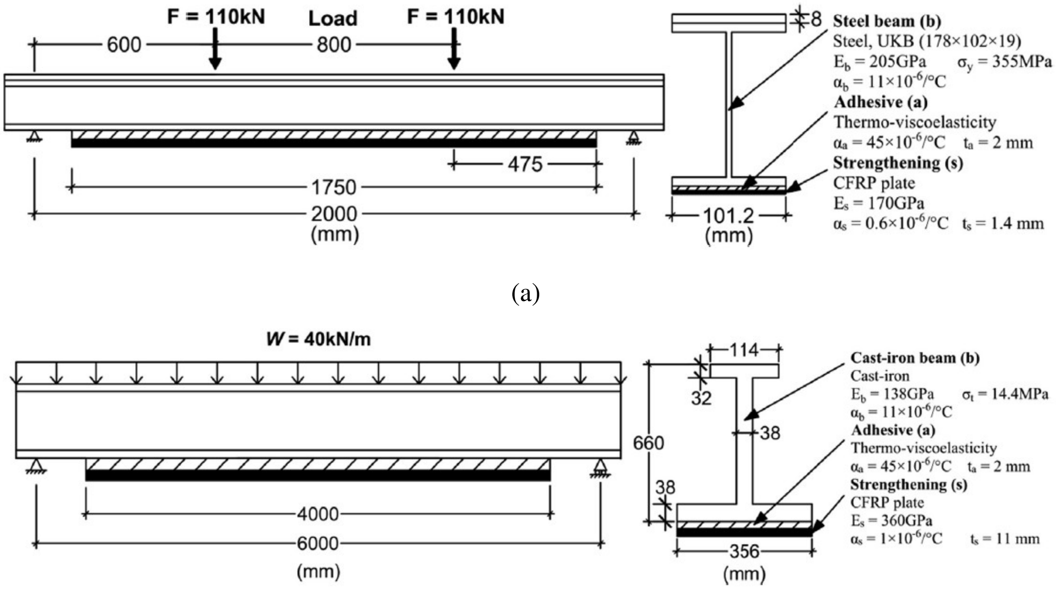

(a)

(b)

Figure 2.27: Model considered by Wang et al. (2021): (a) steel stringer, (b) cast iron stringer.

related these parameters with the appearance of minor cracks, and corresponding relation with the macroscopic major crack tip. Considering this purpose, the crack propagation was controlled *"in situ"*, by using two cameras targeting on both sides of the specimen. A specific image processing methodology was implemented, by observing the modified pixels, called by the authors as *"damaged pixels"*. This type of image processing is exemplified in Figure 2.28.

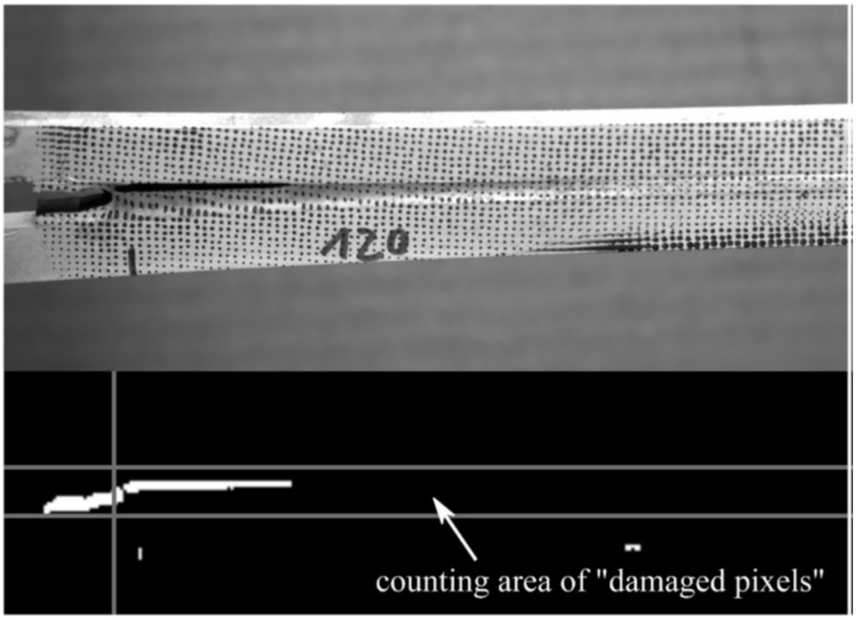

Figure 2.28: Image processing methodology by the concept of *"damaged pixels"* (Schrader et al., 2022).

The type of crack propagation detection presented in Figure 2.28 is compared with the conventional compliance-based method, consisting on a simple beam theory. Differences in the results regarding crack propagation rate between the two methodologies indicate the presence of minor cracks, following Schrader et al. (2022). Corresponding results are shown in Figure 2.29. The difficulty in observing minor cracks, as viscous softening or micro-damage, using optical measurement techniques is markedly noted by the authors. This type of damage was only detected optically by observing surface tearing during crack propagation, which was assessed by counting the *"damaged pixels"*. On the other hand, Schrader et al. (2022) mentioned that compliance-based methods can provide good approximations, even with the presence of those minor cracks. It was stated that the presence of minor cracks away from the major crack tip in the direction of crack propagation is the reason for the difference between results found while optical and compliance-based methods, as shown in Figure 2.29. In this way, it was concluded that the presence of minor cracks is correlated with the observed crack propagation rate. Higher amounts of minor cracks yield a decrease in the crack propagation rate. This conclusion is justified by the fact that minor cracks reduce stress intensity in the macroscopic major crack tip, increasing crack resistance in the structure.

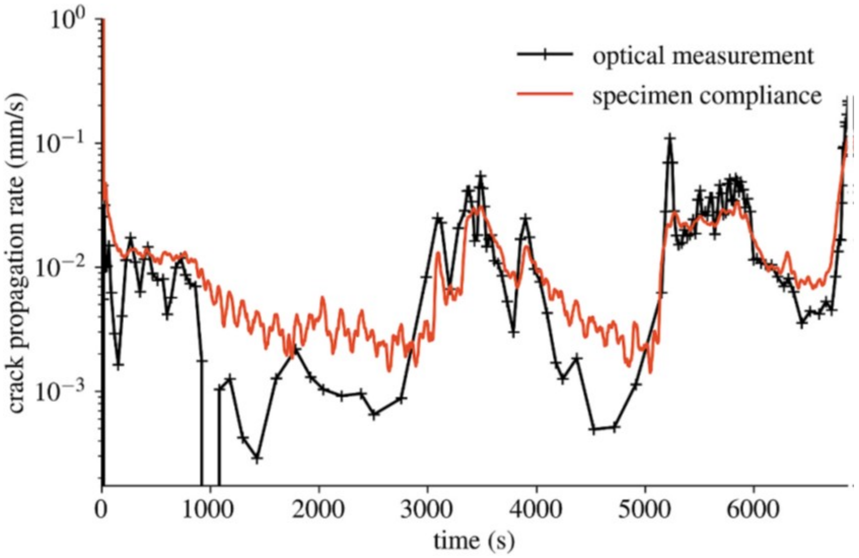

Figure 2.29: Comparison between optical and compliance-based methodologies in the determination of crack propagation rate (Schrader et al., 2022).

Pure mode I loading was also experimentally analysed in studies conducted by Nakamura et al. (2023), where creep crack growth is investigated. Aluminium substrates were bonded using an epoxy adhesive, constituting DCB specimens. Those are immersed in temperature-controlled water, while being creep loaded using a spring. In this way, the influence of creep conditions combined with hydrothermal effects are achieved for pure mode I loading. Different temperature conditions were tested (32°C, 63°C and 90°C), considering two types of surface treatment (sandblasting and pickling). It has to be noted that these different conditions were imposed, but maintaining the initial ERR (energy release rate) of 500 J/m^2, corresponding to 75% of the critical

ERR ($G_{I_c} = 679\ J/m^2$). Other scenarios were considered, where different initial load levels were imposed, corresponding to different values of initial ERR: 253 J/m^2, 372 J/m^2, 500 J/m^2 and 621 J/m^2. In this case, the spring constant, temperature and surface treatment were maintained so that imposing 49 N/mm, 90°C and sandblasting, respectively. This study was capable to predict the ERR by requiring one single parameter, instead of the conventional ones (crack length, load and displacement). This was possible due to the use of a specific data-reduction scheme, while calculating the ERR by the CBBM (compliance-based-beam-method). This data-reduction methodology was proposed by de Moura et al. (2008b). As general conclusions, considering hydrothermal creep conditions, Nakamura et al. (2023) were able to state that the threshold of ERR is solely dependent on thermal conditions, where this threshold increases for lower immersion temperatures. The pickling surface treatment seemed to inhibit more efficiently the crack propagation, rather than sandblasting.

The influence of temperature, humidity and load, as well as their coupled effects, were analysed on creep loaded adhesively bonded single-lap joints by Tan et al. (2023), using an adhesive made of polyurethane. Experimental tests were performed considering different static loads (200 N, 400 N and 600 N), for different exposure times (96 h, 192 h, 288 h, and 384 h). A high temperature environment, imposing 80°C, was considered. An additional scenario of this high temperature environment combined with a wet one was also imposed, for a RH of 95%. Creep strain was significantly larger when specimens are subjected to hot/wet environments, with lower creep lifetimes. These results are related to molecular aspects, where softening and hydrolysis phenomena are involved. It was also proved that the degradation of mechanical properties is substantially more aggressive in scenarios having the combination of hot and wet environments, rather than in scenarios having solely hot environments. Molecular aspects were also mentioned by the authors. During creep phenomena, cracks appeared in the adhesive layer where water molecules are diffused, providing a significant increase in the degradation of mechanical properties.

These are general studies about durability and its relation with creep conditions, while combining with environmental effects or not. The developments shown for adhesively bonded joints are also applied to adhesively bonded repairs. However, future work should be presented specifically regarding bonded repairs. Massive experimental developments are demonstrated in the state-of-art on this subject for adhesive joints, and some literature tried to reproduce the creep response either analytically or numerically. Nevertheless, the application of advanced FE modelling, using CZM, was residually proved. Great efforts should be done in future developments, in order to reproduce easily the creep behaviour of adhesively bonded joints and repairs. First of all, an overview on the classical viscoelasticity should be performed, where analytical models can be developed. Those are reviewed in Section 4.1, being part of this chapter. Analytical models, expressing damage evolution, can be implemented on cohesive zone models within a FE environment. This methodology is performed in Chapter 4. For a complete modelling, considering all loading scenarios (pure mode I, pure mode II, and mixed-mode I+II), an experimental campaign should be performed, whose creep fracture behaviour is characterised. This type of developments are demonstrated in Chapter 3. In this way, this dissertation contributes significantly for developments in the topic under analysis in this section.

2.2.6 Aeronautical Certification of Composite Bonded Repairs

The fundaments of aeronautical certification regarding composite bonded repairs are exposed in this section. The design, as well as the manufacturing of bonded repairs must follow means of compliance indicated by certification authorities such as EASA (European Aviation Safety Agency) and FAA (Federal Aviation Administration). In fact, certification authorities can provide guidelines for engineers, facilitating design and manufacturing procedures.

Before introducing the aeronautical certification topic on composite bonded repairs, the concept of airworthiness has to be highlighted, as well as the definition of *"continuing airworthiness"*. de Florio (2016) defined the concept of airworthiness, following RAI-ENEC technical regulations:

> *"For an aircraft, or aircraft part, (airworthiness) is the possession of the necessary requirements for flying in safe conditions, within allowable limits."*

The same reference defined *"continuing airworthiness"*, following ICAO (International Civil Aviation Organisation):

> *"The set of processes by which an aircraft, engine, propeller or part complies with the applicable airworthiness requirements and remains in a condition for safe operation throughout its operating life."*

Repair operations are processes that can be included in the *"continued airworthiness"* domain, which is distinct from *"continuing airworthiness"*. *"Continued airworthiness"* is more related with maintenance operations (de Florio, 2016). In fact, *"continued airworthiness"* procedures are required in order to achieve *"continuing airworthiness"*. Following an article presented in the subpart M of the FAR 21 (21A.431(b)), a repair operation can be defined as follows (FAA, 2023):

> *"A repair means elimination of damage and/or restoration to an airworthy condition following initial release into service by the manufacturer of any product, part or appliance."*

In fact, a given repair must eliminate the damage, as well as restoring, most of the times, the limit load capability, whose value was stipulated in the structural design. Specifically for a PSE (primary structural element), ultimate load capability must be restored.

The capability to perform a given repair is also mentioned in the subpart M of FAR 21 (FAA, 2023), specifically in the topic 21A.432B(a), so that:

> *"An applicant for a major repair design approval shall demonstrate its capability by holding a design organisation approval, issued by Agency in accordance with subpart J."*

It is explicitly mentioned in this statement that a DOA (design organisation approval) is needed in order to perform a major repair. A repair operation which influences the mechanical properties of the structure is a non-cosmetic repair, and is then intended as a major repair (de Florio, 2016). Following the topic 21A.441(b) (FAA, 2023), it is intended that a given OEM, having a DOA, must transmit to the airliner or other aircraft owner, even if they also possess a DOA to perform repair operations. These instructions constitute to what as known as the SRM (structural repair manual). In this way, it is stated that:

> *"The design organization shall transmit to the organization performing the repair all the necessary installation instructions."*

There are several challenges related to bonded repairs, as it is mentioned in AC20-107B (FAA, 2009), which provides means of compliance related to aircraft composite structures. This advisory circular mentions explicitly that (AC20-107B(10)(b)(3)):

> *"... Of particular safety concern are the issues associated with bond material compatibilities, bond surface preparation, cure thermal management..."*

There is an advisory circular provided by FAA specifically dedicated to composite bonded repairs: AC43-214 (FAA, 2013), providing useful and detailed means of compliance in order to design and manufacture any minor or major repair. A given MO (maintenance organisation) should follow carefully this advisory circular. Guidelines are provided, complementing instructions provided by the DAH (design approval holder) in the SRM. Although, it has to be noted that all the procedures to perform a major repair must be approved by the FAA, so that it is stated in AC43-214 (FAA, 2013), as follows (AC43-214(5)(a)(2)):

> *"Data for major repairs and alterations must be approved by the FAA (or its designee). FAA approval is also required for major changes to technical data that was previously FAA approved..."*

However, it is explicitly mentioned that the FAA approval is not required for minor repairs, where following guidelines related to continued airworthiness documents, as the AMM (aircraft maintenance manual), are sufficient for compliance (AC43-214(5)(a)(2)):

> *"... Minor repairs and alterations, and minor changes to previously approved data, do not require FAA approval. Certain documents associated with the instructions for continued airworthiness (ICA), such as the Aircraft Maintenance Manual (AMM), are acceptable to the Administrator..."*

All the document is analysed in this section, commenting some statements referred by the certification agencies. In fact, AC43-214 (FAA, 2013) describes more explicitly, providing means to comply with specifications presented in FAR 135, 137, and 145, being part of the title 14 of the Code of Federal Regulations (14CFR).

Not only instructions are provided as means of compliance, but also the basic requirements are highlighted. Required data to achieve compliance is enumerated in the referred advisory circular. It is clear that every single element in a repair system must be carefully detailed by MOs (AC43-214(5)(b)):

> *"Each MO must have and maintain data required to define the materials, configuration, and accomplishment procedures for the repairs or alterations it performs..."*

For the effect, several documents, including technical drawings, must be provided by a given MO, in order to show compliance with specifications mandated by the authorities (AC43-214(5)(b)):

> *"Data must include the drawings and specifications that define the repair or alterations, including required dimensions, materials, and processes necessary to achieve structural strength and other design properties (e.g., transmissivity, lightning strike protection, and flammability)..."*

The required data by certification for a given repair or alteration is then specified in the following topics (AC43-214(5)(c)) (FAA, 2013):

1. **Drawings**
   All the involved materials, either related to substrates or adhesive, must be identified, mentioning corresponding properties, proving that the required strength is met, according to material specifications related to the structure under repair procedures. In addition, stacking sequences, and corresponding orientations, as well as the number of plies must be specified for composite substrates. Other parameters must be detailed as the shape, dimensions, and tolerances. Even the manufacturing processes, location of repair in the structure, and additional coatings and sealants must be described in drawings.

2. **Substantiation Documentation**
   Every detail presented regarding the bonded repair must be properly documented, according to orientations provided by authorities, including drawings. Bonded repairs must show compliance with requirements related to static and fatigue loading scenarios, demonstrating proper strength capability. Static and damage tolerance reports must be presented, similar to what happens for any aircraft structure. It was noted that creep loading was not mentioned in AC43-214 (FAA, 2013). Creep loading scenarios can cause structural failure and should be referred in the future by mentioning proper means of compliance, including that mechanical phenomenon on damage tolerance programmes.

3. **Material Specifications**
   Part of the material specifications are provided in drawings, but every step of developments related to materials must be properly detailed, from the reception or bulk material until the final component. A material qualification and substantiation must be performed, identical to what must be developed in any material applied to any structure such as wings and fuselages. Material specifications must also include quality control and inspection and also storage conditions.

4. **Fabrication and Process Specifications**
   Every step related to the manufacturing process must be detailed and documented, whose fabrication procedures are similar to what is described in Section 2.2.4. However, special care must be taken, and it is emphasised with means of compliance in the document under analysis. Further details are mentioned in this section.

5. **NDI Procedures**
   It is clearly referred that the NDI techniques under use must be detailed and documented, identifying corresponding procedures, equipment, acceptance/reject criteria, and also personnel qualifications. Several NDI techniques are recommended in AC43-214 (FAA, 2013), such as visual inspection, tap testing, radiography, ultrasonic (Figure 2.30), infrared thermography and shearography.

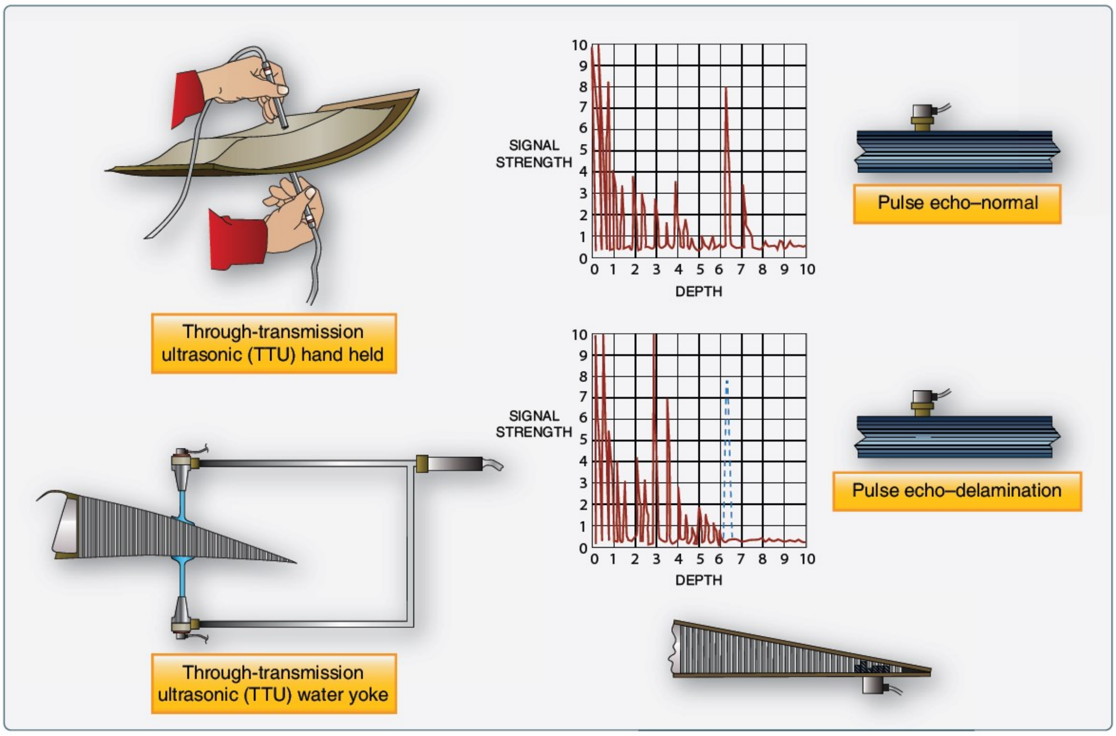

Figure 2.30: Ultrasonic testing explained by FAA (2012).

Several means of compliance are then detailed in the AC43-214 (FAA, 2013), where proper recommendations are provided, specially regarding the manufacturing of bonded repairs. As previously mentioned, all the involved materials must be specified since the acceptance of bulk state until it is found in a final component. In this way, a raw material inspection program is mandatory. This is justified by the authorities, where the following argument is stated (AC43-214(6)(a)(2)) (FAA, 2013):

> *"... The physical, processability, chemical, and mechanical test results are, therefore vital to continued airworthiness of the structure."*

Knowing all the properties related to the materials involved, and if they are properly documented, it is much easier to solve any structural problem. In fact, physical, chemical and mechanical properties are required for design and also for damage tolerance programmes.

Regarding material acceptance, which is described in the topic AC43-214(6)(b) (FAA, 2013), FAA specifies some special cares, as follows (AC43-214(6)(b)(1)):

> *"... The MO is responsible for ensuring that the materials are protected from contamination, temperature deviations, and problems caused by storage and handling after the original manufacturing process after receipt of the material."*

Still regarding raw material inspection, another recommendation mentioned in AC43-214 (FAA, 2013) is related with quality control. All material batches must be referenced, while being accepted from a given supplier, so that (AC43-214(6)(b)(3)):

> *"Copies of the original material manufacturer and supplier laboratory test reports showing actual test results, if applicable, must accompany each batch of material received for purchaser review and approval."*

Quality control is very restrictive not only for material acceptance, but also for the storage of raw material. Every parameters related to material storage must be recorded and reported, complying with certification requirements. These parameters must include temperature, pressure and humidity, and the corresponding time of exposure. These conditions must respect the shelf life of the raw material specified by the supplier, according to data approved by the certification authority. In this way, it is stated that (AC43-214(6)(b)(6)(d)) (FAA, 2013):

> *"Recording of storage time and environmental exposure (i.e., temperature and humidity). The MO must have a system that ensures that knowledge of storage and shipment times and environmental exposures are known, and in compliance with the requirements, through whatever path is taken from the material manufacturer until the material is in environmentally controlled storage at the MO..."*

Still regarding storage, all the restricted quality control procedures are justified by the degradation of mechanical properties that improper storage and handling can induce (AC43-214(7)(a)) (FAA, 2013):

> *"Improper refrigerated storage and handling of materials, such as prepreg tape, core, core splice, fabric, adhesives, potting compounds, and resins can adversely affect the structural integrity of the finished part..."*

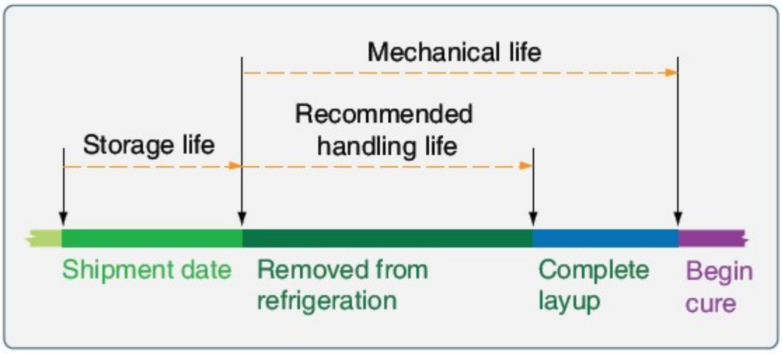

Figure 2.31: Storage of prepregs (FAA, 2012).

The FAA maintenance handbook (FAA, 2012) presents Figure 2.31, recommending procedures for storage, in this case, of prepregs.

In this way, even the equipment must be monitored, ensuring that all the requirements are met for a correct storage procedure. Specific recommendations for the storage of polymer matrix composites and adhesives are further detailed in the topic AC43-214(7)(c) (FAA, 2013).

Still regarding equipment, facilities for curing processes are also mentioned as acceptable means of compliance. In fact, the utilisation of any equipment or facility in a hangar must ensure that (AC43-214(8)) (FAA, 2013):

> *"Repairs/alterations performed on the aircraft in a hangar must have substantiating data that shows it meets the requirements appropriate for a given structure..."*

AC43-214 (FAA, 2013) mentions the use of autoclave, oven, and even clean rooms as possible facilities. However, as mentioned previously, the use of this type of equipment or space is impossible in practical terms for *"in situ"*. In fact, this type of implementation is mentioned implicitly in the same topic (FAA, 2013):

> *"... This would need to be demonstrated for the repair/alteration design and processes to be applied with the structure attached to the aircraft..."*

Repair operations can be performed with the structure attached to the aircraft in a hangar, but it can as well be implemented *"in situ"*. Nevertheless, other methods are referred in AC43-214(8)(c) (FAA, 2013), as vacuum bagging, thermal blanket, mechanical pressure, heat lamp, and heat gun, which the use of these facilities is possible for *"in situ"* repairs. Also for lay-up tooling, the other method being proposed is the use of a heat blanket.

"In situ" repairs not only involve restricted capabilities, but also restricted resources. The material reuse by the MO can be frequently for that type of repair, specially considering composite patches. Those components must be properly dried, if reversible moisture effects exist, recovering most of the mechanical properties (AC43-214(8)(i)) (FAA, 2013):

> *"For bonded repairs/alterations where the MO reuses some composite parts, a moisture dry-out capability should be available to adequately dry the entire part before layup and bonding of the repair/alteration."*

Specifically regarding composite materials, the justification for the loss of mechanical properties, either in the repair system and surrounding structure, and corresponding consequences, is presented in AC43-214(9)(2)(c) (FAA, 2013):

> *"Moisture in composites can frequently cause delaminations away from the repair/alteration location during the repair/alteration cure cycle, and in honeycomb structure it can result in blown face sheets (face sheets separated from the core)."*

After describing the conditions to perform repair operations, fabrication and processes are detailed. Similar to what was presented in Section 2.2.4, fabrication procedures are described in topics, but in this case a certification perspective is presented (AC43-214(9)) (FAA, 2013):

1. **Damage Assessment and Tear-down**
   Before any fabrication procedure, the damaged area must be properly access, and the corresponding extent of damage has to be quantified. Tear-down is an operation which releases significant amounts of dust and dirt. The authorities recommend to perform this operation in a separated area. In this way, the damaged component should be dismounted, only if possible. After any type of tear-down operation, the use of NDI is strongly recommended in order to access the induced additional damage. After all this procedures, surfaces must be properly cleaned and dried.

2. **Surface Preparation**
   In addition to what was already presented in Section 2.2.4, FAA mentions that a given MO must maintain surface preparation solutions at the proper concentration, according to properly approved procedures. Sanding is a common part of the surface preparation methods in composite substrates. A particular care in order to not damage the laminate is emphasised in the advisory circular (FAA, 2013). Alternative methods such as chemical stripping and blasting can also damage the laminate. MO must evaluate those processes, and their use must be approved *"a posteriori"*. Inspection is strongly recommended by FAA after all these procedures. The use of protective clothing is mandatory during sanding operations: *"sanding composite fiber may pose a health risk"*.

3. **Composite Ply Cutting**
   FAA essentially presents acceptable means of compliance regarding tool handling while cutting composite sheets. It is mentioned that the composite should not be cutted directly in order to not damage cutting tools. In addition, it emphasised that folding or creasing of

plies are not allowed.

4. **Lay-up**
Ply orientation specified by OEM in the SRM must be respected. The certification authority also mentioned that the methodology of laying-up must be coherent to procedures properly approved, following instructions provided by the DAH.

5. **Bagging**
It is mandatory that the bagging process is capable to remove all trapped air, while producing the desired adhesive flow. A pressure of 0.5 atm is produced in order to consolidate the composite.

6. **Curing**
It is mandatory that FAA approved procedures are correctly followed and implemented. During curing, parameters such as temperature, pressure and viscosity must be properly controlled. Nevertheless, the application of controlling procedures for this purpose is very difficult for *"in situ"* repairs. In those cases, appropriate adhesives can be used, such as the ARALDITE® 2015, which can cure in ambient condition for 24 h (Samaro, 2023).

7. **Inspection**
NDI techniques should be used after a curing cycle, specially when the repaired structure is subjected to high temperatures. Those conditions can cause damage of heat affected zones (Figure 2.32). In fact, for *"in situ"* repairs the inspection phase is just needed to check if any defect is presented in the adhesive layer, due to the absence of heat affected zones.

8. **QC and Documentation**
A plan must established in order to process critical parameters, such as temperature and pressure. All steps in a fabrication procedure must be recorded and properly documented, while included in the QC (quality control) process.

As a final statement in the considered advisory circular (AC43-214) (FAA, 2013), it is referred that every record must be retained, respecting FAA requirements specified in parts 121, 125, 129, 135, 137, and 145.

Not only certification documents present means to comply with requirements defined by authorities such as FAA and EASA, but also scientific papers within the state-of-art published in the last few decades. In fact, the compliance with requirements related to composite bonded repairs involve difficult processes, whose scientific developments are important. Under this purpose,

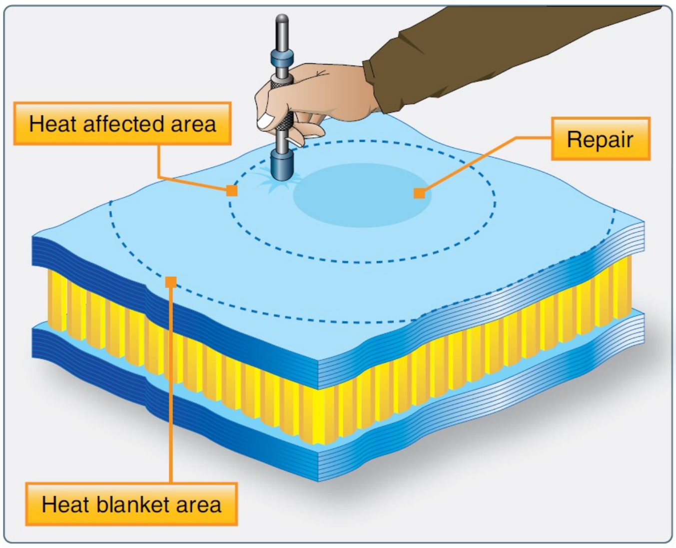

Figure 2.32: Heat affected zones and corresponding inspection (FAA, 2012).

Chalkley and Baker (1999) presented a certification procedure for a generic composite bonded repair, which is considered as a structural detail in the testing pyramid (Figure 2.33). Experimental, analytical and FE analyses were demonstrated at the corresponding testing scale level, studying de-bonding growth phenomena. Chalkley and Baker (1999) proposed a resumed certification approach in Table 2.2. This certification process, in fact, describes a design procedure.

Baker et al. (2015) presented a study on the certification of bonded repairs to primary composite aircraft components. The authors mention the two main issues related with certification:

- determination and validation of the bonded strength by using NDI techniques accessing anomalies in the adhesive layer;
- development of generic design allowables, representing actual failure modes, specially for fatigue loading, where validation tests of numerical simulations are cost and time consuming.

The absence of a generalised methodology to evaluate bonded joints and repairs is responsible for these difficulties, as mentioned by Baker et al. (2015). Consequently, alternate methods, some of those experimentally based, have to be implemented, such as proof testing of traveller specimens, laser shock proof testing, or SHM (structural health monitoring). Proof testing using traveller specimens seemed to be the most reliable procedure, with an associated low cost, being the most attractive in practical terms. Nevertheless, for hidden structural zones, where bonded repairs have to be inspected, the use of SHM is, sometimes, the only feasible approach. Weak adhesion is impossible to detect by NDI. The authors mentioned the importance of all the recording and documentation within a QC protocol, which can strongly prevent weak adhesion.

The certification of composite bonded repairs applied to a given PSE is an extensive procedure, whose some decisions have to be made with different associated approaches. In this way,

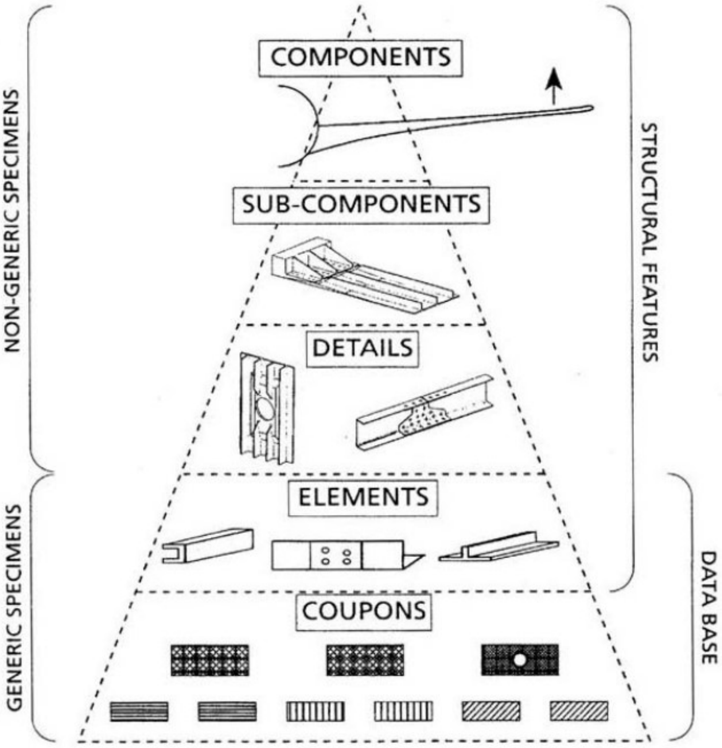

Figure 2.33: Testing pyramid for aircraft structures (FAA, 2009).

Baker et al. (2015) presented a flowchart (Figure 2.34), whose structure helps to understand the certification procedure related to composite bonded repairs in PSEs.

A different flowchart (Figure 2.35) is presented by Poudel et al. (2015), resuming not the certification process, but the design procedure.

This section described the certification process, with emphasis to composite bonded repairs, where design and manufacturing procedures are described. Some requirements are mandated by certification authorities. Nevertheless, most of the times, the documented acceptable means of compliance can constitute a guideline for MOs in order to design and manufacture, correctly, composite bonded repairs. As a future perspective, design methodologies must be improved, increasing the level of confidence on the bonding technology. Creep loading has not been investigated massively in the last years, considering bonded repairs. Novel methods should be created in order to access easily design allowables for all mechanical loading phenomena. In addition, novel NDI techniques should be studied, developing easier means to analyse the integrity of the adhesive layer.

Table 2.2: Certification approach for a bonded repair proposed by Chalkley and Baker (1999).

Step	Approach
Qualification of processes and repair materials	Follow prescribed quality procedures
Obtain information on DUL (design ultimate load) and fatigue spectrum load requirements	Obtain OEM design data for DUL. Current fatigue spectrum best obtained from instrumented aircraft, if available
Design repair based on model for bonded repairs	Use allowable data from generic coupons and generic repair joints
Design representative bonded joint and structural detail specimens to interrogate differences with generic repair	Use detailed FE models of the actual repair to design specimens (highlight differences with generic specimen)
Check the safety margin of the repair joint	Test sufficient representative bonded joints to obtain indication of fatigue performance compared with generic joint. Test at constant amplitude up to the DLL (design limit load) capability
Check damage growth and residual strength are in accordance with expectation from the validated model	Test representative structural details under spectrum loading, ambient and representative hot/wet conditions. It could use elevated load at a level based on representative bonded joint tests instead of hot/wet test
Check for unexpected secondary stresses (e.g. due to neutral axis offset) of unacceptable strain elevations in the surrounding structure	Static strain survey on instrumented subcomponent specimen may be adequate to check similarity to structural detail. Possibility to undertake test program under specimen loading, if required

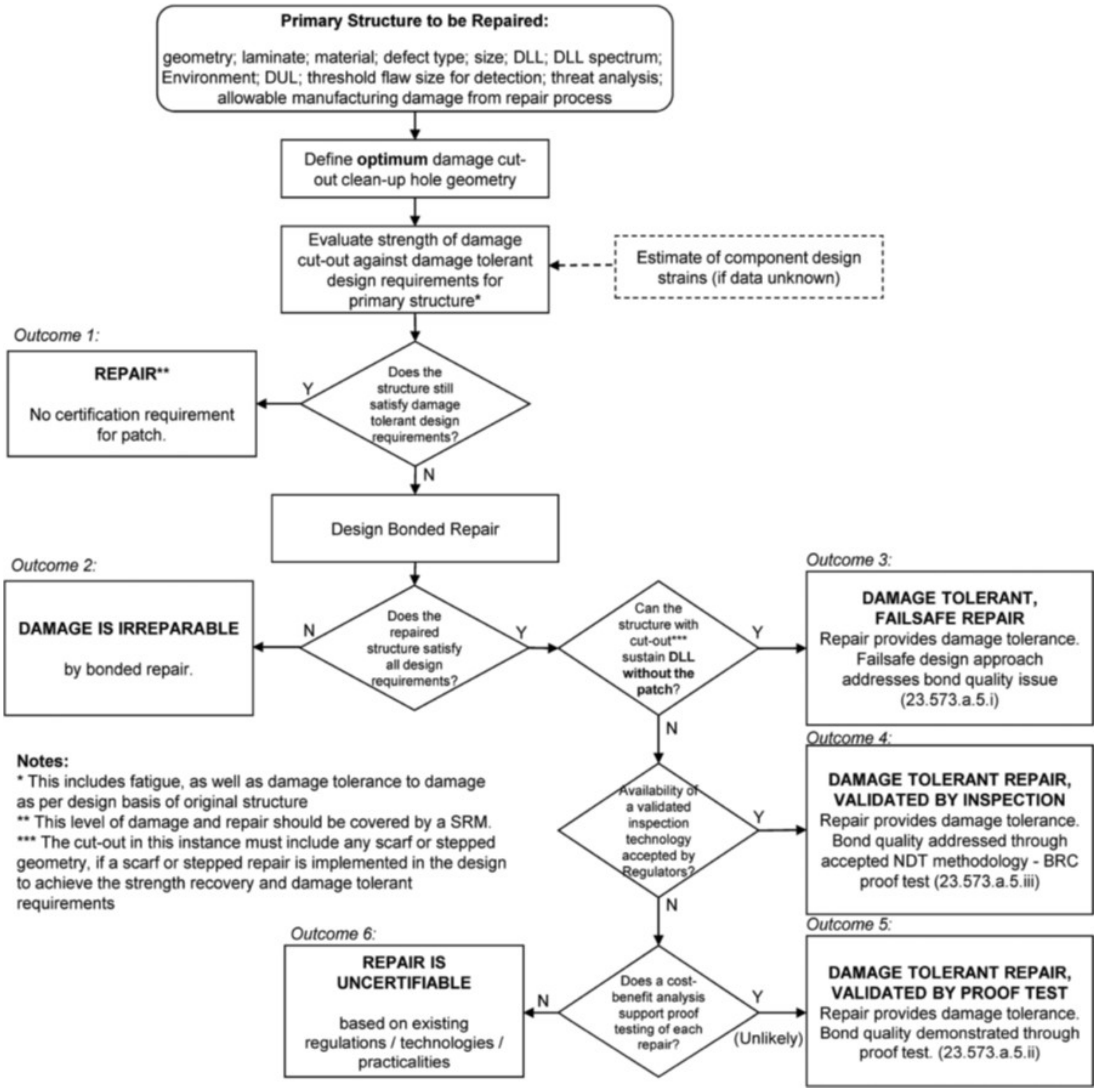

Figure 2.34: Flowchart related to certification process of repairs on PSEs (Baker et al., 2015).

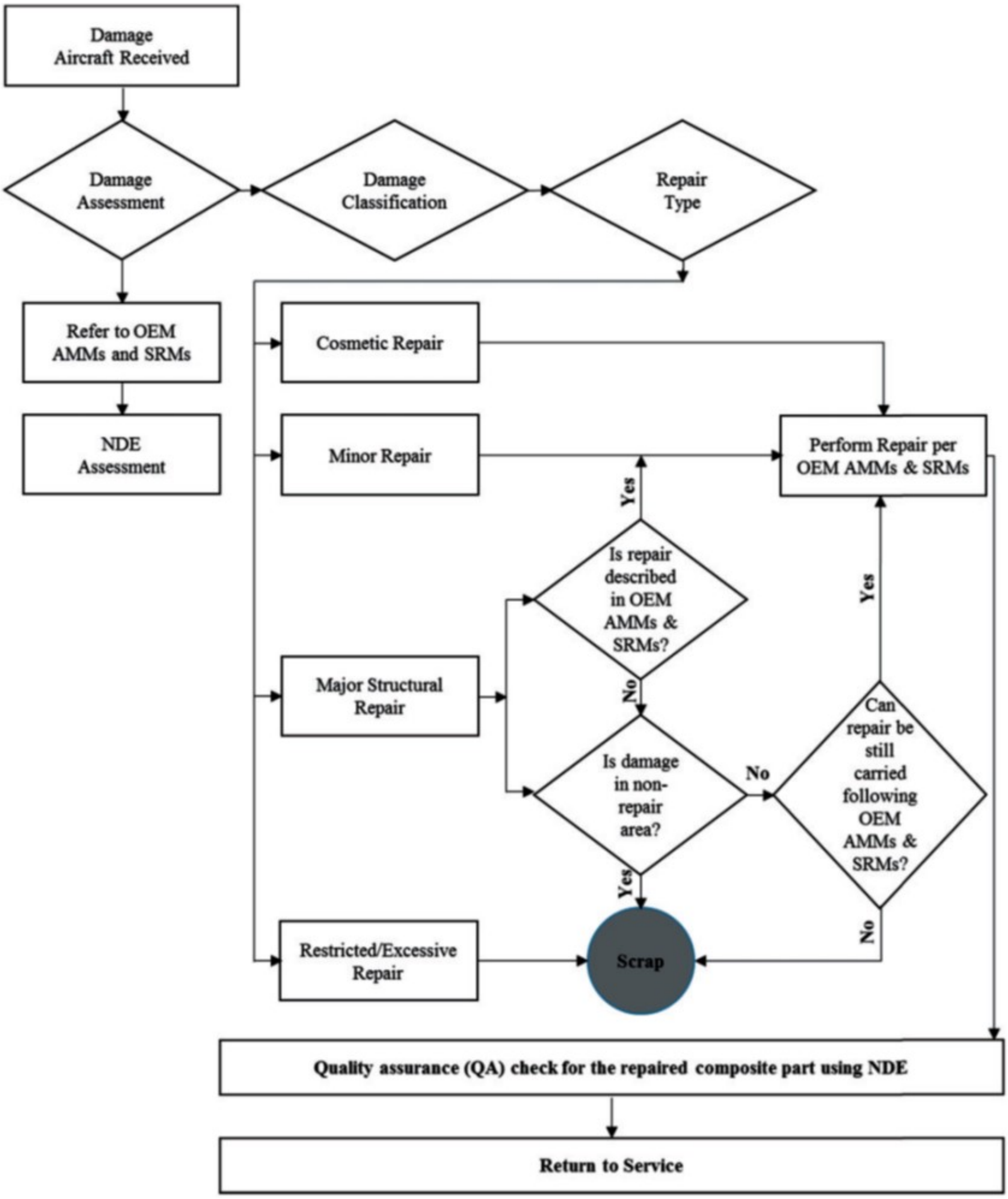

Figure 2.35: Flowchart describing the design procedure of a repair (Poudel et al., 2015).

Chapter 3

Experimental Procedures

Creep behaviour considering pure modes I and II loading scenarios is analysed, while establishing a cohesive zone model capable to predict damage evolution within the adhesive layer, where creep damage laws are included. Chapter 4 presents the statement of several damage laws, where corresponding parameters are evaluated. The demonstrated creep responses need to be validated, where results are compared with experimental data. Proposed models are calibrated in Chapter 4, using experimental results demonstrated in this Chapter.

Double-cantilever-beam (DCB) tests are performed in order to assess creep responses related to pure mode I loading. End-notched-flexure (ENF) tests are also performed, but assessing the real creep behaviour in pure mode II loading.

First of all, materials are specified in Section 3.1, both considering substrates and adhesive, presenting corresponding properties. This section also includes manufacturing operations regarding the preparation of substrates.

Geometries, and nominal dimensions, regarding both DCB and ENF specimens are shown in Section 3.2. Specimens with those geometries and dimensions are then prepared. All the procedure for specimen preparation is presented in Section 3.3, explaining the moulding process constituting the bonding operation. Surface preparation procedures as well as cutting operations are carefully demonstrated.

All specimens are measured, and a statistical analysis is performed. Before each creep test, the maximum sustaining load is measured in each specimen. Deviations in dimensions are related with different strength properties found. These properties are directly related with the amount of defects contained in the specimens, whose effects are also notable in the creep response.

Finally, creep behaviour considering both pure modes I and II loading conditions is analysed in Sections 3.4.1 and 3.4.2, respectively, where primary, secondary, and even tertiary phases are experimentally captured.

3.1 Materials

Epoxy reinforced with carbon fibres was used for the substrates, whose specifications are detailed in Section 3.1.1, including the manufacturing procedure. ARALDITE® 2015-1 was used to bond the substrates, whose properties are exposed in Section 3.1.2.

3.1.1 Carbon-Epoxy HS160REM

Carbon-epoxy was used for the substrates. Corresponding prepregs have origin in the company CIT - COMPOSITE MATERIALS®, from Italy, whose reference is HS160REM.

The used substrates have a thickness of 2.4 mm. Each ply has a thickness of 0.15 mm. In this way, carbon-epoxy laminates containing 16 unidirectional plies are manufactured: $[0]_{16}$. This unidirectional laminate presents properties defined in Table 3.1.

Table 3.1: Material properties of carbon-epoxy HS160REM (Moreira, 2021; Moreira et al., 2018a,b; Silva et al., 2020).

Young's Modulus [GPa]	Poisson's Ratio [-]	Shear Modulus [MPa]
$E_1 = 109$	$\nu_{12} = 0.25$	$G_{12} = 4315$
$E_2 = 8.819$	$\nu_{13} = 0.25$	$G_{13} = 4315$
$E_3 = 8.819$	$\nu_{23} = 0.40$	$G_{23} = 3200$

Regarding the manufacturing process related to the carbon-epoxy laminates, a roll of prepreg was cutted into strips, resulting finally in squared plies of 300 × 300 [mm], using a cutting machine WENDT® (Figure 3.1) with a diamond rotative disk . A total of 16 plies were cut, in order to produce, *"a posteriori"*, a 16-ply laminate with a total thickness of 2.4 mm. At the Laboratory of Composite Materials, at INEGI, hot compression moulding was the used process in order to consolidate the final laminate. After these process, the resulted carbon-epoxy plates have the aspect shown in Figure 3.2.

3.1.2 Adhesive ARALDITE® 2015-1

ARALDITE® 2015-1 was the used adhesive, being used with bi-component cartridges of 200 mL, as portrayed in Figure 3.3. It has origins in the company HUNSTMAN®, from Switzerland.

ARALDITE® 2015-1 is an epoxy based adhesive, presenting a ductile behaviour, demonstrating nominal properties shown in Table 3.2.

3.2 Geometries and Nominal Dimensions

Geometries related with DCB and ENF specimens are shown in Sections 3.2.1 and 3.2.2, respectively. Nominal dimensions are also mentioned.

Figure 3.1: WENDT® cutting machine.

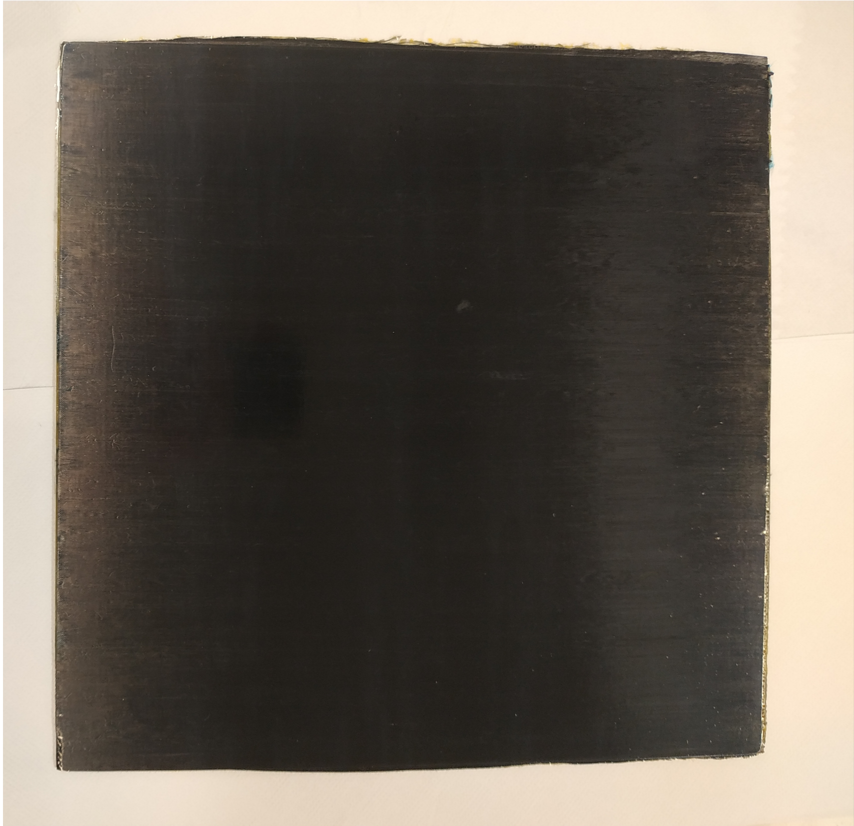

Figure 3.2: Carbon-epoxy plate with 16 unidirectional layers.

Figure 3.3: 200 mL bi-component cartridges corresponding to ARALDITE® 2015-1.

Table 3.2: Material properties of ARALDITE® 2015-1 (Samaro, 2023; Moreira, 2021; Alves et al., 2018; Barbosa et al., 2018).

Properties	ARALDITE® 2015-1
Young's Modulus, E [GPa]	1.60
Poisson's Ratio, ν [-]	0.33
Yield Stress, σ_y [MPa]	12.63 ± 0.61
Ultimate Stress, σ_u [MPa]	21.63 ± 1.61
Elongation at Break, ε_u [%]	4.77 ± 0.15
Shear Modulus, G [GPa]	0.60
Yield Shear Stress, τ_y [MPa]	14.60 ± 1.30
Ultimate Shear Stress, τ_u [MPa]	17.90 ± 1.80
Shear Elongation at Break, γ_u [%]	43.90 ± 3.40

3.2.1 Double-Cantilever-Beam (DCB)

Two carbon-epoxy substrates, constituting the two arms, are adhesively bonded using ARALDITE® 2015-1. The left end of the specimen is subjected to tensile loading. This type of specimen allows to characterise the peeling behaviour of the considered adhesive. Geometry, as well as boundary conditions are possible to identify in Figure 3.4. Corresponding dimensions are exposed in Table 3.3.

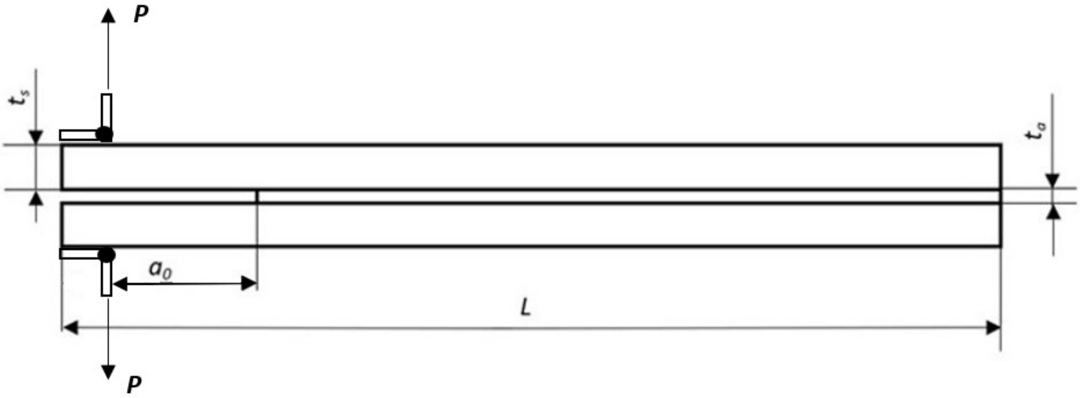

Figure 3.4: DCB geometry and boundary conditions.

Table 3.3: Geometric dimensions: DCB.

L [mm]	a_0 [mm]	t_s [mm]	t_a [mm]
140	40	2.4	0.2

3.2.2 End-Notched-Flexure (ENF)

The same substrates constitute the two arms, being adhesively bonded using ARALDITE® 2015-1. This type of specimen is subjected to flexural loading, with a 3-point-bending test. These conditions allow to characterise the behaviour of the adhesive considering pure shear. Geometry, as well as boundary conditions are represented in Figure 3.5. The geometric dimensions are exposed in Table 3.4.

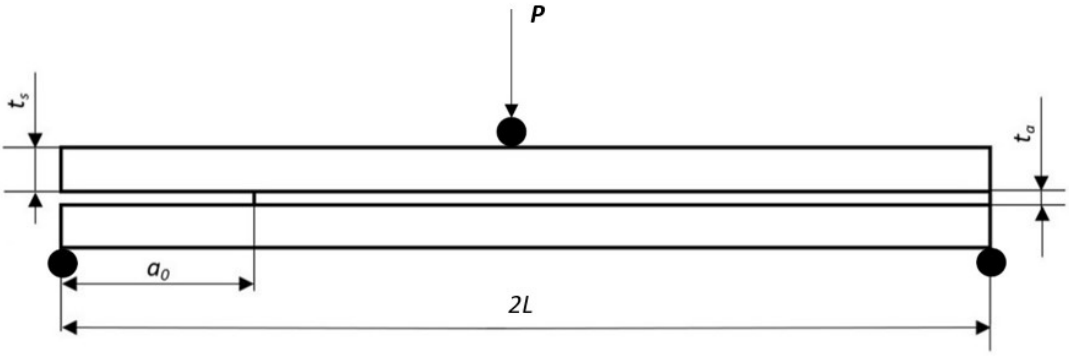

Figure 3.5: ENF geometry and boundary conditions.

An unstable configuration ($a_0 < 0.7L$) was used for both configurations (Trethewey et al., 1988). The reason is related with expected extensive fracture process zones that could develop under creep for this adhesive. Thus, it was decided to consider a reasonable distance between the pre-crack tip and the central loading point.

Table 3.4: Geometric dimensions: ENF.

$2L$ [mm]	a_0 [mm]	t_s [mm]	t_a [mm]
230	60	2.4	0.2

3.3 Specimen Preparation

All the steps regarding the preparation of specimens are exposed in this section. Both DCB and ENF specimens are prepared exactly in the same manner. As a post-process, different dimensions are considered in cutting operations. Same procedures were already explained by Moreira (2021), whose experimental protocol was followed.

1. **Pre-process Cutting Operations**

   The first step is to cut the substrates, using a cutting machine and a guillotine, from the produced carbon-epoxy plate with 300 × 300 [mm]. Those substrates have a width of 25 mm.

2. **Surface Preparation**

   The second step is to guarantee that the surface of the substrates is sufficiently cleaned. Surface preparation is a crucial step to avoid adhesive failure (da Silva et al., 2007, 2011; Moreira, 2021), where those are a result of weak adhesion due to impurities. First of all, the surfaces are sanded, with a sand paper with P220 of granulometry. Surfaces are then cleaned using isoproyl alcohol. This cleaning process eliminates grease, which could harm the adhesion of the adhesive to the surface of the substrate. In addition, surface roughness is increased, favouring the penetration of the adhesive in the interstices of the surface of the substrate. All these procedure must avoid any damage in the fibres (Moreira, 2021). Figure 3.6 shows the final aspect of the surfaces of the used substrates.

3. **Mould Preparation**

   Before inserting the substrates, the mould has to be properly prepared. Positioning pins have to be disposed correctly, in order to fix the substrates. Before any procedure, the mould is cleaned using LOCTICE® PMC (Figure 3.7).

   A semi-permanent mould release agent has also to be applied, in order to become possible the unmould operation after curing. In this way, the specimens are extracted easily from the mould, without damage risks caused forced handling. LOCTICE® 770-NC was used for this effect, being presented in Figure 3.8. Special care must be taken, while using the semi-permanent mould release agent, where the use of mask and gloves is mandatory. Their importance is explicitly demonstrated by the danger caution also shown in Figure 3.8.

Figure 3.6: Substrates after surface preparation.

(a) (b)

Figure 3.7: Mould cleaner: (a) product reference, (b) danger caution.

4. **Pre-crack Preparation**

   Pre-cracks are prepared using calibration strips with a thickness of 0.05 mm, and razor blades with a thickness of 0.1 mm. A razor blade is bonded between two calibration strips, constituting a total of 0.2 mm of thickness, corresponding to the thickness of the adhesive layer. In this way, this strategy is not only appropriate to prepare the pre-crack, but also to make sure the desired thickness for the adhesive layer (Moreira, 2021). Figure 3.9 demonstrates the used strategy, while showing the mounted accessories and also, particularly, the razor blades. The LOCTITE® 770-NC semi-permanent mould release agent is applied to the pre-crack accessories, in order to remove them more easily after the curing process, during the unmould.

(a) (b)

Figure 3.8: Semi-permanent mould release agent: (a) product reference, (b) danger caution.

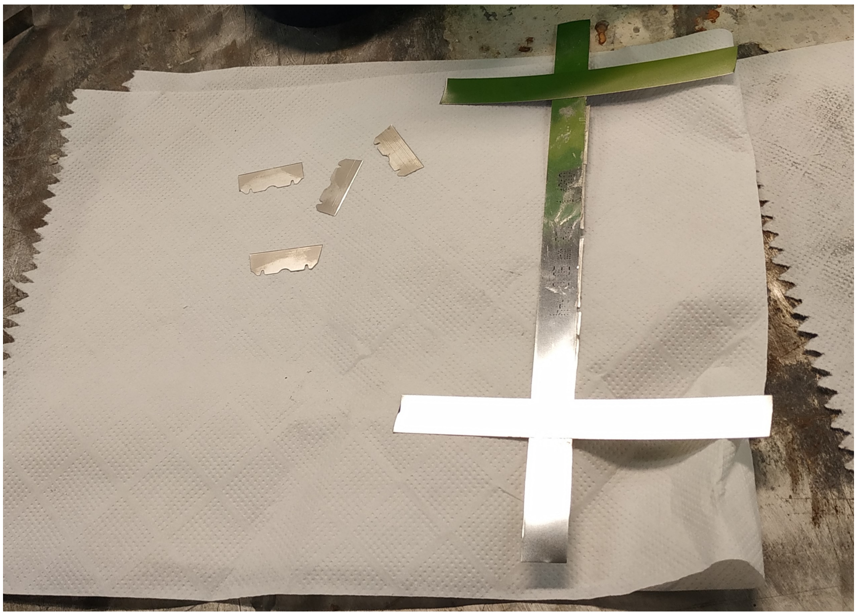

Figure 3.9: Accessories for pre-crack preparation.

5. **Adhesive Application**
   The bi-component cartridges presented in Figure 3.3 are used, with the aid of an application gun. The adhesive is applied in all substrates, respecting the pre-crack size. After deposition, the adhesive is spread along the surface, providing the final aspect shown in Figure 3.10. This figure already includes the accessories to control the adhesive layer, as well as ensuring the correct pre-crack size.

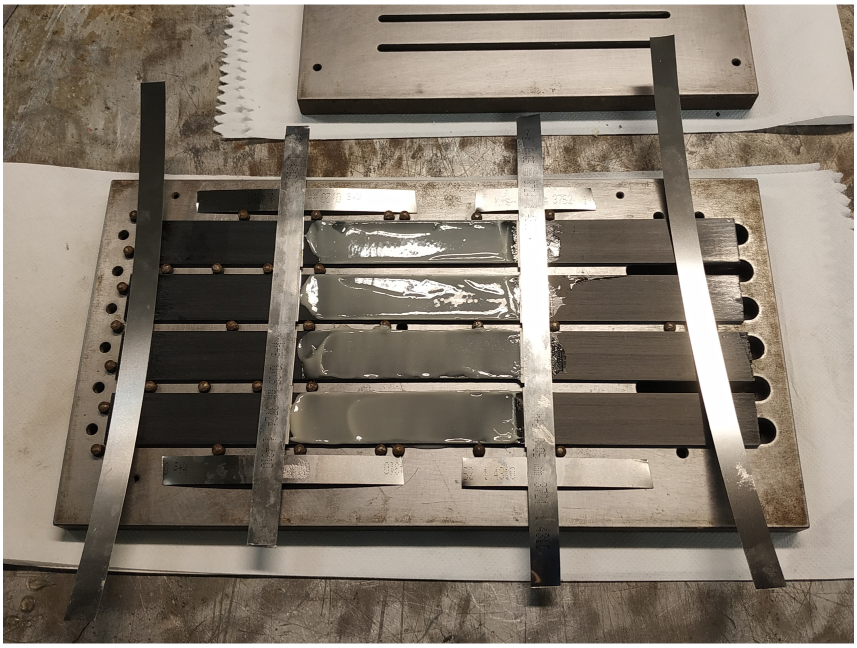

Figure 3.10: Substrates after adhesive application.

6. **Final Assembly**
   Corresponding paired substrates are bonded, after adhesive application. While joining substrates, a pressure should be applied manually in order to guarantee the desired thickness for the adhesive layer. For this purpose, that pressure is applied in the pre-crack, corresponding to the zones where pre-crack accessories of 0.2 mm of thickness are found. Figure 3.11 shows the aspect of the specimens after joining the substrates. After closing the mould, heavy blocks are inserted over the mould, in order to guarantee the desired thickness for the adhesive layer, while curing.

7. **Curing**
   ARALDITE® 2015-1 is an adhesive which is capable to cure at ambient conditions, for 24 h. After that period of time, the specimens can be easily handled for post-process operations.

Those post-process operations are slightly different for DCB and ENF specimens. The common procedure for both types of specimen consists in removing the excessive adhesive, after extraction from the mould, using the PROXXON® disc sander presented in Figure 3.12.

At the end of this process, the preparation related to ENF specimens is complete. However, DCB specimens need an additional procedure. Hinges, presented in Figure 3.13, are used for load application, and those are bonded to the substrates. Before bonding hinges to substrates, the corresponding surface is cleaned using isopropyl alcohol. Also the zone of the substrate to be bonded is properly prepared with a similar procedure as described previously. Figure 3.14 shows the final aspect of a DCB specimen. The same adhesive (ARALDITE® 2015-1) was used to bond the hinges to the substrates. In this way, the bond line between hinges and substrates is cured for 24 h at ambient conditions, using a fixation tool as represented in Figure 3.14.

Figure 3.11: Specimens after joining substrates.

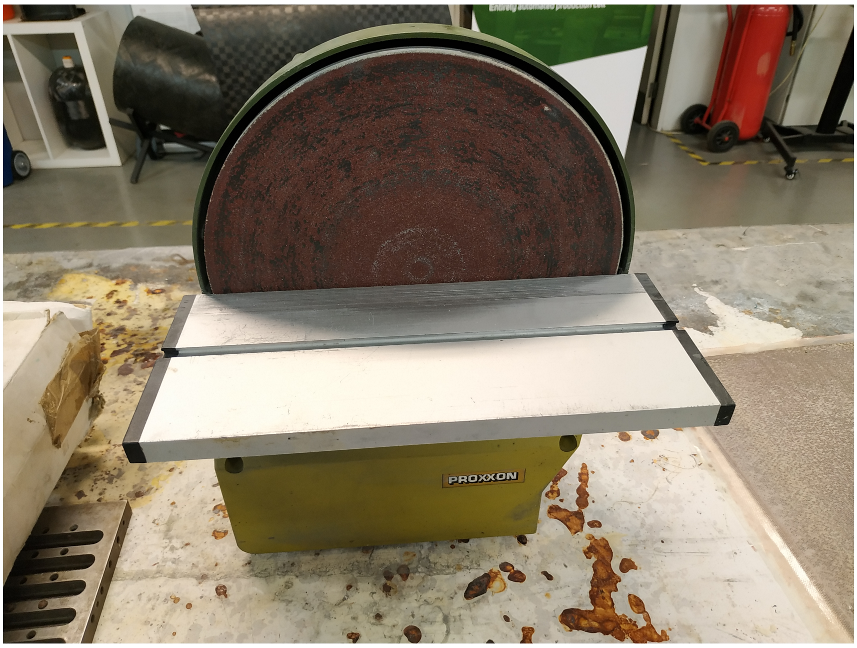

Figure 3.12: PROXXON® disc sander.

The cured adhesive must stand in a dry room at ambient temperatures at least for 5 days, in order to achieve the mature properties. In this way, the adhesive reaches the mechanical strength specified by the manufacturer.

Figure 3.13: Hinges for load application.

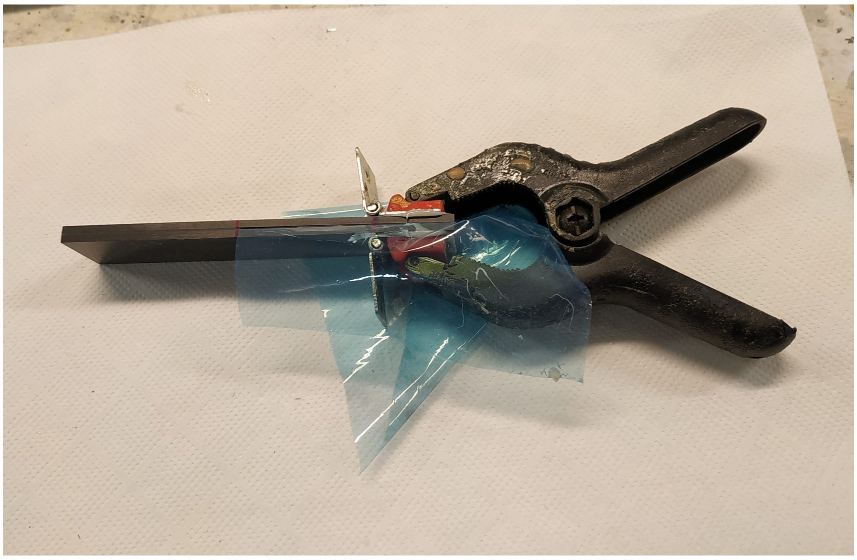

Figure 3.14: DCB specimen with bonded hinges.

3.4 Experimental Testing for Fracture Characterisation

The experimental campaign was performed at the Laboratory of Technological Testing of the School of Engineering of Polythecnic of Porto (ISEP). The specimens were tested in a universal testing machine SHIMADZU® AG-I with a load cell of 10 kN (Figure 3.15).

For both specimens the testing procedure consisted, firstly, in the strength measurement, followed by creep testing. A quasi-static test, only in the elastic regime, is performed until the maximum sustaining load, with a velocity of 1 mm/min. The variability in terms of dimensions and material defects provide different strength levels. Corresponding values of strength has to be

Figure 3.15: SHIMADZU® AG-I universal testing machine.

known, in order to calculate the applied creep load. Before stationary creep, the load is applied slowly with a velocity of 5 mm/min, considering an appropriate accommodation of the specimen.

Experimental testing on DCB specimens is detailed in Section 3.4.1, while analysing corresponding results. Section 3.4.2 is presenting details regarding the testing of ENF specimens, as well as corresponding results.

3.4.1 Experimental Testing considering Pure Mode I Loading

The experimental tests for the evaluation of the creep behaviour under pure mode I loading was constituted by two campaigns. The first campaign brought some problems in terms of consistency of the results, as proved in Figure 3.16. In fact, the strength of each of specimen should be measured before a creep test, in order to assess the correct amount of load to apply. This methodology allows to overcome the differences in terms of strength. In the first campaign (DCB 1 to DCB 8), a numerical strength of 150 N was employed as a reference (see Chapter 4), where 105 N is equivalent to 70% of the load in a numerical point of view, corresponding to a completely different loading level experimentally. Only the DCB 8 provided successful results, being considered and analysed within the second campaign. Corresponding load level is assessed by comparing the slope of the secondary phase, with other slopes from specimens of the second campaign.

The second campaign was also composed by 8 specimens (DCB 9 to DCB 16). Various loading levels were tested, taking corresponding strength values as reference: 70%, 75%, 80%, and 85% of P_{max}. Strength of each specimen was assessed through $P-\delta$ curves, represented in Figure 3.17.

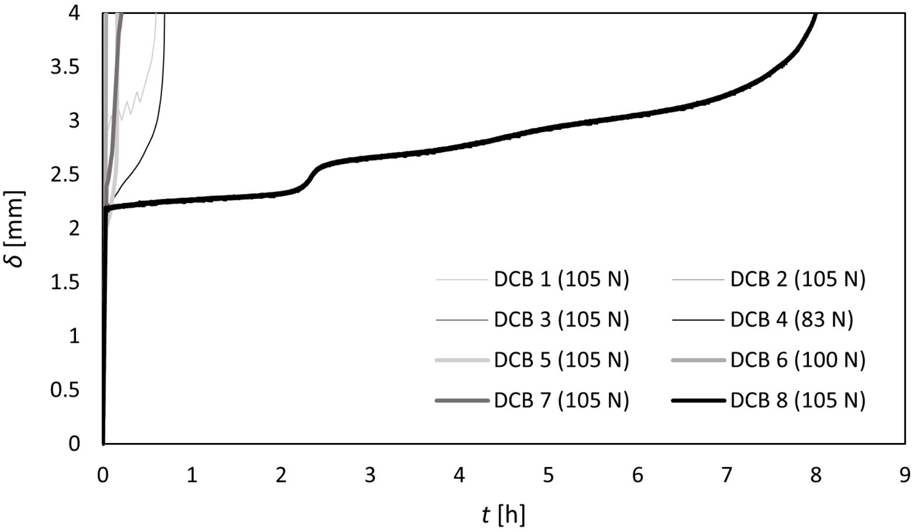

Figure 3.16: Creep curves of DCB tests from the first campaign.

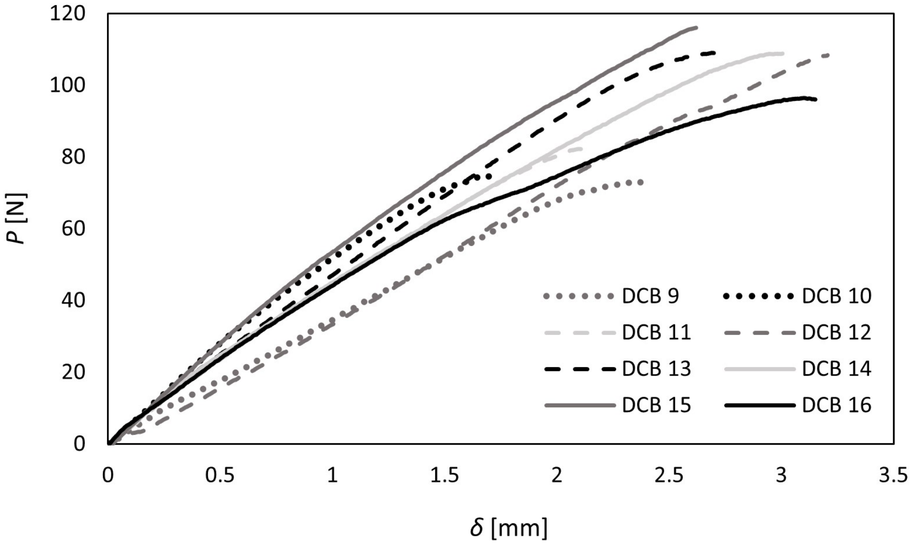

Figure 3.17: Load-displacement curves of DCB tests.

For a comparison between the geometrical and dimensional characteristics and the strength and stiffness properties, Table 3.5 is presented. DCB 15 demonstrated the highest strength, with the highest stiffness, with a displacement at failure of 2.62 mm. DCB 9 presented the lowest strength and stiffness, corresponding to a maximum displacement of 2.37 mm. The highest displacement at failure was shown by DCB 12, with a considerable sustaining load of 108.4 N. DCB 13 and DCB 14 are considerably stiffer, even with the same level of strength. It seemed that the strength and stiffness properties were more affected by possible defects in the adhesive layer, such as voids, rather than differences in geometrical and dimensional characteristics. Specimens 9, 10, and 11 demonstrated to be negatively affected by material defects.

Table 3.5: Dimensions and maximum values for strength and displacement considering DCB specimens.

Specimen	Dimensions					Properties	
	L **[mm]**	W **[mm]**	t_{s_1} **[mm]**	t_{s_2} **[mm]**	a_0 **[mm]**	P_{max} **[N]**	δ_{max} **[mm]**
DCB 8	117	24.0	2.3	2.2	40.1	—	—
DCB 9	119	24.1	2.2	2.2	40.6	73.1	2.37
DCB 10	117	23.5	2.2	2.2	41.0	74.9	1.70
DCB 11	123	23.4	2.2	2.2	41.0	82.3	2.12
DCB 12	118	24.1	2.2	2.2	41.1	108.4	3.21
DCB 13	118	24.0	2.2	2.2	41.0	109.2	2.75
DCB 14	117	24.1	2.2	2.2	40.0	108.8	3.00
DCB 15	118	24.0	2.2	2.2	40.1	116.0	2.62
DCB 16	117	24.1	2.2	2.2	40.3	96.5	3.15

All specimens were subjected to creep tests in the second campaign, whose successful results were provided by specimens 12, 13, 14, and 15. DCB 8, from the first campaign was also considered a successful result. Corresponding results are presented in Figure 3.18.

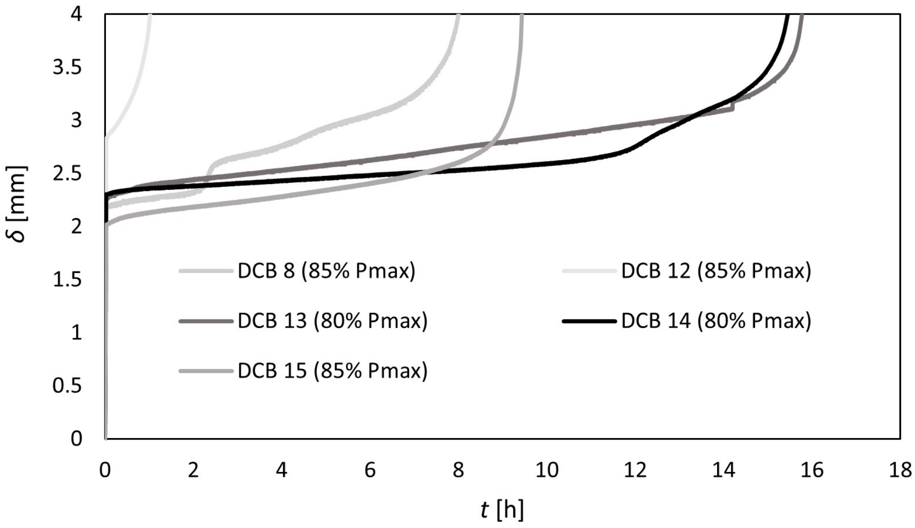

Figure 3.18: Creep curves of DCB tests.

Figure 3.18 demonstrated clearly that a higher load level correspond to reduced creep lifetimes. A load level of 85% of P_{max} provided a creep lifetime between 8 and 9 hours. Creep lifetimes around 16 hours were seen by applying a load level corresponding to 80% of P_{max}. An exception was seen in the result provided by DCB 12, where the specimen resisted to a load corresponding to 85% of P_{max} for only 1 hour. As seen in Figure 3.17, as well as in Table 3.5, DCB 12 showed the highest displacement at failure, comparing to the rest of the specimens. Consequently, the displacement in secondary creep phase was higher, being sufficient to significantly reduce the creep lifetime. With this result, it is proved that the creep lifetime depends specially on displacement at failure.

A detailed perspective of the results is observed in Figure 3.19 for relative applied loads of 80% and 85%. DCB 13 and DCB 14 demonstrated very similar results, showing consistency in results related with the application of a load level corresponding to 80% of P_{max}. Nevertheless, a difference between results provided by DCB 8 and DCB 15 was seen. In fact, the secondary phase of the specimen 8 is not perfectly continuous, demonstrating the existence of a possible void in the middle of the adhesive layer. In fact, this can be the main reason for the differences observed. The slope of the first stage of the secondary creep phase of DCB 8 is identical to the slope of the secondary creep phase presented by DCB 15.

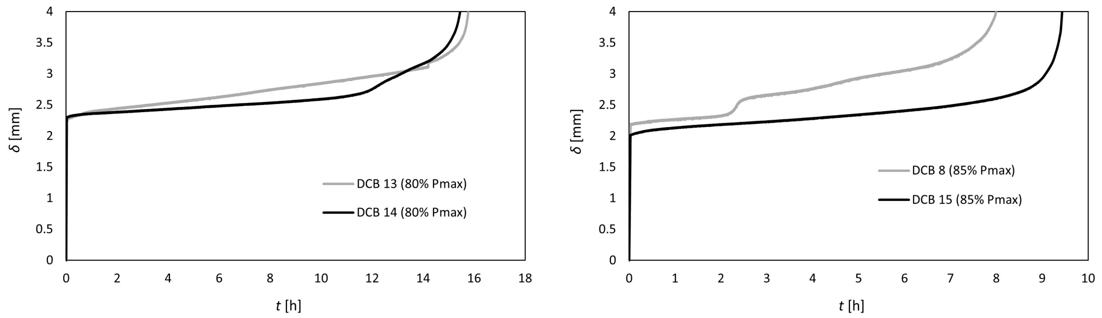

(a) (b)

Figure 3.19: Creep curves of DCB tests: (a) 80% of P_{max}, (b) 85% of P_{max}.

As previously mentioned, quasi-static tests were not performed *"a priori"* in the first campaign, not being able to determine experimental the relative level of applied load in DCB 8. For the determination of the relative applied load, the slope of the secondary phase of other specimens in the second campaign, showing coherent results, was calculated. The slope of the secondary phase presented by the creep curve of DCB 8 was compared, and a relative load level was associated. It was concluded that a relative load of approximately 85% of P_{max} was applied to DCB 8. Values for the slope of the secondary creep phase are shown in Table 3.6, being associated to a given relative load level. The slope related to DCB 12 was not taken into account in the determination of the slope corresponding to DCB 8. In fact, results associated to DCB 12 showed an excessively low creep lifetime, due to the presence of material defects.

Table 3.6: Slope of the secondary phase on experimental DCB creep curves.

	DCB 8	DCB 12	DCB 13	DCB 14	DCB 15
P/P_{max} [-]	***	85%	80%	80%	85%
$\Delta\delta/\Delta t$ [mm/s]	0.1325	0.7213	0.05062	0.02650	0.05554

Specimens 9 and 11 were tested with an applied load corresponding to 70% of P_{max}, while specimen 16 was tested with 75% of P_{max}. DCB 10 was tested with a higher load level, corresponding to 85% of P_{max}. Results are shown in Figure 3.20.

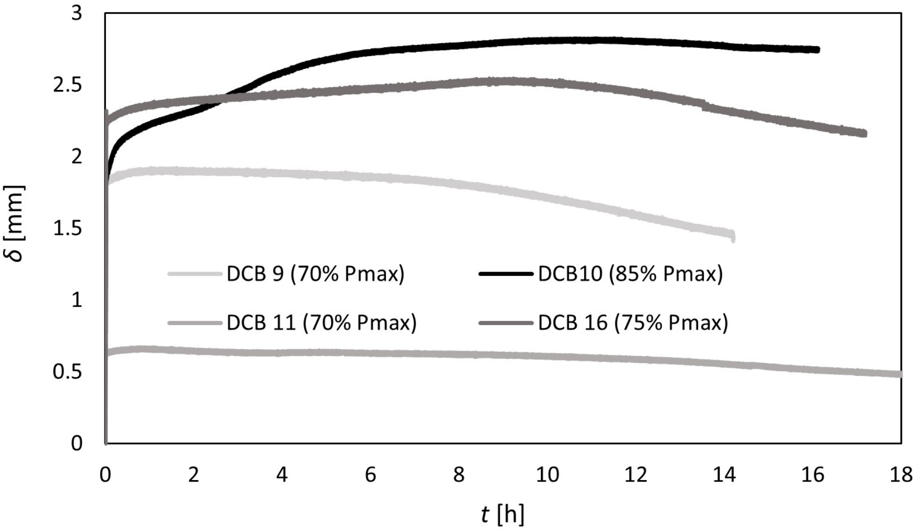

Figure 3.20: Creep curves of DCB tests presenting adhesive failure.

In fact, specimens 9, 10, and 11 seemed to be significantly affected by material defects, since a lower strength was demonstrated, when compared to other strength levels provided by similar specimens in the same campaign. This argument fully explains the result of the creep test in DCB 10, where the displacement started to decrease at the end of the secondary phase. In fact, a decrease in displacement was reported after 1 or 2 hours of testing time in specimens 9, 11, 16. A creep threshold can also be presented, corresponding to a relative load of 75%, constituting possibly an additional justification for this phenomenon. This can be assumed due to the fact that the properties corresponding to the DCB 16 are similar to the ones corresponding to DCB 13, 14, and 15, not presenting any indication of material defect. A general justification is the relation of this phenomenon with the failure path along the adhesive layer. Experimentally, even with a cohesive failure, the rupture plan is closer to a substrate, rather than the other. The initiation of a decrease in displacement can also be explained by a change in the failure path, where the rupture plan changes its position in the *"in situ"* direction. More tests would be needed to fully validate a final justification. Nevertheless, for the experimental results seen in Figure 3.20, an existence of a creep threshold can be assumed as a possible explanation.

Globally, it can be concluded that the creep behaviour of adhesive joints under pure mode I loading is very sensitive to general testing conditions, such as the applied load, geometry, dimensions, and specially material defects. In this way, moderate creep lifetimes, possible of being analysed, are also provided by relative applied loads between 80% and 85%. This sensible behaviour are considered in the numerical modelling presented in Chapter 4.

3.4.2 Experimental Testing considering Pure Mode II Loading

The experimental results of ENF tests are presented in this section, evaluating the curve shape, as well as the lifetime of each specimen, considering constant applied loads corresponding to 70% (ENF 3, ENF 8), 75% (ENF 4, ENF 5), 80% (ENF 6, ENF 7), and 85% (ENF 2) of P_{max}.

First of all, all tested specimens were measured, analysing variations in geometric parameters, such as length (L), width (W), substrate thicknesses (t_{s_1}, t_{s_2}), and pre-crack (a_0), whose corresponding values are demonstrated in Table 3.7. Relating to $P-\delta$ curves, presented in Figure 3.21, Table 3.7 also shows results regarding strength and ultimate displacement, as a function of the measured parameters. In this way, variations in geometry could explain variations in terms of strength and ultimate displacement, influencing also results in terms of creep behaviour.

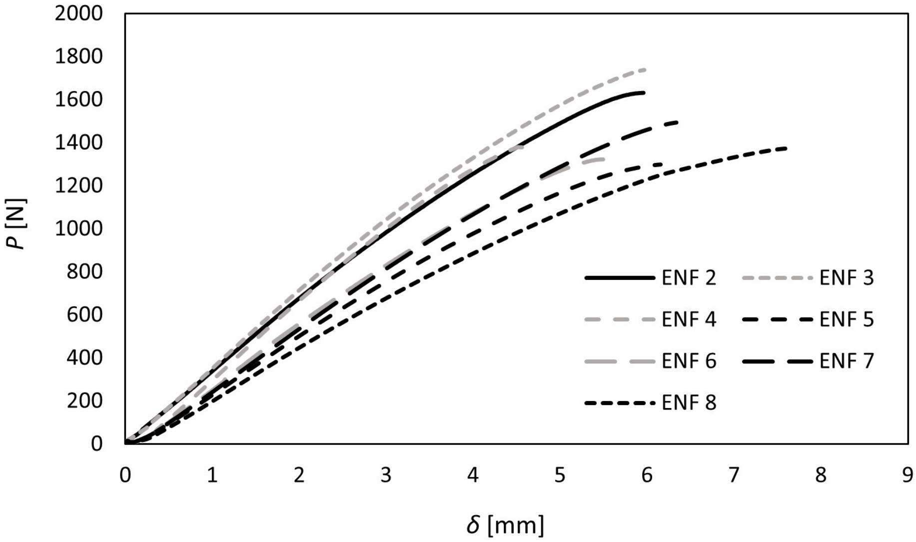

Figure 3.21: Load-displacement curves of ENF tests.

Table 3.7: Dimensions and maximum values for strength and displacement considering ENF specimens.

Specimen	Dimensions					Properties	
	L [mm]	W [mm]	t_{s_1} [mm]	t_{s_2} [mm]	a_0 [mm]	P_{max} [N]	δ_{max} [mm]
ENF 2	230	24.5	2.1	2.3	61.4	1631	5.96
ENF 3	231	23.4	2.2	2.1	60.4	1738	5.97
ENF 4	230	24.4	2.3	2.6	61.1	1380	4.57
ENF 5	229	24.6	2.2	2.2	60.4	1298	6.16
ENF 6	229	24.4	2.3	2.2	61.1	1322	5.49
ENF 7	229	23.2	2.3	2.1	60.6	1493	6.34
ENF 8	230	24.2	2.1	2.2	61.7	1375	7.67

While analysing Figure 3.21, as well as Table 3.7, it is proved that ENF 3 presented the highest strength, and also the highest stiffness, demonstrating a ultimate displacement of 5.97 mm. A similar value of strength was achieved by ENF 2 (1631 N), with also a similar ultimate displacement of 5.96 mm. These results corresponded to a slightly higher stiffness. ENF 4, ENF 6, and ENF 8 also presented similar values of strength: 1380 N, 1322 N, and 1375 N, respectively. Nevertheless, the stiffness demonstrated by these specimens was significantly different, resulting in different conditions in terms of ultimate displacement: 4.57 mm, 5.49 mm, and 7.67 mm, respectively. The lowest strength was presented by ENF 5, corresponding to a value of 1298 N, at the same time, demonstrating a ultimate displacement of 6.16 mm. Even with these conditions, its stiffness proved to be higher in comparison to ENF 8. Intermediate conditions can be seen by ENF 7, presenting a maximum load of 1493 N, and a ultimate displacement of 6.34 mm.

Differences in terms of mechanical properties reproduced by static loading conditions are not related, in fact, with differences in geometry. However, it can be related to specimen preparation conditions, as specified in Section 3.3, which can introduce variability in terms of defects, especially voids in the adhesive layer. These conditions are possible to correspond to real scenario, where adhesively bonded repairs are prepared *"in situ"*, using manual based procedures, which can provide a high portion of voids.

Corresponding creep results of the mentioned ENF specimen are presented in Figures 3.22 and 3.23. All results are directly compared in Figure 3.22, where is possible to verify the differences introduced by different loading conditions in the creep behaviour. The existence of a creep threshold in pure mode II loading was proved: it is demonstrated in Figure 3.22, that applied loads lower than 75% of P_{max}, do not cause tertiary creep, i.e., not corresponding to creep failure. A criterion was assumed, so that for creep times higher than 24 h without showing tertiary creep, it can be considered that the applied load is lower than the creep threshold load. This assumption is based on results demonstrated by Neto et al. (2022b). Only loads corresponding to 80% and 85% of P_{max} were sufficient to provide a creep tertiary zone, observing failure in pure mode II. Differences in the slope related to the secondary creep phase were coherent with the magnitude of applied load. The lowest slope was demonstrated by specimens tested under 70% of P_{max}, followed by specimens tested under 75%. Specimens tested under 85% of P_{max} presented the highest slope corresponding to the secondary creep phase, followed by specimens considering 80% of P_{max}.

A detailed perspective on the results regarding the creep behaviour under pure mode II loading are observed in Figure 3.23, as well as demonstrating corresponding fracture aspect.

Considering all scenarios, the slope of the secondary phase is similar for specimens tested under identical loading conditions, but presenting different displacement levels. Only for cases where the applied load is lower than the creep threshold, a lower displacement level provided a slight reduction in the slope related to the secondary phase. Differences in the displacement are directly related to the variability in terms of defects, where higher displacements are related to a higher percentage of voids in the adhesive layer.

Analysing the case (a), where results for an applied load corresponding to 70% of P_{max} are shown, it is noted that the steady displacement associated to ENF 8 is higher than the one presented

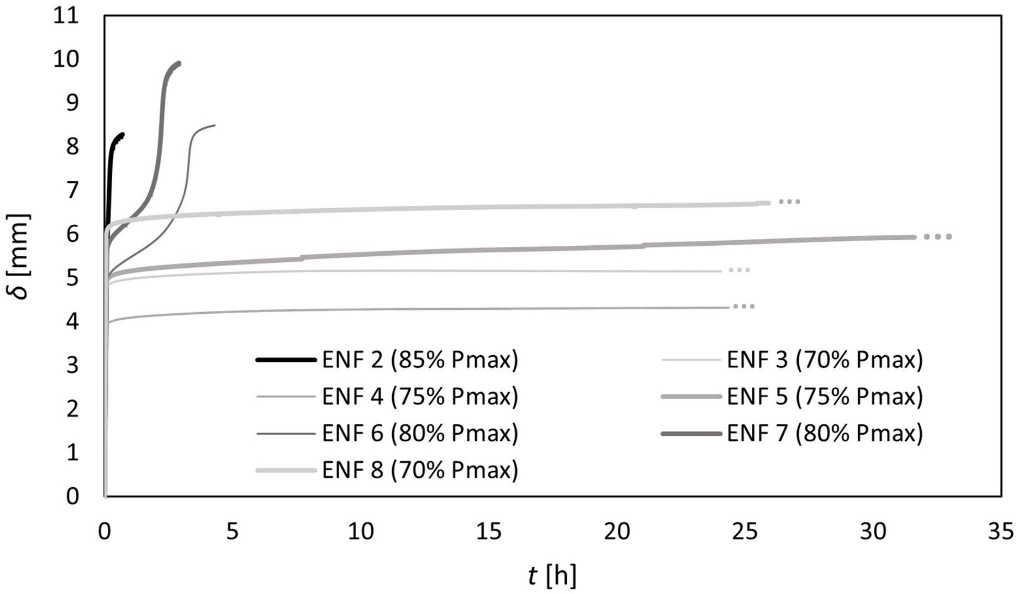

Figure 3.22: Creep curves of ENF tests.

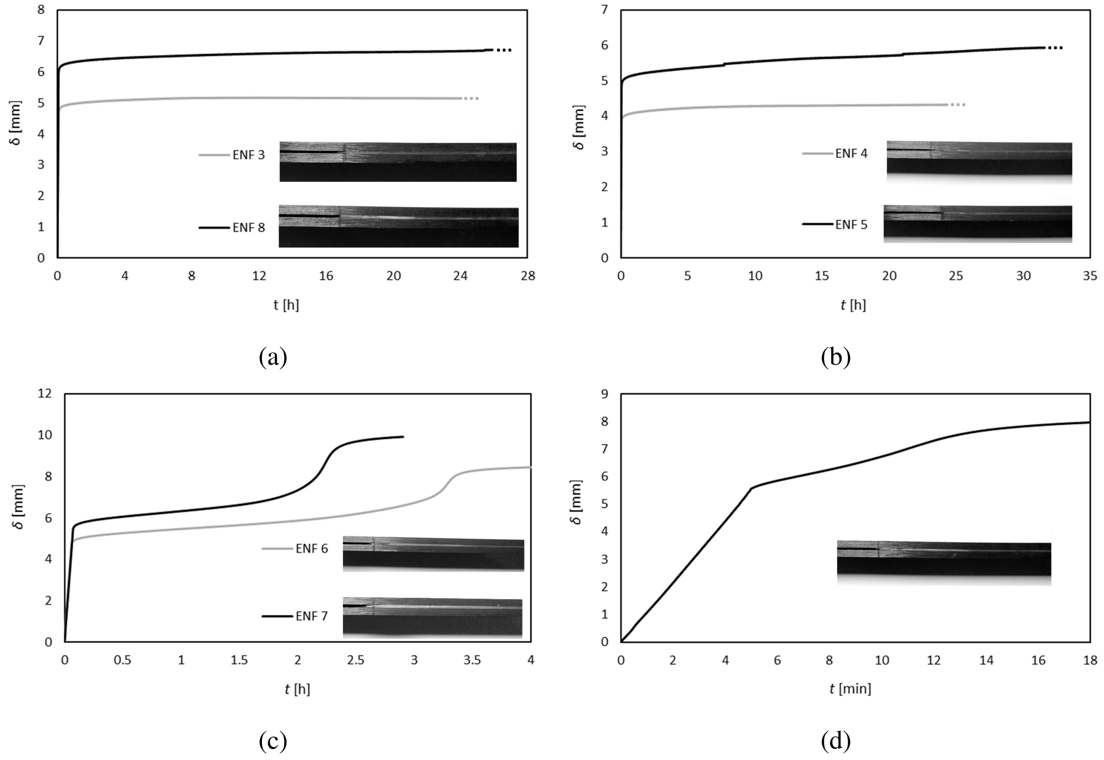

(a) (b)

(c) (d)

Figure 3.23: Creep curves of ENF tests and corresponding failure aspects: (a) 70% of P_{max}, (b) 75% of P_{max}, (c) 80% of P_{max}, (d) 85% of P_{max}.

by ENF 3. This is related to the lower stiffness of the specimen ENF 8, proved in Figure 3.21. As previously mentioned, it is possibly related to the amount of voids presented in the adhesive layer, which consequently can provide conditions for a higher slope of the secondary creep zone. Regarding the aspect of the specimen after the creep test, it is seen that the adhesive layer of ENF 8 is considerably lighter, until the point where the load is applied, in comparison to the adhesive layer of ENF 3. In this case, this is related to the lower stiffness associated to the specimen ENF 8 and, consequently, to a higher resulting displacement.

Regarding case (b), where it is considered an applied corresponding to 75% of P_{max}, approximately the same difference between the two specimens is found, comparing to what is observed in case (a). ENF 5 has a lower stiffness when compared to ENF 4 (Figure 3.21), providing a higher steady displacement in creep loading conditions. In terms of failure aspect, the differences are not so significant between the two specimens. In fact, ENF 4 presented a high stiffness compared to the overall specimens. ENF 5 presented the lowest strength. A lower strength can possibly inhibit the lighter aspect along the adhesive layer.

An applied load corresponding to 80% of P_{max} was presented in case (c), where tertiary creep phase was captured. A higher steady displacement is shown by the specimen ENF 7, and it is related to its lower stiffness when compared to ENF 6, even with slight differences. This is possibly due to a higher amount of defects in the adhesive layer of the specimen ENF 7. Despite of presenting similar slopes related to secondary creep zone, ENF 7 showed a lower creep lifetime in comparison to ENF 6. In this way, the reduction of creep lifetime was directly related to the displacement level and, consequently, to the amount of defects. Regarding the fracture aspect, ENF 7 presented a considerably lighter adhesive layer, when compared to ENF 6, which is coherent to the higher displacement level (or lower stiffness), and also to the reduced creep lifetime.

Case (d) reported the unique specimen tested under the load corresponding to 85% of P_{max}, which resulted in a creep lifetime of about 14 minutes. This level of applied load seemed to be the maximum where creep phenomena is demonstrated. In fact, even in this case, the extent of secondary creep phase was significantly low. In terms of fracture aspect, the adhesive layer seemed to be only slightly lighter. This is probably related to the observed abrupt failure.

There are some additional observations regarding the aspect of the specimen after being subjected to creep loading conditions. It was observed that the lighter aspect of the adhesive layer was not completely coherent with the displacement level and the slope of secondary phase. Considering results presented in Figure 3.23, it seemed that the presence of voids in the adhesive layer, strength and stiffness levels, as well as the extent of creep phenomenon, in a molecular level, were more related with the lighter aspect. ENF 8 was the specimen with the lowest stiffness, and suffered a long secondary creep phase, with an extent of about 24 h. This same specimen showed the lighter aspect only until the point where the load is applied, while ENF 7 demonstrated the lighter aspect along all the adhesive layer. This was related to the presence of tertiary phase. ENF 2 demonstrated a slight lighter aspect in the adhesive layer, due to the low extent of creep phenomenon, being associated with a premature failure. A lighter aspect in the adhesive layer was not notably verified in ENF 5, and it can be related to a lower strength value. The molecules along the adhesive layer fail completely before reaching an extent of *"smooth"* damage during creep loading. It seemed that the mentioned *"smooth"* damage in the molecules is responsible for the appearance of the lighter aspect, and it is favoured by a higher strength, a lower stiffness, and, at the same time, a long extent of creep phenomena.

As a final note, results were not presented for ENF 1, since it was used a dummy specimen, in order to prepare the correct experimental apparatus.

All these experimental data will be used to validate numerical results, under developments presented in Chapter 4. Proper creep damage laws will be calibrated to experimental results, considering the analysed loading scenarios.

Chapter 4

Numerical Developments

Numerical developments on quasi-static and fatigue loading phenomena have been widely investigated on adhesively bonded joints/repairs. First of all, fundaments on classic viscoelasticity are presented in Section 4.1, constituting the introduction to analytical and numerical modelling. Linear viscoelastic models are exposed in Section 4.1.1, such as Maxwell, Voigt-Kelvin and Burgers. Nonlinear models are also studied in Section 4.1.2. Advanced constitutive relations for creep applications are also analysed in this chapter. In this way, Section 4.1 presents the fundaments for developments proposed in this chapter.

Few studies have demonstrating investigations on creep phenomena, while establishing numerical methodologies. These few studies presented numerical methods which depend strongly on experimental data, being dependent not only on material properties, but also on geometry and dimensions. A new CZM law, predicting the fracture behaviour in creep loaded adhesive joints, is proposed in this chapter, considering pure modes I and II loading scenarios. This new CZM law is identical to ones being developed in the literature for quasi-static and fatigue applications, but with a different expression for damage evolution, where degradation due to creep phenomena is taken into account. In this way, laws establishing the creep damage evolution have to be proposed and included in the CZM formulation.

A theoretical background on creep crack growth prediction is presented in Section 4.2, demonstrating further developments in comparison to what is presented in Section 4.1. From this established background, twelve creep damage laws are developed and proposed in Section 4.3, where rheological parameters are included, i.e., taking into account viscoelastic phenomena, instead of only empirical parameters, which is a novel contribution for numerical developments in the field. In this same section, the proposed laws are implemented in a user subroutine environment, using ABAQUS®, constituting a new CZM law. Parametric studies are conducted in order to assess the behaviour of the derived laws. A parametric calibration, followed by a numerical validation is performed, considering experimental results presented in Chapter 3. Final recommendations of the most appropriate laws for each loading condition, pure mode I or pure mode II, are then presented.

4.1 Viscoelastic Models for Creep and Stress Relaxation

As proved in Section 2.2.5.1, adhesive joints can also suffer failure under creep, which is related to the extensive time period in service under the same load, or under the same displacement. Under creep, it is observed the increase in displacement, even maintaining a constant load. For relaxation, it is observed a stress alleviation under the same displacement. Both phenomena are related to a behaviour associated with ductile materials: viscoelasticity.

Viscoelasticity is demonstrated by a given material when viscous and elastic behaviours are combined. Under a given loading conditions, a structure can demonstrate changes in viscous flow while still presenting a common elastic behaviour (Findley et al., 1976). This is a phenomenon related to creep and relaxation, where the strain/stress behaviour is time-dependent. For the case of polymers under creep, i.e. under a constant stress state, the strain is increased as function of time. In the second phase of creep where a constant strain rate is verified, viscous flow of the molecular chains contributes to the mechanical behaviour. Analogously, similar behaviour is observed but for stress relaxation in polymers. Under a constant strain state, the stress decreases over time.

Creep and stress relaxation, imposing a viscoelastic behaviour, can be explained by several constitutive relations postulated in the literature. Some of the basic models are briefly presented by da Silva et al. (2007), when they can be applied in adhesive joints. Despite of the possible implementation of stress relaxation models in adhesively bonded joints/repairs, da Silva et al. (2007) clearly mentioned that adhesives are not prone to suffer failure due to relaxation phenomena, in a considerable period of time. Only creep conditions can influence significantly the durability of bonded joints and repairs.

This section is reserved for the presentation of analytical models that predict the creep and stress relaxation behaviour of materials. Classical models, presenting linear viscoelastic constitutive equations are presented in Section 4.1.1, Methodologies for the analysis of nonlinear creep and stress relaxation are demonstrated in Section 4.1.2. The book presented by Findley et al. (1976), is considered as the main reference to explain the linear and nonlinear viscoelastic models. Finally, current research developments of constitutive models for creep and stress relaxation are presented in Section 4.1.3, focusing on the behaviour of ductile polymers, essential epoxy resins, and adhesives.

4.1.1 Linear Viscoelastic Constitutive Models

Linear viscoelastic models are based on the association of springs and dashpots. In fact, it is intended that the elastic component of a material can be modelled by a spring, or a group of springs, and the viscous component can be modelled by a dashpot, or a group of dashpots. From the basics of mechanics and dynamics, and using a nomenclature compliant with Findley et al. (1976), the elastic stress component can be determined following the Hooke's Law by equation 4.1 and the viscous stress component can be obtained following the equation 4.2,

$$\sigma_1 = R\varepsilon \tag{4.1}$$

$$\sigma_2 = \eta \frac{d\varepsilon}{dt} \tag{4.2}$$

where R is the spring elastic constant and η is the viscous constant. σ is the stress, and ε is the strain. These equations provide behaviours for the spring and dashpot, individually, being shown in Figure 4.1.

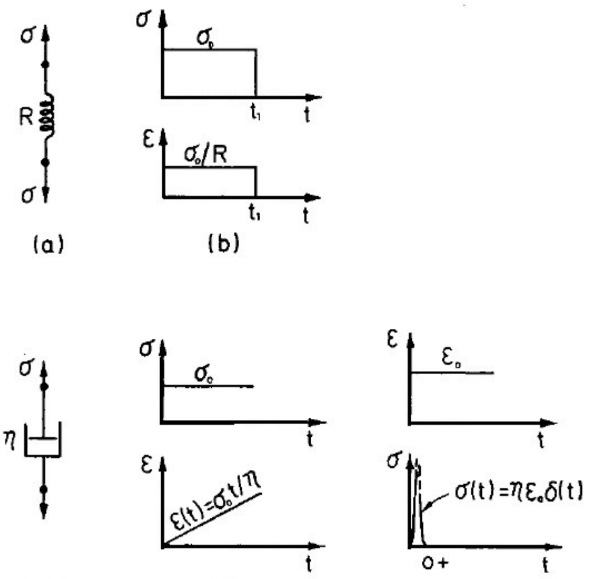

Figure 4.1: Individual behaviours of a spring and dashpot (Findley et al., 1976).

Basing on Figure 4.1, it is observed that the time-dependent behaviour is introduced by the dashpot. It is seen an instantaneous infinite stress that resulted from a constant strain in dashpot, and it is mathematically modelled with the Dirac delta function, $\delta(t)$. In fact, infinite stresses are impossible, however, it is impossible to impose instantaneously finite strains on dashpots as well. The spring introduces the linear elastic component: beyond a constant stress, a constant strain is verified. This element is suitable to model the instantaneous elastic deformation in creep, and also the elastic restoration after unloading.

There are several linear viscoelastic models presented in the aforementioned literature (Findley et al., 1976) such as: Maxwell (Section 4.1.1.1), Voigt-Kelvin (Section 4.1.1.2), and Burgers (Section 4.1.1.4). Maxwell and Kelvin models are then generalised in Section 4.1.1.5. Introducing the possibility of using those analytical models under complex loading conditions, Boltzmann's superposition principle is exposed in Section 4.1.1.6.

4.1.1.1 Maxwell Model

Maxwell (1867) proposed a two-element model, combining a spring and dashpot in series. Consequently, the strain is determined by equation 4.3,

$$\varepsilon = \varepsilon_1 + \varepsilon_2 \tag{4.3}$$

where ε_1 is referred to the strain of the dashpot, while ε_2 is referred to the strain of the spring. An equation for strain rates can be obtained by deriving the equation 4.3. The corresponding representative behaviour is illustrated in Figure 4.2.

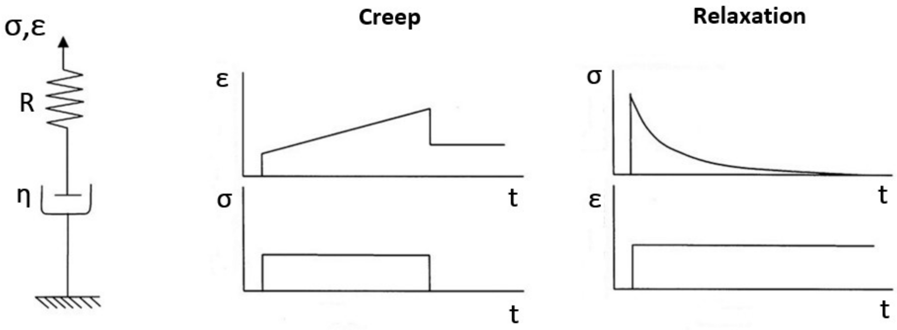

Figure 4.2: Representative creep and relaxation behaviour by Maxwell model (Findley et al., 1976; Tanaka and Eijden, 2003).

Creep and relaxation representative behaviours are shown under an instantaneous constant stress and strain, respectively. The presented behaviour related to the strain rate is governed by equation 4.4,

$$\frac{d\varepsilon}{dt} = \frac{1}{R}\frac{d\sigma}{dt} + \frac{\sigma}{\eta} \tag{4.4}$$

It is observed the introduction of the elastic strain component, being represented by the first term. The second term represents the evolution of strain, being related to viscous effects. Corresponding strain is obtained by solving this differential equation, 4.4, for a creep phenomenon under a constant stress applied instantaneously, obtaining the equation 4.5,

$$\varepsilon(t) = \frac{\sigma_0}{R} + \frac{\sigma_0}{\eta}t \tag{4.5}$$

where σ_0 corresponds to the instantaneously applied constant stress. It is observed in Figure 4.2 a permanent strain after unloading, however an elastic recovery given by $\varepsilon_{rec} = -\sigma_0/R$ is verified. The permanent strain is caused by viscous effects, so that it is given by $\varepsilon_\infty = (\sigma_0/\eta)t_1$, where t_1 is the instant referred to unloading. In fact, this type of phenomenon could represent approximately, and in a very simplistic manner, the creep behaviour of metallic materials, where a permanent strain is verified. Nevertheless, the Maxwell model seemed to be inappropriate to represent the creep behaviours of ductile polymers: the strain is completely recovered slowly after unloading (Lejeune et al., 2018).

The relaxation behaviour of the model, presented in Figure 4.2, associating a spring and a dashpot in series, is represented when a constant strain, ε_0 is instantaneously applied. This behaviour is governed by equation 4.6,

$$\sigma(t) = \sigma_0 e^{-\frac{Rt}{\eta}} = R\varepsilon_0 e^{-\frac{Rt}{\eta}} \tag{4.6}$$

where the evolution of the stress state can be determined by the differentiation of equation 4.6, obtaining the equation 4.7.

$$\frac{d\sigma}{dt} = -\frac{\sigma_0}{\eta} R e^{-\frac{Rt}{\eta}} \tag{4.7}$$

Relaxation time of the Maxwell model, t_R, is determined by a linear stress relaxation, assuming a slope equal to the slope of the tangent at the initial instant ($t = 0^+$) of the equation 4.6. This results in the following equation:

$$\sigma = \sigma_0 \left(1 - \frac{Rt}{\eta}\right) \tag{4.8}$$

so that the relaxation time is referred to the instant $t_R = \eta/R$, corresponding to a null stress. This parameter is responsible for the characterisation of a viscoelastic property. Most of the relaxation happens before the instant of time corresponding to t_R. According to the Maxwell model, 63% of relaxation is verified at $t = t_R$. Generally, for ductile polymers, Maxwell model seemed to suite better in a stress relaxation analysis than in a creep analysis.

4.1.1.2 Voigt-Kelvin Model

Woldemar Voigt and Kelvin also proposed a two-element model, but combining a spring and a dashpot in parallel. In this way, both elements presented equal strain, but the actuating stress is distributed, so that:

$$\sigma = \sigma_1 + \sigma_2 \tag{4.9}$$

where σ_1 and σ_2 are stresses corresponding to the elastic component and viscous component, respectively. Figure 4.3 presents the representative behaviour of the model for creep and relaxation.

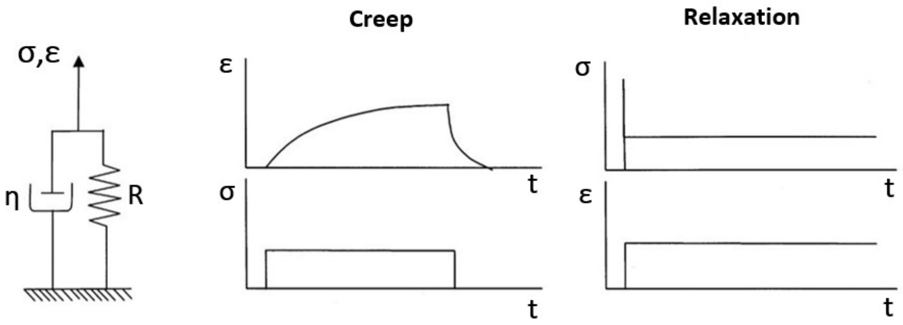

Figure 4.3: Representative creep and relaxation behaviour by Voigt-Kelvin model (Findley et al., 1976; Tanaka and Eijden, 2003).

Applying equations 4.1 and 4.2 in equation 4.9, the following differential equation can be obtained:

$$\dot{\varepsilon} + \frac{R}{\eta}\varepsilon = \frac{\sigma}{\eta} \tag{4.10}$$

The solution of this differential equation is presented as follows:

$$\varepsilon = \frac{\sigma_0}{R}\left(1 - e^{-\frac{Rt}{\eta}}\right) \tag{4.11}$$

corresponding to the equation describing mathematically the strain under creep for the Voigt-Kelvin model. The corresponding strain rate in creep is obtained by differentiating equation 4.11, which allows the determination of equation 4.12.

$$\frac{d\varepsilon}{dt} = \frac{\sigma_0}{\eta} e^{-\frac{Rt}{\eta}} \tag{4.12}$$

Following equations 4.11 and 4.4, and also observing Figure 4.3, it is seen that initially ($t = 0^+$) the strain increases only due to the contribution of the viscous component, so that $\dot{\varepsilon}(t = 0^+) = \sigma_0/\eta$. Then, the load is gradually transmitted to the elastic component, as the strain tends asymptotically to a given value: $\varepsilon(t = \infty) = \sigma_0/R$. This is known as *"delayed elasticity"*. Nevertheless, if the material is unloaded, a recovery governed by the following equation is verified (Findley et al., 1976):

$$\varepsilon = -\frac{\sigma_0}{R}\left(1 - e^{-\frac{R(t-t_1)}{\eta}}\right) \tag{4.13}$$

where t_1 is the instant where an hypothetical load corresponding to $-\sigma_0$ is added, which in reality represents the unloading condition. In this way, after unloading, the material is fully recovered for $t = \infty$. The shape of the strain is obtained by the superposition of both equations 4.11 and 4.13, so that equation 4.14 is obtained.

$$\varepsilon = \frac{\sigma_0}{R} e^{-\frac{Rt}{\eta}} [e^{-\frac{Rt_1}{\eta}} - 1] \text{ , } t > t_1 \tag{4.14}$$

Summarising, the strain under creep following the Voigt-Kelvin model is given by equation 4.15.

$$\begin{cases} \varepsilon = \dfrac{\sigma_0}{R}\left(1 - e^{-\frac{Rt}{\eta}}\right) \text{ , } t \leq t_1 \\ \varepsilon = \dfrac{\sigma_0}{R} e^{-\frac{Rt}{\eta}} [e^{-\frac{Rt_1}{\eta}} - 1] \text{ , } t > t_1 \end{cases} \tag{4.15}$$

The retardation time in creep, t_c, is related to the crossing point between a linear function with a slope corresponding to σ_0/η and the strain $\varepsilon = \sigma_0/R$. 63% of the of the steady-state strain is obtained in $t = t_c$.

Regarding relaxation, Voigt-Kelvin model is not capable of demonstrating a time-dependent behaviour. Under an instantaneously applied constant strain, there is a resultant infinite stress, as shown in Figure 4.3, which is caused mainly by the viscous component. After the impulse, a stress is maintained constant, due to the presence of the elastic component. These conditions correspond mathematically to equation 4.16,

$$\varepsilon_0 \delta(t) + \frac{R}{\eta} \varepsilon_0 H(t) = \frac{\sigma}{\eta} \tag{4.16}$$

where ε_0 is the actuating strain, $\delta(t)$ is the Dirac delta function, and $H(t)$ is the Heaviside function.

Voigt-Kelvin model is more suitable for the representation of the creep behaviour for ductile polymers, rather than for the representation of relaxation. The model is capable to demonstrate the full recovery typical of ductile polymers (Lejeune et al., 2018).

4.1.1.3 Zener Model

Tanaka and Eijden (2003) analysed a different version, consisting only in the Zener model. It is presented by the association in parallel between a Maxwell model and a spring. This model is capable to demonstrate a time-dependent stress relaxation. The Voigt-Kelvin model presented by Findley et al. (1976), is not also capable of capture the instantaneous elastic deformation at $t = 0^+$, which is typical to a creep behaviour. Figure 4.4 shows this model presented by Tanaka and Eijden (2003), as well as the corresponding behaviours representative of creep and relaxation.

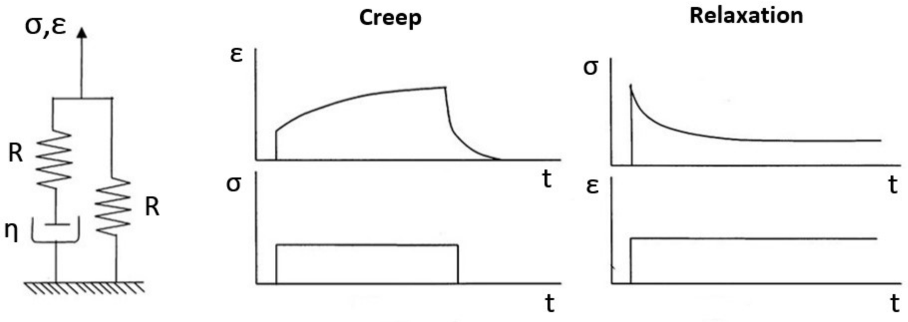

Figure 4.4: Representative creep and relaxation behaviour by a Zener model, following Tanaka and Eijden (2003).

Despite of improvements in terms of accuracy how the demonstrated behaviour is representative of the real creep and relaxation, this model is still unsuitable to describe completely the referred phenomena in ductile polymers. In fact, neither Maxwell nor Voigt-Kelvin models can predict completely the creep and relaxation behaviours of the ductile polymers. More complex associations of springs and dashpots are needed for a more accurate representation.

4.1.1.4 Burgers or Four-Element Model

Burgers model consists in the association of four elements, composed by springs and dashpots, making a combination of Maxwell and Voigt-Kelvin models. The Maxwell spring-dashpot association is combined in series with a Voigt-Kelvin spring-dashpot association. Consequently, the total strain is governed by three components as follows:

$$\varepsilon = \varepsilon_1 + \varepsilon_2 + \varepsilon_3 \tag{4.17}$$

where ε_1, ε_2, and ε_3 are strain components of the Maxwell's spring, Maxwell's dashpot, and Voigt-Kelvin's parallel association, respectively. Figure 4.5 shows the model, as well as corresponding creep and relaxation behaviours.

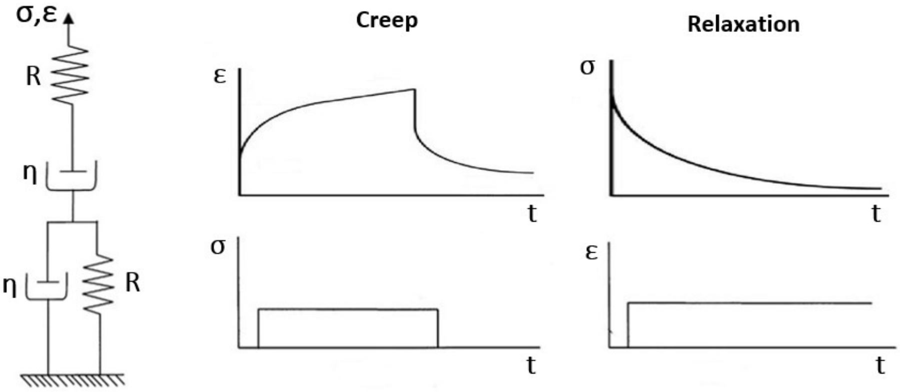

Figure 4.5: Representative creep and relaxation behaviour by Burgers model, following (Findley et al., 1976; Arrospide et al., 2017).

Laws related to the behaviour of springs and dashpots presented previously, combined resulting constitutive equation, that translates the relation between stresses and strains, is postulated as follows (Findley et al., 1976):

$$\sigma+\left(\frac{\eta_1}{R_1}+\frac{\eta_1}{R_2}+\frac{\eta_2}{R_2}\right)\dot{\sigma}+\frac{\eta_1\eta_2}{R_1R_2}\ddot{\sigma}=\eta_1\dot{\varepsilon}+\frac{\eta_1\eta_2}{R_2}\ddot{\varepsilon} \tag{4.18}$$

Analysing this model for a representation in terms of creep, i.e. under the instantaneous application of constant stress σ_0, the following initial conditions are considered:

$$\begin{cases}\varepsilon_1(t=0^+)=\dfrac{\sigma_0}{R_1}\ ,\ \varepsilon_2(t=0^+)=\varepsilon_3(t=0^+)\\ \dot{\varepsilon}(t=0^+)=\dfrac{\sigma_0}{\eta_1}+\dfrac{\sigma_0}{\eta_2}\end{cases} \tag{4.19}$$

where those are inserted in the second-order differential equation, presented in 4.18, resulting in the time-dependent strain that is governed by equation 4.20.

$$\varepsilon(t)=\frac{\sigma_0}{R_1}+\frac{\sigma_0}{\eta_1}t+\frac{\sigma_0}{R_2}\left(1-e^{-\frac{R_2t}{\eta_2}}\right) \tag{4.20}$$

The first two terms correspond to the instantaneous elastic strain and viscous flow, and the last term is representative of the aforementioned *"delayed elasticity"*. In other words, the Burgers model for creep is a sum of effects of the creep behaviours related to the Maxwell and Voigt-Kelvin models.

The corresponding creep strain rate is obtained by differentiating the equation 4.20, which results in equation 4.21.

$$\frac{d\varepsilon}{dt}=\frac{\sigma_0}{\eta_1}+\frac{\sigma_0}{\eta_2}e^{-\frac{R_2t}{\eta_2}} \tag{4.21}$$

The creep strain rate at the initial instant is given as:

$$\dot{\varepsilon}(t=0^{+})=\left(\frac{1}{\eta_1}+\frac{1}{\eta_2}\right)\sigma_0=tan(\alpha) \tag{4.22}$$

and, if the load is maintained, it approaches asymptotically the following value:

$$\dot{\varepsilon}(t=\infty)=\frac{\sigma_0}{\eta_1}=tan(\beta) \tag{4.23}$$

This model is more realistic in terms of the prediction of the initial elastic strain component, which the slope of increase is correspondent to the angle α, rather than the theoretical consideration of the instantaneous elastic strain. Nevertheless, in practical terms, the initial elastic strain is still very fast and difficult to capture. Even an angle of α very close to 90° would not define accurately the phenomenon. The literature taken as the main reference for these classic models, Findley et al., 1976, mentions a general difficult to calibrate Burgers models with experimental results, also for the determination of the angle β.

By a superposition principle, applying a stress equal to $-\sigma_0$ at $t=t_1$, it is possible to obtain the equation that governs the strain behaviour, considering $t>t_1$:

$$\varepsilon(t)=\frac{\sigma_0}{\eta_1}t_1+\frac{\sigma_0}{R_2}\left(e^{-\frac{R_2t_1}{\eta_2}}-1\right)e^{-\frac{R_2t}{\eta_2}}\;,\;t>t_1 \tag{4.24}$$

where an instantaneous elastic recovery is seen, from the second term. This term also produces a gradual recovery when the viscous effect starts to actuate. The first term is referred to the unrecoverable strain component, which is caused solely by viscous effects. For ductile polymers, this is not completely true, constituting a limitation of the Burgers model.

For stress relaxation, and introducing the following initial conditions in equation 4.18:

$$\varepsilon(t=0^{+})=\varepsilon_0H(t)\;,\;\dot{\varepsilon}(t=0^{+})=\varepsilon_0\delta(t)\;,\;\ddot{\varepsilon}(t=0^{+})=\varepsilon_0\frac{d\delta(t)}{dt} \tag{4.25}$$

the constitutive equation, that relates stresses with strains, particularly for relaxation becomes:

$$\sigma+\left(\frac{\eta_1}{R_1}+\frac{\eta_1}{R_2}+\frac{\eta_2}{R_2}\right)\dot{\sigma}+\frac{\eta_1\eta_2}{R_1R_2}\ddot{\sigma}=\eta_1\varepsilon_0\delta(t)+\frac{\eta_1\eta_2}{R_2}\varepsilon_0\frac{d\delta(t)}{dt} \tag{4.26}$$

This second order differential equation is then solved in order to σ, where the result is presented in equation 4.27. All the details regarding the calculation are mentioned in Findley et al. (1976), involving Laplace transforms.

$$\sigma(t)=\frac{\varepsilon_0}{A}\left[\left(\eta_1-\frac{\eta_1\eta_2}{R_2}r_1\right)e^{-r_1t}-\left(\eta_1-\frac{\eta_1\eta_2}{R_2}r_2\right)e^{-r_2t}\right] \tag{4.27}$$

r_1 and r_2 are obtained by equations 4.28 and 4.29, respectively,

$$r_1 = \frac{\left(\frac{\eta_1}{R_1} + \frac{\eta_1}{R_2} + \frac{\eta_2}{R_2}\right) - A}{2\frac{\eta_1\eta_2}{R_1R_2}} \tag{4.28}$$

$$r_1 = \frac{\left(\frac{\eta_1}{R_1} + \frac{\eta_1}{R_2} + \frac{\eta_2}{R_2}\right) + A}{2\frac{\eta_1\eta_2}{R_1R_2}} \tag{4.29}$$

where A is determined by the following equation:

$$A = \sqrt{\left(\frac{\eta_1}{R_1} + \frac{\eta_1}{R_2} + \frac{\eta_2}{R_2}\right)^2 - 4\frac{\eta_1\eta_2}{R_1R_2}} \tag{4.30}$$

In this way, the stress relaxation behaviour is time-dependent. If the applied strain is maintained, the stress tends to an asymptotic value governed by viscous effects.

In fact, several associations of springs and dashpots can be done, constituting three-element or four-element models. Examples are presented by Findley et al. (1976). Indeed, a generalisation of Maxwell and Voigt-Kelvin is presented in Section 4.1.1.5.

4.1.1.5 Generalised Maxwell and Voigt-Kelvin Models

Models proposed by Maxwell and in works developed by Voigt and Kelvin, can be generalised improving the accuracy related to the representation of real behaviours both under creep and relaxation.

Regarding the generalisation of the Maxwell model, the two-element presented in Figure 4.2 can be multiplied in multiple associations in series, so that an equivalent stiffness and viscosity are determined following equations 4.31 and 4.32, respectively.

$$R_{eq} = \left(\sum_{i=1}^{N} \frac{1}{R_i}\right)^{-1} \tag{4.31}$$

$$\eta_{eq} = \left(\sum_{i=1}^{N} \frac{1}{\eta_i}\right)^{-1} \tag{4.32}$$

Corresponding strain rate, representative of the creep behaviour, is consequently presented in equation 4.33, constituting a generalised version of equation 4.4.

$$\dot{\varepsilon} = \dot{\sigma}\sum_{i=1}^{N} \frac{1}{R_i} + \sigma\sum_{i=1}^{N} \frac{1}{\eta_i} \tag{4.33}$$

Stress relaxation can be also represented by a generalised Maxwell, but with an association in parallel of the model presented in Figure 4.2, instead of an association in series. The total stress in the system is sum of the contribution of the stress in each Maxwell element, so that:

$$\sigma = \sum_{i=1}^{a} \sigma_i = \left(\sum_{i=1}^{a} \frac{D}{\frac{D}{R_i} + \frac{1}{\eta_i}} \right) \varepsilon \tag{4.34}$$

where D is a differential operator in time: $D = d/dt$.

By the association in parallel of several Voigt-Kelvin models, which are presented in Figure 4.3, following equivalent stiffness and viscosity are then determined by equations 4.35 and 4.36, respectively.

$$R_{eq} = \sum_{i=1}^{N} R_i \tag{4.35}$$

$$\eta_{eq} = \sum_{i=1}^{N} \eta_i \tag{4.36}$$

The association in parallel provides an expression for the stress evolution when the system is subjected to relaxation, so that:

$$\sigma = R_{eq}\varepsilon + \eta_{eq}\dot{\varepsilon} \tag{4.37}$$

A representation of the creep can also be provided by a generalised Voigt-Kelvin model. However, several systems, as one presented in Figure 4.3, have to be associated in series. Consequently, the total strain is the sum of the contribution of the strain in each Voigt-Kelvin element, obtaining the equation 4.38

$$\varepsilon = \sum_{i=1}^{a} \varepsilon_i = \left(\sum_{i=1}^{a} \frac{1}{D\eta_i + R_i} \right) \sigma \tag{4.38}$$

It has to be noted that the association in series of multiple Maxwell models provides a more accurate result, rather than the association in parallel of the same multiple models. Analogously, the association in parallel of multiple Voigt-Kelvin models is more suitable than the association in series of those same multiple models. Indeed, it is observed that the generalised Maxwell model provides better results for creep, while the generalised Voigt-Kelvin model is more suitable for the representation of relaxation phenomena.

A generalised model, combining both Maxwell and Voigt-Kelvin elements, is possible to construct, by combining a spring, a dashpot, and a multiple Voigt-Kelvin models associated in series, as shown in Figure 4.6. This model allows the combination of the elastic and viscous effects, but also including multiple retardation times, guaranteeing the effect of the *"delayed elasticity"* previously described.

This combination allows the definition of the representative creep strain by the generalised Voigt-Kelvin model more accurately, being determined by equation 4.39.

$$\varepsilon(t) = \sigma_0 \sum_{i=1}^{a} \phi_i \left(1 - e^{-\frac{t}{t_c^i}} \right) \tag{4.39}$$

ϕ is referred to the compliance, which is defined as $\phi = 1/R_i$, and t_c^i is the retardation time, whose

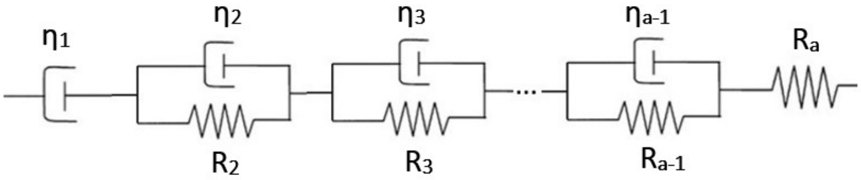

Figure 4.6: Generalised model to represent the elastic and viscous components, as well as the *"delayed elasticity"* (Findley et al., 1976; Arrospide et al., 2017).

value can be calculated as $t_c^i = \eta_i / R_i$. For a an infinite number of Voigt-kelvin elements, the creep strain is then defined by equation 4.40.

$$\varepsilon(t) = \sigma_0 \int_0^{\infty} \phi(t_c) \left(1 - e^{-\frac{t}{t_c}}\right) dt_c \tag{4.40}$$

On the other hand, the stress relaxation is also defined with a better accuracy for a generalised Maxwell model, being expressed by equation 4.41,

$$\sigma(t) = \varepsilon_0 \sum_{i=1}^{a} R_i e^{-\frac{t}{t_R^i}} \tag{4.41}$$

where t_R^i is the relaxation time, being expressed as $t_R^i = \eta_i / R_i$. In the same manner, as previously described, if the an infinite number of Voigt-Kelvin elements is considered, the time-dependent stress is then defined by the following equation:

$$\sigma(t) = \varepsilon_0 \int_0^{\infty} R(t_R) e^{-\frac{t}{t_R}} dt_R \tag{4.42}$$

4.1.1.6 Boltzmann's Superposition Principle

Under complex loading scenarios, the problem can be subdivided in multiple problems, and then summing all the effects. For a given material with an actuation of multiple different loads, the strain in creep can be obtained by the sum of the individual strains referred to each load individually. Similarly, regarding relaxation, the time-dependent stress resulting from multiple applied strains, can be obtained by the superposition of each stress referred to each applied strain individually.

The objective of the following explanation is only to provide numerical procedures for the usage of the Boltzmann's superposition principle. Consequently, the following description is based in explanations presented by da Silva et al. (2007).

Under a complex loading scenario, the corresponding creep strain can then be determined by equation 4.43.

$$\varepsilon(t) = \sum_{i=1}^{N} \Delta\sigma_i S(t - t_i) \tag{4.43}$$

Generalising, and for an infinite number of load cases, σ_i, the creep strain is then determined as follows:

$$\varepsilon(t) = \int_{-\infty}^{t} S(t-t_i)\frac{d\sigma(t_i)}{dt_i}dt_i \tag{4.44}$$

Graphically, the determination of the creep strain is described in Figure 4.7.

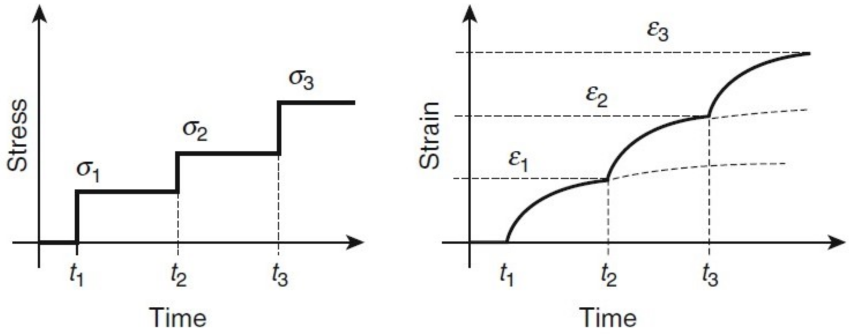

Figure 4.7: Demonstration of the Boltzmann's superposition principle in creep (Geiss, 2011).

Analogously, this same superposition principle can also be applied to the stress relaxation cases, where the generalised time-dependent stress is determined by equation 4.45.

$$\sigma(t) = \int_{-\infty}^{t} C(t-t_i)\frac{d\varepsilon(t_i)}{dt_i}dt_i \tag{4.45}$$

Boltzmann's superposition principle can only be applied for linear viscoelasticity, providing, in those cases, an incremental analysis, allowing the fragmentation of a complex engineering problem into several simple engineering problems. This method can be extended for triaxial stress states, as shown by da Silva et al. (2007).

4.1.2 Nonlinear Creep and Stress Relaxation

In the last section, an overview on the classic viscoelastic models was presented. Nevertheless, most of the times, the accuracy related to the representative behaviour in creep and relaxation is not sufficient for further analysis, especially in the fracture mechanics domain. da Silva et al. (2007) summarised the application for two nonlinear models for the analysis of adhesively bonded joints. The authors presented the Schapery law, here discussed in Section 4.1.2.1, and also the Findley law, which is presented in Section 4.1.2.2, being detailed in depth by Findley et al. (1976). This same literature also presents an alternative methodology for the Boltzmann's superposition principle, since it is only applicable to linear viscoelasticity. So, the method of multiple integral representation is exposed in Section 4.1.2.3.

4.1.2.1 Schapery Law

Schapery Law (Schapery, 1969) is essentially based in thermodynamic principles, considering irreversible processes. In fact, Findley et al. (1976) mentions this law as the thermodynamic constitutive theory.

da Silva et al., 2007 presented the creep strain formulation for isothermal conditions, under an uniaxial loading, being expressed by equation 4.46,

$$\varepsilon(t) = g_0 S_0 \sigma(t) + g_1 \int \Delta S(\Psi - \Psi') \frac{d}{d\tau}[g_2 \sigma(\tau)]\, d\tau \tag{4.46}$$

where S_0 is the initial compliance, while Δ_S represents the corresponding variation. Ψ and Ψ' are reduction time functions, being expressed as follows:

$$\Psi = \int_0^t \frac{1}{a_\sigma} dt' \tag{4.47}$$

$$\Psi' = \int_0^\tau \frac{1}{a_\sigma} dt' \tag{4.48}$$

The nonlinear behaviour is expressed by constants g_0, g_1, g_2, and a_σ, which properties that depend on the stress state, temperature and humidity. Those are empirically determined.

Analogously, the time-dependent stress for relaxation scenarios is also possible to determine using the Schapery law, following Findley et al. (1976). Corresponding expression is presented in equation 4.49 or ,alternatively, it can be expressed as in equation 4.50.

$$\sigma(t) = h_\infty E_\infty \varepsilon(t) + h_1 \int_0^t E_t \left(\xi - \xi'\right) \frac{d h_2 \varepsilon(\tau)}{d\tau} d\tau \tag{4.49}$$

$$\sigma(t) = h_0 E_0 \varepsilon(t) - h_3 \int_0^t \phi \left(\xi - \xi'\right) \frac{d h_4 \varepsilon(\tau)}{d\tau} d\tau \tag{4.50}$$

where ξ and ξ' can be obtained as follows:

$$\xi = \int_0^t \frac{1}{a_\varepsilon} dt' \tag{4.51}$$

$$\xi' = \int_0^\tau \frac{1}{a_\varepsilon} dt' \tag{4.52}$$

Similar to what happens in creep, there are empirical terms here defined as h_1, h_2, h_3, h_4, h_∞, and a_ε. E_∞ is the steady-state modulus at a constant stress, E_0 is the initial modulus, E_t is the transient modulus during relaxation phenomenon, and ϕ is the relaxation modulus. Relation between all the mentioned moduli is expressed in equation 4.53.

$$E_0 = \phi + E_t + E_\infty \tag{4.53}$$

4.1.2.2 Findley Law

Findley law is purely empirical as mentioned by da Silva et al. (2007), being proved by Findley et al. (1976). For the representation of creep strain, da Silva et al. (2007) presents the following expression:

$$\varepsilon(t) = \varepsilon_0 sinh(a\sigma) + bt^n sinh(c\sigma) \tag{4.54}$$

whose values for a, b, and c are defined experimental for given temperature and humidity conditions. The constant n is independent on the stress level.

Empirical models for relaxation are analogous to the ones for creep, as deeply detailed by Findley et al. (1976).

4.1.2.3 Multiple Integral Representation

For nonlinear creep and relaxation conditions, the determination of the global response as the sum of the individual effects is not valid. A multiple integral methodology is presented by Findley et al. (1976), being analogous to the Boltzmann's superposition principle, but valid for nonlinear cases.

Under creep conditions, Findley et al. (1976) presented an example of three individual loading scenarios, referred to a stress $\Delta\sigma$. The authors proposed a polynomial for each strain component contribution, so that the first strain contribution, due to the actuation of $\Delta\sigma_0$ is given as:

$$\varepsilon_0(t) = \Delta\sigma_0\phi_1(t) + \Delta\sigma_0^2\phi_2(t) + \Delta\sigma_0^3\phi_3(t) + \ldots + \Delta\sigma_0^n\phi_n(t) \tag{4.55}$$

where $\phi_i(t)$ are time-dependent material functions. The accuracy of the model increases with the number (n) of the used terms. When a given stress condition, $\Delta\sigma_1$, is added, at a given time $t = t_1$ to the loading scenario, its individual contribution of strain is presented by the polynomial in equation 4.56.

$$\begin{cases} \varepsilon_1(t) = \Delta\sigma_1\phi_1(t-t_1) + \Delta\sigma_1^2\phi_2(t-t_1) + \Delta\sigma_1^3\phi_3(t-t_1) + \ldots + \Delta\sigma_1^n\phi_n(t-t_1)\ ,\ t \geq t_1 \\ \varepsilon_1(t) = 0\ ,\ t < t_1 \end{cases} \tag{4.56}$$

In the same manner, adding the third loading conditions, referred to a stress state $\Delta\sigma_2$, the corresponding individual contribution is given as:

$$\begin{cases} \varepsilon_2(t) = \Delta\sigma_2\phi_1(t-t_2) + \Delta\sigma_2^2\phi_2(t-t_2) + \Delta\sigma_2^3\phi_3(t-t_2) + \ldots + \Delta\sigma_2^n\phi_n(t-t_2)\ ,\ t \geq t_2 \\ \varepsilon_2(t) = 0\ ,\ t < t_2 \end{cases} \tag{4.57}$$

In this way, the total response related to the creep strain, considering the superposition of loading scenarios corresponding to $\Delta\sigma_0$, $\Delta\sigma_1$, and $\Delta\sigma_2$ is presented in equations 4.58, 4.59, and 4.60, for $t < t_1$, $t_1 \leq t < t_2$, and $t \geq t_2$, respectively. For sake of simplicity, only the first three terms were considered in the polynomial series.

$$\varepsilon(t) = \Delta\sigma_0\phi_1(t) + \Delta\sigma_0^2\phi_2(t,t) + \Delta\sigma_0^3\phi_3(t,t,t)\ ,\ t < t_1 \tag{4.58}$$

$$\begin{aligned}\varepsilon(t) = \Delta\sigma_0\phi_1(t) + \Delta\sigma_0^2\phi_2(t,t) + \Delta\sigma_0^3\phi_3(t,t,t) + \Delta\sigma_1\phi_1(t-t_1) + \Delta\sigma_1^2\phi_2(t-t_1,t-t_1)+ \\ \Delta\sigma_1^3\phi_3(t-t_1,t-t_1,t-t_1) + 2\Delta\sigma_0\Delta\sigma_1\phi_2(t,t-t_1) + 3\Delta\sigma_0^2\Delta\sigma_1\phi_3(t,t,t-t_1)+ \\ 3\Delta\sigma_0\Delta\sigma_1^2\phi_3(t,t-t_1,t-t_1)\ ,\ t_1 \leq t < t_2\end{aligned} \tag{4.59}$$

$$\begin{aligned}\varepsilon(t) = \Delta\sigma_0\phi_1(t) + \Delta\sigma_0^2\phi_2(t,t) + \Delta\sigma_0^3\phi_3(t,t,t) + \Delta\sigma_1\phi_1(t-t_1) + \Delta\sigma_1^2\phi_2(t-t_1,t-t_1)+ \\ \Delta\sigma_1^3\phi_3(t-t_1,t-t_1,t-t_1) + \Delta\sigma_2\phi_1(t-t_2) + \Delta\sigma_2^2\phi_2(t-t_2,t-t_2) + \Delta\sigma_2^3\phi_3(t-t_2,t-t_2,t-t_2)+ \\ 2\Delta\sigma_0\Delta\sigma_1\phi_2(t,t-t_1) + 2\Delta\sigma_0\Delta\sigma_2\phi_2(t,t-t_2) + 2\Delta\sigma_1\Delta\sigma_2\phi_2(t-t_1,t-t_2)+ \\ 3\Delta\sigma_0^2\Delta\sigma_1\phi_3(t,t,t-t_1) + 3\Delta\sigma_0\Delta\sigma_1^2\phi_3(t,t-t_1,t-t_1) + 3\Delta\sigma_0^2\Delta\sigma_2\phi_3(t,t,t-t_2)+ \\ 3\Delta\sigma_0\Delta\sigma_2^2\phi_3(t,t-t_2,t-t_2) + 3\Delta\sigma_1^2\Delta\sigma_2\phi_3(t-t_1,t-t_1,t-t_2)+ \\ 3\Delta\sigma_1\Delta\sigma_2^2\phi_3(t-t_1,t-t_2,t-t_2) + 6\Delta\sigma_0\Delta\sigma_1\Delta\sigma_2\phi_3(t,t-t_1,t-t_2)\ ,\ t \geq t_2\end{aligned} \tag{4.60}$$

Generalising this formulation for N loading scenarios, the creep strain is governed by equation 4.61, extended for a infinite number of terms.

$$\begin{aligned}\varepsilon(t) = \sum_{i=1}^{N}\Delta\sigma_i\phi_1(t-t_i) + \sum_{i=0}^{N}\sum_{j=0}^{N}\Delta\sigma_i\Delta\sigma_j\phi_2(t-t_i,t-t_j)+ \\ \sum_{i=0}^{N}\sum_{j=0}^{N}\sum_{k=0}^{N}\Delta\sigma_i\Delta\sigma_j + \Delta\sigma_k\phi_3(t-t_i,t-t_j,t-t_k)\end{aligned} \tag{4.61}$$

All this methodology is intended as the extension of linear superposition principle, proposed by Boltzmann, but adding nonlinear effects.

Generalising even more, and including the situation of considering an infinite number of infinitesimal stepwise stress inputs, the sums presented in equation 4.61 become integrals as shown in equation 4.62.

$$\begin{aligned}\varepsilon(t) = \int_0^t \phi_1(t-\xi_1)\dot{\sigma}(\xi_1)\,d\xi_1 + \int_0^t\int_0^t \phi_2(t-\xi_1,t-\xi_2)\dot{\sigma}(\xi_1)\dot{\sigma}(\xi_2)\,d\xi_1 d\xi_2+ \\ \int_0^t\int_0^t\int_0^t \phi_3(t-\xi_1,t-\xi_2,t-t\xi_3)\dot{\sigma}(\xi_1)\dot{\sigma}(\xi_2)\dot{\sigma}(\xi_3)\,d\xi_1 d\xi_2 d\xi_3\end{aligned} \tag{4.62}$$

$\phi_1(t-\xi_1)$, $\phi_2(t-\xi_1,t-\xi_2)$, and $\phi_3(t-\xi_1,t-\xi_2,t-\xi_3)$ are kernel functions of first, second, and third order, respectively.

The time-dependent stress, related to relaxation phenomenon, under multiple strain scenarios, can be determined by an analogous procedure as previously described.

4.1.3 Applied Models on the Material Characterisation under Creep and Stress Relaxation

Since the beginning of the 20^{th} century, several authors have been published constitutive models representative of creep and relaxation behaviours in many materials. The historic perspective on the classic literature about the remaining subject shows some models representative of the time-dependent creep strain, consisting on empirical equations, derived from experimental results. Some of the models are power laws, as ones presented by Bailey (1935), Findley (1944), also included by Findley et al. (1976), with a modified version exposed in equation 4.54, and Graham and Walles (1955). In fact, Paola et al. (2011) mentioned that the power law is representative of the creep and relaxation behaviours for various materials, including polymers, which was noted by Nutting (1921), and Gemant (1936). From that concept, accuracy with experimental results are improved by employing fractional derivatives, which is a subject investigated in this section.

Historically framing, Table 4.1 is synthesising the principal empirical models, considering as classic, describing developments performed between 1910 and 1975.

Table 4.1: Classical empirical laws for time-dependent creep strain.

Creep Model	**Reference**
$\varepsilon = ln\left(1+\beta t^{\frac{1}{3}}\right)+kt$	Andrade, 1910
$\varepsilon = G\left(1-e^{-qt}\right)+Ht$	McVetty, 1934
$\varepsilon = Ft^n$	Bailey, 1935
$\varepsilon = \varepsilon_1 + \varepsilon_2^n \ (n<1)$	Findley, 1944
$\varepsilon = \sum_{j=1}^{M} a_j t^{m_j}$	Graham and Walles, 1955
$\varepsilon = \varepsilon_t\left(1-e^{-rt}\right)+\dot{\varepsilon}_s t$	Garofalo, 1963
$\varepsilon = \frac{a_1 t}{1+b_1 t}+\frac{a_2 t}{1+b_2 t}+\dot{\varepsilon}_m t$	Pugh, 1975

Creep models have been widely studied, applying to polymers that can suffer creep deformations even at ambient temperatures. Some literature, recently, has developing models to apply on adhesively bonded joints, and those can be extended for the use in bonded repairs. Mathematically, the most interesting creep models consist in power laws, which can be analogous to already known fatigue models, being applied for the prediction of crack growth. In addition, classical models, essentially the ones proposed by Maxwell and Voigt-Kelvin, have been modified with fractional calculus, in order to approximate more accurately and easily, with experimental data.

Even in to predict creep behaviour in composite laminates, several models have been adapted. Guedes et al. (1998) used the Schapery single integral equation, described previously in Section 4.1.2.1, calculating the integrals numerically with a Prony's series. The objective was to express, not only a representative behaviour under creep, but also under stress relaxation, of composite laminates. The authors implemented the Schapery nonlinear model into the CLT (Classical Laminate Theory). Good accuracy, according to experimental results, was reported when the method was applied to T300/5208, which is a CFRP laminate.

Spathis and Kontou (2012) applied an empirical creep model proposed by Brauwens-Crowet et al. (1969), being presented in equation 4.63.

$$\dot{\varepsilon} = Ce^{-\frac{Q}{kT}} e^{\frac{\sigma v_p}{3kT}} e^{\frac{(\sigma-\sigma_{int})v_s}{kT}} \tag{4.63}$$

where the several parameters consist on:

- $\dot{\varepsilon}$ - creep strain rate;
- C - empirical constant;
- Q - activation energy;
- k - Boltzmann's constant;
- T - temperature;
- v_p - pressure activation volume;
- v_s - shear activation volume;
- σ_{int} - internal stress.

The internal stress depends on the residual strain, ε_R, and is calculated following a parameter proportional to the temperature, K_2:

$$\sigma_{int} = K_2 \varepsilon_R \tag{4.64}$$

Plastic effects were taken into account by the authors, so that a superposition is considered between the elastic (ε_{el}), plastic (ε_p), and also the residual components (ε_R).

$$\varepsilon = \varepsilon_{el} + \varepsilon_p + \varepsilon_R \tag{4.65}$$

An integration of the function form is proposed to determined the plastic strain rate, ε_p, which is presented in equation 4.66. This model takes into account defects with a normal distribution density. Those regions are where plastic deformation can emerge and grow.

$$\dot{\varepsilon}_p = \frac{\dot{\varepsilon}}{(1+\varepsilon)\mu} \frac{1}{s\sqrt{2\pi}} \int_0^{\varepsilon} e^{-\frac{1}{2}\left(\frac{\varepsilon_i - \mu}{s}\right)^2} d\varepsilon_i \tag{4.66}$$

μ and s are the mean value of the probability density and the standard deviation respectively. Those are important parameters to express of the plastic strain grows. A successful implementation of this model in polymers and composites was reported by the authors.

The characterisation of creep behaviour considering several materials does not only involve the determination of time-dependent strain under a given constant stress. The obtention of creep compliance, from experimental results, has also a huge importance. Simsiriwong et al. (2015) presented a methodology to determine creep compliance of a vinyl ester polymer. The authors applied a Voigt-Kelvin model generalised with a Prony series, which allowed to calculate the creep compliance based on experimental data. Figure 4.8 summarises the applied methodology. A Weidbull distribution was then used for a statistical approach.

Song et al. (2016) presented an empirical approach to characterise the creep behaviour of polyimide PMR-15, and carbon-polyimide composites. This paper applied the Shelby-Dorn model, presented in equation 4.67, which represents the steady-state creep strain rate behaviour, being

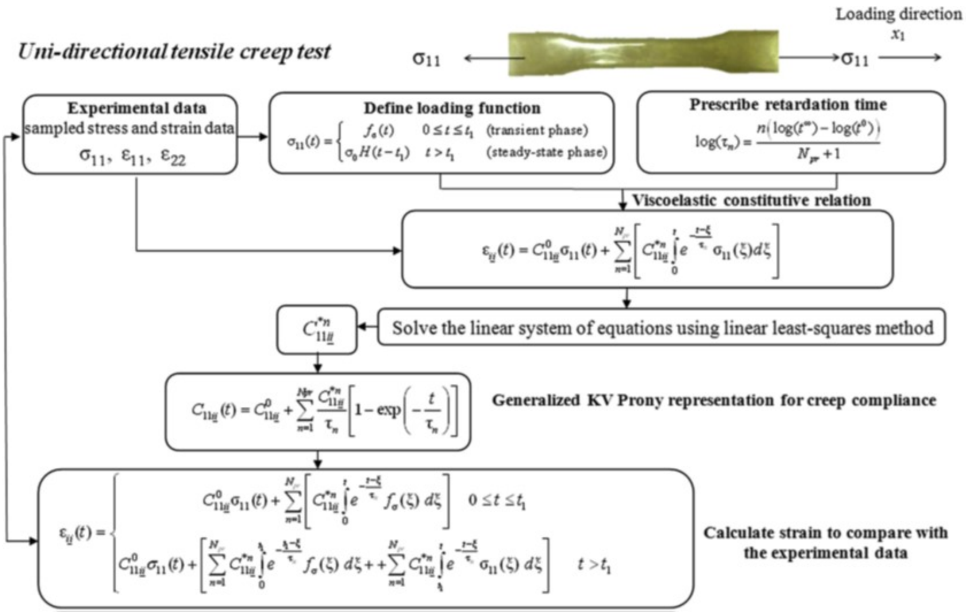

Figure 4.8: Creep compliance calculation using a Prony series (Simsiriwong et al., 2015).

directly dependent on the applied stress and temperature conditions.

$$\dot{\varepsilon}_{ss} = A\sigma^n e^{\left(-\frac{Q}{RT}\right)} \tag{4.67}$$

where σ is the applied stress, A is a material parameter, n is the power-law exponent, Q is the activation energy, and R is the gas constant, being considered as $R = 8.314J/(mol.k)$. n can be determined empirically, depending on temperature conditions. The time-dependent plastic strain is determined by equation 4.68, and depends on the steady-state creep strain rate.

$$\varepsilon_p = \varepsilon_t \left(1 - e^{-C\dot{\varepsilon}_{ss}t}\right) + \dot{\varepsilon}_{ss}t \tag{4.68}$$

where C and ε_t are material constants determined empirically, depending on the applied stress and temperature conditions. The total strain, including the instantaneous elastic component, is then defined by equation 4.69.

$$\varepsilon = \frac{\sigma}{E} + \varepsilon_p \tag{4.69}$$

where E is the elastic modulus. Further detailed analysis is done for composites in this study. This power-law based model characterised, with a good precision, the creep behaviour of the polyimide PMR-15, as well as of the carbon-polyimide composite by considering an extension of this analysis.

More recently, the Schapery model presented in Section 4.1.2.1 was applied in Jafaripour and Taheri-Behrooz (2020) both in polymers and composites. The authors mention the importance of modelling both linear and nonlinear behaviours. Constants associated with the mathematical formulation are determined empirically from experiments considering different stress levels and temperature conditions. Even the threshold between linear and nonlinear behaviour is obtained from experimental data. The Prony series terms used in Schapery's integral were obtained for a given stress and temperature range. In fact, the authors advised to the risk of inaccuracy if extrapolations are done. This is valid not only for the application of the Schapery model, but to all viscoelastic models in general, either linear or nonlinear.

Schapery model was also applied in Sun et al. (2020), whose mathematical formulation was extended to use in composite materials under humid environments. Corresponding numerical predictions were developed using ABAQUS®, with a user-defined material subroutine (UMAT) and a user-defined field variable subroutine (USDFLD). For the establishment of the model, parameters were defined empirically using hygrothermal-mechanical coupling moisture absorption, static, and short-term tensile creep-recovery tests. Good accuracy was achieved, proving that even with the application of well known models in the literature, it is possible to characterise precisely the creep behaviour, considering various materials, even if those are applied numerically, being integrated in a finite element (FE) software.

Recently, one of the main goals in the characterisation of creep and relaxation behaviours is to bring more realistic models in order to increase the accuracy in comparison to experimental data. Lin et al. (2022), presented constitutive equations, being consistent with standard linear solid models, but considering a finite loading rate. In fact, most of the numerical models mentioned in the literature, consider an infinite loading rate, i.e. the load is applied instantaneously, which is not coherent with the reality. The referred study demonstrated the improved accuracy, analysing errors, for various values of viscoelastic materials and loading rate. The authors modified models related to the characterisation of a representative behaviour under creep and stress relaxation.

Regarding creep, the strain associated at the end of loading process, ε_0, occurring at the instant $t = t'$ is then obtained as a function of the steady-state applied stress, σ_0:

$$\varepsilon_{loading}(t') = \varepsilon_0 = \frac{r}{E_1}t' + \frac{r}{E_1}(\tau_R - \tau_C)\left(1 - e^{-\frac{t'}{\tau_C}}\right) = \frac{\sigma_0}{E_1} + \frac{r}{E_1}(\tau_R - \tau_C)\left(1 - e^{-\frac{t'}{\tau_C}}\right) \tag{4.70}$$

where r is the loading rate, and E_1 is an elastic parameter with the material, related to its Young's modulus. In this case, $\sigma_0 = rt'$. In addition, τ_R is the relaxation time, and τ_C is the retardation time, which can be determined by the following equations:

$$\tau_R = \frac{\eta}{E_2} \tag{4.71}$$

$$\tau_C = \frac{\eta\,(E_1 + E_2)}{E_1 E_2} \tag{4.72}$$

E_2 is referred to an elastic constant related to the viscoelastic behaviour, while η is the viscous parameter of the material. In this way, the creep constitutive equation, governed by a finite loading rate, is then presented as follows:

$$\varepsilon_{creep}(t) = \left[\frac{r}{E_1}(\tau_R - \tau_C)\left(1 - e^{-\frac{\sigma_0}{\tau_C r}}\right)\right] e^{-\left(\frac{t}{\tau_C}\right)^k} + \frac{\sigma_0}{E_1} \tag{4.73}$$

where k is an empirical fractional constant $(0 < k \leq 1)$ which improves the accuracy.

Errors were analysed for different stress loading rates, considering three different materials with Young's modulus of 5000 Pa, 10000 Pa, and 30000 Pa. The improved accuracy, of the finite loading formulation, in comparison to the classical infinite loading formulation was proved. Maximum errors of 20% are registered for the new formulation, while for the traditional one, the maximum error can be of 100% for lower loading rates, which are common in real applications. The increase in the relaxation time seemed to decrease the error. In fact, there is a threshold whose errors are practically null, for a given load rate. The lower the relaxation time is, the higher is that threshold. An increase in E_1, allows an increase in the error. However, variations of E_2 and η, which are parameters that characterise the viscoelastic behaviour, seemed to be insignificant.

Regarding stress relaxation, the equation governing the loading phase is presented as follows:

$$\sigma_{loading}(t') = \sigma_0 = E_1 r t' + E_1 r\left(\tau_C - \tau_R\right)\left(1 - e^{-\frac{t'}{\tau_R}}\right) = E_1 \varepsilon_0 + E_1 r\left(\tau_C - \tau_R\right)\left(1 - e^{-\frac{t'}{\tau_R}}\right) \tag{4.74}$$

considering that $\varepsilon_0 = rt'$, where $t = t'$ is the instant referred to the end of the loading process, and ε_0 is the steady-state applied strain. Corresponding constitutive equation considering stress relaxation is then presented:

$$\sigma_{relaxation}(t) = \left[E_1 r\left(\tau_C - \tau_R\right)\left(1 - e^{-\frac{\varepsilon_0}{\tau_R r}}\right)\right] e^{-\left(\frac{t}{\tau_R}\right)^k} + E_1 \varepsilon_0 \tag{4.75}$$

Errors were also analysed considering stress relaxation, considering the same materials with the following Young's moduli: 5000 Pa, 10000 Pa, and 30000 Pa. The improved accuracy was even greater for relaxation, rather than for creep. Independently on the strain rate, an almost 100% accuracy is proved, registering errors bellow 2%. For low strain rates, almost 100% of error is verified for the traditional infinite loading formulation, similarly to what was seen for creep conditions. The decrease in the relaxation time also allowed an increase in the aforementioned threshold. For relaxation conditions, it was observed that variations in E_1, E_2, and η seemed to be insignificant to the accuracy, consequently errors are insensible to changes in the Young's modulus.

The authors have proved accurate results while applying these models, considering a finite loading rate, to FE simulations. Since the flexibility of the application of the proposed models was demonstrated, for various materials, with different viscoelastic properties, and for all stress/strain rates, the replacement of the traditional models is recommended. In addition, more realistic scenarios are considered in simulation, being the main advantage of the aforementioned models.

Current state-of-art has making efforts to represent means of demonstrating more easily, but, at the same time, more accurately, creep and relaxation behaviours. Formulations constituted by fractional derivatives are a way of getting simpler mathematical representations, simultaneously accurately reproducing creep and relaxation behaviours. A recent study presented by Lazopoulos et al. (2022), mentioned an important conference paper in the subject related to the fractional calculus: Ross, 1977. This study mentioned the true origin of the fractional calculus, which, in fact, was an indirect development. Lagrange, in 1772, made the first step by presenting the law of exponents for differential operators, being presented in equation 4.76

$$\frac{d^m}{dx^m}\frac{d^n}{dx^n}y = \frac{d^{m+n}}{dx^{m+n}}y \tag{4.76}$$

Consequently, Laplace, in 1812, presented a fractional derivative through an integral representation, and, in 1819, this author used a derivative of arbitrary order. With a generalised notation, Lacroix proposed the equation 4.77,

$$\frac{d^n y}{dx^n} = \frac{m!}{(m-n)!}x^{m-n} \text{ , } m \geq n \tag{4.77}$$

where the Legendre's symbol can be used, defining the equation 4.78.

$$\frac{d^n y}{dx^n} = \frac{\Gamma(m+1)}{\Gamma(m-n+1)}x^{m-n} \tag{4.78}$$

Other means of fractional derivatives are derived, but this corresponds to one of the first steps. More recent notations are presented by Lazopoulos et al. (2022), defining, first of all, the Rienmann-Liouville derivative, whose formulation is descendent to the aforementioned history:

$${}_{a}^{RL}D_x^{\gamma}f(x) = \frac{1}{\Gamma(n-\gamma)}\frac{d^n}{dx^n}\int_a^x \frac{f(s)}{(x-s)^{\gamma+1-n}}ds \tag{4.79}$$

where $n-1 \leq \gamma < n$.

Caputo's fractional derivative is also proposed as follows:

$${}_{a}^{C}D_x^{\gamma}f(x) = \frac{1}{\Gamma(n-\gamma)}\int_a^x \frac{f^n(s)}{(x-s)^{\gamma+1-n}}ds \tag{4.80}$$

where $n-1 < \gamma < n$.

Fractionality property is an important feature mentioned by Lazopoulos et al. (2022), dictating that fractional derivatives should coincide with the common derivatives at the orders of natural numbers. Proposed models based on fractional derivatives must consider this property.

As previously mentioned, Paola et al. (2011) referred developments presented by Nutting (1921) and Gemant (1936), demonstrating the high accuracy associated to the use of power laws for the representation of creep and stress relaxation behaviours in ductile materials, essentially polymers. The accuracy can even be improved by using fractional derivatives, which are gaining attention in the current state-of-art. Paola et al. (2011) started by presenting creep and relaxation functions, presented in equations 4.81 and 4.82, respectively, including fractional derivatives.

$$D(t) = \frac{1}{c_\beta \Gamma(1+\beta)}t^{\beta} \tag{4.81}$$

$$E(t) = \frac{c_\beta}{\Gamma(1-\beta)}t^{-\beta} \tag{4.82}$$

$D(t)$ and $E(t)$ are the so called creep and relaxation functions, respectively. Γ is known as Gamma function in the considered study, but it corresponds to the aforementioned Legendre's symbol. c_β and β are controllable parameters, whose c_β is defined as follows:

$$c_\beta = R\tau^\beta \tag{4.83}$$

where τ is the retardation/relaxation time constant. Coherently to what was presented in Section 4.1, R is related to the elastic parameter. The application to stress relaxation was developed by applying in a constitutive law governed by the Boltzmann's principle, presented in equation 4.45, resulting in equation 4.84.

$$\sigma(t) = \frac{c_\beta}{\Gamma(1-\beta)} \int_0^t (t-\bar{t})^{-\beta} \frac{d\varepsilon(\bar{t})}{d\bar{t}} d\bar{t} = c_\beta \left({}_c D_{0^+}^\beta \varepsilon \right)(t) \tag{4.84}$$

$\left({}_c D_{0^+}^\beta \varepsilon \right)(t)$ is the Caputo's fractional derivative, defined previously in equation 4.80. It is seen that the kernel of this convolutional integral is integral is of power law type. A kernel of exponential type would lead to an ordinary differential equation. Due to the fact the kernel is of power law type, a fractional derivative equation is constituted. Also according with Paola et al. (2011), equation 4.84 represents an interpolation between a purely elastic behaviour, assuming $\beta = 0$, and a purely viscous behaviour, where $\beta = 1$ is assumed. A fractional derivative assuming a fractional value of β, so that $0 < \beta < 1$, is capable to represent accurately a viscoelastic behaviour, by combining behaviours of a spring and a dashpot.

Interestingly, Paola et al. (2011) mentioned the facility of use related to fractional derivatives. Only two parameters are needed to be determined, constituting a simple formalisation. The authors suggested the replacement of combinations of Maxwell and Voigt-Kelvin elements, by fractional derivatives, constituted by Caputo's derivative, being based on convolution integrals with a power law kernel. Traditional creep and relaxation models are dependent of several parameters.

An additional fractional derivative, proposed by Gr*ü*nwald-Letnikov was mentioned by Ribeiro et al. (2021). A derivative of an integer order n is then introduced in equation 4.85.

$$\frac{d^n f(t)}{dt^n} = \lim_{h \to 0} \frac{1}{h^n} \sum_{k=0}^{n} (-1)^n \binom{n}{k} f(t-kh) \tag{4.85}$$

where:

$$\binom{n}{k} = \frac{n(n-1)(n-2)\dots(n-k+1)}{k!} \tag{4.86}$$

By replacing the integer order n by a fractional order α, the corresponding fractional derivative is obtained:

$${}_a^{GL}D_t^\alpha f(t) = \lim_{h \to 0} \frac{1}{h^\alpha} \sum_{k=0}^{\frac{t-a}{h}} (-1)^r \binom{\alpha}{k} f(t-kh)\,,\ t > a \tag{4.87}$$

where:

$$\binom{\alpha}{k} = \frac{\Gamma(\alpha+1)}{\Gamma(k+1)\Gamma(\alpha-k+1)} \tag{4.88}$$

whose fractional derivative is calculated using all the values of the function in the interval $[a,t]$. It is mentioned in the literature that $f(t)$ must be continuous with all the derivatives up to the integer part of fractional order (including $t=0$).

Expeditiously, Ribeiro et al. (2021), presented constitutive equations for creep and relaxation. By considering equations 4.81 and 4.82, equations 4.89 and 4.90 are derived, for creep and relaxation, respectively.

$$\varepsilon(t) = \int_0^t D(t-\tau)\, d\sigma(\tau) = \int_0^t D(t-\tau)\dot{\sigma}(\tau)\, d\tau \tag{4.89}$$

$$\sigma(t) = \int_0^t E(t-\tau)\, d\varepsilon(\tau) = \int_0^t E(t-\tau)\dot{\varepsilon}(\tau)\, d\tau \tag{4.90}$$

Also in this study, presented by Ribeiro et al. (2021), creep curves were derived successfully, with errors bellow 1%, for both concrete and polypropylene (PP). As conclusions, the authors mentioned that the fractional calculus is not currently used in structural applications. The main reasons are related with the physical interpretation of the quantities involved in fractional derivatives, and also the lack of knowledge in the subject. Recent literature is being developed on the subject of fractional calculus for current applications. Hristov (2022) presented a chapter investigating modern fractional calculus using Prony's series, specialising on rheological models with Caputo-Fabrizio operator. A fractional model with one single element was capable to reproduce the creep behaviour in two distinct materials, showing an improved accuracy when compared to traditional creep models with complex spring-dashpots associations.

This section presented additional constitutive equations that can be applied for characterisation of the representative behaviour under creep or stress relaxation, by the calculation of corresponding stress and strain states. Most of those models were successfully applied in the current state-of-art. The trend, nowadays, is to derive more realistic constitutive equations being capable to model several phenomena as the finite loading rate, at the instant corresponding to the load application. Fractional derivatives have also being used, specially in polymers, in order to improve the accuracy, in accordance to the experimental data. The proposed models are important for numerical applications, as the scripting of subroutines, embedded in FE models, for the representation of creep and stress relaxation behaviours. Nevertheless, more effort in research must be done in not only to characterise the stress/strain states of materials numerically, considering creep and relaxation, but also to characterise the fracture behaviour, developing cohesive zone models. Some laws, under the subject of continuum fracture mechanics are found in the literature, as demonstrated in Section 4.2. However, very few studies mentioned or proposed cohesive zone models for creep and relaxation, especially, for bonded joints and repairs.

4.2 Creep Crack Growth Prediction

Adhesively bonded joints and repairs are exposed to several mechanical behaviours associated to static and dynamic loads. Within static loads, creep or stress relaxation phenomena are very common in real engineering applications. Since adhesives present a ductile behaviour, they are prone to creep and relaxation even at ambient temperatures. Constitutive models, characterising the stress/strain states, are reviewed in the literature as presented in Section 4.1. Nevertheless, few studies analysed phenomena related with creep/relaxation crack growth, presenting numerical models. Only theoretical developments are demonstrated in the literature, some of the authors presented power laws, relating the crack growth rate with a parameter analogous to the J-integral, called C^*, that comes from energetic principles (Nikbin et al., 1984), as the classical continuum fracture mechanics suggests.

Cohesive zone models have been widely applied in order to predict the damage growth, specially in adhesively bonded joints and repairs. Although, these models have been only applied to static (Campilho et al., 2007; de Moura et al., 2008a) and fatigue (de Moura and Gonçalves, 2015; Moreira et al., 2020b) cases. In the literature, the application of creep crack growth by cohesive zone modelling is not clearly proved. Only theoretical backgrounds are presented (Elmukashfi and Cocks, 2017, 2021). There is the need to convert these theoretical backgrounds to numerical applications, employing CZM, properly.

In fatigue, Paris law can be used to calculate the crack growth rate, being incorporated in a cohesive damage model (Moreira, 2021). In creep and stress relaxation, an analogy can be done, using power laws presented in the literature, relating the crack growth rate with C^*. In this way, a cohesive damage model can be defined, whose properties are only material dependent, modelling the corresponding degradation phenomenon in a continuous manner, as suggested in the literature (Elmukashfi and Cocks, 2017).

This section is crucial for this chapter: a way of converting the theoretical work developed under the subject of continuum fracture mechanics is reviewed, in order to stablish novel laws with CZM applications. Current cohesive zone models are reviewed, even for other mechanical behaviours, as fatigue, in Section 4.2.1. Theoretical background on predicting the creep crack growth rate is analysed and interpreted in Section 4.2.2. Finally, the fundaments for the development of cohesive zone models for creep/relaxation applications are presented in Section 4.2.3.

4.2.1 Cohesive Zone Modelling (CZM)

Elmukashfi and Cocks (2017) mentioned the origin of CZM, referring works developed by Dugdale (1960) and Barenblatt (1962), whose first application in a FE environment was demonstrated by Hillerborg et al. (1976).

Recent studies have been formulating and applying cohesive zone models, incorporated in FE models, in order to simulate adhesively bonded joints and repairs. There are different types of cohesive damage laws, which are triangular, linear-exponential or trapezoidal. Figure 4.9 shows corresponding shapes.

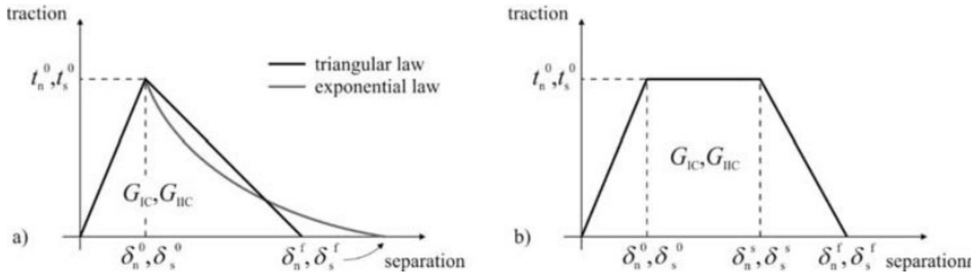

Figure 4.9: Shape of the cohesive damage laws available in the literature (Fernandes and Campilho, 2016): (a) triangular and linear-exponential, (b) trapezoidal.

Fernandes and Campilho (2016) analysed these three different laws, being incorporated in ABAQUS®, investigating what was the most appropriate law to evaluate the tensile behaviour in adhesive joints for three different adhesives: ARALDITE® AV138, ARALDITE® 2015, and SIKAFORCE® 7752. The stiffest adhesive, which is ARALDITE® AV138 is correctly modelled with any cohesive damage law, while more ductile adhesives, such as ARALDITE® 2015, and SIKAFORCE® 7752, are precisely modelled with a trapezoidal law. This study reported an excessive softening in initial stages of damage, resulting in loss of accuracy, while using linear-exponential laws. For these same laws, the obtained strength values were under predicted.

Campilho et al. (2007) described a cohesive zone model applied to the analysis of the tensile behaviour of CFRP single-strap repairs. The authors applied a trapezoidal law, since a ductile adhesive was considered. Indeed, the constitutive relation while loading, and before damage onset, is governed as follows:

$$\sigma = \mathbf{E}\delta_{\mathbf{r}} \tag{4.91}$$

where **E** is a stiffness diagonal matrix. After the *plateau* verified in the trapezoidal law, presented in Figure 4.9, the materials starts to soft. Consequently, a damage parameter should be included in the formulation. The constitutive relation between stresses and strains is then modified, resulting in what is presented in equation 4.92.

$$\sigma = (\mathbf{I} - \mathbf{D})\,\mathbf{E}\delta_{\mathbf{r}} \tag{4.92}$$

I is identified as the identity matrix and **D** is a diagonal matrix containing damage parameters (d_i). In the *plateau* region, those are defined in equation 4.93.

$$d_i = 1 - \frac{\delta_{1,i}}{\delta_i} \tag{4.93}$$

$\delta_{1,i}$ corresponds to the first inflexion point in the *plateau* region, and δ_i is the current relative displacement. The index $_i$ corresponds to the mode type: i =I,II. In the softening part, i.e. when the material is properly degraded, the damage parameter is given as follows:

$$d_i = 1 - \frac{\delta_{1,i}\left(\delta_{u,i} - \delta_i\right)}{\delta_i\left(\delta_{u,i} - \delta_{2,i}\right)} \tag{4.94}$$

where $\delta_{2,i}$ corresponds to the second inflexion point in the trapezoidal law. $\delta_{u,i}$ is the maximum relative displacement, and can be obtained from the critical fracture energy in the respective mode, G_{ic}. This fracture energy is defined as the area under the softening curve, so that:

$$G_{ic} = \frac{\sigma_{u,i}}{2}\left(\delta_{2,i} - \delta_{1,i} + \delta_{u,i}\right) \tag{4.95}$$

where $\sigma_{u,i}$ is the local strength, which, considering a mixed-mode loading, is defined a quadratic stress criterion:

$$\begin{cases} \left(\frac{\sigma_I}{\sigma_{u,I}}\right)^2 + \left(\frac{\sigma_{II}}{\sigma_{u,II}}\right)^2 = 1 \ , \ \sigma_I > 0 \\ \sigma_{II} = \sigma_{u,II} \ , \ \sigma_I \leq 0 \end{cases} \tag{4.96}$$

where σ_I and σ_{II} represent stresses in modes I and II, respectively. In the same manner, a quadratic criterion is established to the relative displacements, so that:

$$\left(\frac{\delta_{1m,I}}{\sigma_{1,I}}\right)^2 + \left(\frac{\sigma_{1m,II}}{\sigma_{1,II}}\right)^2 = 1 \tag{4.97}$$

where $\delta_{1m,I}$ and $\delta_{1m,II}$ are relative displacements corresponding to damage initiation, for both modes I and II, respectively. The mixed-mode equivalent relative displacement is then defined in equation 4.98.

$$\delta_m = \sqrt{\delta_I^2 + \delta_{II}^2} \tag{4.98}$$

In this stage, the mixed-mode ratio, β_i, is introduced in equation 4.99.

$$\beta_i = \frac{\delta_i}{\delta_I} \tag{4.99}$$

With this formulation, the equivalent relative displacement corresponding to the damage initiation, can be obtained by the following expression:

$$\delta_{1m} = \delta_{1,I}\delta_{1,II}\sqrt{\frac{1+\beta_{II}^2}{\delta_{1,II}^2 + \beta_{II}^2\delta_{1,I}^2}} \tag{4.100}$$

where at each mode, it is defined as follows:

$$\delta_{1m,i} = \frac{\beta_i \delta_{1,I}\delta_{1,II}}{\sqrt{\delta_{1,II}^2 + \beta_{II}^2\delta_{1,I}^2}} \tag{4.101}$$

The relative displacement corresponding to the softening onset is defined through a quadratic criterion, similar to equation 4.97, being expressed in equation 4.102.

$$\left(\frac{\delta_{2m,I}}{\sigma_{2,I}}\right)^2 + \left(\frac{\sigma_{2m,II}}{\sigma_{2,II}}\right)^2 = 1 \tag{4.102}$$

$\delta_{2m,i}$ (i = I,II) are the relative displacements, corresponding to the softening onset, for each mode, which can be obtained as follows:

$$\delta_{2m,i} = \frac{\beta_i \delta_{2,I} \delta_{2,II}}{\delta_{2,II}^2 + \beta_{II}^2 \delta_{2,I}^2} \tag{4.103}$$

The equivalent component, δ_{2m} is then obtained in equation 4.104.

$$\delta_{2m} = \delta_{2,I} \delta_{2,II} \sqrt{\frac{1 + \beta_{II}^2}{\delta_{2,II}^2 + \beta_{II}^2 \delta_{2,I}^2}} \tag{4.104}$$

As stresses and displacements are defined through a quadratic formulation, a linear fracture energetic formulation is considered, as presented in equation 4.105.

$$\frac{G_I}{G_{Ic}} + \frac{G_{II}}{G_{IIc}} = 1 \tag{4.105}$$

This equation constitutes a failure criterion. The energy released in each mode (G_i, i = I,II) is obtained as follows, considering the trapezoid law portrayed in Figure 4.9:

$$G_i = \frac{\sigma_{um,i}}{2} \left(\delta_{2m,i} - \delta_{1m,i} + \delta_{um,i} \right) \tag{4.106}$$

It is possible to combine equations 4.95, 4.105, and 4.106, obtaining the ultimate mixed-mode relative displacement, δ_{um}, being written as:

$$\delta_{um} = \frac{2 G_{Ic} G_{IIc} \left(1 + \beta_{II}^2\right) - \delta_{1m} \left(\delta_{2m} - \delta_{1m}\right) \left(e_I G_{IIc} + \beta_{II}^2 e_{II} G_{Ic}\right)}{\delta_{1m} \sqrt{1 + \beta_{II}^2} \left(e_I G_{IIc} + \beta_{II}^2 e_{II} G_{Ic}\right)} \tag{4.107}$$

where e_i (i = I,II) are parameters of the aforementioned stiffness matrix, **E**. Components in each mode, $\delta_{um,i}$ (i = I,II), are obtained by combining equations 4.98, 4.99, and 4.107, resulting in equation 4.108.

$$\delta_{um,i} = \beta_i \frac{2 G_{Ic} G_{IIc} \left(1 + \beta_{II}^2\right) - \delta_{1m} \left(\delta_{2m} - \delta_{1m}\right) \left(e_I G_{IIc} + \beta_{II}^2 e_{II} G_{Ic}\right)}{\delta_{1m} \sqrt{1 + \beta_{II}^2} \left(e_I G_{IIc} + \beta_{II}^2 e_{II} G_{Ic}\right)} \tag{4.108}$$

Equivalent components, represented as δ_{1m}, δ_{2m}, and δ_{um}, are used in equations 4.93 and 4.94, defining the damage parameters.

This formulation constitutes a CZM law, considering a trapezoidal shape, under mixed-mode loading, which is a generalised situation. It can be adapted for situations in pure mode loading and using a triangular shape.

As already mentioned, CZM laws for quasi-static conditions are well established in the literature, as what was already mentioned. Recent studies, as Moreira et al. (2020b), have adopted CZM laws considering fatigue loading. An additional simulation imposing dynamic conditions has to be taken into account, so that a new damage law is added. Moreira et al. (2020b) started by a chain rule, for a damage law formulation based on the Paris law:

$$\frac{d(d_f)}{dN} = \frac{d(d_f)}{d\delta_{m,k}} \frac{d\delta_{m,k}}{dA_{p,k}} \frac{dA_{p,k}}{dN} \tag{4.109}$$

where the index k stands for a given integration point. d_f is the fatigue damage parameter, N represents the number of cycles, and $A_{p,k}$ is the local damaged area. Moreira et al. (2020b) considered a triangular shape for the CZM law, in order to model the quasi-static component. Beyond their formulation, the first term of the equation 4.109 can be obtained from the second term of the equation 4.94, so that:

$$\frac{d(d_f)}{d\delta_{m,k}} = \frac{\delta_{um,k}\delta_{1m,k}}{(\delta_{um,k} - \delta_{1m,k})\,(\delta_{m,k})^2} \tag{4.110}$$

The second term of equation 4.109 is defined by assuming that the ratio between $A_{p,k}$ and the corresponding area related to a given integration point, $A_{t,k}$, is equal to the ratio between the dissipated energy in mixed-mode (G_{Td}) and the fracture energy also in mixed-mode (G_{Tc}), resulting in equation 4.111.

$$\frac{\delta_{m,k}}{dA_{p,k}} = \frac{\delta_{um,k} - \delta_{1m,k}}{A_{t,k}} \tag{4.111}$$

The evolution of the local damaged area, at a given integration point k, as a function of the number of cycles, N, is defined by the last term presented in equation 4.109. This term is formulated by a modified Paris law, as follows:

$$\frac{dA_{p,k}}{dN} = \frac{C_{1m,k} r_{w,k}}{\eta_{FPZ}} \left(\frac{\Delta G_{T,k}}{G_{Tc,k}}\right)^{C_{2m,k}} \tag{4.112}$$

where $r_{w,k}$ is the relative weight at the integration point k, and η_{FPZ} is the total number of integration points undertaking softening, involved in the fracture process zone. For a given mode ratio, $C_{1m,k}$ and $C_{2m,k}$ are fatigue parameters, being obtained by equations 4.113 and 4.114.

$$ln(C_{1m,k}) = ln(C_{1I}) + \frac{[ln(C_{1II}) - ln(C_{2II})]G_{II,k}}{G_{T,k}} \tag{4.113}$$

$$C_{2m,k} = C_{2I} + \frac{(C_{2II} - C_{2I})\,G_{II,k}}{G_{T,k}} \tag{4.114}$$

C_{1i} and C_{2i}, considering i = I,II, are fatigue parameters in pure mode loading. In this manner, the chain rule presented in equation 4.109 can then be expressed as follows:

$$\Delta d_f(\Delta N) = \frac{\delta^j_{um,k}\delta_{1m,k}C_{1m,k}r_{w,k}}{A_{t,k}\eta_{FPZ}\,(\delta_{m,k})^2} \left(\frac{\Delta G_{T,k}}{G_{Tc,k}}\right)^{C_{2m,k}} \Delta N \tag{4.115}$$

where ΔN is the cycle jump, and, according to the authors, it should be defined by the user so that accuracy and minimisation of the computational effort are conciliated. The calculated fatigue damage parameter, d_f, is included in the diagonal matrix **D**, adding damage effects to the damage corresponding to the quasi-static loading.

Analogously, a damage law for creep conditions can be found, for the implementation in CZM law. Theoretically, in the literature, creep damage laws are well established, as demonstrated in Section 4.2.2, but only beyond the continuum damage mechanics (CDM) concepts. Those formulations should be adapted and used in CZM laws, adding damage effects to quasi-static phenomena.

4.2.2 Theoretical Background on Creep Crack Growth

In the past century, Findley et al. (1976) and other authors have postulated constitutive laws, describing the creep behaviour as a function of the applied stress conditions. Nevertheless, few studies have explained mathematically the creep behaviour considering crack growth. Derived formulations are most of the times applicable to metallic materials. Proper research is needed in order to formulate the creep crack growth process in polymers, including adhesives.

Elmukashfi and Cocks (2017) mentioned that, during creep crack growth, the damage accumulates in the crack tip region, whose propagation occurs by meeting a given failure criteria. The authors described the creep fracture process, also called FPZ (fracture process zone), as follows:

1. A small-scale creep zone appears surrounded by an elastic medium.
2. Even if the primary creep zone is large, it is surrounded by the elastic medium.
3. The secondary creep zone appears inside the primary creep zone, but still being surrounded by the elastic medium.
4. Secondary creep zone continues to grow until it becomes dominant.

Analogous to the J-integral, Elmukashfi and Cocks (2017) presents the C^*-integral, which is also path-independent. Equation 4.116 defines this parameter:

$$C^* = \int_\Gamma W dx_2 - T_i \frac{\partial \dot{u}_i}{\partial x_1} ds \tag{4.116}$$

where Γ is an arbitrary contour surrounding the crack tip, with unit outward normal n_i. T_i is defined as the traction considering ds and the displacement rate $\dot{u}_i$, being given as $T_i = \sigma_{ij} n_j$.

This parameter, C^*, is proposed by Nikbin et al. (1984), while defining mathematically the damage rate due to creep conditions. The author started by defining the creep strain, constitutively, by the following power law:

$$\frac{\dot{\varepsilon}}{\varepsilon_0} = \left(\frac{\sigma}{\sigma_0} \right)^n \tag{4.117}$$

where ε_0 and σ_0 are designated in the literature as a reference strain/stress state. n is the power law exponent. All those three constants are determined empirically.

By considering that C^* is constant during secondary creep, which is not necessarily valid for ductile polymers, Nikbin et al. (1984) used that parameter to characterise the stress and strain rate fields around a crack tip, so that:

$$\frac{\sigma_{ij}}{\sigma_0} = \left(\frac{C^*}{I_n \sigma_0 \dot{\varepsilon}_0 r}\right)^{\frac{1}{n+1}} \tilde{\sigma}_{ij}(\theta, n) \tag{4.118}$$

where I_n is an empirical value that depends on the value of n, and it is presented in Hutchinson (1968). r is the radial position along the crack tip, and θ stands for the corresponding circumferential position. In practical terms, for metals, n can be defined as 3 for plane stress, and 4 for plane strain.

After the definition of the constitutive equations, and after including C^* in the localised stress state, the crack growth rate is then defined as:

$$\frac{da}{dt} = (n+1)\frac{\dot{\varepsilon}_0}{\varepsilon_f^*}\left(\frac{C^*}{I_n \sigma_0 \dot{\varepsilon}_0}\right)^{\frac{n}{n+1}} r_c^{\frac{1}{n+1}} \tag{4.119}$$

where r_c is the FPZ size, and ε_f^* is the empirically determined strain to failure.

This formulation of crack growth rate is for secondary creep, not including the structural damage state, D, not considering also the time to failure (t_r). In order to include primary and tertiary creep, Nikbin et al. (1984) proposed a linear method, that considers a fictitious constant creep strain rate ($\dot{\varepsilon}_A$), in order to determine the strain and time to failure: ε_f and t_f, respectively. This process is portrayed in Figure 4.10.

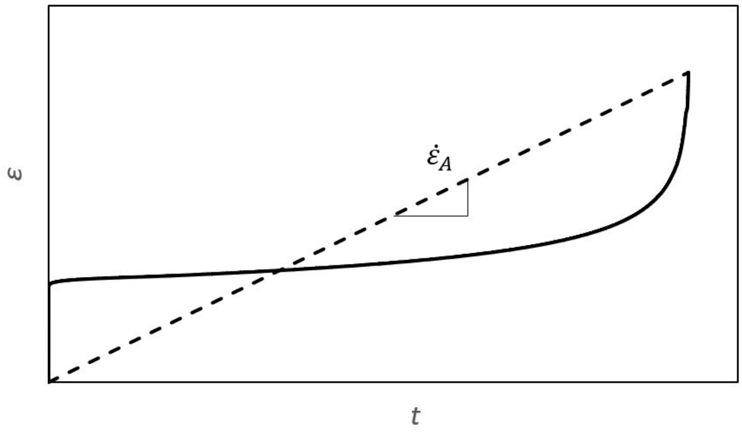

Figure 4.10: Strain and time to failure determination method considered in Nikbin et al. (1984).

Despite of the inaccuracy associated with this method, it can be useful to determine the strain and time to failure, when the analytical methods are not capable of modelling primary and tertiary creep. $\dot{\varepsilon}_A$ can be defined by equation 4.120, following the linearity represented in Figure 4.10.

$$\dot{\varepsilon}_A = \frac{\varepsilon_f}{t_r} \tag{4.120}$$

By considering the aforementioned constitutive equation, governed by a power law, $\dot{\varepsilon}_A$ can be then expressed as presented in equation 4.121.

$$\dot{\varepsilon}_A = \dot{\varepsilon}_0 \left(\frac{\sigma}{\sigma_0} \right)^n \tag{4.121}$$

$\dot{\varepsilon}_0$ is an empirical creep strain rate taken as a reference.

A stress degradation is considered in methods presented by Nikbin et al. (1984), where Figure 4.11 represents the degradation evolution.

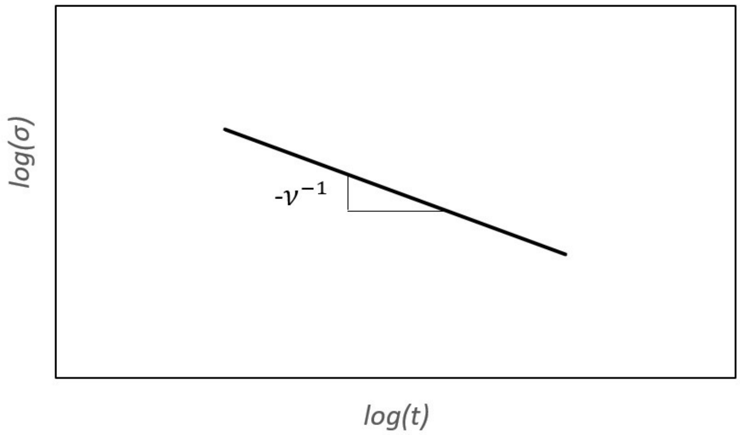

Figure 4.11: Stress degradation during creep, considered in Nikbin et al. (1984).

In this way, the time to failure due to creep conditions is governed as follows:

$$t_r = \frac{D}{\sigma^\nu} \tag{4.122}$$

where D and ν are material constants. By substituting equations 4.121 and 4.122 into equation 4.120, it is possible to define strain to failure as follows:

$$\varepsilon_f = \dot{\varepsilon}_0 \left(\frac{D\sigma^{(n-\nu)}}{\sigma_0} \right)^n \tag{4.123}$$

In this way, it is possible to define the strain and time to failure as a function of the stress state and degradation evolution. Concepts of ε_f and t_r can be used to define failure criteria, being exposed in equations 4.124 and 4.125, respectively.

$$\int \frac{d\varepsilon_{ij}}{\varepsilon_f} = 1 \tag{4.124}$$

$$\int \frac{dt}{t_r} = 1 \tag{4.125}$$

Failure criteria are based in the damage model presented by Rabotnov (1969). Substituting

4.118 and 4.122 into 4.125, the following criteria is obtained:

$$\int_{r=r_c}^{r=0}\left(\frac{C^*}{I_n\sigma_0\dot{\varepsilon}_0 r}\right)^{\frac{\nu}{n+1}}\frac{1}{D}\left(\sigma_0\tilde{\sigma}_{ij}\right)^{\nu}\frac{dt}{dr}dr=1 \tag{4.126}$$

Knowing that $dr/dt = da/dt$, and solving the equation 4.126, the equation for crack propagation can be restated as follows:

$$\frac{da}{dt}=\left(\frac{C^*}{I_n\sigma_0\dot{\varepsilon}_0}\right)^{\frac{\nu}{n+1}}\frac{\sigma_0^{\nu}}{D}\frac{n+1}{n+1-\nu}r_c^{\frac{n+1-\nu}{n+1}} \tag{4.127}$$

This damage model is considered by the principle of stress degradation, but it still depends on C^*, which is a parameter intrinsically related with analytical formulations associated with continuum fracture mechanics, not being completely appropriate for numerical implementations, using cohesive damage models. Also other studies, as the ones presented by Yatomi et al. (2003) and Yatomi and Tabuchi (2010), used this model of Nikbin et al. (1984), known as NSW, in computational applications. Computational fracture mechanics is used, but not applying CZM.

In the literature, damage-based models have been derived, but widely for metallic materials. There are three main damage models to consider: Kachanov-Rabotnov (Rabotnov, 1969), already used by Nikbin et al. (1984), Sin-Hyperbolic, and Liu-Murakami.

4.2.2.1 Kachanov-Rabotnov Damage Law

Nikbin et al. (1984) simply exposed the derivation of the Kachanov-Rabotnov damage law. Rabotnov (1969), extended the Kachanov model, including the degradation state, and started by the definition of the constitutive equation which includes a damage variable, D, describing the material degradation induced by the presence of cracks, cavities, and voids, resulting in an amplification of stress which is a consequence of the reduction of the net-area. Presenting means for obtaining the creep strain rate, equation 4.128 is presented.

$$\dot{\varepsilon}=\dot{\varepsilon}_0\left(\frac{\sigma}{\sigma_0(1-D)}\right)^n \tag{4.128}$$

Assuming the criteria associated with equation 4.125, and knowing that $dD = \dot{D}dt$, Rabotnov (1969) derived the following equation that allows the definition of damage rate ($\dot{D}$):

$$dD=\frac{1}{(\theta+1)t_r(1-D)^{\theta}}dt \tag{4.129}$$

where θ is the exponent regulating damage evolution.

In this way, the damage growth rate ($\dot{D}$) is then obtained in equation 4.130.

$$\dot{D}=\frac{\dot{D}_0}{(1-D)^{\theta}}\left(\frac{\sigma}{\sigma_0}\right)^n \tag{4.130}$$

where $\dot{D}_0$ is an empirically determined damage rate taken as a reference.

In this formulation, it was possible to derive the expression that allows the determination of the time to failure, being exposed in equation 4.131.

$$t_r = \left[(\theta+1)\dot{D}_0 \left(\frac{\sigma}{\sigma_0} \right)^n \right]^{-1} \tag{4.131}$$

This law has been widely adapted for particular cases in the literature. Hayhurst et al. (1984) started by presenting the aforementioned laws applied in uniaxial loading. The authors mentioned the importance of modelling, not only secondary creep fracture behaviour, but also the tertiary one. They also emphasised that both creep strain rate and damage rate are functions of the local stress state, and corresponding degradation. So, any law describing the damage rate should be based in those assumptions. Instead of using empirically determined reference stress states and strain rates, σ_0 and $\dot{\varepsilon}_0$ respectively, or even reference damage rates, $\dot{D}_0$, the authors proposed the use of material constants. In this way, creep strain rate is then defined constitutively as follows:

$$\dot{\varepsilon} = A \left(\frac{\sigma}{(1-D)} \right)^n \tag{4.132}$$

where the corresponding damage rate is defined in equation 4.133.

$$\dot{D} = \frac{M\sigma^{\psi}}{(1-D)^{\theta}} \tag{4.133}$$

In this case, A, M, n, ψ, and θ, are all defined as material constants, being still determined experimentally, where A and n are known as Norton power law constants in the literature.

Time to failure was also derived by Hayhurst et al. (1984) and it was presented as follows:

$$t_r = \frac{\sigma^{-\psi}}{M(1+\theta)} \tag{4.134}$$

More recently, Bouvard et al. (2009) were inspired in the Kachanov-Rabotnov law to derive a creep damage model. The authors developed a cohesive zone model for the prediction of crack growth under creep-fatigue in single crystal superalloys, considering pre-cracked specimens. The model started to be calibrated in pure fatigue loading, and an extension is done in order to include creep loading, but only *"a posteriori"*. Pure creep was not analysed in this study, but still a creep damage law with good numerical potential is presented. Using a nomenclature coherent with what was presented before, Bouvard et al. (2009) proposed the creep damage law exposed in equation 4.135.

$$\dot{D} = (1-D)^{-\theta} \left\langle \frac{\sigma - T_c}{C} \right\rangle^n \tag{4.135}$$

In this case, σ is defined as the equivalent stress considering a mixed-mode loading I+II. T_c is a traction threshold for creep damage. C, θ, and n are defined as empirical material constants. Macaulay brackets ("$\langle\rangle$") are used, setting a null damage rate under compressive stress states, which is coherent with the already known CZM formulations.

Sun et al. (2012) developed a cohesive damage model to predict grain boundary crack growth in nickel-based superalloys, considering creep-fatigue loading. While modelling creep damage, the authors proposed the use of an expression based on the Kachanov-Rabotnov law, also referencing Bouvard et al. (2009). In fact, the law presented by Bouvard et al. (2009) only imposed degradation in a term that has mathematical origins from the Kachanov-Rabotnov model, as presented in equation 4.135. In this case, Sun et al. (2012) proposed the degradation of the stress, even if that stress is still degraded as a consequence of the degradation of stiffness, typical of CZM. In this way, the damage rate is then expressed as demonstrated in equation 4.136.

$$\dot{D} = \left\langle \frac{\sigma - (1-D)T_c}{T_0} \right\rangle^n \tag{4.136}$$

Once again, the Macaulay brackets, "$\langle\rangle$", are ensuring that no damage occurs in a compressive stress state. T_c is also defined as a traction threshold, so that if $\sigma < T_c$, no creep damage occurs. In this case, T_0 is defined as a reference stress, analogous to the material property C defined by Bouvard et al. (2009) in equation 4.135.

Also for creep-fatigue, Diel and Huber (2017) adapted the Kachanov-Rabotnov damage law for the application in cellular composites with an epoxy matrix and glass foam granules. The authors used the same expression presented in equation 4.133 for the damage rate. In a CDM environment, the authors managed to describe the determination of the parameters M, ψ, and θ.

Diel and Huber (2017) mentioned that the nonlinear damage accumulation is described if the damage exponent, θ, is a function of stress state, which was already postulated in the past by Lemaitre and Chaboche (1975). From several tensile tests, at different stress levels, it was possible to derive an expression for the damage exponent as a function of stress, resulting in a linear relation of the type presented in equation 4.137.

$$\theta = \alpha - \beta \frac{\sigma}{\sigma_0} \tag{4.137}$$

Here, α and β are empirical constants. With this relation, it is seen that the damage exponent decreases along the increase of the stress state. For the material studied by Diel and Huber (2017), it was seen that $\alpha = 8.0$ and $\beta = 4.5$.

Regarding the stress exponent, n, a failure condition assuming half of the degradation can be considered, however it was intended the empirical nature of this parameter. For the analysed material, it was found that $n = 40$ provided results coherent with experimental data, considering the combination of creep with fatigue.

According to Diel and Huber (2017), the other Norton power law constant, A, determines the horizontal position of the creep strength line, i.e. governs the secondary creep slope. It was mentioned by the authors the interconnection between A and n. An iterative process should be done until a pair of A and n is found to be coherent with experimental results, expressing the empirical nature of this process. For cellular composites, a value of 2.7×10^{-29} was found for A.

Haque and Maurice (2019) applied the Kachanov-Rabotnov damage law while modelling creep damage in 304 stainless steel at temperatures of 600° and 700°. This study demonstrates the limitations of the Kachanov-Rabotnov, despite of the good accuracy achieved. It was mentioned that the prediction of minimum creep strain, damage evolution, and rupture is deficient using the Kachanov-Rabotnov damage law, exposed in equation 4.133. In addition, the authors found some cases where the critical damage was lower than unity, which constitutes a violation of CDM concepts.

After presenting equation 4.133 as the applicable model to describe the creep damage rate, Haque and Maurice (2019) demonstrated expressions for time to failure and critical damage (D_r), being presented in equations 4.138 and 4.139, respectively.

$$t_r = \frac{1-(1-D)^{\theta+1}}{(\theta+1)M\sigma^{\psi}} \tag{4.138}$$

$$D_r = 1-[1-(\theta+1)M\sigma^{\psi}t]^{\frac{1}{\theta+1}} \tag{4.139}$$

Haque and Maurice (2019) mentioned M as a tertiary creep constant that can be calculated manipulating equation 4.138, so that obtaining equation 4.140

$$M = \frac{1-(1-D_r)^{\theta+1}}{(\theta+1)\sigma^{\psi}t_r} \tag{4.140}$$

If $D_r = 1$, the following equation results:

$$M = \frac{1}{(\theta+1)\sigma^{\psi}t_r} \tag{4.141}$$

Even by presenting equations 4.138, 4.139, 4.140, and 4.141, it is mentioned that difficulty for the determination of damage constants associated with tertiary creep. In order to overcome those limitations, two models are proposed: strain approach and damage approach.

In the strain approach, damage evolution is included into creep strain rate. In this way, damage constants can be determined through an experimental creep strain. This approach considers the creep strain as follows:

$$\varepsilon = \frac{A(\theta+1)}{1+\theta-n}\left[t\left(\frac{\sigma}{\tau}\right)^{n} - t_r\left(\frac{\sigma}{\tau}\right)^{n} + t_r\sigma^{n}\right] \quad \tau = \left(1-\frac{t}{t_r}\right)^{\frac{1}{1+\theta}} \tag{4.142}$$

eliminating M and ψ from the formulation, that would be associated with tertiary creep.

In the damage approach, an analytical damage is considered to calibrate the damage rate equation. This analytical damage is calculated from the application of the finite difference on creep strain rate. Haque and Maurice (2019) proposed the manipulation of equation 4.132, obtaining the analytical damage, so that:

$$D(\dot{\varepsilon}_{cr}) = 1-\sigma\left(\frac{\dot{\varepsilon}_{cr}}{A}\right)^{n} \tag{4.143}$$

where $\dot{\varepsilon}_{cr}$ constitutes a creep rate determined experimentally. Introducing equation 4.140 into 4.139, an expression for D is obtained, being presented in equation 4.144.

$$D(t) = 1 - \left[\frac{t}{t_r}\left((1-D_r)^{\theta+1} - 1\right) + 1\right]^{\frac{1}{\theta+1}} \tag{4.144}$$

Here, this expression is presented under the absence of M and ψ, overcoming the limitation associated with the prediction of tertiary creep. In this way, the only unknown is the damage exponent, θ.

Other limitations associated with the Kachanov-Rabotnov damage law are emphasised by Haque and Maurice (2019). The authors mentioned the follow:

- the local CDM approach associated with the Kachanov-Rabotnov model shows stress sensitivity;
- a local cross-sectional area reduction is used to account for effective stress amplification during damage, while, in reality, microscopic damage gives a little loss of effective area before crack propagation;
- possibility over-predicted damage rates (there are cases reporting damage rates about 90% higher in comparison to real values);
- critical damage values can be significantly lower than unity, which could not be valid under a CDM environment.

Also about limitations associated with the Kachanov-Rabotnov damage model, Calì et al. (2010) reported numerical instabilities associated with the appearance of the term $(1-D)$ in the denominator of the Kachanov-Rabotnov law, presented in equation 4.133. The authors used a maximum damage of 0.9, instead of 1, which can be unrealistic in terms of fracture mechanics, and can be physically questionable. In addition, difficulties achieving convergence were also reported, so that very small increments were used having sufficient computational stability allowing to achieve satisfactory results. The convergence velocity associated with the Norton-Bailey constitutive power law was also referred as satisfactory, describing the steady creep state.

Haque and Maurice (2019) applied other damage laws, such as the Liu-Murakami, which is discussed in 4.2.2.2.

4.2.2.2 Liu-Murakami Damage Law

Calì et al. (2010) and Haque and Maurice (2019) mentioned limitations associated with the Kachanov-Rabotnov models, so that Haque and Maurice (2019) presented alternatives, such as the Liu-Murakami damage model (Murakami et al., 2000), which is based on an exponential damage evolution.

Murakami et al. (2000) emphasised the singular stress sensitivity at the crack tip, associated with the Kachanov-Rabotnov law, demonstrating an additional limitation. The authors proposed a modified law, known as Liu-Murakami law, expressing damage with an exponential evolution, improving the singular stress sensitivity at the crack tip. Equation 4.145 was postulated.

$$\dot{D} = A\frac{1-e^{-\phi}}{\phi}(\sigma_D)^{-p}e^{\phi D} \tag{4.145}$$

A, p, and ϕ are defined as empirical material constants. σ_D is intended as a degraded stress, similar to what is proposed by Sun et al. (2012) when adapted a Kachanov-Rabotnov model. Murakami et al. (2000) showed examples where $A = 1.38 \times 10^{-10}$, $p = 4.42$, and $\phi = 2.0$. Those constants were found for a metallic material.

Wu et al. (2022) was able to solve equation 4.145, obtaining an analytical expression translating the damage as a function of time, obtaining equation 4.146.

$$D = -\frac{ln(1-A(1-e^{\phi})\sigma^{-p}(t-t_0))}{\phi} \tag{4.146}$$

t_0 is the instant of time when damage initiates. In this way, the authors were also able to find an expression to obtain the time to failure (t_r):

$$t_r = \frac{\sigma^p}{A} + t_0 \tag{4.147}$$

Wu et al. (2022) applied successfully the Liu-Murakami damage model, being able to predict the three creep stages precisely, in high alumina bricks under high temperatures, demonstrating that this formulation has potential not only for applications involving metallic materials, but also using other material types, such as ceramics.

While applying a Liu-Murakami damage model, Haque and Maurice (2019) started by introducing the constitutive model associated to secondary creep by the so called McVetty equation, based in a sin-hyperbolic formulation, so that determining the minimum creep strain rate ($\dot{\varepsilon}_{min}$) being presented as follows:

$$\dot{\varepsilon}_{min} = Bsinh\left(\frac{\sigma}{\sigma_s}\right) \tag{4.148}$$

where this law is capable to fit the nonlinear bend which is possible to occur in the secondary creep stage. Haque and Maurice (2019) referred B, with units s^{-1}, as a creep coefficient, and σ_s, with units MPa, as a creep mechanism-transition stress. This sin-hyperbolic constitutive equation is usually integrated in the Liu-Murakami damage model. This same law is derived from the Prandtl-Garofalo law, exposed by Yousseff (2022).

Within a CDM environment, Haque and Maurice (2019) used three functions in order to include the prediction of tertiary creep, as well as determining creep rupture time and corresponding strain state. Following the same nomenclature, analogous to what had been previously described, the authors defined a damage variable, D, and coupled to a second viscous function, obtaining equation 4.149.

$$\dot{\varepsilon} = f(\sigma)g(T)h(D) \tag{4.149}$$

$h(D)$ function describes how the damage state influences creep strain rate. The authors then presented this function in order to a total creep strain rate ($\dot{\varepsilon}_{cr}$) so that:

$$h(D) = \frac{\dot{\varepsilon}_{cr}}{Bsinh\left(\frac{\sigma}{\sigma_s}\right)} \tag{4.150}$$

where $h(D)$ is proposed to be stated in equation 4.151.

$$h(D) = e^{\lambda D^p} \tag{4.151}$$

λ and p are dimensionless constants, which can be determined empirically. In this wa, the analytical damage variable is then written as a function of time:

$$D^* = \left\{\frac{1}{\lambda} ln\left[\frac{\dot{\varepsilon}_{cr}}{Bsinh\left(\frac{\sigma}{\sigma_s}\right)}\right]\right\}^{\frac{1}{p}} \tag{4.152}$$

At this stage, it is possible to define the final creep strain rate, being obtained in equation 4.153.

$$\dot{\varepsilon}_{final} = Bsinh\left(\frac{\sigma}{\sigma_s}\right) e^{\lambda} \tag{4.153}$$

At the end, the equation for the total creep strain rate is then derived:

$$\dot{\varepsilon}_{cr} = Bsinh\left(\frac{\sigma}{\sigma_s}\right) e^{\lambda D^p} \tag{4.154}$$

Other constitutive models can be employed, such as ones demonstrated by Sattar et al. (2023). Even constitutive relations presented in Section 4.1 can be used, being more appropriated for polymers. After establishing the constitutive relation, Haque and Maurice (2019) presented the following expression for the calculation of damage rate, based in the Liu-Murakami damage law, obtaining the equation 4.155.

$$\dot{D} = Q\frac{1-e^{-\phi}}{\phi} sinh\left(\frac{\sigma}{\sigma_t}\right)^{\chi} e^{\phi D} \tag{4.155}$$

Q, ϕ, χ, and σ_t are defined as material constants that can be determined empirically. The term $(1-e^{-\phi})/\phi$ is used to avoid undefined errors while integrating the damage evolution equation. Similar derivations were performed by Cano and Stewart (2020), intending ϕ as a constant that defines the damage trajectory, which can be determined as $\phi = ln(\dot{D}_f/\dot{D}_i)$, being a balance between the final and the initial damage rates. When equation 4.155 is solved, the damage evolution as a function of time is obtained, so that:

$$D = -\frac{1}{\phi} ln\left[1-(1-e^{-\phi})\frac{t}{t_r}\right] \tag{4.156}$$

where t_r is defined as rupture time, which is governed by equation 4.157.

$$t_r = \left[Qsinh\left(\frac{\sigma}{\sigma_t}\right)^{\chi} \right]^{-1} \tag{4.157}$$

The aforementioned formulations allow to model creep damage successfully, but most of the studies presented applications in metallic materials. Only Wu et al. (2022) were able to predict creep damage, using a Liu-Murakami based model, in ceramic materials, demonstrating that those formulations can be adapted for other situations not using metals. In addition, in most of the times, those models were applied in a CDM environment, instead of being implemented within a CZM environment. However, Calì et al. (2010) implemented a Kachanov-Rabotnov based model in a CZM approach, demonstrating pros and cons that are useful to establish new models, even for adhesive joints and repairs.

In this chapter, viscoelastic models presented in Section 4.1.1 are implemented as constitutive relations in the Kachanov-Rabotnov and Liu-Murakami damage laws, in order to derive expressions of the damage rate to apply in a CZM environment. The presence of rheological parameters on the laws translating damage rates, representing elastic and viscous effects, can adapt the Kachanov-Rabotnov and Liu-Murakami laws to use in polymers, including adhesives. The developed approaches are able to model the three stages of creep in adhesive joints.

4.2.3 Principles of CZM applied to Creep of Bonded Joints

CZM has been widely applied in order to model damage in bonded joints, computationally, for static loading conditions, and more recently, also for fatigue. For creep phenomena, very few studies are reported with applications of CZM laws, and most of them are for metallic structural applications (Calì et al., 2010). Bouvard et al. (2009) adapted a Kachanov-Rabotnov damage law for CZM applications, although it was applied to investigate creep, combined with fatigue, in single crystal superalloys. Also Sun et al. (2012) adapted a Kachanov-Rabotnov law, within a creep-fatigue environment, but with a successful implementation on the prediction of grain boundary interface de-cohesion in nickel-based superalloys. Applying another Kachanov-Rabotnov based law in a CZM approach, Li et al. (2017) studied the creep-fatigue phenomenon, predicting crack propagation in nickel-based superalloys under high temperatures.

The application of CZM to adhesively bonded joints is performed by Ciavarella et al. (2022), while modelling viscoelastic phenomena, but not creep, of zero degree peeling tape from a substrate. Satisfactory results were achieved, obtaining a fully analytical closed-form solution, and those were validated either numerically and experimentally. As conclusion, a CZM approach was established for this PSA (pressure-sensitive-adhesive) joint under peeling conditions.

Also analysing viscoelastic phenomena of bonded joints, instead of creep, Škec and Alfano (2022) performed an experimental-numerical study in order to investigate the effect of the loading rate in the fracture energy of DCB specimens. 24 experimental tests were performed, with loading rates from 0.1 to 5000 mm/min, demonstrating an increase on the fracture energy, with the increase in the loading rate. It would be expected, theoretically, from those results, a minimum value of fracture energy associated to a null loading rate, which is representative of creep conditions. Fractional viscoelastic laws were applied, within a CZM environment, demonstrating good correlation between numerical and experimental results. Nevertheless, the authors referred seven parameters to use, two of them being rate-dependent, showing the amount of tests needed, *"a priori"*, in order to perform numerical simulations. The importance of having a lower number of parameters, and with physical meaning, instead of being only empirical, was emphasised so that better numerical models can prevent higher amounts of experimental data needed. Associated limitations in relation with extrapolations outside the tested loading rate range are emphasised. Numerical errors can possibly occur. In addition, it was mentioned that the numerical model is capable of predicting the viscoelastic behaviour for a DCB at different loading rates between 0.1 and 5000 mm/min, not referring clearly the possibility to apply the same numerical model with the same parameters but to other geometries. In other words, the developed CZM approach is not only material dependent, but also geometrically dependent.

Studies developed by Neto et al. (2022c) were mentioned as being the first ones to apply a CZM approach in adhesively bonded joints, predicting creep crack growth. The authors exposed several studies in the literature, predicting the creep behaviour of bonded joints, but not using cohesive elements, so not predicting creep crack growth. It was also mentioned that no CZM approach was reported to apply in ENF samples, i.e. in pure mode II. Neto et al. (2022c) analysed ENF samples under creep conditions. The authors started by presenting two models for the calculation of the modified fracture energy in mode II (G_{II}), during creep loading. Considered laws are exposed in equations 4.158 and 4.159.

$$G_{II_c}(t,F) = z_1 g_1(t,F) + \ldots + z_m g_m(t,F) \tag{4.158}$$

$$G_{II_c}(t,F) = \left(\frac{1}{z_1}\right)(1.93z_1 + t)\left(1 - \frac{t}{720}\right)^{z_2}[z_3 F + z_4] \tag{4.159}$$

Equation 4.158 was called as a polynomial equation, and equation 4.159 was called as a mixed equation. In fact, the presence of constants of type z_m, and of functions of type $g_m(t,F)$ expose the empirical nature of equation 4.158. Also additional constants of type z_m appears in equation 4.159, whose assigned values come from experimental data. Both formulations are dependent on time (t) and loading conditions (F).

Results from the numerical model were reported and compared with experimental data provided in Neto et al. (2021). In the study developed by Neto et al. (2022c), also a creep test was performed to a ENF sample, with a load that corresponds to 70% of the maximum sustaining load in static conditions, for 24h. Figure 4.12 shows the errors related to the determination of G_{II_c}, when numerical and experimental results are compared.

In fact, it is observed, in general, a better behaviour associated with the mixed equation, presented in equation 4.159. This model is not dependent of functions $g_m(t,F)$, reducing the corresponding empirical nature, and dependency of time and loading conditions. It is notable that the

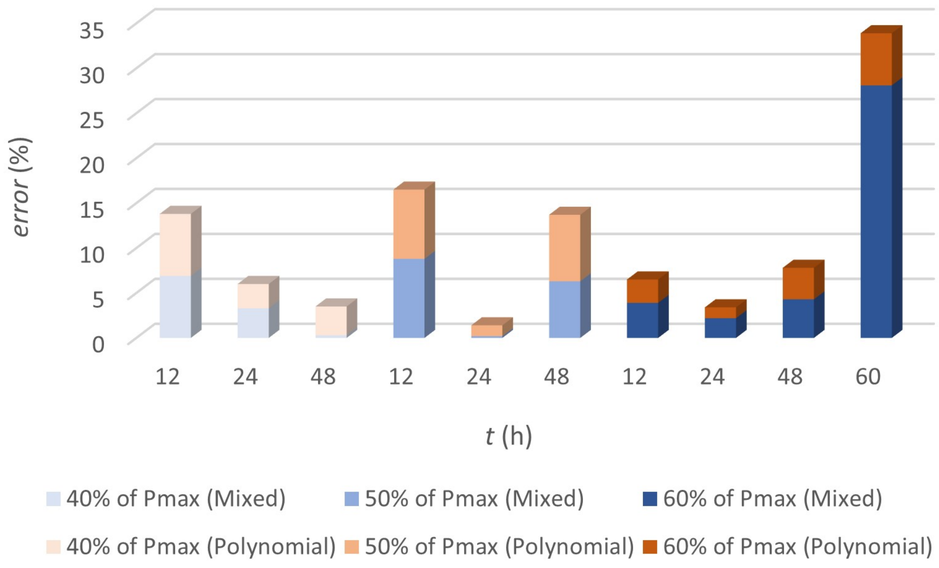

Figure 4.12: Errors in the determination of shear fracture energy: comparison between numerical and experimental results (data provided in Neto et al. (2022c)).

highest errors were registered for time conditions correspondent to 12h and 48h, which are the limits of the range of creep time imposed in experimental tests. The highest error was reported for a simulation imposing 60h of creep time. This is justified by the fact that this creep time is outside the range tested experimentally ([12h;48h]). This result indicates the empirical dependency of the models proposed in equations 4.158 and 4.159. In fact, there is not a defined tendency for error variations between different loading conditions, suggesting that the proposed models have a lower dependency on loading conditions, rather than in time conditions.

Ideally, a CZM approach embedded in a numerical model should be dependent only on material parameters, so that being flexible to different geometries, dimensions, time, and loading conditions. In addition, the developed numerical model was not capable to predict tertiary creep since the experimental creep tests were only carried out until the instant of time exactly before crack initiation.

Other study was presented by the same authors (Neto et al., 2022b), describing deeply the implementation of the CZM approach. Neto et al. (2022b) started by mentioning that creep effects are responsible for the modification of adhesive properties due to viscous flow that occurs in the adhesive layer resulting in viscous deformation. Within this statement, the degradation of fracture energy is proposed, in addition to the degradation of shear traction. It can also be justified by a stress redistribution, during creep, where the crack nucleation process is different when compared to the one possible to occur in static conditions. An empirical approach is suggested, applying methods described in Neto et al. (2022c), determining the residual fracture energy, due to creep, being function of time and load conditions. Consequently, a modification of the CZM law during creep phenomenon is proposed, being portrayed in Figure 4.13. It was emphasised by the authors that the displacement would never increase, under a constant applied load, if a conventional CZM was used, i.e., if the CZM law was maintained along the numerical simulation.

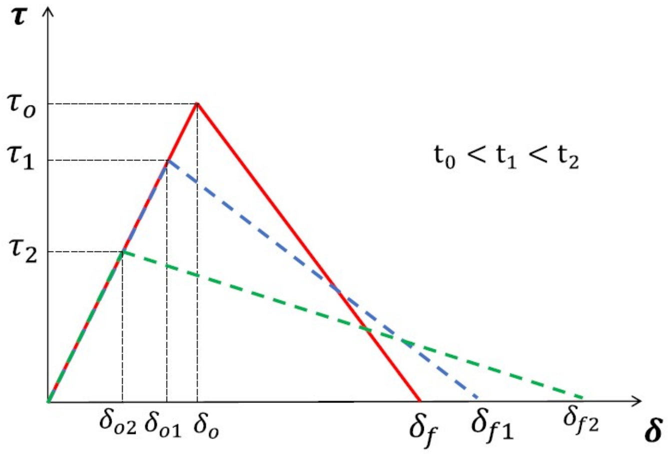

Figure 4.13: Degradation during phenomena of the CZM law (Neto et al., 2022b).

As it was mentioned in the study described previously (Neto et al., 2022c), the fracture energy depends on time and loading conditions, however, it is defined by the authors with a complete empirical formulation. In addition, the modification of the CZM law is dependent of two empirical constants, being defined as b and k. The numerical accuracy is strongly affected by the variation of those parameters. Consequently, the effectiveness of the considered numerical model is always dependent on experimental data. The modification of the shear fracture energy (G_{II_c}) was assessed experimentally by performing, in total, 9 tests with the following conditions: 40%, 50%, and 60% of the maximum sustaining load (P_{max}), and under creep times of 12h, 24h, and 48h. This resulted in 3 points of interpolation, obtaining the variation of G_{II_c} with creep time and load.

Consequently, this CZM formulation, and corresponding computational implementation, is very sensible to changes in the problem itself. If a situation where G_{II_c} has a value out of the range that was tested experimentally, the numerical accuracy decreases significantly. The same happens if the geometry and dimensions change, not allowing the investigation of bonded joints and repairs under creep very deeply.

The fact that adhesive properties are degraded during creep conditions are undoubtedly true. The degradation of G_{II_c} can be also true and justified by a physical meaning. However, this degradation remains valid only in the FPZ. In this way, a generalised degradation of fracture energy within the entire adhesive layer may constitute an incorrect assumption. Additionally, the phenomenon was mathematically formulated only empirically, without variables with physical meaning, taking to a numerical model that is particularly fitted for a given case.

There are studies related to fatigue phenomena, presenting CZM formulations (Moreira et al., 2020b; Moreira, 2021), not proposing any degradation of fracture energy in the adhesive layer. It is assumed a degradation of the adhesive layer, where the damage rate is determined by the Paris law. Consequently, the CZM formulation is only dependent on material properties. For a given material for the adhesive, with a given material for the substrates, any geometry with any dimensions can be tested numerically, after experimental fracture characterisation. In fact, creep phenomena is not very different when compared to fatigue phenomena, where creep sometimes is intended as *"static-fatigue"* in the literature (Broughton, 2012). In physical terms, it would be coherent to establish a damage rate law due to creep conditions, but maintaining the CZM law shape through an entire simulation.

In studies developed by Neto et al. (2021, 2022b,c), it was clearly demonstrated that creep conditions cause a degradation of the fracture energy. Nevertheless, this conclusion was drawn by assessing the residual fracture energy in a post-creep condition. Due to this, the inclusion of an empirical model interpolated with residual values of fracture energy within a CZM environment may not constitute a totally correct approach, specially if it is considered that the material was virgin before any loading actuation.

Avoiding empirical mathematical formulations, and bringing physical logics to the numerical laws integrated in a CZM environment, rheological parameters should be considered in the damage rate models. The degradation of the adhesive properties, due to creep, should consider the degradation of creep localised stress (Sun et al., 2012), as fatigue formulations consider a stress intensity factor while using the Paris law, but also the degradation of rheological parameters in the case of adhesives, due to their ductile nature. In this way, it may be correct to assume a constant initial fracture energy, while considering virgin materials at an initial instant of time. The calculated damage due to creep is then summed to the damage resulting from static conditions.

Chapter 3 presents experimental results using DCB samples, assessing the creep curve in pure mode I, and also using ENF samples, assessing the creep curve in pure mode II. The corresponding fracture characterisation allows the establishment of damage rate laws, derived containing rheological parameters. Those derivations and corresponding numerical implementation are exposed in this chapter. In this way, it is possible to establish a CZM law in order to predict damage, under creep conditions, in bonded joints and repairs.

4.3 Crack Damage Laws considering Rheological Parameters

The proposed damage laws are derived in this section. Constitutive equations governed by rheological models and also additional laws accounting for creep stress effects are used. Those laws were mentioned in Sections 4.1.1 and 4.2.2. After presenting damage laws proposed by Kachanov-Rabotnov and Liu-Murakami, novel laws are established with the inclusion of rheological parameters and also additional laws are derived accounting for stress effects introduced by Sun et al. (2012) and Li et al. (2017). Finally, a parametric analysis is performed to assess the behaviour of the proposed laws, both considering pure modes I and II.

Sun et al. (2012) presented modifications on the Kachanov-Rabotnov model, where equation 4.136 is proposed establishing the damage rate mathematically. In fact, the Kachanov-Rabotnov law is presented usually and originally (Rabotnov, 1969) using a power law as presented in equation 4.130, exposed by Nikbin et al. (1984). It is notable that the constitutive law used dictates the creep strain rate as defined in equation 4.128. Consequently, the Kachanov-Rabotnov law can be generalised as follows:

$$\frac{dD}{dt}=\frac{A\dot{\varepsilon}}{(1-D)^{\theta}} \tag{4.160}$$

where parameters previously presented as $\dot{D}_0$ and σ_0 are merged into the empirical parameter A. In this way, equation 4.160 is ready for the incorporation of rheological models presented in equations 4.4, 4.12, and 4.21.

Haque and Maurice (2019), while mentioning limitations associated with the Kachanov-Rabotnov model, demonstrated the use of an alternative law that was proposed by Liu and Murakami, defining damage as an exponential function, as defined in equation 4.155. Consequently, creep strain rate was defined by equation 4.148. In this way, the Liu-Murakami damage law can be then generalised in an expression presented in equation 4.161, where equations 4.4, 4.12, and also 4.21 are easily applicable.

$$\frac{dD}{dt}=Q\dot{\varepsilon}\frac{\left(1-e^{-\phi}\right)e^{\phi D}}{\phi} \tag{4.161}$$

After this procedure, generalised Kachanov-Rabotnov and Liu-Murakami based damage models can be modified by introducing viscoelastic phenomena, implementing Maxwell, Voigt-Kelvin, and Burgers viscoelastic models as creep strain rate formulation.

Substituting equation 4.4, the KRM (Kachanov-Rabotnov-Maxwell) law is then defined as follows:

$$\frac{dD}{dt}=A\frac{\sigma}{(1-D)^{\theta}\eta+\eta_{res}} \tag{4.162}$$

where A, θ, η, and η_{res} are all material constants, being η the well known viscous parameter. In this case, A and θ are non-dimensional, but η and η_{res} are defined in [MPas]. In fact, several limitations are associated with the Kachanov-Rabotnov damage model, so that Haque and Maurice (2019) referred the stress-sensitivity and mesh-dependence characteristic of this law. Also, Calì et al. (2010) reported difficulties associated with the implementation of the Kachanov-Rabotnov law into a CZM numerical model, due to singularities, by the presence of the factor $(1-D)^{\theta}$ in the denominator. Due to this, the authors proposed the use of a damage range only until 0.9, which is not truly valid, following the classic theories of fracture mechanics. It would be assumed that any material particle was fully degraded even in case of failure. By introducing the rheological parameters into the Kachanov-Rabotnov law, such as the case of η, it may be valid, in practice, to assume a residual viscous parameter, η_{res}, assuming a non-null material viscosity even in the case of full degradation ($D=1$). Consequently, problems related with singularities are vanished by imposing a possible real scenario, represented by a physical parameter.

Voigt-Kelvin viscoelastic model can also be used in equation 4.160. Nevertheless, equation 4.12, which is presenting the corresponding creep strain rate, is time-dependent. In the literature, Findley et al. (1976) referred the use of the retardation time, τ, considering creep conditions. This parameter is related to the crossing point between a linear function with a slope equal to σ/η and the strain value correspondent to σ/R. It is assumed that 63% of the steady-state creep strain is attained when $t = \tau$. If relaxation phenomena was considered, an analogous parameter would be defined, known as relaxation time (Findley et al., 1976). In this way, the time variable presented in equation 4.12 is substituted by the retardation time, obtaining the modified Voigt-Kelvin model, being defined in the following equation:

$$\dot{\varepsilon} = \frac{\sigma}{\eta} e^{-\frac{R}{\eta}\tau} \tag{4.163}$$

By replacing equation 4.163 into equation 4.160, the KRVK (Kachanov-Rabotnov-Voigt-Kelvin) damage law is postulated as follows:

$$\frac{dD}{dt} = A \frac{\sigma}{(1-D)^{\theta}\,\eta + \eta_{res}} e^{-\frac{R}{\eta}\tau} \tag{4.164}$$

where the unities are the same as mentioned previously, with the retardation time (τ) being defined in [s].

The KRB (Kachanov-Rabotnov-Burgers) model is derived by using equation 4.21, where the same adaptations are done as it was presented in order to obtain equation 4.165. A modified version is then introduced into equation 4.160, obtaining equation 4.166.

$$\dot{\varepsilon} = \frac{\sigma}{\eta} \left(1 + e^{-\frac{R}{\eta}\tau}\right) \tag{4.165}$$

$$\frac{dD}{dt} = A \frac{\sigma}{(1-D)^{\theta}\,\eta + \eta_{res}} \left(1 + e^{-\frac{R}{\eta}\tau}\right) \tag{4.166}$$

In fact, the KRB model resulted in a more conservative version of the KRVK law.

The power law based stress degradation concept, due to creep conditions, introduced by Sun et al. (2012) can also be implemented in laws derived in equations 4.162, 4.164, and 4.166. In this way, equations 4.167, 4.168, and 4.169 are derived, constituting the KRMS (Kachanov-Rabotnov-Maxwell-Sun), KRVKS (Kachanov-Rabotnov-Voigt-Kelvin-Sun), and KRBS (Kachanov-Rabotnov-Burgers-Sun) models, respectively.

$$\frac{dD}{dt} = B \frac{[\sigma - (1-D)T_c]^n}{(1-D)^{\theta}\,\eta + \eta_{res}} \tag{4.167}$$

$$\frac{dD}{dt} = B \frac{[\sigma - (1-D)T_c]^n}{(1-D)^{\theta}\,\eta + \eta_{res}} e^{-\frac{R}{\eta}\tau} \tag{4.168}$$

$$\frac{dD}{dt} = B \frac{[\sigma - (1-D)T_c]^n}{(1-D)^{\theta}\,\eta + \eta_{res}} \left(1 + e^{-\frac{R}{\eta}\tau}\right) \tag{4.169}$$

In this case, the parameter A is replaced by the parameter B being expressed in [MPa^{1-n}].

Same adaptations are proposed for the Liu-Murakami damage model, where viscoelastic models can be applied. The LMM (Liu-Murakami-Maxwell) damage law is established by substituting equation 4.4 into equation 4.161, as follows:

$$\frac{dD}{dt} = Q\sigma \frac{\left(1 - e^{-\phi D}\right) e^{\phi D}}{\phi D} \tag{4.170}$$

which in this case the use of a residual viscous parameter is unnecessary, due to the absence of singularities. Q and ϕ are still non-dimensional in this case, as in further Liu-Murakami based laws.

By replacing equation 4.163 into equation 4.161, the LMVK (Liu-Murakami-Voigt-Kelvin) model is then obtained, being represented in equation 4.171.

$$\frac{dD}{dt} = Q\sigma \frac{\left(1 - e^{-\phi D}\right)}{\phi D} e^{\phi D - \frac{R}{\eta}\tau} \tag{4.171}$$

The LMB (Liu-Murakami-Burgers) model is achieved by incorporating equation 4.165 into equation 4.161, obtaining equation 4.172. In fact, as it happens with the Kachanov-Rabotnov based models, LMB is a more conservative version of LMVK.

$$\frac{dD}{dt} = Q\sigma \frac{\left(1 - e^{-\phi D}\right) e^{\phi D}}{\phi D} \left(1 + e^{-\frac{R}{\eta}\tau}\right) \tag{4.172}$$

Usually, Liu-Murakami based models are presented associated to sin-hyperbolic strain-rate/stress relations (Haque and Maurice, 2019; Cano and Stewart, 2020). In this way, a sin-hyperbolic formulation can be incorporated into the Liu-Murakami based models. By substituting equation 4.148 into equations 4.170, 4.171, and 4.172, equations 4.173, 4.174, and 4.175 are obtained, respectively, constituting the LMMH (Liu-Murakami-Maxwell-Hyperbolic), LMVKH (Liu-Murakami-Voigt-Kelvin-Hyperbolic), and LMBH (Liu-Murakami-Burgers-Hyperbolic) laws, respectively.

$$\frac{dD}{dt} = Qsinh\left(\frac{\sigma}{\sigma_t}\right)^{\chi} \frac{\left(1 - e^{-\phi D}\right) e^{\phi D}}{\phi D} \tag{4.173}$$

$$\frac{dD}{dt} = Qsinh\left(\frac{\sigma}{\sigma_t}\right)^{\chi} \frac{\left(1 - e^{-\phi D}\right)}{\phi D} e^{\phi D - \frac{R}{\eta}\tau} \tag{4.174}$$

$$\frac{dD}{dt} = Qsinh\left(\frac{\sigma}{\sigma_t}\right)^{\chi} \frac{\left(1 - e^{-\phi D}\right) e^{\phi D}}{\phi D} \left(1 + e^{-\frac{R}{\eta}\tau}\right) \tag{4.175}$$

KRM, KRVK, KRB, KRMS, KRVKS, KRBS, LMM, LMVK, LMB, LMMH, LMVKH, and LMBH are, in this way, postulated as novel laws to be applied in bonded joints and repairs, predicting creep damage of adhesives accounting for rheological effects, specially, viscous effects. Table 4.2 resumes all the derived creep damage laws.

The influence of the several parameters on the creep damage rate is described in Section 4.3.1.1, considering pure mode I loading, and in Section 4.3.2.1, considering pure mode II loading. The creep response considering all the derived damage laws is analysed in Sections 4.3.1.3 and 4.3.2.3, respectively. Parametric influence on the curve shape is also assessed for pure modes I and II in Sections 4.3.1.4 and 4.3.2.4, respectively.

Table 4.2: Creep damage laws applicable on bonded joints.

Damage Law	Equation
KRM (4.162)	$\frac{dD}{dt} = A\frac{\sigma}{(1-D)^{\theta}\eta+\eta_{res}}$
KRVK (4.164)	$\frac{dD}{dt} = A\frac{\sigma}{(1-D)^{\theta}\eta+\eta_{res}}e^{-\frac{R}{\eta}\tau}$
KRB (4.166)	$\frac{dD}{dt} = A\frac{\sigma}{(1-D)^{\theta}\eta+\eta_{res}}\left(1+e^{-\frac{R}{\eta}\tau}\right)$
KRMS (4.167)	$\frac{dD}{dt} = B\frac{[\sigma-(1-D)T_c]^n}{(1-D)^{\theta}\eta+\eta_{res}}$
KRVKS (4.168)	$\frac{dD}{dt} = B\frac{[\sigma-(1-D)T_c]^n}{(1-D)^{\theta}\eta+\eta_{res}}e^{-\frac{R}{\eta}\tau}$
KRBS (4.169)	$\frac{dD}{dt} = B\frac{[\sigma-(1-D)T_c]^n}{(1-D)^{\theta}\eta+\eta_{res}}\left(1+e^{-\frac{R}{\eta}\tau}\right)$
LMM (4.170)	$\frac{dD}{dt} = Q\sigma\frac{\left(1-e^{-\phi D}\right)e^{\phi D}}{\phi D}$
LMVK (4.171)	$\frac{dD}{dt} = Q\sigma\frac{\left(1-e^{-\phi D}\right)}{\phi D}e^{\phi D-\frac{R}{\eta}\tau}$
LMB (4.172)	$\frac{dD}{dt} = Q\sigma\frac{\left(1-e^{-\phi D}\right)e^{\phi D}}{\phi D}\left(1+e^{-\frac{R}{\eta}\tau}\right)$
LMMH (4.173)	$\frac{dD}{dt} = Qsinh\left(\frac{\sigma}{\sigma_t}\right)^{\chi}\frac{\left(1-e^{-\phi D}\right)e^{\phi D}}{\phi D}$
LMVKH (4.174)	$\frac{dD}{dt} = Qsinh\left(\frac{\sigma}{\sigma_t}\right)^{\chi}\frac{\left(1-e^{-\phi D}\right)}{\phi D}e^{\phi D-\frac{R}{\eta}\tau}$
LMBH (4.175)	$\frac{dD}{dt} = Qsinh\left(\frac{\sigma}{\sigma_t}\right)^{\chi}\frac{\left(1-e^{-\phi D}\right)e^{\phi D}}{\phi D}\left(1+e^{-\frac{R}{\eta}\tau}\right)$

4.3.1 Pure Mode I Loading

This section provides a detailed analysis, considering creep loading, under pure mode I, using the aforementioned damage laws.

4.3.1.1 Parametric Analysis

This section is destinated to present a parametric analysis, understanding the behaviour of the derived laws, as well as deciding which range of parameters are feasible for their application.

Several reference parameters are considered as fixed through the whole analysis, while a single parameter under investigation is varied within a given range. Table 4.3 is summarising values taken as references while considering pure mode I loading.

Table 4.3: Reference parametric values for analysis considering pure mode I loading.

Parameter	Kachanov-Rabotnov based		Liu-Murakami based	
	Classic	*Sun* based	Classic	Hyperbolic based
A[-]	2.50×10^{-7}	—	—	—
B[MPa^{1-n}]	—	5.00×10^{-8}	—	—
Q[-]	—	—	2.25×10^{-4}	5.00×10^{-1}
η[MPas]	2.50×10^{10}			
η_{res}[MPas]	1.00			
R[MPa]	1600			
τ[s]	5.00×10^{5}			
θ[-]	4	2	—	—
ϕ[-]	—	—	20	
n[-]	6		—	—
χ[-]	—	—	6	
T_c[MPa]	10.0		—	—
σ_t[MPa]	—	—	25.0	

These values for the presented parameters are based in the literature. Material parameters A, B, and Q are based in works developed by Haque and Maurice (2019) and by Kamau-Devers and Miller (2022). The choice of the viscous parameter (η) is thoughtful in data presented in Kamau-Devers and Miller (2022), Brown et al. (2018) Koyanagi et al. (2021), Ribeiro et al. (2021) and de Zeeuw et al. (2019). Some of them used a particular Maxwell viscosity, which is different from the real material viscosity presented in data sheets. However, Kamau-Devers and Miller (2022), Brown et al. (2018) and Ribeiro et al. (2021) used physical values for epoxies. Regarding the residual viscous parameter, a unitary viscosity was considered. The same concept was adopted for the stiffness R, intending that parameter as the Young's modulus of the adhesive, being presented in Samaro (2023). This concept applied to the stiffness parameter seemed to be used by Ribeiro et al. (2021). Studies conducted by Brown et al. (2018) and Nuwayer and Newaz (2018) presented data related to the retardation time constant (τ), which in fact can be related to the creep life-time of the adhesive. An in-depth justification for the chosen value is presented further. θ, ϕ, n, and χ are exponents related to power laws associated with damage or stress evolutions. There are data presented in Bouvard et al. (2009), Sun et al. (2012), Haque and Maurice (2019), Cano and Stewart (2020), Diel and Huber (2017), Pandey et al. (2023), Sattar et al. (2023), and Tomczyk and Seweryn (2021), which are indicative of which values should be used. T_c is the stress threshold considering creep conditions, used by Sun et al. (2012). It can be assumed that only stresses above T_c can induce creep phenomena. In this case, 10 MPa is considered. Haque and Maurice (2019) used σ_t in the sin-hyperbolic formulation. This parameter is intended as the ultimate stress of the material, being presented in Samaro (2023). Applications to other materials were presented in the mentioned literature background. However, the parameters exposed in Table 4.3 were adapted to polymers. In a further section, all the developed numerical models will be calibrated according to the experimental data. In this phase, the investigation of the parameters on the creep damage rate is crucial to understand the feasibility of the proposed laws, before numerical implementation.

Figure 4.14 represents the variation of the damage rate, with material parameters A and B. The studied range was $[1 \times 10^{-12}; 1]$. It is expected that these parameters are solely material dependent, being possible to determine experimentally. Logarithmic scales are imposed in both horizontal and vertical axes.

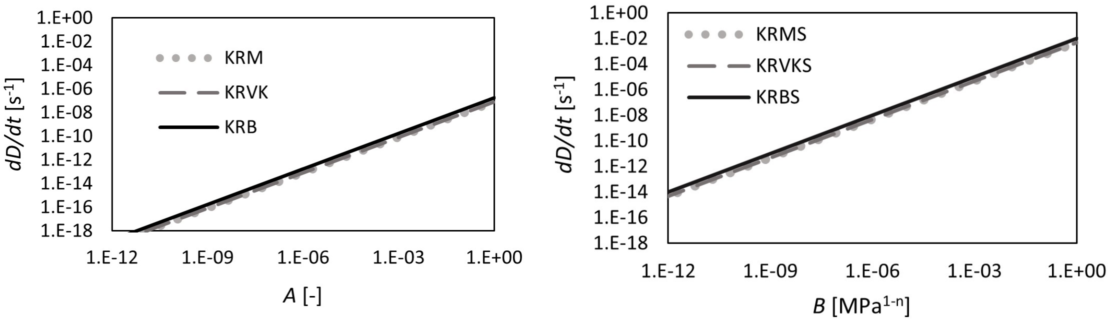

(a) (b)

Figure 4.14: Parametric effects on the creep damage rate considering pure mode I loading: (a) A, (b) B.

Almost the same response is demonstrated by all laws, that are based in the Kachanov-Rabotnov damage model, where the increase in A and B allowed an increase in the creep damage rate. Considering the same range, the inclusion of stress degradation formulation proposed by Sun et al. (2012) increases the effect of the B parameter, resulting in higher values for creep damage rate.

Regarding the Liu-Murakami based damage laws, the Q parameter is then analysed, producing results shown in Figure 4.15.

A more pronounced difference between different laws is registered for Q, when compared directly with A and B. Nevertheless, the slope of variation is essentially the same, proving the same sensitivity. In this case, the creep damage rate values are higher for models not affected by a modified stress. The introduction of a sin-hyperbolic stress formulation provided a reduction in creep damage rate, while varying Q.

All laws include the viscous parameter, as rheological effects are taken into account. Figure 4.16 presents the effect of the viscous parameter on the creep damage rate.

Globally, the Liu-Murakami based damage laws present higher creep damage rate values, when compared to the Kachanov-Rabotnov based damage laws, while variations on η are analysed. Within the evaluated range, there is a maximum local for values around $\eta = 1.00 \times 10^{-9}$ MPas, for laws where the retardation time is considered. In this way, this effect is verified for KRVK, KRVKS, LMVK, LMVKH, and LMBH. Using the Burgers viscoelastic model, LMBH

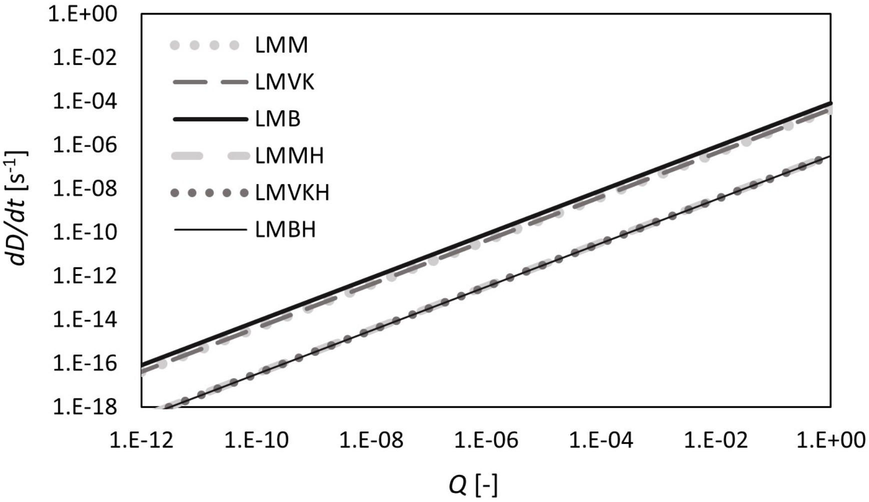

Figure 4.15: Parametric effects on the creep damage rate considering pure mode I loading: Q.

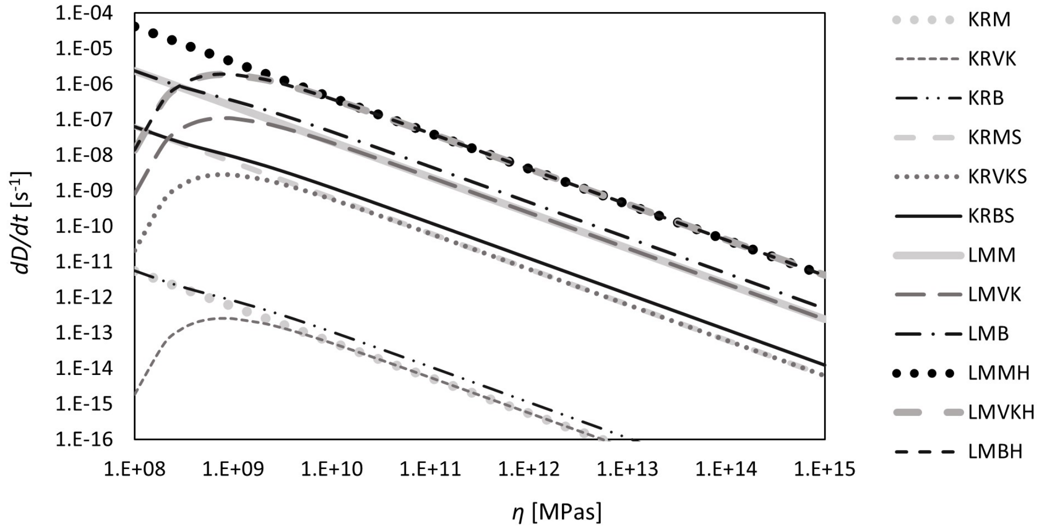

Figure 4.16: Parametric effects on the creep damage rate considering pure mode I loading: η.

was an exception showing this effect. Nevertheless, considering a logarithmic scale, Maxwell derived models presented a linear variation of creep damage rate with the evolution on the viscous parameter, while the Burgers derived model, such as KRB, KRBS, and LMB showed a tendency to present a local maximum. It can be concluded that the increase in the viscous parameter allows a decrease in the creep damage rate, in general terms.

Figure 4.17 presents the effect on creep damage rate, but considering the other rheological parameter, which is stiffness, analysing within a range between 1000 MPa and 20000 MPa.

Only laws based on Voigt-Kelvin and Burgers viscoelastic models were capable to take into account stiffness effects. Within the analysed range, the creep damage rate is approximately the same by stiffness variations. LMVK, LMVKH, LMB, and LMBH presented higher creep damage

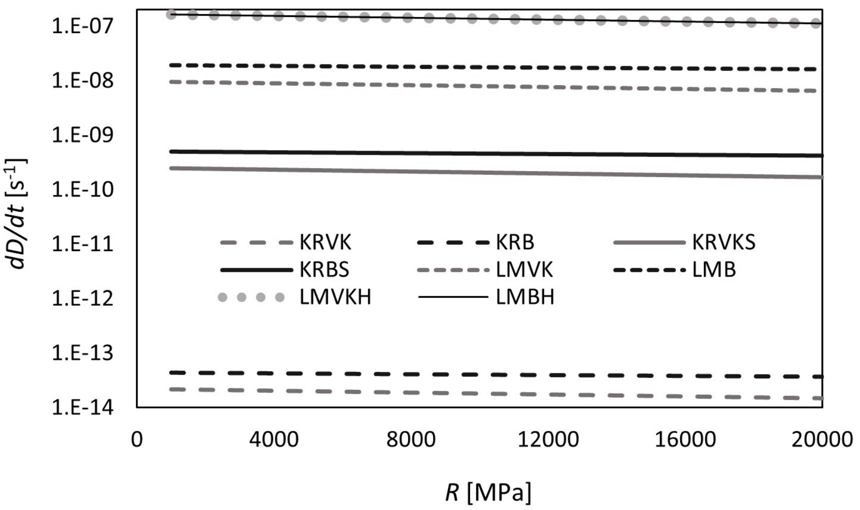

Figure 4.17: Parametric effects on the creep damage rate considering pure mode I loading: R.

rates, while the lowest creep damage rate values were registered for KRVK and KRB laws. While varying stiffness, it seemed that the introduction of the stress degradation concept under creep, proposed by Sun et al. (2012) favoured significantly the increase in creep damage rate in the Kachanov-Rabotnov based laws. Generally, Liu-Murakami based laws presented higher creep damage rate values in comparison to the Kachanov-Rabotnov based laws, when stiffness variations are analysed. It is notable that adhesives with Young's moduli within a range between 1000 MPa and 20000 MPa do not differ significantly in terms of creep damage.

Another parameter only captured by damage laws based on Voigt-Kelvin and Burgers viscoelastic models is the retardation time, whose effects on creep damage rate are showed in Figure 4.18.

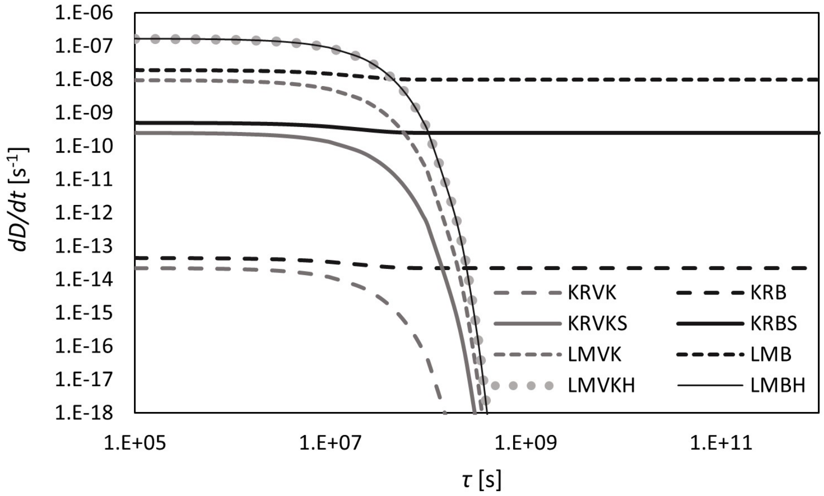

Figure 4.18: Parametric effects on the creep damage rate considering pure mode I loading: τ.

Only laws based on the Voigt-Kelvin viscoelastic model are significantly influenced by the retardation time constant, within the studied range with the exception of LMBH. Between those laws, higher creep damage rates were registered for LMVKH and LMBH, presenting exactly the same response, being followed by LMVK, KRVKS, and KRVK. Considering the other laws, and while varying the retardation time, higher creep damage is verified using LMB, followed by KRBS and KRB.

Regarding exponents, and considering characteristic parameters related to the Kachanov-Rabotnov damage law (θ), and also to the Liu-Murakami damage law (ϕ), Figure 4.19 presents corresponding effects on creep damage rate.

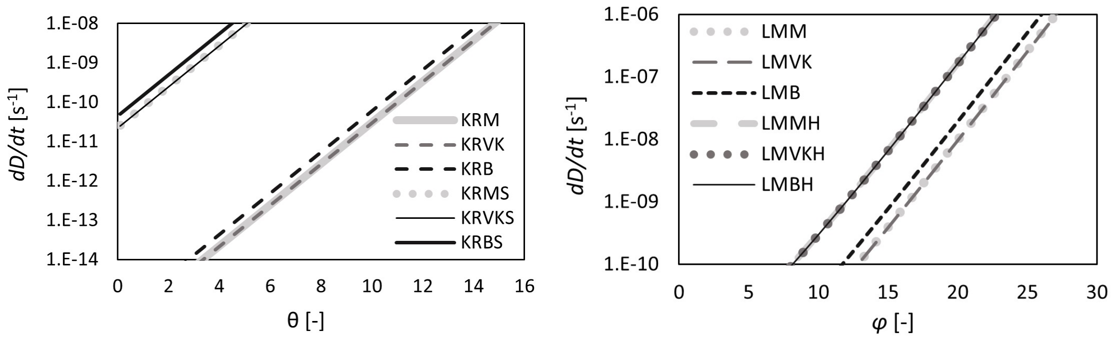

(a)

(b)

Figure 4.19: Parametric effects on the creep damage rate considering pure mode I loading: (a) θ, (b) ϕ.

Despite of the different analysed ranges, the Liu-Murakami based laws, with the exponent ϕ showed higher values of creep damage rate, increasing with the increase of this parameter with a higher slope. Same behaviour was verified for LMMH, LMVKH, and LMBH. Also a coincident tendency was observed for LMM and LMVK. A more pronounced difference is seen between the models using the stress degradation concept in the Kachanov-Rabotnov based laws (KRMS, KRVKS, and KRBS), and the others (KRM, KRVK, and KRB). Coincident behaviours were captured between KRVKS and KRMS, and also KRM and KRVK. Generally, considering variations in both θ and ϕ, laws based on the Burgers viscoelastic model presented slightly higher creep damage rate values.

Considering laws with modified stress functions, using exponents n and χ for Kachanov-Rabotnov and Liu-Murakami based laws, respectively, Figure 4.20 presents the corresponding parametric analysis.

By not using logarithmic scales, shortened ranges were analysed considering both parameters. In fact, analysing n, an exponential increase is registered, but only for values higher than 6. Coincident behaviours were captured for KRMS and KRVKS. However, slightly higher creep damage rate values were verified for KRBS, while varying n. All the behaviours presented by the Liu-Murakami based damage laws (LMMH, LMVKH, and LMBH) were coincident. An exponential

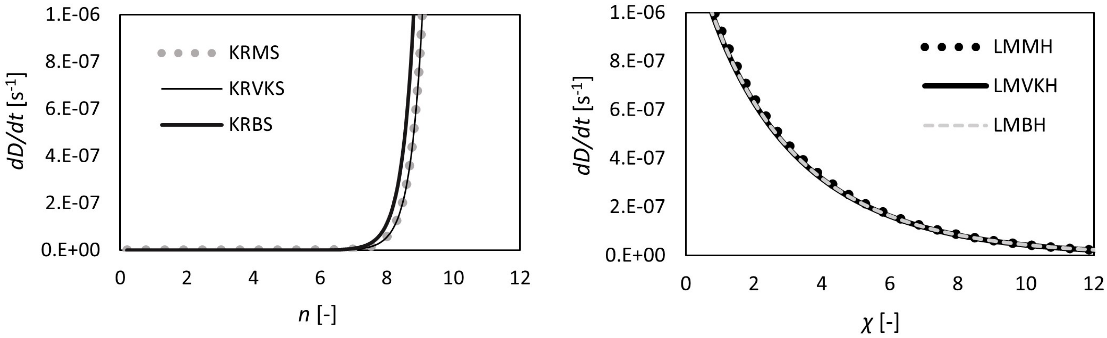

(a) (b)

Figure 4.20: Parametric effects on the creep damage rate considering pure mode I loading: (a) n, (b) χ.

decay, even with a smoother tendency when compared to n, was seen within the range of values tested for χ.

Modified stress concepts used by Sun et al. (2012) and Haque and Maurice (2019) also considered the creep stress threshold (T_c) and ultimate stress (σ_t) in the corresponding models. Figure 4.21 presents the effect of their variations in the creep damage rate.

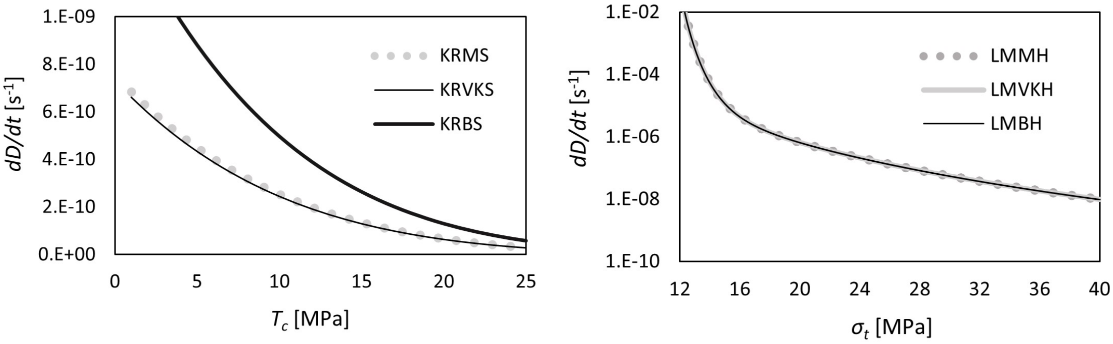

(a) (b)

Figure 4.21: Parametric effects on the creep damage rate considering pure mode I loading: (a) T_c, (b) σ_t.

A wider range was needed to evaluate the effect of σ_t related to the Liu-Murakami based damage models, using a logarithmic scale. In this case, LMMH, LMVKH, and LMBH presented coincident behaviours, while showing clearly that the increase in the ultimate stress allowed a decrease in the creep damage. Regarding T_c, similar behaviours were captured for KRMS and KRVKS, while KRBS presented higher values of creep damage rate, but with a more pronounced decaying tendency. Asymptotic values of creep damage rate would be achieved for higher values of T_c and σ_t.

4.3.1.2 New CZM to Predict Creep under Pure Mode I Loading

The proposed creep damage laws were implemented in a finite element model, using a CZM approach for pure mode I loading in order to predict the degradation of the adhesive layer. Consequently, material properties, geometry and corresponding dimensions were imposed, as well as the boundary conditions and mesh. Carbon-epoxy was used for the substrates, while ARALDITE® 2015 was the adhesive used for the considered model. Corresponding properties are presented in Tables 4.5 and 4.4, respectively.

Table 4.4: Material properties of carbon-epoxy.

Young's Modulus [GPa]	Poisson's Ratio [-]	Shear Modulus [MPa]
$E_1 = 130$	$\nu_{12} = 0.25$	$G_{12} = 4315$
$E_2 = 8.819$	$\nu_{13} = 0.25$	$G_{13} = 4315$
$E_3 = 8.819$	$\nu_{23} = 0.40$	$G_{23} = 3200$

Table 4.5: Material properties of ARALDITE® 2015.

Ultimate Stress [MPa]	Fracture Toughness [N/mm]
$\sigma_{uI} = 25$	$G_{Ic} = 0.5$
$\sigma_{uII} = 25$	$G_{IIc} = 4.5$

In order to analyse pure mode I loading, a double-cantilever-beam (DCB) specimen is considered as the geometric model, whose corresponding representation is shown in Figure 3.4, which is the same as the one used experimentally in Chapter 3.

L, a_0, t_s, and t_a are the total length, initial crack, substrate thickness, and adhesive thickness, respectively, whose corresponding dimensions are presented in Table 4.6.

Table 4.6: Geometric dimensions: DCB.

L [mm]	a_0 [mm]	t_s [mm]	t_a [mm]
140	40	2.4	0.2

Figure 4.22 presents the applied load, as well as boundary conditions. Using ABAQUS® 6.11, a mesh configuration is generated being also shown in the same figure. A load of 100 N is applied, which is equivalent to approximately 70% of the maximum sustaining load. A maximum sustaining load of 150 N was obtained also numerically, in a quasi-static simulation, using the commercial CZM approach. Extended Finite Element Method (XFEM) was also used as a validation. The corresponding load-displacement curve is presented in Figure 4.23.

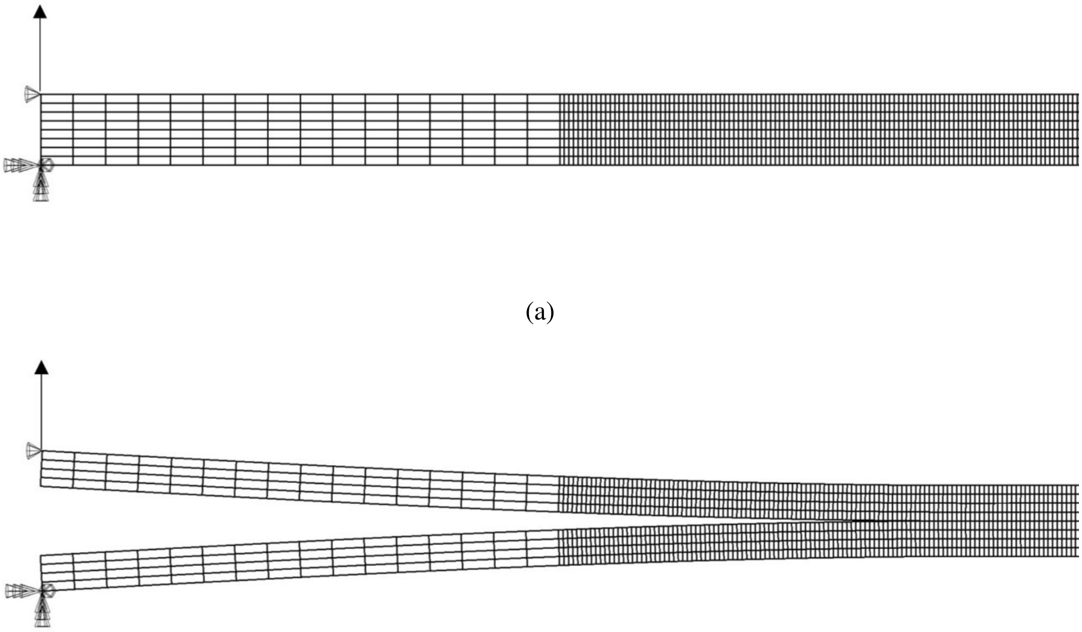
(a)

(b)

Figure 4.22: Boundary conditions and mesh for a DCB: (a) undeformed, (b) deformed.

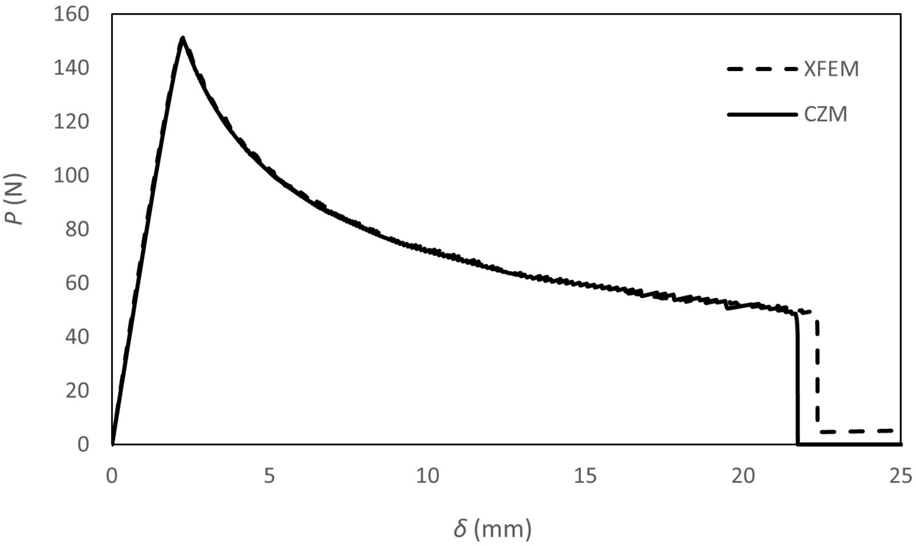

Figure 4.23: Strength prediction: DCB.

Quadrilateral plane stress elements were used, with 8 nodes, being known as CPS8 following the ABAQUS® nomenclature. A total of 2742 of solid elements are used, while a total of 343 cohesive elements are presented in the model.

As aforementioned, a new pure mode I cohesive zone model was developed and implemented in the ABAQUS® software as a user subroutine in order to analyse creep fracture phenomena. The simplest bilinear cohesive law (Figure 4.24) was adopted. In the initial linear part, up to local strength is attained, the relation between relative displacements (δ_r) and traction (σ_r) is governed by equation 4.176,

$$\sigma_r = k\delta_r \tag{4.176}$$

where k represents the interfacial stiffness, being equal to $1.0 \times 10^6\ N/mm^3$ (Gonçalves et al., 2000). From the local strength σ_{r_u}, it is possible to obtain the damage onset relative displacement δ_{r_o}. After damage onset, a linear softening relationship is established between tractions and relative displacements occurring at the homologous points belonging to the cohesive element faces:

$$\sigma_r = (1-D)\,k\delta_r \tag{4.177}$$

being D the damage parameter ranging between 0 (undamaged state, i.e., $\delta_r = \delta_{r_o}$) and 1 (complete failure, i.e., $\delta_r = \delta_{r_u}$), and is given by:

$$D = \frac{\delta_{r_u}\left(\delta_{r_{max}} - \delta_{r_o}\right)}{\delta_{r_{max}}\left(\delta_{r_u} - \delta_{r_o}\right)} \tag{4.178}$$

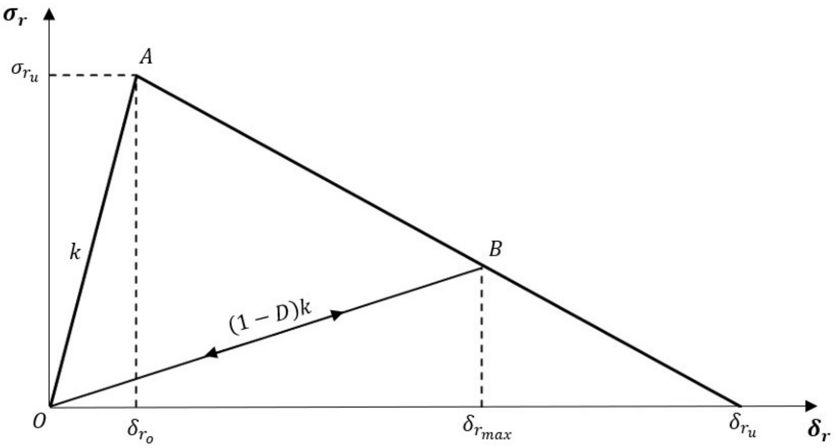

Figure 4.24: Bilinear cohesive law for pure mode I loading.

This equation is valid for quasi-static monotonic loading and the evolution of damage is accomplished by continuous update of $\delta_{r_{max}}$ that increases with applied remote loading. The ultimate relative displacement δ_{r_u} is obtained equating the area of the triangle OAB (Figure 4.24 to the fracture energy G_{I_c},

$$\delta_{r_u} = \frac{2G_{I_c}}{\sigma_{r_u}} \tag{4.179}$$

In the case of creep loading, the applied remote loading keeps constant and damage should progress as a function of time following a pre-established law. In a given increment j, the damage parameter writes,

$$D_j = D_{j-1} + dD_{creep} \tag{4.180}$$

being dD_{creep} the increment of creep damage in the current increment. As an example, using LMVKH (4.174), it can be written,

$$dD_{creep} = Qsinh\left(\frac{\sigma}{\sigma_t}\right)^{\chi}\frac{\left(1-e^{-\phi D}\right)}{\phi D}e^{\phi D-\frac{R}{\eta}\tau}dt \tag{4.181}$$

where dt identifies the current time increment. Since $\delta_{r_{max}}$ is the parameter defining damage state, the following update using equation 4.178 is necessary:

$$\delta_{r_{max}} = \frac{\delta_{r_u}\delta_{r_o}}{\delta_{r_u}-(\delta_{r_u}-\delta_{r_o})D_j} \tag{4.182}$$

With this strategy, damage evolves as a function of time according to the adopted creep law. Corresponding creep response is presented and analysed in Section 4.3.1.3.

4.3.1.3 Creep Response

Numerical results are presented in this section, where the proposed creep damage laws were implemented within a CZM environment. Creep response considering the proposed damage laws is demonstrated, comparing directly with models presented by Sun et al. (2012) and Haque and Maurice (2019), being mentioned in equations 4.136 and 4.155, respectively. Those creep responses are demonstrated by considering parameters presented in Table 4.3. Additionally, in the model presented in equation 4.136, a value of 10 MPa is considered for T_c, 90 MPa is considered for T_0, and n is considered to be equal to 6. For the model proposed by Haque and Maurice (2019), being exposed in equation 4.155, Q was considered to be 2.00×10^{-11}, still imposing σ_t as 25 MPa, ϕ as 20, and χ as 6. It has to be mentioned that all the parameters were calibrated in order to provide creep times within a range between 7 and 9 hours, considering 100 N. This assumption is based on data presented in the literature Neto et al. (2022a), but it requires clearly experimental validation, and also numerical calibration after experimental work, which constitutes a step further presented in Section 4.3.1.5. After presenting creep responses considering the proposed damage laws, an additional parametric analysis is performed, by assessing the effects on the curve shape by the variation of several parameters.

Before analysing creep responses demonstrated by the proposed laws (KRM, KRVK, KRB, KRMS, KRVKS, KRBS, LMM, LMVK, LMB, LMMH, LMVKH, and LMBH), models proposed in the literature (Sun et al., 2012; Haque and Maurice, 2019) are compared in the Figure 4.25.

Using comparable parameters, the creep response demonstrated by laws exposed in equations 4.136 and 4.155 are very similar, both regarding creep time, displacement, and also the curve shape, essentially, the slope of the secondary phase. The secondary phase was almost perfectly coincident, while a slightly difference is observed in the increasing tendency in terms of displacement associated to the tertiary phase.

Nevertheless, different responses are captured between the models modified with the stress degradation concept introduced by Sun et al. (2012), or the sin-hyperbolic concept introduced by

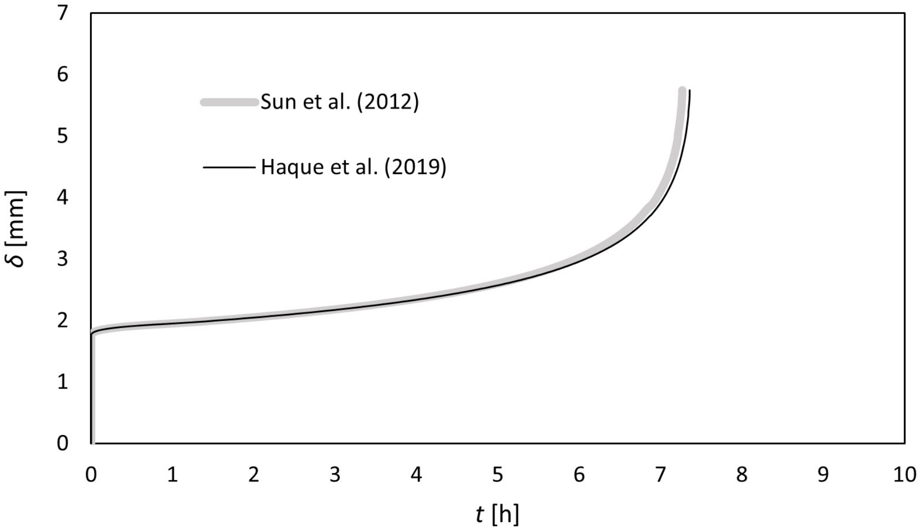

Figure 4.25: Creep response, considering pure mode I loading, of damage laws proposed by Sun et al. (2012) and Haque and Maurice (2019).

Haque and Maurice (2019). Figure 4.26 is presenting the comparison between all laws based on the Maxwell viscoelastic model (KRM, KRMS, LMM, and LMMH).

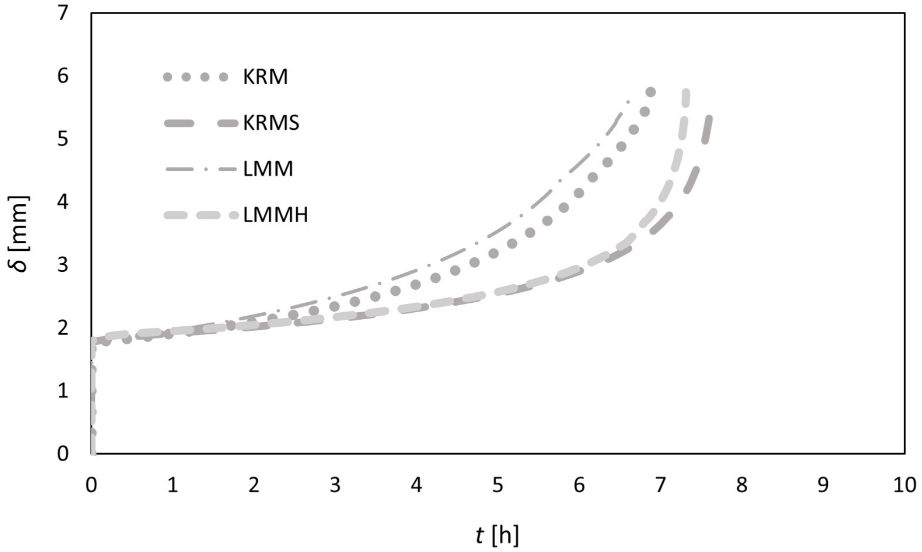

Figure 4.26: Creep response, considering pure mode I loading, of damage laws based on the Maxwell viscoelastic model.

It is notable the different response demonstrated by KRM and LMM, in comparison to KRMS and LMMH. A higher slope associated with the creep secondary phase is demonstrated by KRM and LMM. In addition, the slope is so high that the distinction between secondary and tertiary phase is not clearly identified. Due to the higher increasing tendency associated with KRM and

LMM, when compared to KRMS and LMMH, creep time was lower, achieving around 6 hours of life time, while KRMS and LMMH showed responses corresponding to a life time of about 7 hours. Similarly to what was verified when models developed by Sun et al. (2012) and Haque and Maurice (2019) were compared, the secondary phase showed by KRMS and LMMH was coincident, however, and, antagonistically, the tertiary phase is slightly more abrupt if LMMH is used. Displacement increasing tendency was also higher by using LMM, rather than using KRM.

The same comparison is shown in Figure 4.27, but considering laws based on the Voigt-Kelvin viscoelastic model.

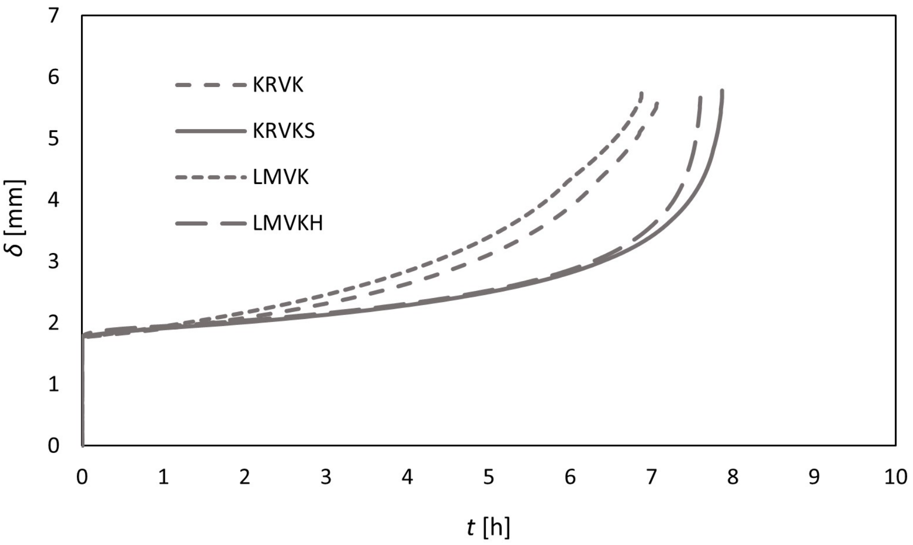

Figure 4.27: Creep response, considering pure mode I loading, of damage laws based on the Voigt-Kelvin viscoelastic model.

Similar conclusions are taken when KRVK, KRVKS, LMVK, and LMVKH are analysed, in comparison with what was mentioned by observing Figure 4.26. Liu-Murakami based laws (LMVK and LMVKH) presented slightly lower creep life time when compared to Kachanov-Rabotnov based laws (KRVK and KRVKS). It is also verified that the introduction of modified stress concepts can improve the curve shape. A distinction between secondary and tertiary phase is not also captured while using KRVK and LMVK, similarly to what was verified by using KRM and LMM.

The same analysis is done for laws based on the Burgers viscoelastic model (KRB, KRBS, LMB, and LMBH), which is shown in Figure 4.28.

As aforementioned, laws derived using the Burgers viscoelastic model are generally more conservative when compared to laws derived using Maxwell or Voigt-Kelvin viscoelastic models. Consequently, KRB, KRBS, LMB, and LMBH provided considerably lower creep life time values, in comparison to damage laws whose creep responses were presented previously in Figures 4.26 and 4.27. In this case, a life time of around 3 hours was predicted while using KRB or LMB, and a life time of almost 4 hours is verified for KRBS and LMBH. Same numerical tendencies are

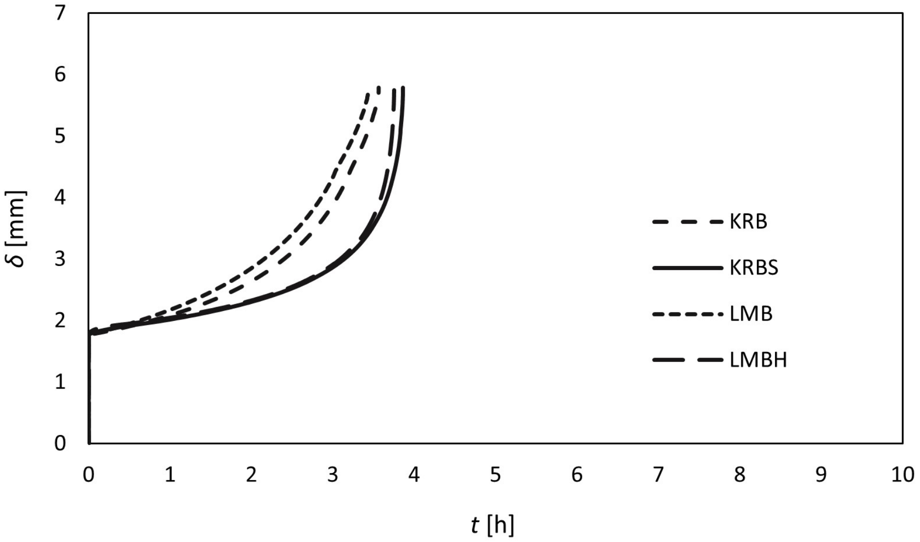

Figure 4.28: Creep response, considering pure mode I loading, of damage laws based on the Burgers viscoelastic model.

demonstrated: secondary and tertiary phases are not well captured by KRB and LMB, and Liu-Murakami based damage laws (LMB and LMBH) presented a more pronounced creep damage. This last effect is also demonstrated in the tertiary phase for LMBH.

A direct comparison between all creep damage laws is presented in Figure 4.29. The conservatism associated to laws based on the Burgers viscoelastic model is confirmed. In addition, it is also verified that laws based on the Maxwell model are slightly more conservative when compared to laws based on the Voigt-Kelvin model. The same level of conservatism, in terms of the prediction of creep life time is observed when Kachanov-Rabotnov based damage laws are compared to Liu-Murakami based damage laws. KRM, KRVK, KRB, LMM, LMVK, and also LMB were not capable to demonstrate the correct creep response. On the other hand, KRMS, KRVKS, KRBS, LMMH, LMVKH, and LMBH defined correctly the curve shape associated to the displacement evolution as a function of time, confirming responses shown by models proposed by Sun et al. (2012) and Haque and Maurice (2019), imposing comparable parameters, demonstrating literature validation. Further experimental validation is needed, as mentioned previously. Laws proposed by Sun et al. (2012) and Haque and Maurice (2019) are appropriate for metallic alloys. Parameters are calibrated in further in this chapter for adhesives, demonstrating that the proposed laws are capable for that purpose.

4.3.1.4 Parametric Effects on the Curve Shape

Exponents θ, n, ϕ, and χ seemed to influence significantly the curve shape. Not only the slope related to the secondary phase is changed, but also the accuracy being related with the number of points that the creep curve contains. Only laws based on the Voigt-Kelvin viscoelastic model are

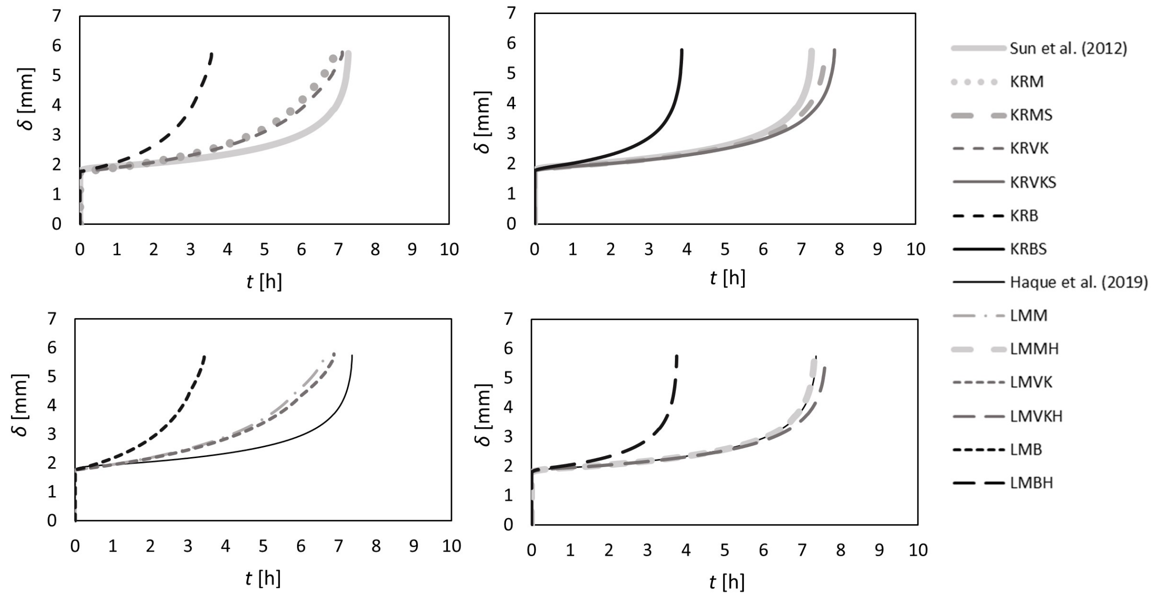

Figure 4.29: Creep response comparison, considering pure mode I loading, between the proposed laws and the literature (Sun et al., 2012; Haque and Maurice, 2019).

used for this analysis. In fact, the Voigt-Kelvin viscoelastic model is more appropriate for creep, rather than relaxation, according to Findley et al. (1976).

In order to present comparable curves, with comparable creep life time values, A and Q parameters were adjusted, while the exponent under analysis is varied. Figure 4.30 presents the effect of θ on the curve shape related to the creep response. This parameter is associated with the Kachanov-Rabotnov damage based laws.

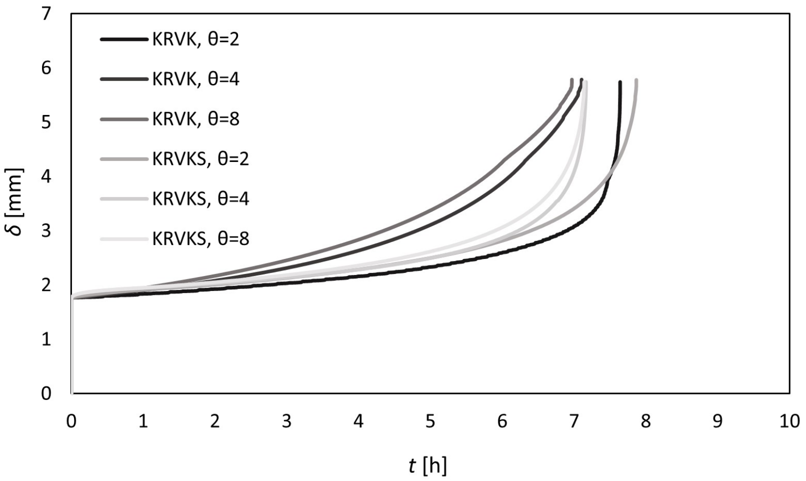

Figure 4.30: Effects of θ on the curve shape considering pure mode I loading.

It is rather notable that the decrease in θ allows the decrease in the slope of the secondary phase. As verified in Section 4.3.1.3, the slope of the secondary phase was always higher for

KRVK, in comparison to the corresponding slope but for KRVKS. Nevertheless, an exception is verified in Figure 4.30, where the KRVK law using θ=2 provided the lowest slope in the secondary phase. It seemed that lower values of θ favours the curve shape, however, the numerical accuracy can be reduced as proved in Figure 4.31.

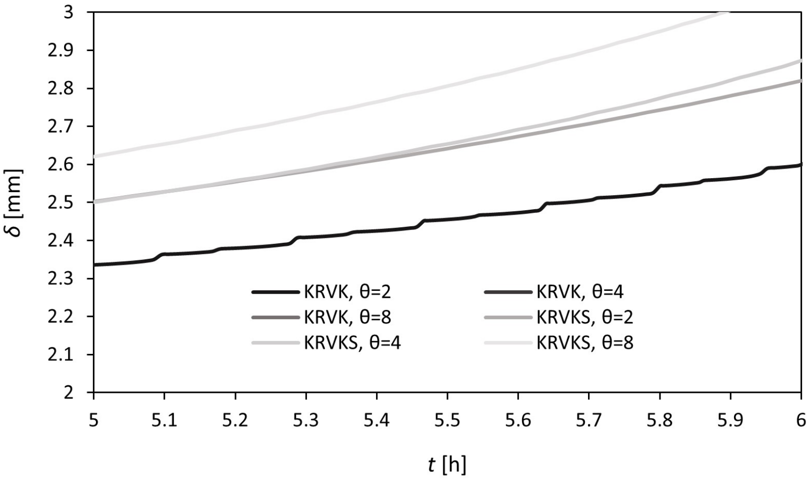

Figure 4.31: Effects of θ on the curve shape considering pure mode I loading: amplified scale.

It is seen, by reducing the value of θ, that the numerical accuracy is substantially reduced, which can harm the results in some situations. Although, if the average curve shape is maintained, the use of θ=2 in the KRVK can be considered.

The analysis of the exponent *n* on the curve shape, while using KRVKS, is performed by observing the Figure 4.32.

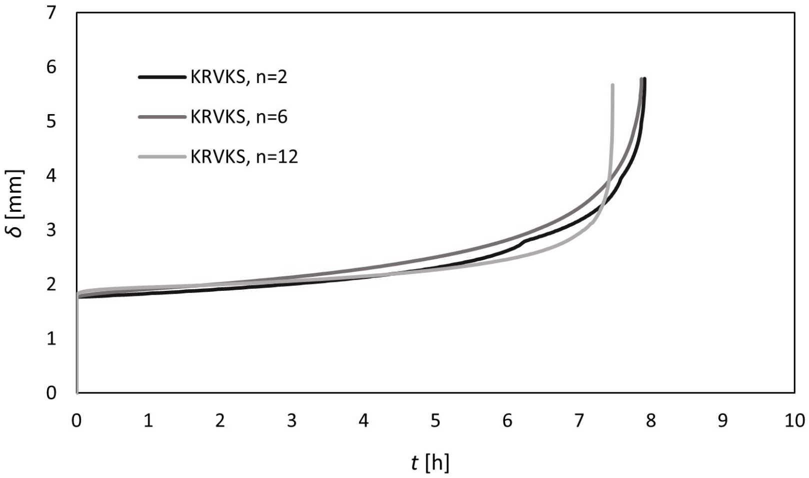

Figure 4.32: Effects of *n* on the curve shape considering pure mode I loading.

Comparing the curve produced while using *n*=2, with the curve produced while using *n*=6, it can be concluded that the numerical accuracy is considerably lower for excessively reduced values of the parameter *n*. By observing the curve produced when *n*=12 is imposed, it can be seen that the slope related to the secondary phase is reduced. It seemed that, from values of *n* producing a sufficient numerical accuracy, the increase of *n* results in the decrease of the slope of the secondary phase, and a distinction between secondary and tertiary creep is highly accentuated, which can be more appropriate for ductile materials as adhesives.

The lack of numerical accuracy when low values of n are used is deeply proved in Figure 4.33, where it is seen clearly the higher numerical instability in comparison to the use of higher values of *n*. In this case, the use of excessively low values of n is not justifiable even if the general curve shape is maintained.

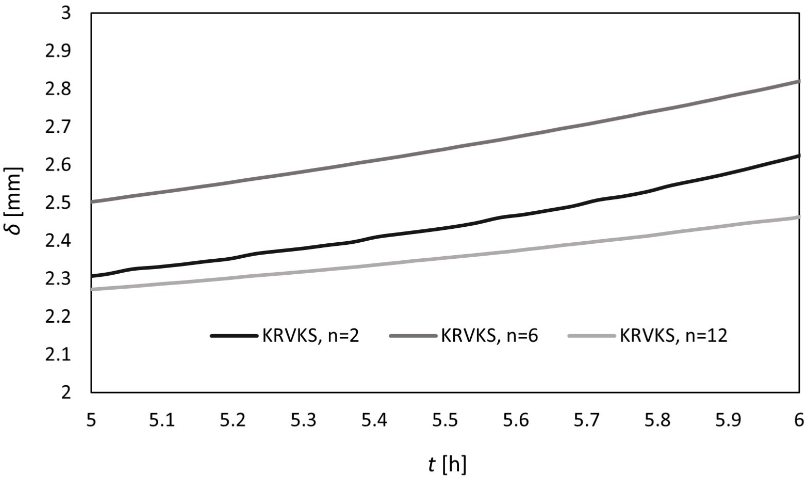

Figure 4.33: Effects of *n* on the curve shape considering pure mode I loading: amplified scale.

Regarding the Liu-Murakami based damage laws ϕ can be analysed in terms of the effect exerted in the curve shape, where results for different values of this parameter are shown in Figure 4.34.

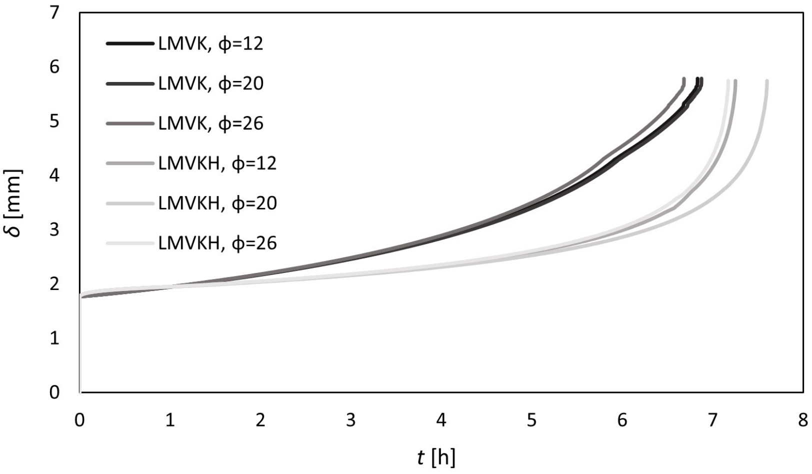

Figure 4.34: Effects of ϕ on the curve shape considering pure mode I loading.

The effect induced on the curve shape associated with ϕ is not so significant when compared to the parameters analysed previously. In fact, only minor changes are captured due to variations in ϕ, and only in tertiary creep phase. Changes seemed to be more significant on LMVKH, rather than LMVK. The reported general tendency is that an increase in the slope of the tertiary phase is seen for higher values of ϕ. Although, this was not well captured for LMVKH while using ϕ=12, due to the adjustments done in A and Q parameters, in order to present comparable lifetime values.

A detailed perspective on the numerical accuracy is assessed by observing Figure 4.35. Residual oscillations are captured while using lower values of ϕ, considering the LMVKH law, but not harming significantly the overall curve shape, i.e. the overall result. Depending on experimental results, the use of lower values of ϕ might be justifiable in order to assess a more accentuated distinction between secondary and tertiary creep.

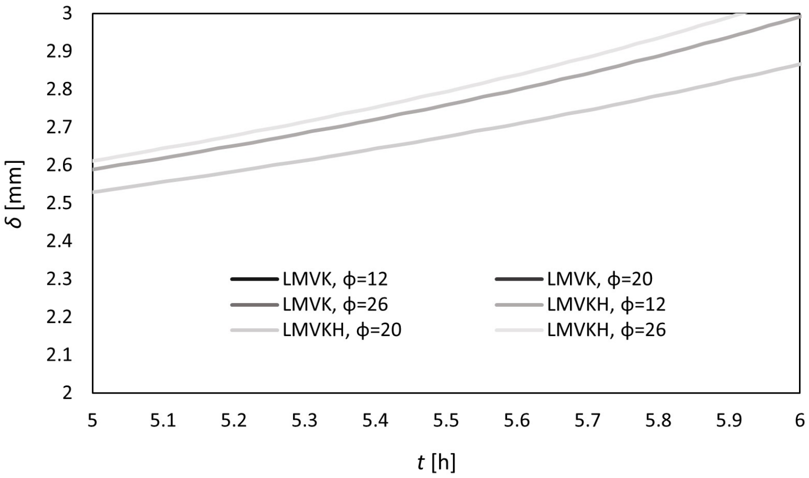

Figure 4.35: Effects of ϕ on the curve shape considering pure mode I loading: amplified scale.

Another exponent characteristic of the Liu-Murakami based damage laws, but using the sin-hyperbolic stress formulation, is χ, whose effects on the creep curve shape are presented in Figure 4.36.

Figure 4.36 clearly demonstrates that the decrease in the slope of the secondary creep phase is registered when the parameter χ is increased. For the highest value tested (χ=12), two secondary creep phases were captured. In fact, LMVKH using χ=12 is capable of predicting any phenomenon related to two secondary phases. In reality, two or more secondary creep stages are possible to occur in pure mode I, specially in ductile adhesives, due to abrupt crack propagation moments, which are produced from material defects in the adhesive layer. The strong capability of the LMVKH law is consequently, where material defects can be predicted thanks to just one parameter.

A detailed view on the numerical accuracy in seen in Figure 4.37, where it is seen that it is reduced slightly for the highest value of χ. Although, it is not sufficient, clearly, to harm the final result, i.e. the final curve shape and consequently the predicted creep life and corresponding displacement values.

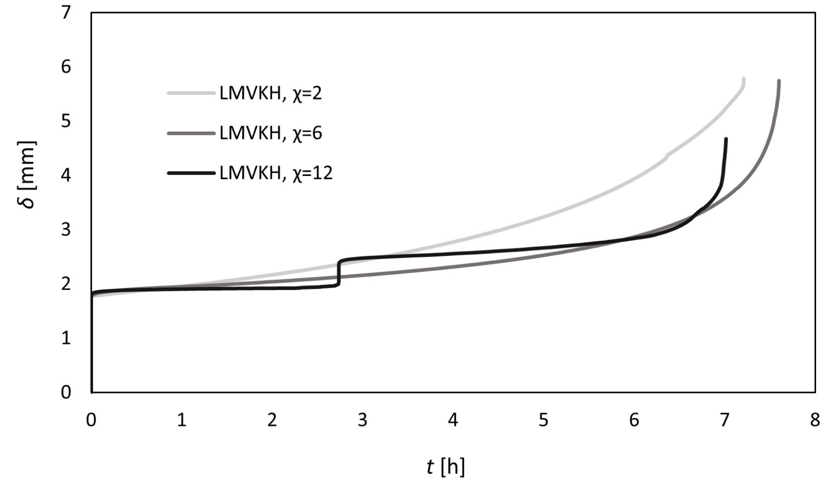

Figure 4.36: Effects of χ on the curve shape considering pure mode I loading.

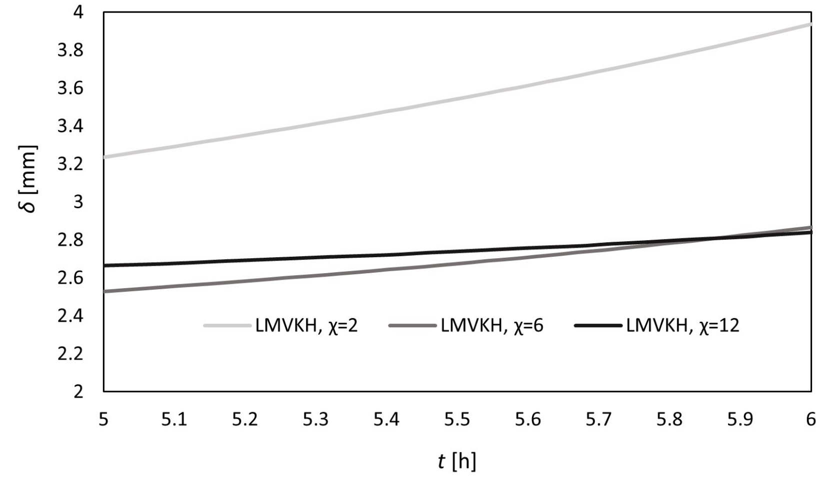

Figure 4.37: Effects of χ on the curve shape considering pure mode I loading: amplified scale.

This section is very useful to assess the effects of several parameters on the curve shape, showing the flexibility of the proposed damage laws to several types of adhesives, presenting different properties and, consequently, creep responses. Further developments will be presented regarding experimental data, for specific adhesives, where laws can be calibrated. It is expected that those laws are solely material dependent, being possible to be calibrated for different materials.

4.3.1.5 Numerical Validation

A validation was performed for the numerical evaluation of the creep behaviour of adhesively bonded joints under pure mode I loading, considering experimental results demonstrated in Chapter 3. Laws based on the Voigt-Kelvin viscoelastic model were selected, since theoretically this type of formulations are more appropriate for creep conditions (Findley et al., 1976), including more physical parameters, without being excessively conservative in the estimation of creep lifetime.

Parametric values were calibrated according to experimental results, for all considered laws: KRVK, LMVK, KRVKS, and LMVKH, whose comparison is represented in Figure 4.38. Several criteria were imposed, such as the maintenance of parameters when the applied load is modified. An appropriate law must have parameters insensitive to the modifications of load conditions. Calibrated parameters are exposed in Table 4.7 for KRVK and LMVK, and in Table 4.8 for KRVKS and LMVKH. Only proportional empirical parameters, such as A, B, and Q, as well as exponential constants as n and χ were considered for numerical calibration. Other parameters are material properties as mentioned previously. θ and ϕ are still exposed in Tables 4.7 and 4.8, but they can be determined for a given adhesive, being essentially dependent on ductility. However, their different laws can possibly correspond to different values of θ and ϕ.

Table 4.7: Calibrated parameters of KRVK and LMVK for numerical validation considering pure mode I loading.

Parameter	KRVK	LMVK
A[-]	3.0×10^{-8}	—
Q[-]	—	3.0×10^{-5}
θ[-]	4	—
ϕ[-]	20	—

Table 4.8: Calibrated parameters of KRVKS and LMVKH for numerical validation considering pure mode I loading.

Parameter	KRVKS			LMVKH		
	$n = 2$	$n = 6$	$n = 12$	$\chi = 2$	$\chi = 6$	$\chi = 12$
B[MPa^{1-n}]	2.0×10^{-5}	3.5×10^{-9}	1.5×10^{-15}	—	—	—
Q[-]	—	—	—	2.0×10^{-3}	3.0×10^{-2}	1.5
θ[-]		2		—	—	—
ϕ[-]	—	—	—		20	

Numerical validation was performed for applied loads corresponding to 80% and 85% of P_{max}, whose graphical representation is exposed in Figure 4.38. All laws were initially calibrated for a relative load of 80%. *A posteriori*, the applied load was just modified to 85% of P_{max}, i.e. considering the same parametric values.

Analysing Figure 4.38, the slope of the secondary creep phase revealed by using both KRVK and LMVK is higher than the slope demonstrated by experimental data. This difference was more pronounced in the lower relative load (80%), rather than the higher load (85%). Nevertheless, the creep lifetime was respected, according to experimental results, by using the same parameters for both relative applied loads. Numerically, KRVK and LVMK laws showed essentially the same

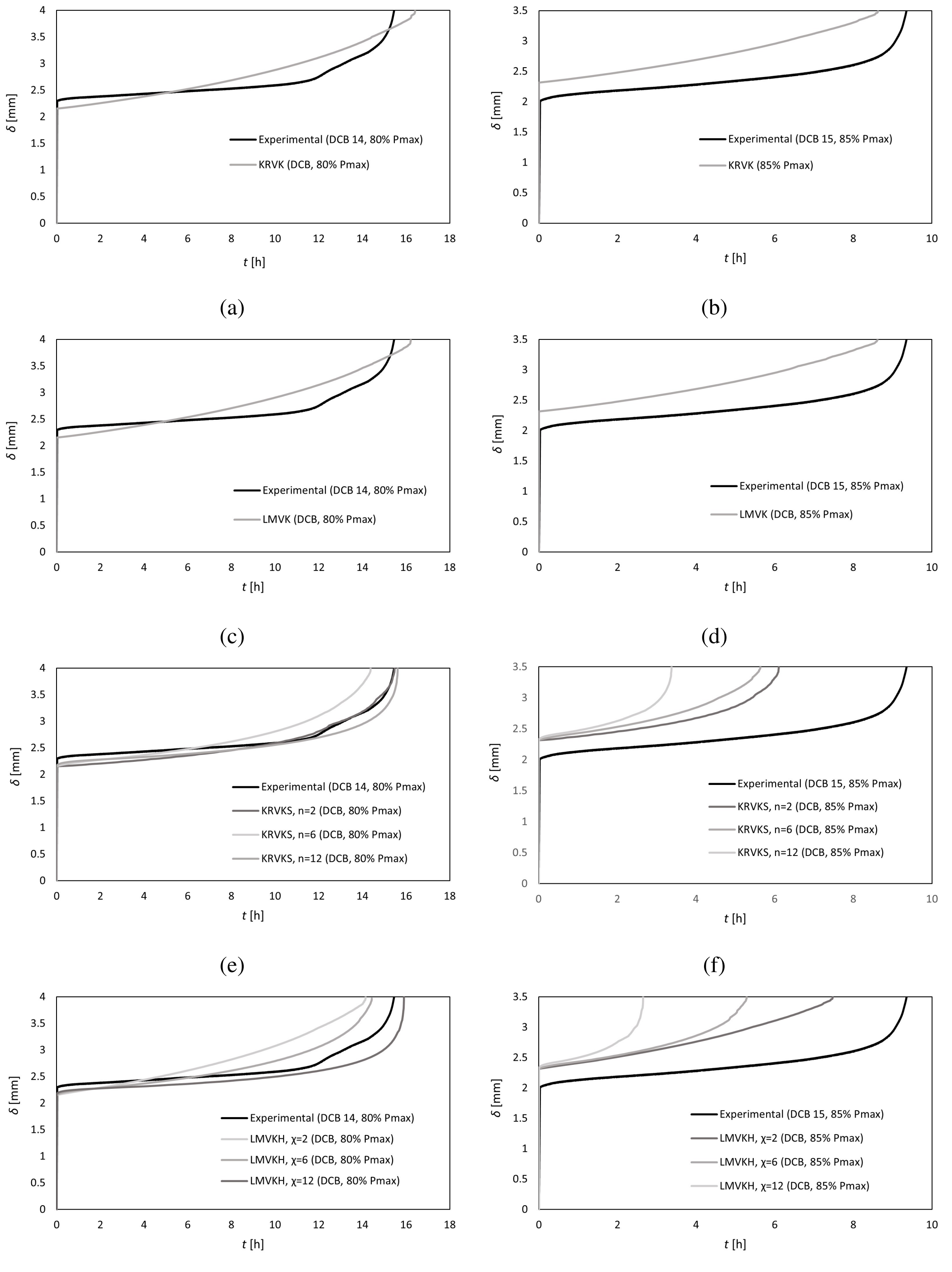

(a) (b)

(c) (d)

(e) (f)

(g) (h)

Figure 4.38: Numerical validation considering pure mode I loading: (a) KRVK (80% P_{max}), (b) KRVK (85% P_{max}), (c) LMVK (80% P_{max}), (d) LMVK (85% P_{max}), (e) KRVKS (80% P_{max}), (f) KRVKS (85% P_{max}), (g) LMVKH (80% P_{max}), (h) LMVKH (85% P_{max}).

response. In relation to experimental results, KRVKS and LMVKH showed identical slopes of the secondary creep phase. However, the numerical difference in creep lifetime introduced by the increase in relative applied load, from 80% to 85%, was more pronounced when compared to the same difference, but considering experimental results. Consequently, an additional parametric calibration would be needed, in order to compensate differences in the applied load, which is not appropriate, since a given law should not be dependent on the load level.

Different parameters of n and χ were tested for KRVKS and LMVKH, respectively. As previously proved in Section 4.3.1.4, by using $n = 12$ and $\chi = 12$, a lower slope in terms of the secondary creep phase is provided, which is adequate for the representation of ductile behaviours. In fact, it is proved in Figure 4.38 that the slope demonstrated by using $n = 12$ and $\chi = 12$ is identical to the slope shown by experimental results, considering a relative applied load of 80%. By the calibration of the proportional empirical parameters A and Q, creep lifetime is respected for that applied load. Consequently, KRVKS and LMVKH, using $n = 12$ and $\chi = 12$, respectively, proved to more coherent with experimental data, rather than other laws, even KRVK and LMVK. However, the behaviour of those laws are dependent on the applied load. Interestingly, even showing lower creep lifetimes, comparing to what is proved in experimentally for a relative applied load of 80%, slopes related with steady-creep were identical, specially using $n = 12$ and $\chi = 12$. This behaviour demonstrated laws can be considered while introducing improvements in future developments.

KRVK and LMVK are selected as the most appropriate laws for the prediction of creep lifetime. If only the prediction of the slope of the secondary creep phase is needed, KRVKS and LMVKH have to be use, not requiring additional parametric calibration. Consequently, for a complete characterisation of creep behaviour a combined use of KRVK and KRVKS, or LMVK and LMVKH can be performed. As a future perspective, a tool can be developed for this purpose, for automatic output of results.

4.3.2 Pure Mode II Loading

Exactly the same analysis is presented in this section, but regarding pure mode II loading. In this way, a parametric analysis is performed in Section 4.3.2.1. The numerical model, using CZM and FEM is presented in Section 4.3.2.2, where subsequent creep responses are demonstrated in Section 4.3.2.3. Finally, parametric effects on the curve shape related to creep response are assessed in Section 4.3.2.4, verifying what are the most suitable parameters for different types of adhesive.

4.3.2.1 Parametric Analysis

As presented in Section 4.3.1.1, the several parameters used in the proposed laws are analysed but considering pure mode II loading. Different reference parameters are considered, being more appropriate for creep times regarding pure shear conditions. Fixed parameters are summarised in Table 4.9

Table 4.9: Reference parametric values for analysis.

Parameter	Kachanov-Rabotnov based		Liu-Murakami based	
	Classic	*Sun* based	Classic	Hyperbolic based
A[-]	7.00×10^{-6}	—	—	—
B[MPa^{1-n}]	—	4.00×10^{-7}	—	—
Q[-]	—	—	8.50×10^{-3}	3.50×10^{-1}
η[MPas]	2.50×10^{10}			
η_{res}[MPas]	1.00			
R[MPa]	1600			
τ[s]	5.00×10^{5}			
θ[-]	2		—	—
ϕ[-]	—	—	12	
n[-]	2		—	—
χ[-]	—	—	2	
T_c[MPa]	10.0		—	—
σ_t[MPa]	—	—	25.0	

Exactly the same literature references were used for the consideration of these fixed parameters. Those references are mentioned in Section 4.3.1.1, while considering pure mode I loading. Values for adjustable parameters, as A, B, Q, θ, ϕ, n, and χ were chosen in order to provide acceptable creep life times when pure shear is considered.

Since the same laws are considered, the same tendency regarding parametric variations are verified for pure mode II loading, when compared with pure mode I loading. By considering some different reference values for the aforementioned parameters, slightly differences can be observed.

The influence of the parameters A and B on creep damage rate is seen in Figure 4.39.

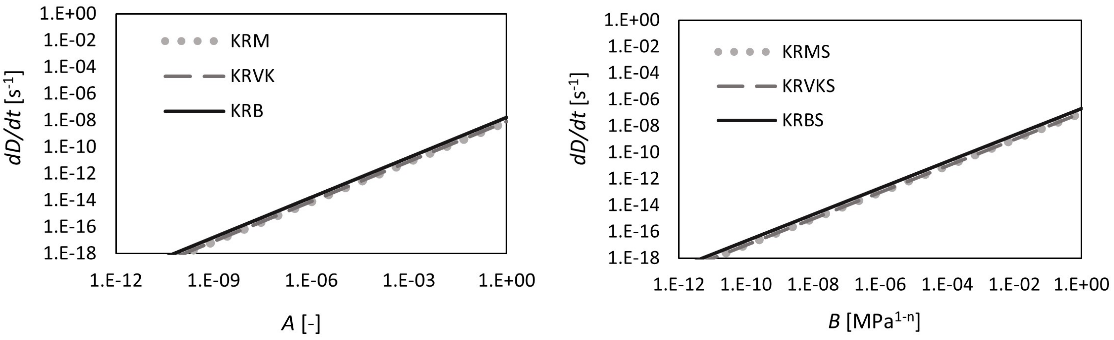

(a)

(b)

Figure 4.39: Parametric effects on the creep damage rate considering pure mode II loading: (a) A, (b) B.

Similar responses are demonstrated by all laws, where the increase in A and B allowed an increase in the creep damage rate. A is associated related to KRM, KRVK, and KRB, while B is related to KRMS, KRVKS, and KRBS. As previously seen for pure mode I loading, considering the same range, the inclusion of stress degradation formulation proposed by Sun et al. (2012) increases the effect of the B parameter, resulting in higher values for creep damage rate. In fact, all the tendency is exactly the same when compared with the pure mode I loading. The values for the creep damage rate are slightly higher when pure mode II loading is considered, specially when B is varied.

Q is related to Liu-Murakami based damage laws: LMM, LMVK, LMB, LMMH, LMVKH, and LMBH. Corresponding parametric analysis is presented in Figure 4.40.

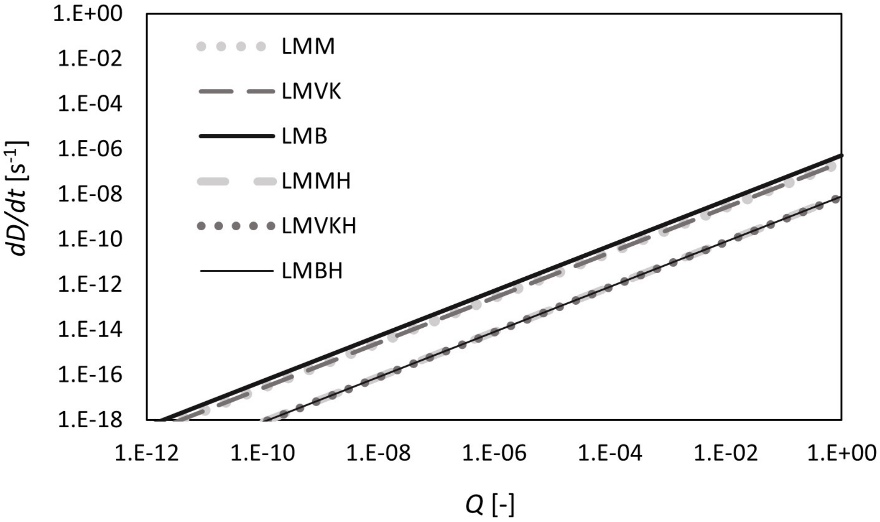

Figure 4.40: Parametric effects on the creep damage rate considering pure mode II loading: Q

Variations in Q promote the same tendency as variations in A or B, but with a more pronounced increase. In comparison to pure mode I loading, also the same tendency is captured, as well as identical values of creep damage rate. Creep damage rate values are higher for models not affected by a modified stress. The introduction of a sin-hyperbolic stress formulation provided a reduction in creep damage rate, while varying Q.

Figure 4.41 presents the effect of the viscous parameter on the creep damage rate, where all laws included.

Similar tendency is verified for pure mode II loading, in comparison to the pure mode I loading. Nevertheless, lower differences related to the creep damage rate values are seen in this case, for the different laws. Generally, the Liu-Murakami based damage laws are presenting higher creep damage rate values, when compared to the Kachanov-Rabotnov based damage laws, while variations on η are analysed. Within the evaluated range, there is a maximum local for values around $\eta = 1.00 \times 10^{-7}$ MPas or $\eta = 1.00 \times 10^{-12}$ MPas considering the Liu-Murakami and Kachanov-Rabotnov based laws, respectively, but only for laws where the retardation time is considered. In this way, this effect is verified for KRVK, KRVKS, LMVK, LMVKH, and LMBH. Using the Burgers viscoelastic model, LMBH was an exception showing this effect. Nevertheless,

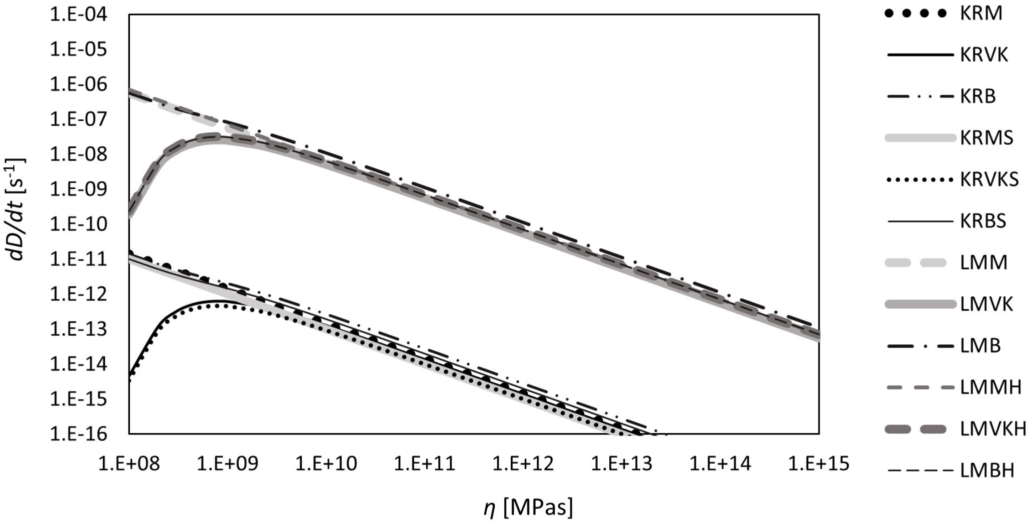

Figure 4.41: Parametric effects on the creep damage rate considering pure mode II loading: η

considering a logarithmic scale, Maxwell derived models presented a linear variation of creep damage rate with the evolution on the viscous parameter, while the Burgers derived model, such as KRB, KRBS, and LMB showed a tendency to present a local maximum. It can be concluded that the increase in the viscous parameter allows a decrease in the creep damage rate, in general terms.

Stiffness (R) is also analysed, being other rheological model taken into account in the following laws. KRVK, KRB, KRVKS, KRBS, LMVK, LMB, LVKH, and LMBH. Figure 4.42 presents the corresponding parametric analysis.

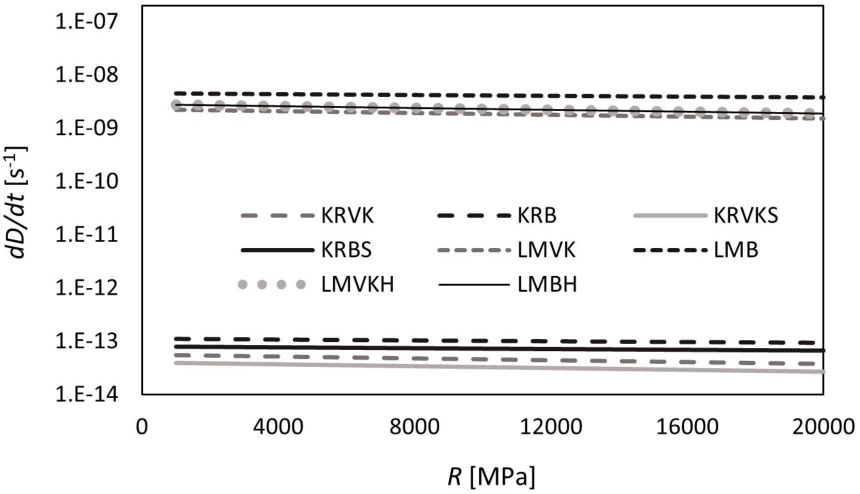

Figure 4.42: Parametric effects on the creep damage rate considering pure mode II loading: R

In comparison to pure mode I loading, pure mode II loading is even less sensible to changes in stiffness. Within the analysed range, Liu-Murakami based laws presented higher creep damage rate values in comparison to the Kachanov-Rabotnov based laws, when stiffness variations are analysed.

Another parameter only captured by KRVK, KRB, KRVKS, KRBS, LMVK, LMB, LMVKH, and LMBH is the retardation time, whose effects on creep damage rate are shown in Figure 4.43.

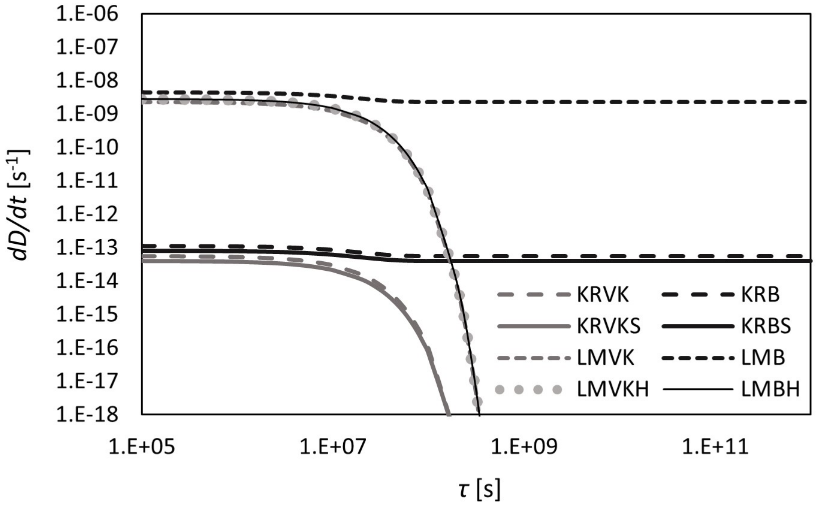

Figure 4.43: Parametric effects on the creep damage rate considering pure mode II loading: τ

Only laws based on the Voigt-Kelvin viscoelastic model are significantly influenced by the retardation, within the studied range, with the exception of LMVKH and LMBH. Between those laws, higher creep damage rates were registered for LMVKH and LMBH, presenting exactly the same response, being followed by LMVK, KRVK, and KRVKS. Considering the other laws, and while varying the retardation time, higher creep damage is verified using LMB, followed by KRB and KRBS.

Analysing exponents, parametrically, Figure 4.44 shows the influence of the parameters θ and ϕ, on creep damage rate, corresponding to Kachanov-Rabotnov and Liu-Murakami based damage laws, respectively.

Despite of the different analysed ranges, the Liu-Murakami based laws, with the exponent ϕ showed higher values of creep damage rate, increasing with the increase of this parameter with a higher slope. Same behaviour was verified for LMMH, LMVKH, and LMBH. Also, a coincident tendency was observed for LMM and LMVK. Coincident behaviours were captured between KRVKS and KRMS, and also KRM and KRVK. Generally, considering variations in both θ and ϕ, laws based on the Burgers viscoelastic model presented slightly higher creep damage rate values. All the differences mentioned are slightly noted. Generally, the difference between the creep damage rate values between laws is not so significant, specially in comparison with the same analysis but considering pure mode I loading, being presented in Figure 4.19.

n and χ are exponents related with laws using modified stress functions, where n is referred to the Kachanov-Rabotnov based damage laws and χ is referred to the Liu-Murakami based damage

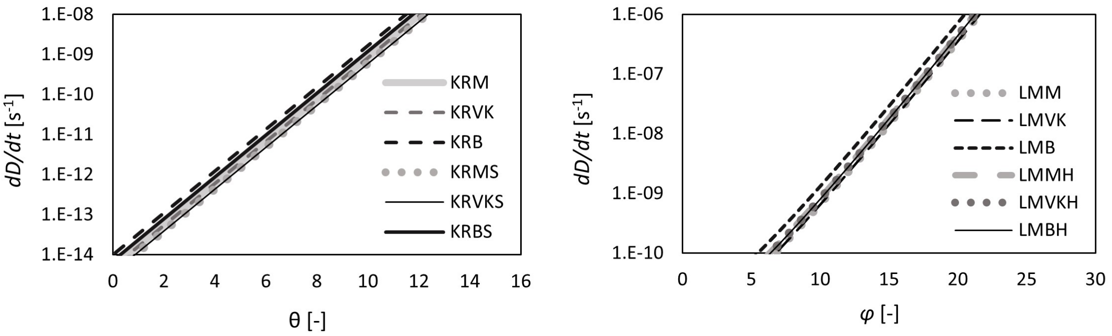

(a) (b)

Figure 4.44: Parametric effects on the creep damage rate considering pure mode II loading: (a) θ, (b) ϕ.

laws. Figure 4.45 is presenting the corresponding influence on creep damage rate.

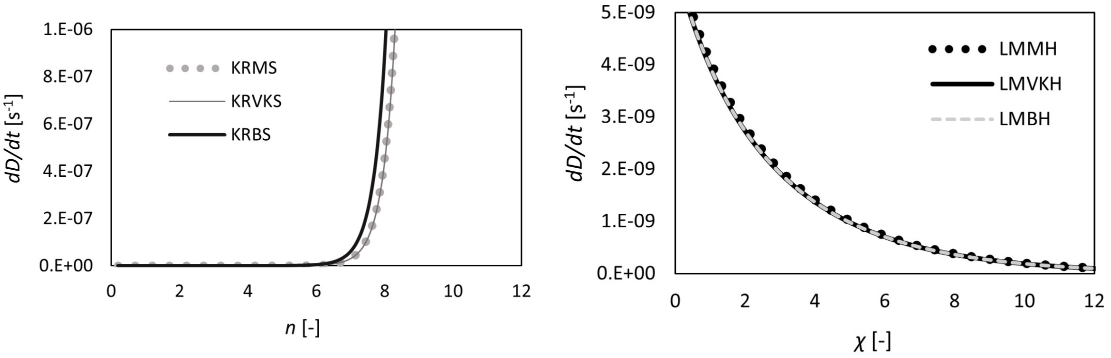

(a) (b)

Figure 4.45: Parametric effects on the creep damage rate considering pure mode II loading: (a) n, (b) χ.

Exactly the same analysis is verified, when compared to pure mode I loading, where corresponding parametric analysis can be assessed in Figure 4.20. Nevertheless, different ranges are shown regarding variations in χ. In fact, lower creep damage rate values are verified, while varying χ, considering pure mode II loading. Coincident behaviours were captured for KRMS and KRVKS. However, slightly higher creep damage rate values were verified for KRBS, while varying n. All the behaviours presented by the Liu-Murakami based damage laws (LMMH, LMVKH, and LMBH) were coincident. An exponential decay, even with a smoother tendency when compared to n, was seen within the range of values tested for χ.

A creep stress threshold (T_c) and the ultimate stress (σ_t) are also included in laws using modified stress functions, introduced by Sun et al. (2012) and Haque and Maurice (2019), respectively. Figure 4.46 is demonstrating the parametric analysis considering T_c and σ_t.

A slightly different tendency is captured when these results are compared to the ones presented for pure mode I loading in Figure 4.21. However, the same comments done in Section 4.3.1.1

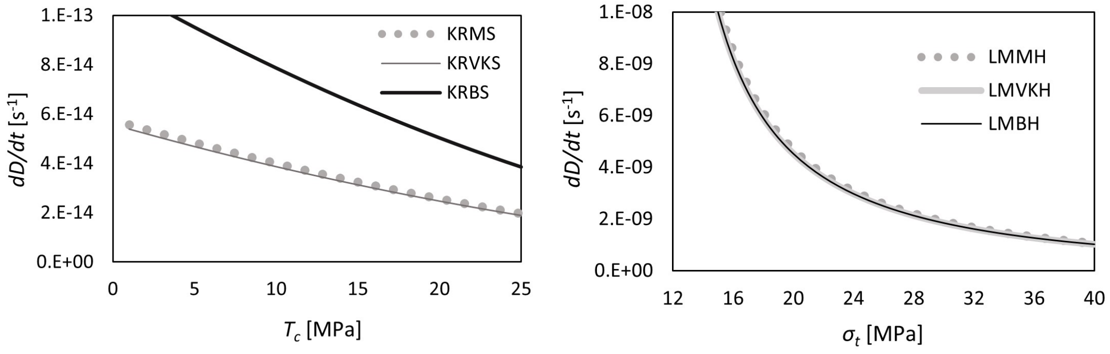

(a) (b)

Figure 4.46: Parametric effects on the creep damage rate considering pure mode II loading: (a) T_c, (b) σ_t.

regarding differences between the analysed laws, when T_c and σ_t are analysed parametrically, are still applicable. Lower values of creep damage rate are verified while varying T_c and σ_t for pure mode II loading. The tendency in reducing creep damage rate, when T_c is increased, is more linear, when compared to the tendency observed while considering pure mode I loading. An exponential decay in creep damage rate is verified by increasing the ultimate stress, considering pure mode II loading. In fact, a different tendency was captured in Figure 4.21, where an exponential decay is not seen. Asymptotic values of creep damage rate would be also achieved, in this case, for higher values of T_c and σ_t, by analysing Figure 4.46.

4.3.2.2 New CZM to Predict Creep under Pure Mode II Loading

Considering the same material properties as presented in Tables 4.4 and 4.5, different dimensions are considered for the geometry, constituting an ENF sample, loaded in 3-point-bending. This model is presented in Figure 3.5, already presented in Chapter 3, demonstrating the geometry, dimensions and boundary conditions. Corresponding dimensions are then summarised in Table 4.10.

Table 4.10: Geometric dimensions: ENF.

$2L$ [mm]	a_0 [mm]	t_s [mm]	t_a [mm]
200	60	2.4	0.2

Using ABAQUS® 6.11, a load of 840 N is applied, constituting a 3-point-bending test, where simple supports are considered at the ends of the lower substrate. This load corresponds to 70% of the maximum sustaining load, whose value is obtained by a FE analysis, using commercial CZM and XFEM approaches. Corresponding results are demonstrated in Figure 4.47

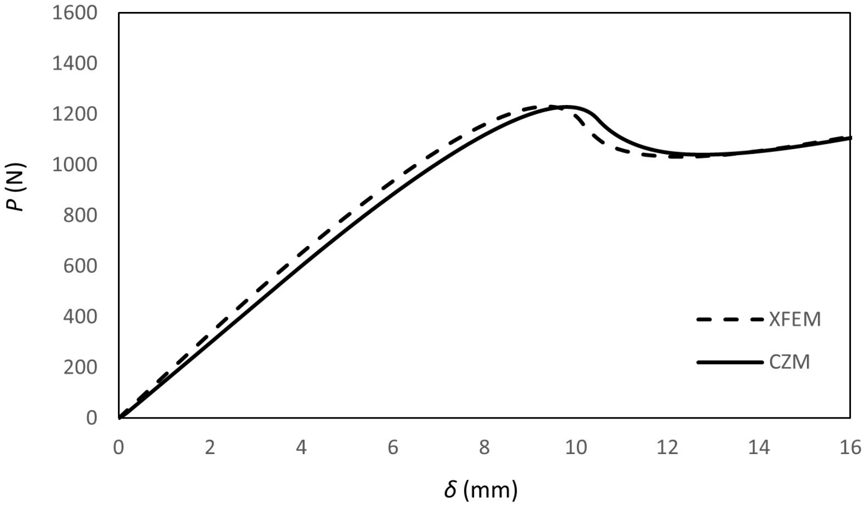

Figure 4.47: Strength prediction: ENF.

Quadrilateral plane stress elements were used, with 8 nodes, being known as CPS8 following the ABAQUS® nomenclature. A total of 1264 of solid elements is used, while a total of 316 cohesive elements are presented in the model. Corresponding mesh is shown in Figure 4.48, where both undeformed and deformed shapes are presented.

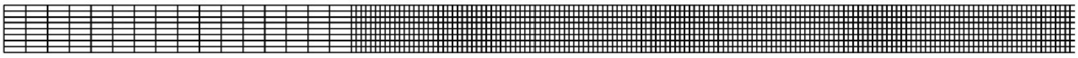

(a)

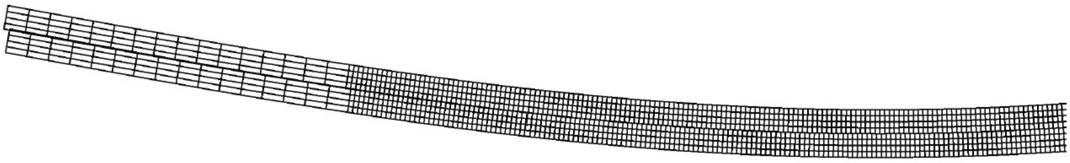

(b)

Figure 4.48: ENF mesh configuration: (a) undeformed, (b) deformed.

A user subroutine containing a bilinear cohesive law for pure mode II loading was developed and implemented in ABAQUS$^{®}$ (Figure 4.49), containing a new cohesive zone model in order to predict creep fracture behaviour. Considering the first linear regime, below ultimate strength, the shear traction (τ_r) is related with displacements (δ_r) as follows:

$$\tau_r = k\delta_r \tag{4.183}$$

where for pure mode II loading, k still corresponds to the interfacial stiffness, assuming the initial value of $1.0 \times 10^6\ N/mm^3$ (Gonçalves et al., 2000). The damage onset relative displacement (δ_{r_u}) is obtained from the local strength τ_{r_u}. A linear softening relationship, for conditions after damage onset, is established between shear traction and relative displacements, occurring at the homologous points belonging to the cohesive element faces:

$$\tau_r = (1-D)\,k\delta_r \tag{4.184}$$

while D the damage parameter, ranging in the same manner as referred previously for pure mode I loading, in Section 4.3.1.2, being governed by equation 4.178.

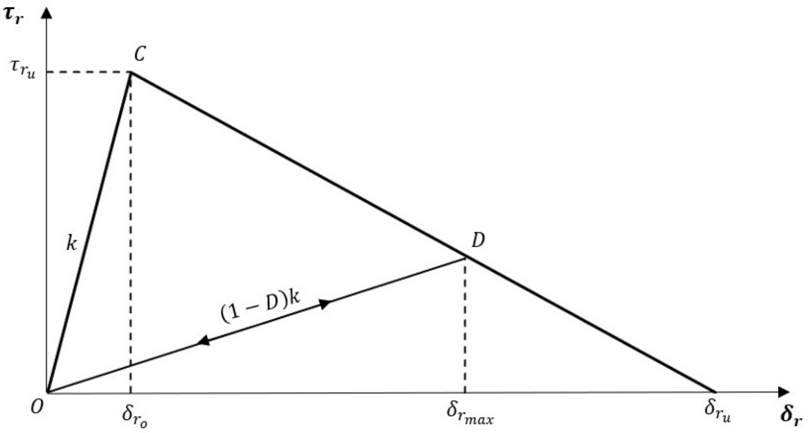

Figure 4.49: Bilinear cohesive law for pure mode II loading.

The parameter $\delta_{r_{max}}$ is updated continuously, where it is increased by the applied remote loading. As aforementioned, equation 4.178 remains valid for quasi-static monotonic loading. In the case of pure mode II loading, G_{II_c}, which is the corresponding fracture energy, is determined by the area OCD (Figure 4.49). The ultimate relative displacement (δ_{r_u}) is then obtained:

$$\delta_{r_u} = \frac{2G_{II_c}}{\tau_{r_u}} \tag{4.185}$$

Modelling creep damage cohesively, in terms of pure mode II loading, the formulation described for pure mode I loading in Section 4.3.1.2 remains valid, while considering equations 4.180, 4.181 and 4.182.

Using this finite element model, while using the described CZM law, the corresponding creep response is presented in Section 4.3.2.3.

4.3.2.3 Creep Response

This section presents the creep responses considering the proposed damage laws. Parameters presented in Table 4.9 were imposed. In addition, damage laws presented by Sun et al. (2012) and Haque and Maurice (2019) were also implemented. In the model presented in equation 4.136, a value of 10 MPa is considered for T_c, 50000 MPa is considered for T_0, and n is considered to be equal to 2. For the model proposed in Haque and Maurice (2019), being exposed in equation 4.155, Q was considered to be 2.00×10^{-11}, still imposing σ_t as 25 MPa, ϕ as 12, and χ as 2. It seemed that the law proposed by Sun et al. (2012) is not suitable for pure mode II, since numerical stability is achieved only by using fictitious values for the reference stress (T_0). This is a consequence of using lower values of n. In fact, higher values increase significantly the computational time, and leads to a more difficult numerical calibration. This is deeply discussed in Section 4.3.2.4, presenting an additional parametric study, where effects on the curve shape are assessed. It has to be mentioned that all the parameters were calibrated in order to provide creep times within a range between 10 and 15 hours, considering 840 N. This assumption is based on data presented in the literature (Neto et al., 2022a), but it requires clearly experimental validation, and also numerical calibration after experimental work, which constitutes a future perspective.

Damage laws proposed by Sun et al. (2012) and Haque and Maurice (2019) present creep responses shown in Figure 4.50.

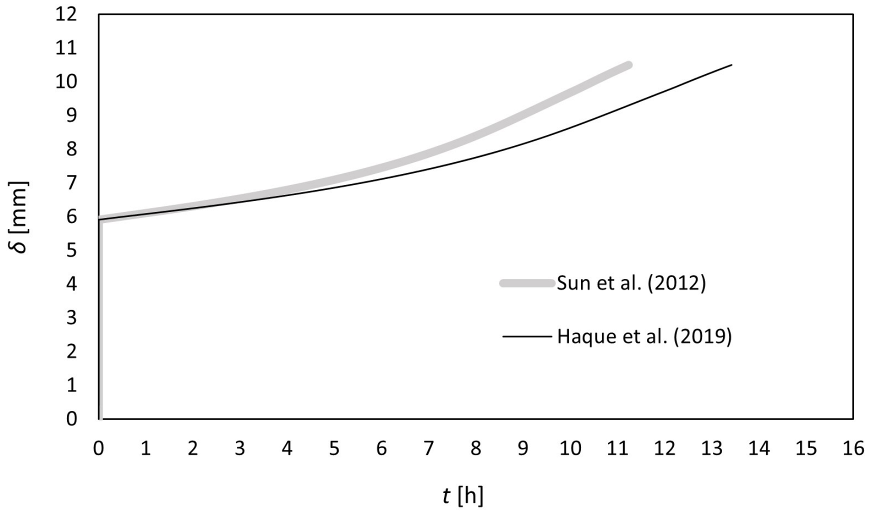

Figure 4.50: Creep response, considering pure mode II loading, of damage laws proposed by Sun et al. (2012) and Haque and Maurice (2019).

As aforementioned, the model developed by Sun et al. (2012) is significantly more unstable in the determination of the creep behaviour in pure shear conditions. A difference is demonstrated between creep responses produced by laws developed by Sun et al. (2012) and Haque and Maurice (2019). A higher creep life time is achieved by using the damage law proposed by Haque and Maurice (2019). A higher slope related to the secondary phase is registered by using the method proposed by Sun et al. (2012). In both laws, the separation between secondary and tertiary phases is not clear.

Although, these models can be included in rheological laws, where different responses are captured between considering a modified with the stress degradation concept. Figure 4.51 is presenting the comparison between all laws based on the Maxwell viscoelastic model (KRM, KRMS, LMM, and LMMH).

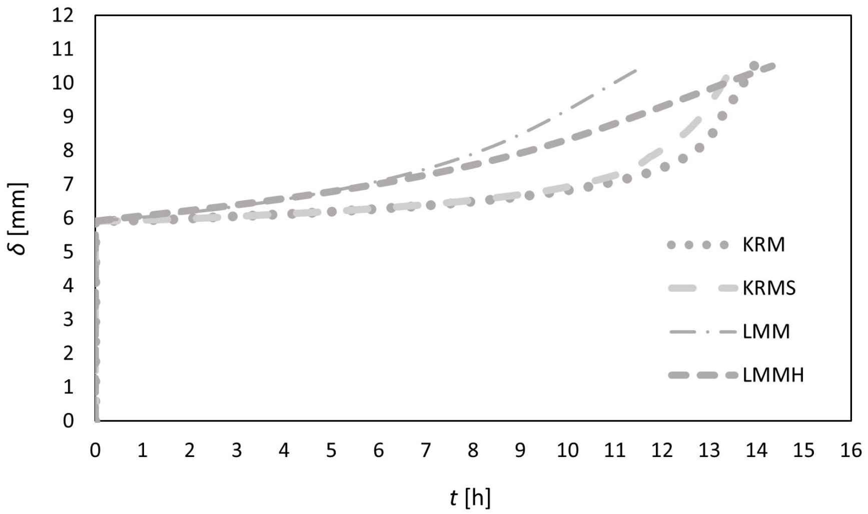

Figure 4.51: Creep response, considering pure mode II loading, of damage laws based on the Maxwell viscoelastic model.

Different responses are notable considering KRM and LMM, in comparison to KRMS and LMMH. A higher slope associated with the creep secondary phase is demonstrated by KRM and LMM. In addition, the slope is so high that the distinction between secondary and tertiary phase is not clearly defined. Due to the higher increasing tendency associated with KRM and LMM, when compared to KRMS and LMMH, creep time was generally lower, when compared to KRMS and LMMH. The secondary phase showed by KRMS and LMMH was coincident, however, the tertiary phase is slightly more abrupt if KRMS is used. Nevertheless, the displacement increasing tendency was higher by using LMM, rather than using KRM.

Same analysis is performed in Figure 4.52, but considering laws based on the Voigt-Kelvin viscoelastic model.

Similar conclusions are taken when KRVK, KRVKS, LMVK, and LMVKH are analysed, in comparison with what was mentioned by observing Figure 4.51. Liu-Murakami based laws (LMVK and LMVKH) presented slightly lower creep life time when compared to Kachanov-Rabotnov based laws (KRVK and KRVKS). A distinction between secondary and tertiary phase is not also captured while using KRVK and LMVK, similarly to what was verified by using KRM and LMM.

Also laws based on the Burgers viscoelastic model (KRB, KRBS, LMB, and LMBH) are analysed in terms of creep response, being shown in Figure 4.53.

As previously mentioned, laws derived using the Burgers viscoelastic model are generally more conservative when compared to laws derived using Maxwell or Voigt-Kelvin viscoelastic models. Consequently, KRB, KRBS, LMB, and LMBH provided considerably lower creep life time values, in comparison to damage laws whose creep responses were presented previously in Figures 4.51 and 4.52. In this case, a life time of between 5 and 7 hours was verified. Same

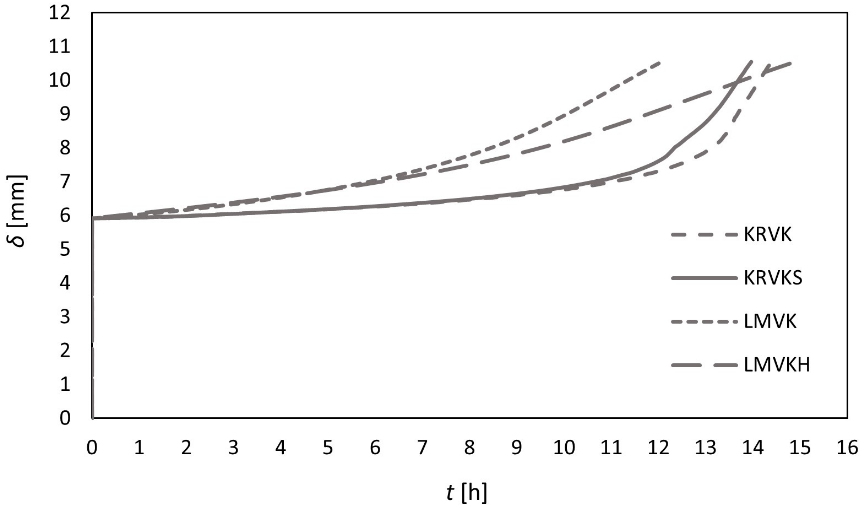

Figure 4.52: Creep response, considering pure mode II loading, of damage laws based on the Voigt-Kelvin viscoelastic model.

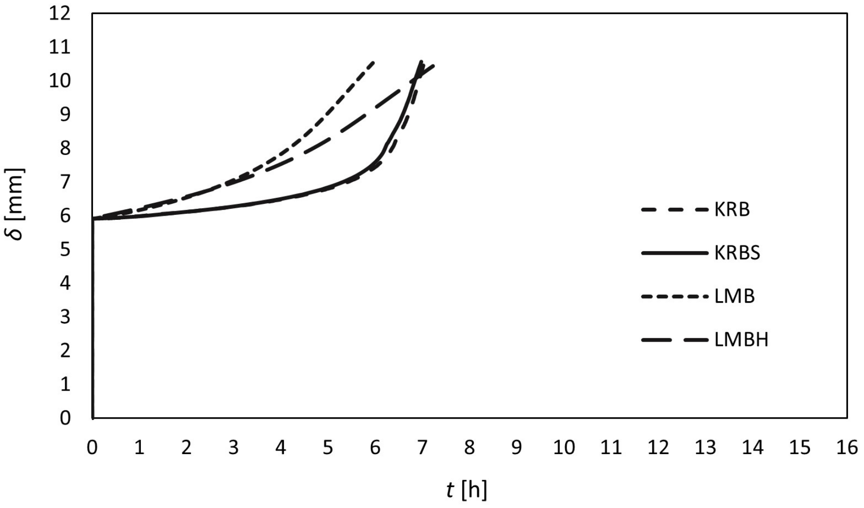

Figure 4.53: Creep response, considering pure mode II loading, of damage laws based on the Burgers viscoelastic model.

numerical tendencies are demonstrated: secondary and tertiary phases are not well captured by KRB and LMB, and Liu-Murakami based damage laws (LMB and LMBH) presented a more pronounced creep damage, in general. This last effect is also demonstrated in the tertiary phase for LMBH.

All laws are directly compared considering creep responses presented in Figure 4.54. The conservatism associated to laws based on the Burgers viscoelastic model is confirmed. In addition, it is also verified that laws based on the Maxwell model are slightly more conservative when compared to laws based on the Voigt-Kelvin model. The same level of conservatism, in terms of the prediction of creep life time is observed when Kachanov-Rabotnov based damage laws are compared to Liu-Murakami based damage laws. KRM, KRVK, KRB, LMM, LMVK, and also LMB were not capable to demonstrate the correct creep response. On the other hand, KRMS, KRVKS, KRBS, LMMH, LMVKH, and LMBH confirmed responses shown by models proposed by Sun et al. (2012) and Haque and Maurice (2019), imposing comparable parameters, demonstrating literature validation. Further experimental validation is needed also in this case where pure mode II loading is considered. Laws proposed by Sun et al. (2012) and Haque and Maurice (2019) are appropriate for metallic alloys. Parameters should be calibrated in the future for adhesives, considering properties presented in 4.5 and the proposed laws are capable for that purpose.

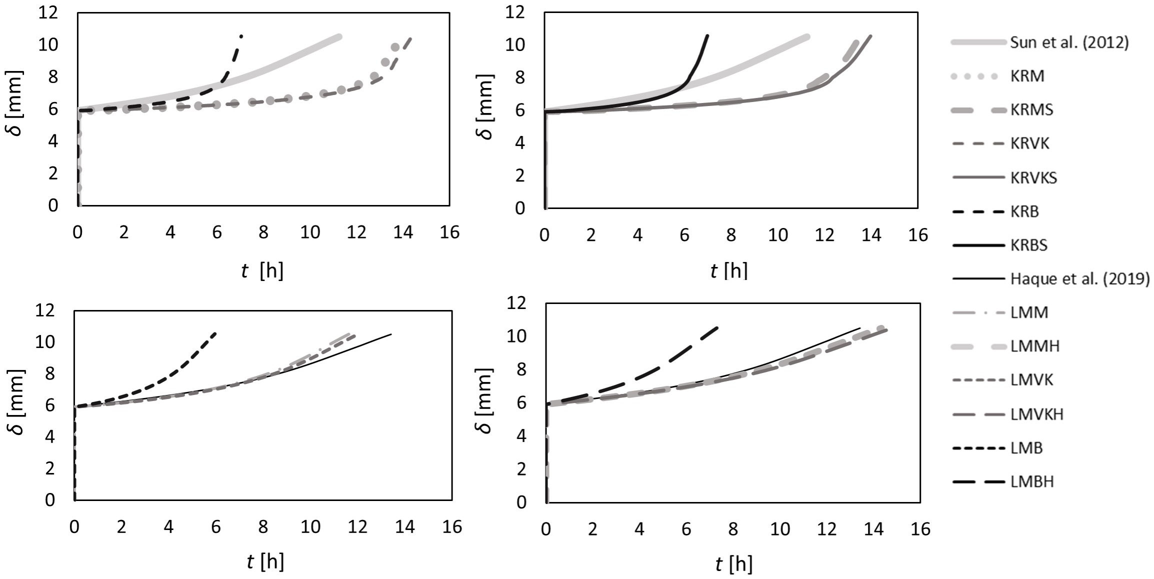

Figure 4.54: Creep response comparison, considering pure mode II loading, between the proposed laws and the literature (Sun et al., 2012; Haque and Maurice, 2019).

4.3.2.4 Parametric Effects on the Curve Shape

Different values for exponents θ, n, ϕ, and χ are analysed, considering pure mode II loading. In this case, parametric effects on numerical accuracy are not presented, since significant differences are not demonstrated. It seemed that, in pure mode II loading, the numerical accuracy is essentially the same considering any law or any parameter. Similarly to what was presented considering pure mode I loading, only laws based on the Voigt-Kelvin viscoelastic model are used for this analysis. In fact, the Voigt-Kelvin viscoelastic model is more appropriate for creep, rather than relaxation, according to Findley et al. (1976).

Figure 4.55 presents the effect of θ on the curve shape related to the creep response. This parameter is associated with the Kachanov-Rabotnov damage based laws.

It is notable that the separation between the secondary and tertiary phases is easily captured by using KRVKS, rather than KRVK, as it was possible to observe in the last section. Considering KRVK, the same slope related to the secondary creep is verified while varying the value of θ.

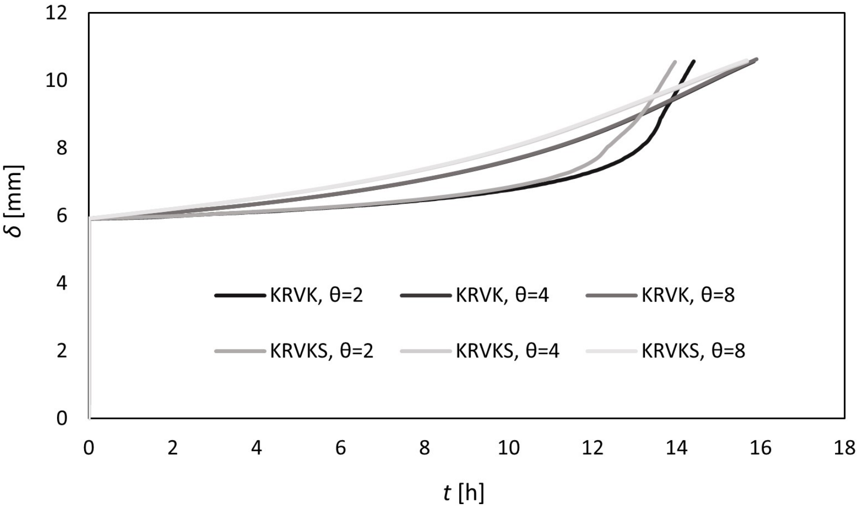

Figure 4.55: Effects of θ on the curve shape considering pure mode II loading.

Nevertheless, higher slopes related to the tertiary phase is registered by increasing the value of θ. On the other hand, considering KRVKS, an increase in the slope related to secondary creep is captured by increasing the value of θ. A smoother transition between secondary and tertiary phases is verified by increasing the value of θ.

Kachanov-Rabotnov based damage laws, using the modified stress concept introduced by Sun et al. (2012), are influenced by an exponent n. Corresponding analysis on the curve shape, while using KRVKS, is performed by observing the Figure 4.56.

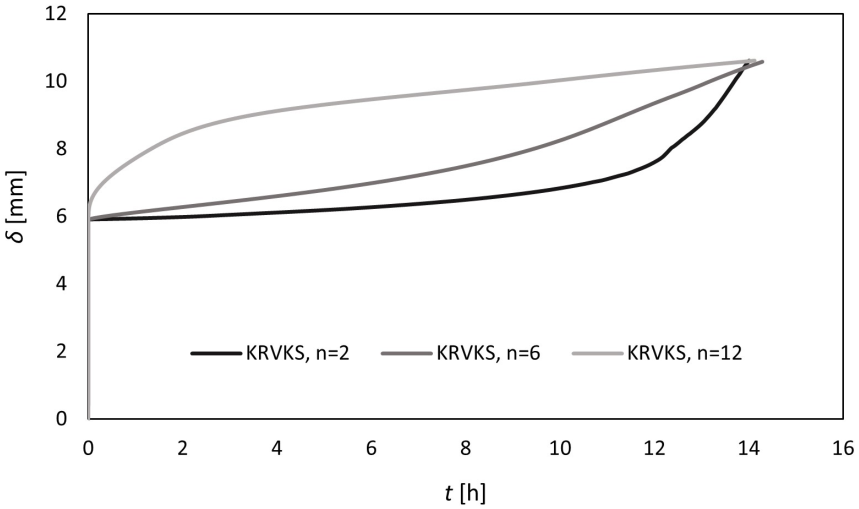

Figure 4.56: Effects of n on the curve shape considering pure mode II loading.

An abrupt rupture is only captured by using lower values of n, where a separation between secondary and tertiary creep phases is clearly defined. Nevertheless, this separation is vanished when n is increased. This is not necessarily a numerical artefact. Depending on the adhesive properties, such as ductility, this type of behaviour can be possible to occur. For higher values of n, the transition between primary and secondary phases is significantly smoother. In fact, the tertiary phase is not captured. After a total damage of the adhesive layer, the displacement state tends to stabilise in a given value. Consequently, an abrupt rupture is not verified, which can be possible in ductile adhesives.

The effect of ϕ is presented in Figure 4.57, where this parameter is directly related only with Liu-Murakami damage based laws.

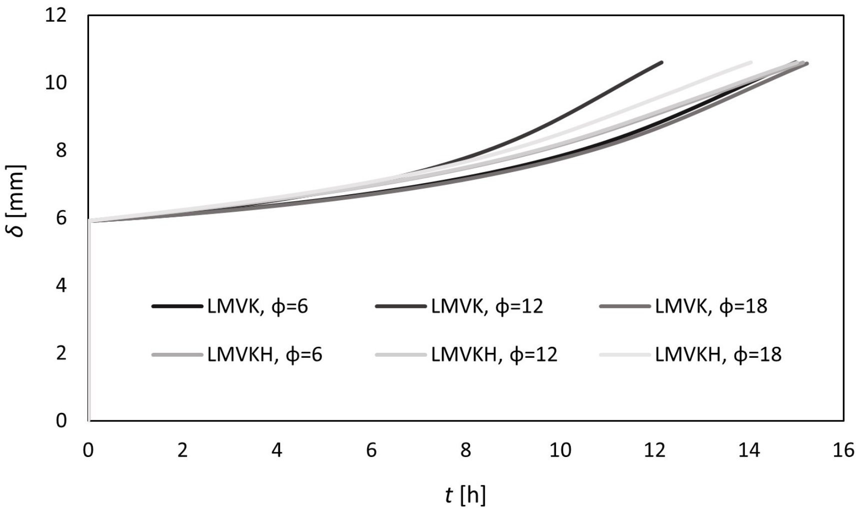

Figure 4.57: Effects of ϕ on the curve shape considering pure mode II loading.

Identical curve shapes are captured by varying the value of ϕ. For an increase in the value of ϕ, a smoother transition between secondary and tertiary phases are registered. Similarly to what was verified when variations in θ were considered, using LMVKH with higher values of ϕ promotes a higher slope related to the secondary phase. On the other hand, almost the same slope is found by using LMVK, considering the secondary creep phase, with minor differences regarding the tertiary phase.

Another exponent related solely to the Liu-Murakami based damage laws is χ, whose influence on the curve shape is assessed by analysing Figure 4.58.

An abrupt rupture is not captured by using higher values of χ, as a smother transition between primary and secondary creep phases is verified. It seems that higher values of χ can be more suitable to predict creep behaviour of ductile adhesives. Instead of observing a tertiary phase, the displacement state tends to converge, when χ=12 is imposed. In fact, this behaviour is analogous to the behaviour observed for higher values of n, when KRVKS is used. Comparing both laws, KRVKS and LMVKH, the observed effect corresponding to a smoother increase in displacement is more pronounced while using LMVKH with higher values of χ.

Every parameter that was analysed, considering all the proposed damage laws can be suitable to model the creep behaviour of different adhesives, depending on the corresponding properties.

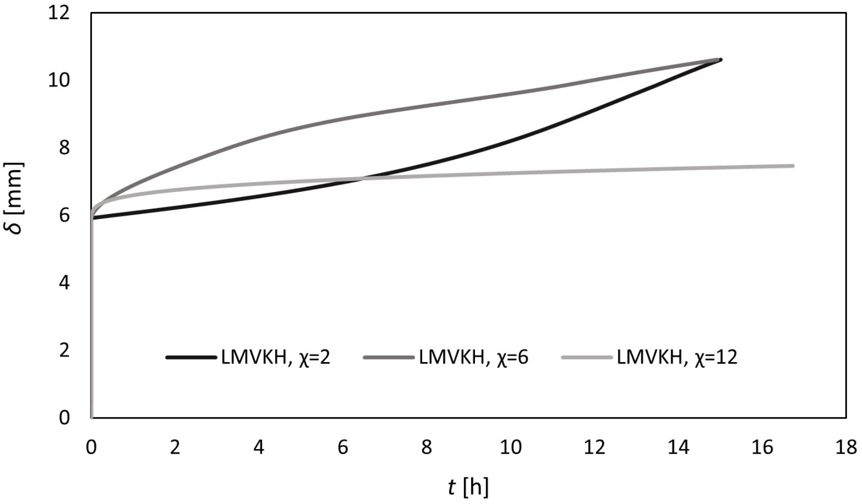

Figure 4.58: Effects of χ on the curve shape considering pure mode II loading.

As a future work, experimental data will be revealed, and the best model with the most suitable parameters will be selected for a given adhesive.

4.3.2.5 Numerical Validation

Similarly to what was presented for pure mode I loading in Section 4.3.1.5, a numerical validation is performed but considering pure mode II loading, in relation to experimental results shown in Chapter 3. Only Voigt-Kelvin based laws (KRVK, LMVK, KRVKS, and LMVKH) were also used, since a better behaviour for creep representation is stated in the literature (Findley et al., 1976). In fact, this type of laws include more physical parameters, such as stiffness, instead of only considering viscous effects. Table 4.11 presents the calibrated parameters (A and Q) for KRVK and LMVK, while Table 4.12 demonstrates calibrated parameters (B and Q) for KRVKS and LMVKH. Even being solely material dependent, which is related with the ductility level of the adhesive, θ and ϕ are also included in referred tables.

Table 4.11: Calibrated parameters of KRVK and LMVK for numerical validation considering pure mode II loading.

Parameter	KRVK	LMVK
A[-]	1.7×10^{-8}	—
Q[-]	—	3.2×10^{-2}
θ[-]	4	—
ϕ[-]	12	—

Figures 4.59 and 4.60 present the numerical validation for the considered laws, at three different loading conditions: 70%, 75%, and 80% of P_{max}.

Table 4.12: Calibrated parameters of KRVKS and LMVKH for numerical validation considering pure mode II loading.

Parameter	KRVKS			LMVKH		
	$n = 2$	$n = 6$	$n = 12$	$\chi = 2$	$\chi = 6$	$\chi = 12$
B[MPa^{1-n}]	2.5×10^{-6}			—	—	—
Q[-]	—	—	—	1.0		
θ[-]	4			—	—	—
ϕ[-]	—	—	—	12		

The same parametric values were imposed for relative applied loads. An appropriate law is independent of load level. Differently from what was considered for pure mode I loading in Section 4.3.1.5, the same proportional empirical parameters (A, B, or Q) were considered for different power constants (n and χ). The higher sensitivity related pure mode I loading, when compared to pure mode II loading, was also proved for pure mode II loading.

Laws were generally calibrated for scenarios where a relative applied load of 80% is applied. It was proved that KRVK, LMVK, and KRVKS are unsuitable for numerical predictions under creep threshold (70% and 75% of P_{max}). For a relative applied load of 80%, KRVK and LMVK demonstrated the capability to replicate the slope of the secondary creep phase. In fact, considering experimental results for the two specimens subjected to a relative load of 80% (Figure 3.23) in Chapter 3, also the creep lifetime was well replicated by KRVK and LMVK.

KRVKS demonstrated to be inappropriate to represent creep behaviour in pure mode II loading for all relative applied loads, when compared to other laws, such as KRVK, LMVK, and even LMVKH. Under creep threshold, LMVKH, using $\chi = 6$, reproduced perfectly the creep behaviour for pure mode II loading, for both relative loads of 70% and 75%. For the same proportional empirical load (Q), using $\chi = 2$ is more suitable for a representative behaviour under a relative load of 80%, rather than using $\chi = 12$. The slope related to steady-creep was well replicated. However, creep lifetime was slightly over estimated, but being still included in a reasonable range. In fact, beyond creep threshold, the ductility level of the adhesive is reduced, explaining the use of a lower value of χ. A unitary Q was used for all loading conditions, demonstrating the robust behaviour of LMVKH, and its superiority when compared to KRVKS in terms of the prediction of the creep behaviour under pure mode II loading.

There is a clear difference in terms of behaviour between under and beyond creep threshold conditions, having impacts on numerical results. The derived numerical laws seemed to provide the capability of being load independent, but the independence of being under or beyond creep threshold seem to be almost unfeasible. The use of LMVKH, associated to the parametric value $\chi = 12$ should be combined with the use of this same law, but associated to the parametric value $\chi = 2$, or with other laws such as KRVK and LMVK.

As a final recommendation in terms of numerical implementation is to use the LMVKH law, associated to the use of $\chi = 12$, for under creep threshold conditions (relative loads below 75%).

LMVK is recommended to be used beyond creep threshold. As a future perspective, a computational tool can be developed in order to combine these laws in a complete prediction of the creep behaviour under pure mode II loading. In fact, this could be implemented in the user subroutine, where the law is switched from LMVKH to LMVK for higher relative loads than 75%.

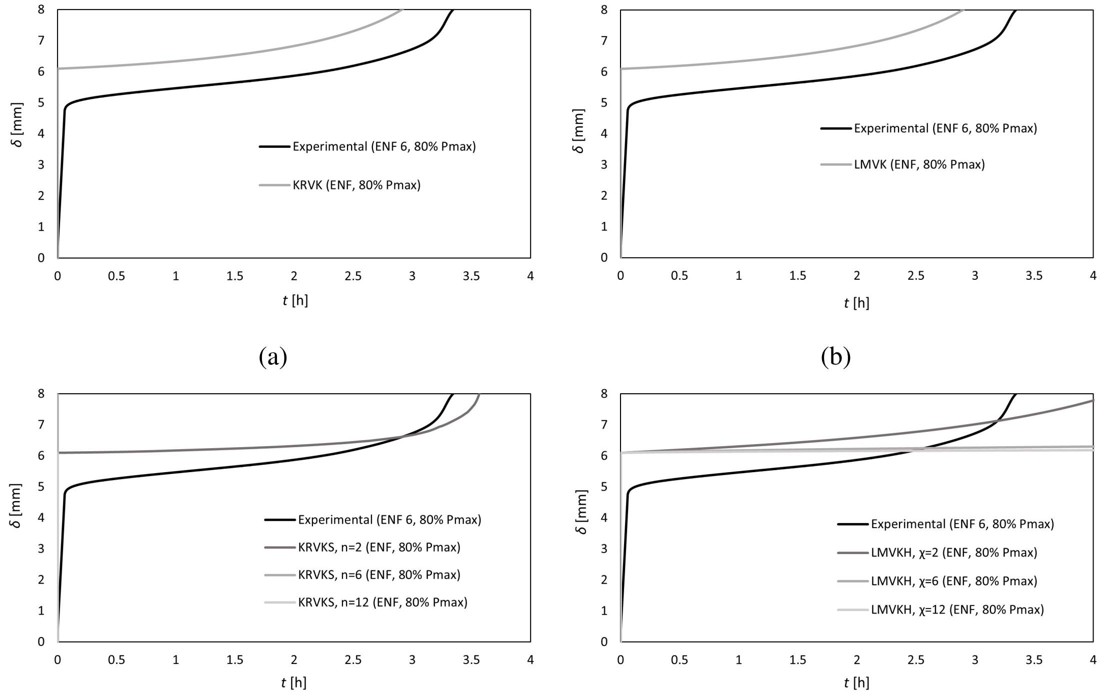

(a) (b)

(c) (d)

Figure 4.59: Numerical validation considering pure mode II loading: (a) KRVK (80% P_{max}), (b) LMVK (80% P_{max}), (c) KRVKS (80% P_{max}), (d) LMVKH (80% P_{max}).

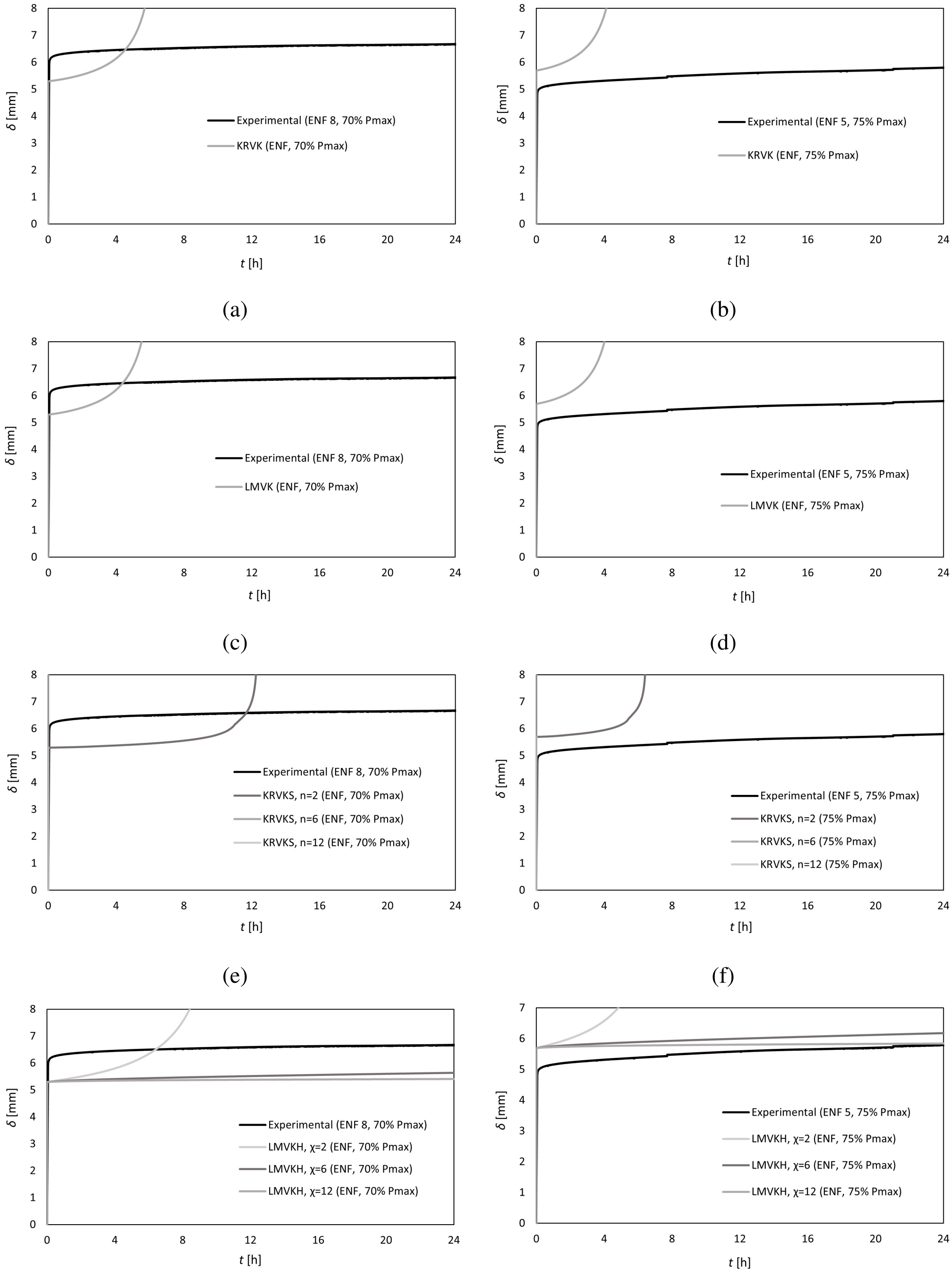

(a) (b)

(c) (d)

(e) (f)

(g) (h)

Figure 4.60: Numerical validation considering pure mode II loading: (a) KRVK (70% P_{max}), (b) KRVK (75% P_{max}), (c) LMVK (70% P_{max}), (d) LMVK (75% P_{max}), (e) KRVKS (70% P_{max}), (f) KRVKS (75% P_{max}), (g) LMVKH (70% P_{max}), (h) LMVKH (75% P_{max}).

Chapter 5

Conclusions

In this work, creep characterization of CFRP/epoxy bonded joints is analysed under pure mode I and pure mode II loading using the DCB and ENF tests, respectively. Experimental tests and numerical analyses using a new developed CZM for creep analysis were performed. This work can be considered a preliminary and crucial task aiming to develop a CZM able to deal with general mixed-mode I+II loading conditions under creep which is essential envisaging its application to structural details as is the case of composite bonded repairs. The establishment of several creep damage laws to employ in a new developed cohesive zone modelling environment was allowed, while using a commercial finite element software as an interface. Creep crack growth was widely investigated in the literature but for metallic materials, stating several laws. Conducted studies were able to join all these concepts from the literature, deriving creep damage laws appropriated for composite bonded joints/repairs. Experimental creep tests were performed, being used for parametric calibration, and corresponding numerical validation.

Regarding results from experimental tests both considering pure modes I and II loading conditions, double-cantilever-beam, as well as end-notched-flexure specimens were tested for several load levels. Quasi-static tests were performed, only for strength measurements, not inducing any damage to the specimens. The maximum load corresponding to the strength of a given specimen was taken as a reference for load application. Applied loads corresponding to 70%, 75%, 80%, and 85% of the maximum sustaining load were imposed considering pure mode I loading. Only results for 80% and 85% of relative loads demonstrated the presence of tertiary phase and, consequently, of creep failure. For relative loads of 80%, double-cantilever-beam specimens were able to show a creep lifetime of around 16 hours, while the application of a relative load of 85% corresponds to creep lifetimes around 9 hours. A creep threshold corresponding to a relative load of 75% was revealed. For specimens tested with relative loads of 70% and 75%, the displacement started to decrease after 1 or 2 hours of testing. Nevertheless, it was not completely proved that this argument is the ultimate justification. A specimen tested with a relative load of 85%, demonstrated a similar phenomenon, proving that it can be related also to the presence of material or geometrical defects. It was concluded that the creep behaviour of pure mode I loading is notably sensible to any testing condition, such as load level, specimen geometry and dimensions. Regarding pure mode II loading, the end-notched-flexure specimens were tested considering also relative loads of 70%, 75%, 80% and 85%. The same procedure was followed, so that the strength properties were measured *"a priori"*, with a quasi-static test, but not inducing any damage to the specimens. A creep threshold was also found, corresponding to a relative load of 75%. Regarding displacement evolution, under creep loading, a plateau was verified after some testing hours, depending on the amount of load. An increase in the applied load, allowed an increase in the slope of the curve related to the secondary creep phase, retarding the plateau state of displacement. Relative loads of 80% and 85% provided conditions for the presence of tertiary creep phase. A creep lifetime of around 4 hours resulted from an application of a relative load of 80%. Higher loads, such as corresponding to 85% of the maximum sustaining load, only demonstrated results with around 20 minutes of creep testing. This level of applied load was considered as the transition between creep and quasi-static loading. An additional study was performed regarding failure modes, specifically for pure mode II loading. It was concluded that the adhesive layer presents a lighter aspect when subjected to higher loads, or longer creep times, even for under creep threshold scenarios. Generally, it can be concluded that the creep behaviour associated to pure mode II loading conditions demonstrated a significant lower sensitivity to testing conditions, when compared to cases under pure mode I loading scenarios.

Combining concepts of already stated creep damage laws for metallic materials, and also mathematical formulations from classic viscoelasticity, twelve creep damage laws, appropriate for adhesively bonded joints or repairs, were derived: KRM, KRVK, KRB, LMM, LMVK, LMB, KRMS, KRVKS, KRBS, LMMH, LMVKH, and LMBH. These laws are adequate for numerical implementations in terms of cohesive zone modelling within a finite element interface. Considering both pure modes I and II, parametric studies were performed *"a priori"*, in order to access the sensitivity of the derived laws to different parametric values. Numerical results of KRVK, LMVK, KRVKS, and LMVKH were then directly compared with experimental data. For pure mode I loading, relative loads of 80% and 85% were considered. Only proportional and power-law parameters were calibrated according to experimental results. KRVK and LMVK demonstrated similar results, being the most suitable from creep lifetime prediction, whose parameters are independent on the difference in terms of applied load. KRVKS and LMVKH, associated with $\chi = 12$, seemed to be more suitable for the prediction of the slope related to steady-creep phase, but the parameters are load dependent, which is unsuitable for a complete creep behaviour representation. A combined use of KRVK and KRVKS or LMVK and LMVKH is then recommended, which is possible to be implemented with a specific computational tool, whose applications constitute a scope for future perspectives. Same laws were also validated but for pure mode II loading conditions, while considering relative loads of 70%, 75%, and 80%. LMVKH, associated with the use of $\chi = 6$, was more suitable to represent the mechanical behaviour under creep threshold conditions (70% and 75% of P_{max}). KRVKS seemed to be completely inappropriate for creep characterisation under pure mode II loading. In fact, the superiority in terms of numerical robustness of LMVKH, when compared to KRVKS was clearly proved. A distinction between under and beyond creep threshold conditions is numerically unavoidable. Consequently, KRVK and LMVK were more suitable for creep characterisation under a relative applied of 80%. A combination of the laws LMVKH and LMVK, between under and beyond creep threshold, respectively, is recommended, and this is possible to implement with the aid of a computational tool. Similarly to pure mode I loading, it constitutes a future perspective.

This dissertation presented the basis on the numerical prediction of the creep behaviour of bonded joints/repairs, constituting a basis for future developments, specially in terms of mixed-mode I+II loading.

Bibliography

Airbus. Airbus A350 XWB starts its China tour with debut at Zhuhai Airshow. https://www.airbus.com/en/newsroom/press-releases/2016-10-airbus-a350-xwb-starts-its-china-tour-with-debut-at-zhuhai-airshow, 2016. [Accessed: 31-January-2023].

D.L. Alves, R.D.S.G. Campilho, R.D.F. Moreira, F.J.G. Silva, and L.F.M. da Silva. Experimental and numerical analysis of hybrid adhesively-bonded scarf joints. *Int J Adhes Adhes*, 83:87–95, 2018. doi: 10.1016/j.ijadhadh.2018.05.011.

E.N.C. Andrade. On the Viscous Flow in Metals, and Allied Phenomena. *Proc R Soc A*, 84:1–12, 1910. doi: 10.1098/rspa.1910.0050.

E. Arrospide, I. Bikandi, I. García, G. Durana, G. Aldabaldetreku, and J. Zubia. 7. Mechanical properties of polymer-optical tests. *Polymer Optical Fibres*, pages 201–216, 2017. doi: 10.1016/B978-0-08-100039-7.00007-5.

R.W. Bailey. The Utilization of Creep Test Data in Engineering Design. *Proceedings of the Institution of Mechanical Engineers*, 131:131–349, 1935. doi: 10.1243/PIME_PROC_1935_131_012_02.

A. Baker. Fibre composite repair of cracked metallic aircraft components — practical and basic aspects. *Compos*, 18:293–308, 1987. doi: 10.1016/0010-4361(87)90293-X.

A. Baker, R.J. Chester, G.R. Hugo, and T.C. Radtke. Scarf repairs to highly strained graphite/epoxy structure. *Int J Adhes Adhes*, 19:161–171, 1999. doi: 10.1016/S0143-7496(98)00031-1.

A. Baker, F. Rose, and R. Jones. *Advances in the Bonded Composite Repair of Metallic Aircraft Structure*, volume 1. Elsevier, Ltd., First edition, 2002. ISBN 0-08-042699-9.

A. Baker, A.J. Gunnion, and J. Wang. On the Certification of Bonded Repairs to Primary Composite Aircraft Components. *J Adhes*, 91:4–38, 2015. doi: 10.1080/00218464.2014.883315.

N.G.C. Barbosa, R.D.S.G. Campilho, F.J.G. Silva, and R.D.F. Moreira. Comparison of different adhesively-bonded joint types for mechanical structures. *Appl Adhes Sci*, 6, 2018. doi: 10.1186/s40563-018-0116-1.

G.I. Barenblatt. Yielding of steel sheets containing slits. *Adv Appl Mech*, 7:55–129, 1962. doi: 10.1016/S0065-2156(08)70121-2.

C.E. Beck. Advanced composite structure repair. *Adv Compos Mater*, pages 1580–1584, 1980. doi: 10.1016/B978-1-4832-8370-8.50124-8.

H. Bendemra, P. Compston, and P.J. Crothers. Optimisation study of tapered scarf and stepped-lap joints in composite repair patches. *Compos Struct*, 130:1–8, 2015. doi: 10.1016/j.compstruct.2015.04.016.

F. Benyahia, M.F. Bouanani, A. Albedah, B.B. Bouiadjra, and T. Achour. Effect of water absorption on the adhesive damage in bonded composite repair of aircraft structures. *Mater Des*, 57: 435–441, 2014. doi: 10.1016/j.matdes.2013.12.081.

J. Bishopp. Aerospace: A pioneer in structural adhesive bonding. *Handbook of Adhesives and Sealents*, 1:215–347, 2005. doi: 10.1016/S1874-5695(02)80006-9.

A. Bona. Theoretical and Experimental Review of Applied Mechanical Tests for Carbon Composites with Thermoplastic Polymer Matrix. *Proceedings of the Third Conference on Object-Oriented Technologies and Systems*, 4(257):55–65, 2019. doi: 10.2478/tar-2019-0023.

J.L. Bouvard, J.L. Chaboche, F. Feyel, and F. Gallerneau. A cohesive zone model for fatigue and creep-fatigue crack growth in single crystal superalloys. *Int J Fatigue*, 31:868–879, 2009. doi: 10.1016/j.ijfatigue.2008.11.002.

C. Brauwens-Crowet, J.C. Bauwens, and G. Homes. Tensile yield stress behaviour of glassy polymers. *J Polym Sci*, 7:735–742, 1969.

C.B.G. Brito, R.C.M. Sales, and M.V. Donadon. Effects of temperature and moisture on the fracture behaviour of composite adhesive joints. *Int J Adhes Adhes*, 100, 2020. doi: 10.1016/j.ijadhadh.2020.102607.

R.F.N. Brito, R.D.S.G. Campilho, R.D.F. Moreira, I.J. Sánchez-Arce, and F.J.G. Silva. Composite stepped-lap adhesive joint analysis by cohesive zone modelling. *Procedia Struct Integr*, 33: 665–672, 2021. doi: 10.1016/j.prostr.2021.10.074.

W. Broughton. *Assessing the moisture resistance of adhesives for marine environments*, pages 155–186. Elsevier, 2012. ISBN 978-0-12-821078-9. doi: 10.1533/9780857096159.2.155.

R. Brown, J. Moidu, P. Colbourne, and J.K. Spelta. Low-stress creep deformation in two opto-electronic glass-epoxy joints: Part I – adhesive creep data. *Int J Adhes Adhes*, 86:139–146, 2018. doi: 10.1016/j.ijadhadh.2018.05.026.

S. Budhe, A. Rodríguez-Bellido, J. Renart, J.A. Mayugo, and J. Costa. Influence of pre-bond moisture in the adherents on the fracture toughness of bonded joints for composite repairs. *Int J Adhes Adhes*, 49:80–89, 2014. doi: 10.1016/j.ijadhadh.2013.12.007.

S. Budhe, M.D. Banea, and S. de Barros. Bonded repair of composite structures in aerospace application: a review on environmental issues. *Appl Adhes Sci*, 6, 2018. doi: 10.1186/s40563-018-0104-5.

C. Calì, G. Cricrì, and M. Perella. An Advanced Creep Model Allowing for Hardening and Damage Effects. *Strain*, 46:347–357, 2010. doi: 10.1111/j.1475-1305.2009.00682.x.

R.D.S.G Campilho, M.F.S.F. de Moura, and J.J.M.S. Domingues. Using a cohesive damage model to predict the tensile behaviour of CFRP single-strap repairs. *Int J Solids Struct*, 45:1497–1512, 2007. doi: 10.1016/j.ijsolstr.2007.10.003.

R.D.S.G. Campilho, M.F.S.F. de Moura, A.M.G. Pinto, J.J.L. Morais, and J.J.M.S. Domingues. Modelling the tensile fracture behaviour of CFRP scarf repairs. *Compos B*, 40:149–157, 2008. doi: 10.1016/j.compositesb.2008.10.008.

R.D.S.G. Campilho, M.F.S.F. de Moura, D.A. Ramantani, J.J.L. Morais, and J.J.M.S. Domingues. Tensile behaviour of three-dimensional carbon-epoxy adhesively bonded single- and double-strap repairs. *Int J Adhes Adhes*, 29:678–686, 2009. doi: 10.1016/j.ijadhadh.2009.02.004.

J.A. Cano and C.M. Stewart. A continuum damage mechanics (CDM) based Whilshire model for creep deformation, damage, and rupture prediction. *Mater Sci Eng A*, 799, 2020. doi: 10.1016/j.msea.2020.140231.

P. Chalkley and A. Baker. Development of a generic repair joint for certification of bonded composite repairs. *Int J Adhes Adhes*, 19:121–132, 1999. doi: 10.1016/S0143-7496(98)90028-8.

M.N. Charalambides, R. Hardouin, A.J. Kinloch, and F.L. Matthews. Adhesively-bonded repairs to fibre-composite materials I: Experimental. *Compos Struct A*, 29:1371–1381, 1998a. doi: 10.1016/S1359-835X(98)00060-8.

M.N. Charalambides, R. Hardouin, A.J. Kinloch, and F.L. Matthews. Adhesively-bonded repairs to fibre-composite materials II: Finite element modelling. *Compos Struct A*, 29:1383–1396, 1998b. doi: 10.1016/S1359-835X(98)00061-X.

M. Ciavarella, S. Zhang, H. Gao, and G. Cricri. A linear cohesive model of zero degree peeling of a viscoelastic tape from a substrate. *J Adhes Sci Tech*, 2022. doi: 10.1080/01694243.2022.2099785.

R. Cruz, L. Correia, S. Cabral-Fonseca, and J. Sena-Cruz. Effects of the preparation, curing and hygrothermal conditions on the viscoelastic response of a structural epoxy adhesive. *Int J Adhes Adhes*, 110, 2021. doi: 10.1016/j.ijadhadh.2021.102961.

L.F.M. da Silva and R.D. Adams. Techniques to reduce the peel stresses in adhesive joints with composites. *Int J Adhes Adhes*, 27:227–235, 2006. doi: 10.1016/j.ijadhadh.2006.04.001.

L.F.M. da Silva, A.G. de Magalhães, and M.F.S.F. de Moura. *Juntas Adesivas e Estruturais*. Publindústria, First edition, 2007. ISBN 978-972-8953-21-8.

L.F.M. da Silva, A. Öchsner, and R.D. Adams. *Handbook of Adhesion Technology*, volume 2. Springer, 2011. ISBN 978-3-642-01168-9. doi: 10.1007/978-3-642-01169-6.

S. Daylan. Failure Analysis of Adhesively Bonded CFRP Joints. Master's thesis, International Technology University (ITU), November 2021.

Development Center Maintenance Composites DCMC. Field & Onsite Repair of Composite Structures. `https://www.composite-maintenance.com/dcmc-innovation-tracks/5-2/`, 2021. [Accessed: 10-April-2023].

F. de Florio. *Airworthiness: An Introduction to Aircraft Certification and Operations*. Elsevier, Ltd., 2016. ISBN 978-0-08-100888-1.

M.F.S.F. de Moura and J.P.M. Gonçalves. Cohesive zone model for high-cycle fatigue of composite bonded joints under mixed-mode I+II loading. *Eng Fract Mech*, 140:31–42, 2015. doi: 10.1016/j.engfracmech.2015.03.044.

M.F.S.F. de Moura, J.P.M. Gonçalves, J.A.G. Chousal, and R.D.S.G. Campilho. Cohesive and continuum mixed-mode damage models applied to the simulation of the mechanical behaviour of bonded joints. *Int J Adhes Adhes*, 28:419–426, 2008a. doi: 10.1016/j.ijadhadh.2008.04.004.

M.F.S.F. de Moura, J.J.L. Morais, and N. Dourado. A new data reduction scheme for mode I wood fracture characterization using the double cantilever beam test. *Eng Fract Mech*, 75:3852–3865, 2008b. doi: 10.1016/j.engfracmech.2008.02.006.

M.F.S.F. de Moura, A.B. de Morais, and A.G. de Magalhães. *Materiais Compósitos: Materiais, Fabrico e Comportamento Mecânico*. Publindústria, Second edition, 2011. ISBN 978-972-8953-00-3.

C. de Zeeuw, S.T. de Freitas, D. Zarouchas, M. Schilling, R.L. Fernandes, P.D. Portella, and U. Niebergall. Creep behaviour of steel bonded joints under hygrothermal conditions. *Int J Adhes Adhes*, 91:54–63, 2019. doi: 10.1016/j.ijadhadh.2019.03.002.

B.V. Deryagin, N.A. Krotova, and V.P. Smilga. Adhesion of Solids. Technical report, Consultants Bureau New York and London, 1978.

S. Diel and O. Huber. A Continuum Damage Mechanics Model for the Static and Cyclic Fatigue of Cellular Composites. *Materials*, 10, 2017. doi: 10.3390/ma10080951.

D.S. Dugdale. Yielding of steel sheets containing slits. *J Mech Phys Solids*, 8:100–104, 1960. doi: 10.1016/0022-5096(60)90013-2.

E. Elmukashfi and A.C.F. Cocks. A theoretical and computational framework for studying creep crack growth. *Int J Fract*, 208:145–170, 2017. doi: 10.1007/s10704-017-0230-2.

E. Elmukashfi and A.C.F. Cocks. A theoretical and computational investigation of mixed mode creep crack growth along an interface. *Int J Fract*, 229:125–159, 2021. doi: 10.1007/s10704-021-00534-x.

Evident. Nondestructive Bond Testing for Aircraft Composites. `https://www.olympus-ims.com/en/applications/non-destructive-bond-testing-aircraft-composites/`, 2022. [Accessed: 10-April-2023].

Federal Aviation Administration FAA. AC 20-107B: Composite Aircraft Structure. Technical report, U.S Department of Transportation, 2009.

Federal Aviation Administration FAA. Aviation Maintenance Technician Handbook - Airframe (Volume 1). Technical report, U.S Department of Transportation, 2012.

Federal Aviation Administration FAA. AC43-214: Repairs and Alterations to Composite and Bonded Aircraft Structure. Technical report, U.S Department of Transportation, 2013.

Federal Aviation Administration FAA. FAR 21: Certification Procedures for Products and Articles (Subpart M). Technical report, U.S Department of Transportation, 2023.

P.A. Fay. *Adhesive Bonding: A history of adhesive bonding*. Elsevier, Ltd., Second edition, 2021. ISBN 978-0-12-819954-1.

R.L. Fernandes and R.D.S.G. Campilho. Testing different cohesive law shapes to predict damage growth in bonded joints loaded in pure tension. *J Adhes*, 93:57–76, 2016.

S. Fevery, S.K. Latré, D. Vandepitte, S. Debruyne, and H. Hallez. Combination and interaction of ageing parameters on single lap shear adhesive joints. *Int J Adhes Adhes*, 111, 2021. doi: 10.1016/j.ijadhadh.2021.102978.

W.N. Findley. Creep Characteristics of Plastics. *Symposium on Plastics, ASTM*, page 118, 1944.

W.N. Findley, J.S. Lai, and K. Onaran. *Creep and Relaxation of Nonlinear Viscoelastic Materials*. North-Holland Publishing Company, First edition, 1976. ISBN 0-444-10775-4.

U. Galietti, R. Dimitri, D. Palumbo, and P. Rubino. Thermal Analysis and Mechanical Characterization of GFRP Joints. In *ECCM15 - 15th European Conference on Composite Materials*, Venice, Italy, June 2012.

F. Garofalo. An Empirical Relation Defining the Stress Dependence to Minimum Creep Rate in Metals. *Trans Metall Soc, AIME*, 227, 1963.

P.L. Geiss. *Creep Load Conditions*, pages 875–902. Springer Berlin Heidelberg, Berlin, Heidelberg, 2011. ISBN 978-3-642-01169-6. doi: 10.1007/978-3-642-01169-6_34.

A. Gemant. A method of analyzing experimental results obtained by elasto-viscous bodies. *Physics*, 7:311–317, 1936. doi: 10.1063/1.1745400.

J.P.M. Gonçalves, M.F.S.F. de Moura, P.M.S.T. de Castro, and A.T. Marques. Interface Element Including Point-to-Surface Constraints for Three-Dimensional Problems with Damage Propagation. *Eng Comput: Int J Comput Aided Eng Technol*, 17:21–47, 2000. doi: 10.1108/02644400010308053.

A. Graham and K. Walles. Relationships between long and short time creep and tensile properties of a commercial alloy. *J Iron Steel Inst*, 179, 1955.

R.M. Guedes, A.T. Marques, and A. Cardon. Analytical and Experimental Evaluation of Nonlinear Viscoelastic-Viscoplastic Composite Laminates Under Creep, Creep-Recovery, Relaxation and Ramp Loading. *Mech Time Depend Mater*, 2:113–128, 1998. doi: 10.1023/A:1009862009738.

M.S. Haque and C.M. Maurice. Comparative analysis of the sin-hyperbolic and Kachanov-Rabotno creep-damage models. *Int J Press Vessel Pip*, 171:1–9, 2019. doi: 10.1016/j.ijpvp.2019.02.001.

L.J. Hart-Smith. Bonded-Bolted Composite Joints. *J Aircraft*, 22, 1985. doi: 10.2514/3.45237.

L.J. Hart-Smith. *Adhesive Bonding: Aerospace Industry Application of Adhesive Bonding*. Elsevier, Ltd., Second edition, 2021. ISBN 978-0-12-819954-1.

D.R. Hayhurst, P.R. Dimmer, and C.J. Morrison. Development of Continuum Damage in the Creep Rupture of Notched Bars. *Phil Trans R Soc Lond A*, 311:103–129, 1984. doi: 10.1098/rsta.1984.0021.

A. Hillerborg, M. Modéer, and P.-E. Peterson. Analysis of crack formation and crack growth in concrete by means of fracture mechanics and finite elements. *Cem Concr Res*, 6:773–781, 1976. doi: 10.1016/0008-8846(76)90007-7.

J. Hristov. *Prony's series and modern fractional calculus: Rheological models with Caputo-Fabrizio operator*, pages 187–200. Elsevier, 2022. ISBN 978-0-323-90032-4. doi: 10.1016/B978-0-323-90032-4.00005-5.

J.W. Hutchinson. Singular behaviour at the end of a tensile crack in a hardening material. *J Mech Phys Solids*, 16:13–31, 1968. doi: 10.1016/0022-5096(68)90014-8.

M. Jafaripour and F. Taheri-Behrooz. Creep behaviour modeling of polymeric composites using Schapery model based on micro-macromechanical approaches. *Eur J Mech A Solids*, 81, 2020. doi: 10.1016/j.euromechsol.2020.103963.

R. Jones, L. Molent, A. Baker, and M.J. Davis. Bonded repair of metallic components: Thick sections. *Theor Appl Fract Mech*, 9:61–70, 1988. doi: 10.1016/0167-8442(88)90049-3.

R. Jones, R. Bartholomeusz, R. Kaye, and J. Roberts. Bonded-composite repair of representative multi-site damage in a full-scale fatigue-test article. *Theor Appl Fract Mech*, 21:41–49, 1994. doi: 10.1016/0167-8442(94)90007-8.

A.W. Judge. Aircraft and Automobile Materials of Construction. *Non-Ferrous & Organic Materials*, 2:391–397, 1921.

K. Kamau-Devers and S.A. Miller. Using a micromechanical viscoelastic creep model to capture multi-phase deterioration in bio-based wood polymer composites exposed to moisture. *Constr Build Mater*, 314, 2022. doi: 10.1016/j.conbuildmat.2021.125252.

K.B. Katnam, L.F.M. da Silva, and T.M. Young. Bonded repair of composite aircraft structures: A review of scientific challenges and opportunities. *Prog Aero Sci*, 61:26–42, 2013. doi: 10.1016/j.paerosci.2013.03.003.

Y.F. Khalil. Comparative environmental and human health evaluations of thermolysis and solvolysis recycling technologies of carbon fiber reinforced polymer waste. *Waste Manage*, 76, 2018. doi: 10.1016/j.wasman.2018.03.026.

A. Kimiaeifar, H. Toft, E. Lund, O.T. Thomsen, and J.D. Sørensen. Reliability analysis of adhesive bonded scarf joints. *Eng Struct*, 35:281–287, 2011. doi: 10.1016/j.engstruct.2011.11.013.

J. Koyanagi, K. Hasegawa, A. Ohtani, T. Sakai, and K. Sakaue. Formulation of non-linear viscoelastic–viscoplastic constitutive equation for polyamide 6 resin. *Heliyon 7*, 2021. doi: 10.1016/j.heliyon.2021.e06335.

S. Kroshmanesh, S.J. Watson, and D. Zarouchas. The effect of the fatigue damage accumulation process on the damping and stiffness properties of adhesively bonded composite structures. *Compos Struct*, 287, 2022. doi: 10.1016/j.compstruct.2022.115328.

K.A. Lazopoulos, D. Karaoulanis, and A.K. Lazopoulos. On Λ-fractional visco-elastic beam. *Forces in Mechanics*, 7, 2022. doi: 10.1016/j.finmec.2022.100075.

J. Lejeune, V. Le Houéron, T. Chatel, H. Pelletier, C. Gauthier, and R. Mülhaupt. Creep and recovery analysis of polymeric materials during indentation tests. *Eur J Mech A Solids*, 68:1–8, 2018. doi: 10.1016/j.euromechsol.2017.10.003.

J.A. Lemaitre and J.L. Chaboche. A nonlinear model of creep-fatigue damage cumulation and interaction. In *In Proceedings of the IUTAM Symposium on Mechanics of Visco-Elastic Media and Bodies*, Berlin, Germany, 1975. Springer.

W. Li, X. Yang, G. Zhang, and Y. Ma. Cohesive zone modeling of creep–fatigue crack propagation with dwell time. *Adv Mech Eng*, 9:1–7, 2017. doi: 10.1177/1687814017721144.

C.-Y. Lin, Y.-C. Chen, C.-H. Lin, and K.-V. Chang. Constitutive Equations for Analyzing Stress Relaxation and Creep Viscoelastic Materials Based on Standard Linear Solid Model Derived with Finite Loading Rate. *Polym*, 14, 2022. doi: 10.3390/polym14102124.

ManoxBlog. Adhesion in Paints and Coatings. `https://manoxblog.com/2020/08/07/adhesion-in-paints-and-coatings/`, 2020. [Accessed: 08-March-2023].

J.C. Maxwell. IV. On the dynamical theory of gases. *Philos Trans R Soc*, 157:49–88, 1867. doi: 10.1098/rstl.1867.0004.

P.G. McVetty. Working stresses for high temperature service. *Mech Eng*, 56:149–154, 1934.

L.O. Meyer, K. Schulte, and E. Grove-Nielsen. CFRP recycling following a pyrolysis route: process optimization and potentials. *J Compos Mater*, 43:1121–1132, 2009. doi: 10.1177/0021998308097737.

I. Moir and A. Seabridge. *Aircraft Systems: Mechanical, Electrical, and Avionics Subsystems Integration*. John Wiley and Sons, Ltd., 2008. ISBN 978-0-470-05996-8.

R.D.F. Moreira. *Estudo do comportamento à fadiga de reparações adesivas de estruturas de alumínio com compósitos de carbono-epóxido*. PhD thesis, Faculdade de Engenharia da Universidade do Porto, 2021.

R.D.F. Moreira, M.F.S.F. de Moura, M.A.V. Figueiredo, R.L. Fernandes, and J.P.M. Gonçalves. Characterisation of composite bonded single-strap repairs under fatigue loading. *Int J Mech Sci*, 103:22–29, 2015. doi: 10.1016/j.ijmecsci.2015.09.001.

R.D.F. Moreira, M.F.S.F. de Moura, R.L. Fernandes, M.A.V. Figueiredo, and J.P.M. Gonçalves. Numerical and experimental analyses of composite bonded double-strap repairs under high-cycle fatigue. *J Adhes*, 93:980–992, 2016. doi: 10.1080/00218464.2016.1195736.

R.D.F. Moreira, V. Oliveira, F.G.A. Silva, R. Vilar, and M.F.S.F. de Moura. Influence of femtosecond laser treated surfaces on the mode I fracture toughness of carbon-epoxy bonded joints. *Int J Adhes Adhes*, 82:108–113, 2018a. doi: 10.1016/j.ijadhadh.2018.01.005.

R.D.F. Moreira, V. Oliveira, F.G.A. Silva, R. Vilar, and M.F.S.F. de Moura. Mode II fracture toughness of carbon–epoxy bonded joints with femtosecond laser treated surfaces. *Int J Mech Sci*, 148:707–713, 2018b. doi: 10.1016/j.ijmecsci.2018.09.029.

R.D.F. Moreira, M.F.S.F. de Moura, F.G.A. Silva, F.M.G. Ramírez, and F.D.R. Silva. Numerical comparison of several composite bonded repairs under fatigue loading. *Compos Struct*, 243, 2020a. doi: 10.1016/j.compstruct.2020.112250.

R.D.F. Moreira, M.F.S.F. de Moura, F.G.A. Silva, and J.P. Reis. High-cycle fatigue analysis of adhesively bonded composite scarf repairs. *Compos B*, 190, 2020b. doi: 10.1016/j.compositesb.2020.107900.

A.P. Mouritz. *Introduction to aerospace materials*. Woodhead Publishing, Ltd., 2012. ISBN 978-0-85709-515-2.

S. Murakami, Y. Liu, and M. Mizuno. Computational methods for creep fracture analysis by damage mechanics. *Comput Methods Appl Mech Eng*, 183:15–33, 2000. doi: 10.1016/S0045-7825(99)00209-1.

K. Nakamura, Y. Sekiguchi, K. Shimamoto, K. Houjou, H. Akiyama, and C. Sato. Creep Crack Growth Behavior during Hot Water Immersion of an Epoxy Adhesive Using a Spring-Loaded Double Cantilever Beam Test Method. *Materials*, 16, 2023. doi: 10.3390/ma16020607.

R.M. Carneiro Neto, A. Akhavan-Safar, E.M. Sampaio, J.T. de Assis, and L.F.M. da Silva. Effect of creep on the mode II residual fracture energy of adhesives. *J Appl Polym Sci*, 138, 2021. doi: 10.1002/app.51387.

R.M. Carneiro Neto, A. Akhavan-Safar, E.M. Sampaio, J.T. Assis, and L.F.M. da Silva. Assessment of the creep life of adhesively bonded joints using the end notched flexure samples. *Eng Fail Anal*, 133, 2022a. doi: 10.1016/j.engfailanal.2021.105969.

R.M. Carneiro Neto, A. Akhavan-Safar, E.M. Sampaio, J.T. de Assis, and L.F.M. da Silva. A customized shear traction separation law for cohesive zone modelling of creep loaded ENF adhesive joints. *Theor Appl Fract Mech*, 119, 2022b. doi: 10.1016/j.tafmec.2022.103336.

R.M. Carneiro Neto, F. de Medeiros Sales, E.M. Sampaio, A. Akhavan-Safar, J.T. de Assis, and L.F.M. da Silva. Cohesive zone models for the shear creep life assessment of bonded joints. *Mech Time-Depend Mat*, 2022c. doi: 10.1007/s11043-022-09548-x.

K.M. Nikbin, D.J. Smith, and G.A. Webster. Predicting of creep crack growth from uniaxial creep data. *Proc R Soc Lond*, 396:183–197, 1984. doi: 10.1098/rspa.1984.0116.

P.G. Nutting. A new general law of deformation. *J Franklin Inst*, 191:679–685, 1921. doi: 10.1016/S0016-0032(21)90171-6.

H.M. Nuwayer and G.M. Newaz. Flexural creep behavior of adhesively bonded metal and composite laminates. *Int J Adhes Adhes*, 84:220–226, 2018. doi: 10.1016/j.ijadhadh.2018.03.010.

C.L. Ong, R.C. Chu, T.C. Ko, and S.B. Shen. Composite patch reinforcement of cracked aircraft upper longeron: analysis and specimen simulation. *Theor Appl Fract Mech*, 14:13–26, 1990. doi: 10.1016/0167-8442(90)90040-7.

W. Oudad, K. Madani, B.B. Bouiadjra, M. Belhouari, S. Cohendoz, and S. Touzain. Effect of humidity absorption by the adhesive on the performances of bonded composite repairs in aircraft structures. *Compos B*, 43:3419–3424, 2012. doi: 10.1016/j.compositesb.2012.01.028.

V.B. Pandey, I.V. Singh, and B.K. Mishra. A new creep-fatigue interaction damage model and CDM-XFEM framework for creep-fatigue crack growth simulations. *Theor Appl Fract Mech*, 124, 2023. doi: 10.1016/j.tafmec.2022.103740.

M. Di Paola, A. Pirrotta, and A. Valenza. Visco-elastic behavior through fractional calculus: An easier method for best fitting experimental results. *Mech Mater*, 43:799–806, 2011. doi: 10.1016/j.mechmat.2011.08.016.

E.M. Petrie. *Handbook of Adhesives and Sealents*. McGraw-Hill, Second edition, 2007. ISBN 978-0-07-170981-1.

S. Pimenta and S.T. Pinho. Recycling carbon fibre reinforced polymers for structural applications: Technology review and market outlook. *Waste Manage*, 31:378–392, 2010. doi: 10.1016/j.wasman.2010.09.019.

A.M.G. Pinto, R.D.S.G. Campilho, M.F.S.F. de Moura, and I.R. Mendes. Numerical evaluation of three-dimensional scarf repairs in carbon-epoxy structures. *Int J Adhes Adhes*, 30:329–337, 2009. doi: 10.1016/j.ijadhadh.2009.11.001.

A. Poudel, K.R. Mitchell, T.P. Chu, S. Neidigk, and C. Jacques. Non-destructive evaluation of composite repairs by using infrared thermography. *J Compos Mater*, 50, 2015. doi: 10.1177/0021998315574755.

C.E. Pugh. Constitutive Equations for Creep Analysis of LFMBR Components. Technical report, Oak Ridge National Laboratory (Reactor Division), 1975.

Y.N. Rabotnov. Creep problems in structural members. Technical report, Amsterdam: North-Holland, 1969.

J.G.T. Ribeiro, J.T.P. de Castro, and M.A. Meggiolaro. Modeling concrete and polymer creep using fractional calculus. *J Mater Res Technol*, 12:1184–1193, 2021. doi: 10.1016/j.jmrt.2021.03.007.

A.N. Rider, C.H. Wang, and P. Chang. Bonded repairs for carbon/BMI composite at high operating temperatures. *Compos A*, 41:902–912, 2010. doi: 10.1016/j.compositesa.2010.03.006.

J.E. Robson, F.L. Matthews, and A.J. Kinloch. The bonded repair of fibre composites: Effect com of composite moisture content. *Compos Sci Tech*, 52:235–246, 1994. doi: 10.1016/0266-3538(94)90208-9.

K.F. Rogers, D.M. Kingston-Lee, and L.N. Phillips. The use of carbon and hybrid woven fabrics in emergency aircraft repair work. *Adv Compos Mater*, pages 1390–1407, 1980. doi: 10.1016/B978-1-4832-8370-8.50111-X.

A.D. La Rosa, S. Greco, C. Tosto, and G. Cicala. LCA and LCC of a chemical recycling process of waste CF-thermoset composites for the production of novel CF-thermoplastic composites. Open loop and closed loop scenarios. *J Clean Prod*, 304, 2021. doi: 10.1016/j.jclepro.2021.127158.

B. Ross. The development of fractional calculus 1695-1900. *Hist Math*, 4:75–89, 1977.

M.A.S. Sadigh, B. Paygozar, L.F.M. da Silva, and F.V. Tahami. Creep deformation simulation of adhesively bonded joints at different temperature levels using a modified power-law model. *Polym Test*, 79, 2019. doi: 10.1016/j.polymertesting.2019.106087.

M.A.S Sadigh, B. Paygozar, L.F.M. da Silva, and E. Martínez-Pañeda. Creep behaviour and tensile response of adhesively bonded polyethylene joints: Single-Lap and Double-Strap. *Int J Adhes Adhes*, 102, 2020. doi: 10.1016/j.ijadhadh.2020.102666.

T. Sadowski, P. Golewski, and E. Zarzeka-Raczkowska. Damage and failure processes of hybrid joints: Adhesive bonded aluminium plates reinforced by rivets. *Comput Mat Sci*, 50:1256–1262, 2010. doi: 10.1016/j.commatsci.2010.06.022.

Samaro. ARALDITE 2015. `samaro.fr/en/product/araldite-2015-1/`, 2023. [Accessed: March-2023].

M. Sattar, A.R. Othman, M. Muzamil, S. Kamaruddin, M. Akhtar, and R. Khan. Correlation Analysis of Established Creep Failure Models through Computational Modelling for SS-304 Material. *Metals*, 13, 2023. doi: 10.3390/met13020197.

R.A. Schapery. On the characterisation of nonlinear viscoelastic materials. *Polym Eng Sci*, 9: 295–310, 1969. doi: 10.1002/pen.760090410.

P. Schrader, C. Schmandt, and S. Marzi. Mode I creep fracture of rubber-like adhesive joints at constant crack driving force. *Int J Adhes Adhes*, 113, 2022. doi: 10.1016/j.ijadhadh.2021.103079.

F.G.A. Silva, M.F.S.F. de Moura, and R.D.F. Moreira. Influence of adverse temperature and moisture conditions on the fracture behaviour of single-strap repairs of carbon-epoxy laminates. *Int J Adhes Adhes*, 96, 2020. doi: 10.1016/j.ijadhadh.2019.102452.

J. Simsiriwong, R.W. Sullivan, T.E. Lacy Jr., and H.H. Hilton. A statistical approach to characterize the viscoelastic creep compliances of a vinyl ester polymer. *Polym Test*, 78:183–198, 2015. doi: 10.1016/j.polymertesting.2015.10.001.

R. Song, A.H. Muliana, and A. Palazotto. An empirical approach to evaluate creep responses in polymers and polymeric composites and determination of design stresses. *Compos Struct*, 148: 207–223, 2016. doi: 10.1016/j.compstruct.2016.03.041.

G. Spathis and E. Kontou. Creep failure time prediction of polymers and polymer composites. *Compos Sci Technol*, 72:959–964, 2012. doi: 10.1016/j.compscitech.2012.03.018.

T. Sun, C. Yu, W. Yang, J. Zhong, and Q. Xu. Experimental and numerical research on the nonlinear creep response of polymeric composites under humid environments. *Compos Struct*, 251, 2020. doi: 10.1016/j.compstruct.2020.112673.

Y. Sun, K. Maciejewski, and H. Ghonem. A damage-based cohesive zone model of intergranular crack growth in a nickel-based superalloy. *Int J Damage Mech*, 22:905–923, 2012. doi: 10.1177/1056789512468917.

W. Tan, Z. Zhou, J. Na, and W. Mu. Influence of Temperature, Humidity and Load Coupling on Mechanical Properties of Adhesive Joints and Establishment of Creep Model. *Polymers*, 15, 2023. doi: 10.3390/polym15020339.

E. Tanaka and T. Van Eijden. Biomechanical Behaviour of the Temporomandibular Joint Disc. *Crit Rev Oral Biol*, 14:75–150, 2003. doi: 10.1177/154411130301400207.

Twin Cities Aviation TCA. Twin Cities Aviation – Composite Repair. `https://tcaviation.com/composite_repair/`, 2022. [Accessed: 10-April-2023].

T. Ting, R. Jones, W.K. Chiu, I.H. Marshall, and J.M. Greer. Composite repairs to rib stiffened panels. *Compos Struct*, 47:737–743, 1999. doi: 10.1016/S0263-8223(00)00046-5.

A. Tomczyk and A. Seweryn. Experimental Investigation and Modeling of Damage Accumulation of EN-AW2024 Aluminum Alloy under Creep Condition at Elevated Temperature. *Materials*, 14, 2021. doi: 10.3390/ma14020404.

B.R. Trethewey, J.W. Gillespie, and L.A. Carlsson. Mode II Cyclic Delamination Growth. *J Compos Mater*, 22:459–483, 1988. doi: 10.1177/002199838802200506.

USAF. Fokker Dr.I. `https://www.nationalmuseum.af.mil/Visit/Museum-Exhibits/Fact-Sheets/Display/Article/197402/fokker-dr-i/`, 2022a. [Accessed: 31-January-2023].

USAF. De Havilland DH 98 Mosquito. `https://www.nationalmuseum.af.mil/Visit/Museum-Exhibits/Fact-Sheets/Display/Article/196281/de-havilland-dh-98-mosquito/`, 2022b. [Accessed: 31-January-2023].

S. Wang, T. Stratford, and T.P.S. Reynolds. Linear creep of bonded FRP-strengthened metallic structures at warm service temperatures. *Constr Build Mater*, 283, 2021. doi: 10.1016/j.conbuildmat.2021.122699.

Y. Wu, G. Li, F. Tan, Y. Li, and Z. He. Research on creep damage model of high alumina bricks. *Ceram Int*, 48, 2022. doi: 10.1016/j.ceramint.2022.06.076.

M. Yatomi and M. Tabuchi. Issues relating to numerical modelling of creep crack growth. *Eng Fract Mech*, 77:3043–3052, 2010. doi: 10.1016/j.engfracmech.2010.04.024.

M. Yatomi, K.M. Nikbin, and N.P. O'Dowd. Creep crack growth prediction using a damage based approach. *Int J Press Vessel Pip*, 80:573–583, 2003. doi: 10.1016/S0308-0161(03)00110-8.

G. Youssef. *Creep behaviour of polymers*, pages 145–164. Elsevier, San Diego State University, San Diego, CA, USA, 2022. ISBN 978-0-12-821078-9. doi: 10.1016/B978-0-12-821078-9.00001-6.

W. Zhou, X. Ji, S. Yang, J. Liu, and L. Ma. Review on the performance improvements and non-destructive testing of patches repaired composites. *Compos Struct*, 263, 2021. doi: 10.1016/j.compstruct.2021.113659.

L. Škec and G. Alfano. Experimental and numerical study of rate-dependent mode-I failure of a structural adhesive. *J Adhes*, 2022. doi: 10.1080/00218464.2022.2106132.